

AFRL-SN-WP-TR-2003-1113

**AlGaN DIRECTIONAL COUPLER
SWITCH**

Antonio Crespo



**Multi-Chip Integration Branch (AFRL/SNDI)
Aerospace Components and Subsystems Technology Division
Sensors Directorate
Air Force Research Laboratory, Air Force Materiel Command
Wright-Patterson Air Force Base, OH 45433-7318**

May 2002

Final Report for 01 June 1997 – 05 May 2002

Approved for public release; distribution is unlimited.

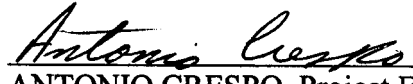
**SENSORS DIRECTORATE
AIR FORCE RESEARCH LABORATORY
AIR FORCE MATERIEL COMMAND
WRIGHT-PATTERSON AIR FORCE BASE, OH 45433-7318**

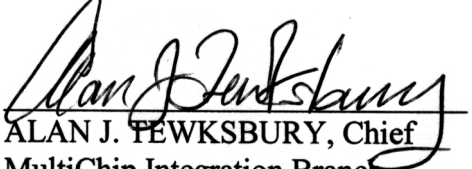
NOTICE

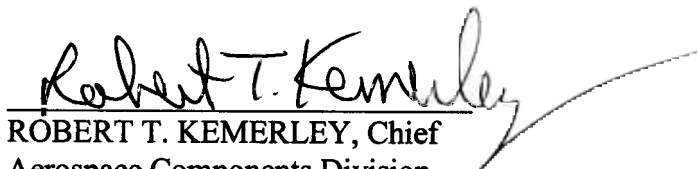
Using government drawings, specifications, or other data included in this document for any purpose other than government procurement does not in any way obligate the U.S. Government. The fact that the government formulated or supplied the drawings, specifications, or other data does not license the holder or any other person or corporation; or convey and rights or permission to manufacture, use, or sell any patented invention that may relate to them.

This report has been reviewed by the Office of Public Affairs (ASC/PA) and is releasable to the National Technical Information Service (NTIS). At NTIS, it will be available to the general public, including foreign nations.

This technical report has been reviewed and is approved for publication.


ANTONIO CRESPO, Project Engineer
Electron Devices Branch
Aerospace Components Division


ALAN J. PEWKSURY, Chief
MultiChip Integration Branch
Aerospace Components Division


ROBERT T. KEMERLEY, Chief
Aerospace Components Division
Sensors Directorate

Copies of this report should not be returned unless return is required by security considerations, contractual obligations, or notice on a specific document.

REPORT DOCUMENTATION PAGE

Form Approved
OMB No. 0704-0188

The public reporting burden for this collection of information is estimated to average 1 hour per response, including the time for reviewing instructions, searching existing data sources, searching existing data sources, gathering and maintaining the data needed, and completing and reviewing the collection of information. Send comments regarding this burden estimate or any other aspect of this collection of information, including suggestions for reducing this burden, to Department of Defense, Washington Headquarters Services, Directorate for Information Operations and Reports (0704-0188), 1215 Jefferson Davis Highway, Suite 1204, Arlington, VA 22202-4302. Respondents should be aware that notwithstanding any other provision of law, no person shall be subject to any penalty for failing to comply with a collection of information if it does not display a currently valid OMB control number. **PLEASE DO NOT RETURN YOUR FORM TO THE ABOVE ADDRESS.**

1. REPORT DATE (DD-MM-YY) May 2002			2. REPORT TYPE Final		3. DATES COVERED (From - To) 06/01/97 – 05/05/02	
4. TITLE AND SUBTITLE AlGaN DIRECTIONAL COUPLER SWITCH			5a. CONTRACT NUMBER IN-HOUSE 5b. GRANT NUMBER 5c. PROGRAM ELEMENT NUMBER N/A			
6. AUTHOR(S) Antonio Crespo			5d. PROJECT NUMBER N/A 5e. TASK NUMBER N/A 5f. WORK UNIT NUMBER N/A			
7. PERFORMING ORGANIZATION NAME(S) AND ADDRESS(ES) Multi-Chip Integration Branch (AFRL/SNDI) Aerospace Components and Subsystems Technology Division Sensors Directorate Air Force Research Laboratory, Air Force Materiel Command Wright-Patterson Air Force Base, OH 45433-7318					8. PERFORMING ORGANIZATION REPORT NUMBER AFRL-SN-WP-TR-2003-1113	
9. SPONSORING/MONITORING AGENCY NAME(S) AND ADDRESS(ES) Sensors Directorate Air Force Research Laboratory Air Force Materiel Command Wright-Patterson Air Force Base, OH 45433-7318					10. SPONSORING/MONITORING AGENCY ACRONYM(S) AFRL/SNDI 11. SPONSORING/MONITORING AGENCY REPORT NUMBER(S) AFRL-SN-WP-TR-2003-1113	
12. DISTRIBUTION/AVAILABILITY STATEMENT Approved for public release; distribution is unlimited.						
13. SUPPLEMENTARY NOTES This report contains color.						
14. ABSTRACT (Maximum 200 Words) The dissertation describes an attempt to develop, including material processing, a zero-gap directional coupler using the AlGaN material system in an n-i-n configuration that was grown by MBE. This work compiles the optical and electro-optical properties and models the behavior of AlGaN integrated optic waveguides. The switches are based on the zero-gap electro-optic directional coupler. The models are compared with the experimental results that were obtained. The models used were the Marcatili and the beam propagation method. Models for predicting the index of refraction of AlGaN versus AL concentration are treated. An advantage of the AlGaN integrated optic waveguides and switches is the potential to work at wavelengths from IR to the blue region. AlGaN has the potential to work at high temperatures and in harsh environments. The wavelength chosen for this work is 632.8 nm for a HeNe laser.						
The results show that an electro-optic switch is viable in the AlGaN system. Material maturity is necessary to improve performance. The models chosen were shown to be inaccurate by themselves. Together, they are a viable source for the development of a directional coupler surround by air.						
15. SUBJECT TERMS Directional Coupler, Optics, Gallium Nitride, AlGaN, Optical Modulator, Optical Switch						
16. SECURITY CLASSIFICATION OF:			17. LIMITATION OF ABSTRACT: SAR	18. NUMBER OF PAGES 198	19a. NAME OF RESPONSIBLE PERSON (Monitor) Antonio Crespo 19b. TELEPHONE NUMBER (Include Area Code) (937) 255-4557 x3450	
a. REPORT Unclassified	b. ABSTRACT Unclassified	c. THIS PAGE Unclassified				

TABLE OF CONTENTS

I. INTRODUCTION	1
<u>Dissertation Organization</u>	12
II. WAVEGUIDES	13
<u>Rectangular Waveguides</u>	17
<u>Beam Propagation Method</u>	23
III. ELECTRO-OPTIC EFFECT	27
IV. DIRECTIONAL COUPLER	36
<u>Active Directional Coupler</u>	41
<u>Symmetrical Directional Coupler</u>	44
<u>Crosstalk</u>	46
<u>Bending Sections</u>	48
V. AlGaN	51
<u>Crystal Growth</u>	54
<u>Optical Properties</u>	59
VI. EXPERIMENTATION AND RESULTS	63
<u>Design</u>	64
<u>First Mask Set Processing, and Results</u>	74
<u>Second Mask Set Design, Processing, and Results</u>	89
<u>Third Mask Set Processing, and Results</u>	115
VII. DISCUSSION OF RESULTS AND CONCLUSION	128
<u>Future Work</u>	135
APPENDIX A. CONFIGURATION OF MASK 1	136
APPENDIX B. ETCHING MASK AND RECIPIE DEVELOPEMENT	138
B.1 <u>Initial Mask and ICP Recipe Development</u>	139
B.2 <u>ICP Recipe Development for Sidewall Improvement</u>	142

APPENDIX C. PROCESS FOLLOWERS	144
C.1 <u>First process follower for passive Waveguides</u>	144
C.2 <u>Process follower for second Mask set</u>	146
C.3 <u>Process follower for Third Mask set</u>	159
APPENDIX D. MASK TEMPLATE ARRANGEMENT	169
D.1 <u>Second mask template arrangement</u>	169
D.2 <u>Third mask template arrangement</u>	170
REFERENCES	171

LIST OF FIGURES

Figure 1.1 Packaging interconnection levels, (a) level 3 (wirebond), (b) level 2 (TAB), and (c) level 1 (C4); from reference [4]	2
Figure 1.2 Incidence at an interface	3
Figure 1.3 Basic electro-optic switching structure.....	7
Figure 1.4. Mach-Zehnder interferometer.....	7
Figure 1.5 Active Directional coupler.....	8
Figure 1.6 Three electrode directional coupler	10
Figure 2.1 Slab Waveguide	13
Figure 2.2 Illustration of the phase condition that leads to the eigenvalue equation, from reference 22.....	14
Figure 2.3. Mode chart for a symmetric slab waveguide	16
Figure 2.4. Rectangular Waveguide	17
Figure 2.5. Mode chart for a rectangular waveguide	22
Figure 3.1 Spring model of Crystal bonding, from reference [24, 25]	27
Figure 3.2 Index ellipsoid of a uniaxial crystal, from reference [25,26].....	30
Figure 4.1 Even and odd mode of a Directional coupler	37
Figure 4.2 a) mode's field pattern for the two separated waveguides, b) sum of the odd and even fields	37
Figure 4.3 Push pull directional coupler	42
Figure 4.4 Switching a directional coupler	43
Figure 4.5 Effects of asymmetries in a directional coupler. Eigenmode profiles for various fabrication differences. From reference 28	47
Figure 4.6 Bending sections of a directional coupler.....	49

Figure 5.1 Hexagonal Unit Cell (heavy lines)	51
Figure 5.2 Threading dislocations in GaN Grown by MOCVD from reference 47.....	53
Figure 5.3 Dual Flow MOCVD, from reference 66.....	55
Figure 5.4 Basic MBE design from reference 54 and 55	56
Figure 5.5 TEM showing dislocation density reduction via LEO, from reference 61	58
Figure 5.6 AlGaN transmissivity	59
Figure 6.1 Proposed structure a) single waveguide b) interaction region	63
Figure 6.2 Refraction index variation for $I = 632.8$ nm from ref 71	65
Figure 6.3 Cross sectional view of a directional coupler in the interacting region.....	66
Figure 6.4 Mode chart for the single mode rectangular waveguide using the Marcatili's model, waveguide width 2.0 μm	67
Figure 6.5 Mode chart for the single mode rectangular waveguide using the Marcatili's model, waveguide width 1.5 μm	68
Figure 6.6 Side view of the single mode waveguide structure for AlGaN, x is chosen to be 1.5 and 2.0 μm	69
Figure 6.7 Intensity profile of a straight directional coupler, Waveguide width 2.0 μm Based on Brunner <i>et al.</i> ⁷¹	70
Figure 6.8 Mode power for each waveguide, waveguide width 2.0 μm . Based on Brunner <i>et al.</i> ⁷¹	71
Figure 6.9 Cross sectional view of the directional coupler in the direction of propagation, according to the beam propagation method by BeamProp. Waveguide width is 2.0 μm . Based on Brunner <i>et al.</i> ⁷¹	72
Figure 6.10 Mode chart for the interaction region of the directional coupler, using the Marcatili's model, corresponding to the 2 μm . Total width is 4 μm . Based on Brunner <i>et al.</i> ⁷¹	72
Figure 6.11 Mode power for each waveguide, Waveguide width 1.5 μm . Based on Brunner <i>et al.</i> ⁷¹	73

Figure 6.12 Mode chart for the interaction region of the directional coupler, using the Marcatili's model, corresponding to the 1.5 μm . Total width is 3 μm . Based on Brunner <i>et al.</i> ⁷¹	73
Figure 6.13 Crystal orientation between sapphire and AlGaN	74
Figure 6.14 Process flow for the transfer of the Mask template pattern into the sample..	76
Figure 6.15 End polishing of a waveguide using the FIB	77
Figure 6.16 Etched mirror (a) close up of the mirror, (b) mirror with respect to spec present near the waveguide	77
Figure 6.17 Schematic of testing setup	78
Figure 6.18 Light guidance. Both images are of the same region (a) output with lights on and (b) output with lights off	79
Figure 6.19 Light coupling into the spec shown in Figure 6.16 b)	79
Figure 6.20 Light being launch in a directional coupler and viewed a), c) at 11° from normal, b), d) viewed normal to the sample. c) and d) were taken 1.2 mm down from a) and b)	80
Figure 6.21 Output of the directional coupler. a) electron micrograph b) optical output .	81
Figure 6.22 1.4 μm waveguides using AlGaN at 5% Al concentration for cladding layer	82
Figure 6.23 Simulation of a 1.4 μm waveguide by the beam propagation method. Based on Brunner <i>et al.</i> ⁷¹	82
Figure 6.24 Indices of refraction based on Bergman et al. at room temperature and 632.8 nm, reference 69.....	83
Figure 6.25 New simulations of the waveguide that shows strong guidance. The parameters for this one is as follows: width 1.4 μm , core 0.8 μm , Al concentration 5%. Based on Bergmann <i>et al.</i> ⁶⁹	84
Figure 6.26 Marcatili's simulation using the new refraction indices and the 1.4 μm waveguide, Al concentration 5%. Based on Bergmann <i>et al.</i> ⁶⁹	85
Figure 6.27 Marcatili's simulation using the new refraction indices and the 2.0 μm waveguide, Al concentration 5%. Based on Bergmann <i>et al.</i> ⁶⁹	85

Figure 6.28 Mode chart for the interaction region of the directional coupler, using the Marcatili's model, corresponding to the 2 μm . Total width is 4 μm . Based on Bergmann <i>et al.</i> ⁶⁹	86
Figure 6.29 An entire directional coupler simulated by the beam propagation method. The waveguide branches are 1.4 μm wide. The coupling region is 3750 μm long.....	87
Figure 6.30 New directional coupler design.	89
Figure 6.31 Metal contacts on the directional coupler.....	90
Figure 6.32 Test for placing a metal contact on top of the coupling region in a directional coupler.....	91
Figure 6.33 Ohmic contact configuration with metal pad and an air bridge.....	92
Figure 6.34 Overview of the processing steps that were implemented on the second mask set.	93
Figure 6.35 Top view diagram of the active directional coupler. Not to scale	94
Figure 6.36 Waveguide Junction in a directional coupler a) sketch of the template mask for the 1.4 μm , b) failed transfer of the pattern to the photoresist.	95
Figure 6.37 Crossectional view of the photoresist pattern transfer of the junction region of the directional coupler.....	96
Figure 6.38 SEM of etched samples with uneven etching	97
Figure 6.39 EDAX of sample after freon over etch	98
Figure 6.40 Directional coupler output region.....	99
Figure 6.41 Launching convention for the experiments	99
Figure 6.42 Light exiting the directional coupler with a theoretical interaction length of 3190 μm . Magnification is 200x.....	100
Figure 6.43 Higher magnification (800x)of the directional coupler of Figure 6.42 with a) the lights off and b) the lights on.	101
Figure 6.44 Attenuation of the laser using the directional coupler of Figure 6.43. Light was launched on the left side. Light launched at the left side.....	101

Figure 6.45 Right side launching in same structure as in Figure 6.44 and with attenuation	102
Figure 6.46 Measured data and corrected data taken from the directional couplers of a single sample. The values are in the P_2/P_1 ratio form.	105
Figure 6.47 Detailed dimensions of a directional coupler sample	106
Figure 6.48 Comparison of the data from sample A12941 with theoretical predictions for 1.71 μm width branches.....	107
Figure 6.49 Comparison of the data from sample A28542 with theoretical predictions for 1.73 μm width branches.....	109
Figure 6.50 SEM image of contact on top of the directional coupler.	110
Figure 6.51. First annealing attempt with an RTA at 850° C for 30s	110
Figure 6.52 Lower magnification than figure Figure 6.51	111
Figure 6.53 EDAX analysis of the contacts after annealing. The Black outline is from the center section and the solid graph is from the morphologically different tip.	111
Figure 6.54 SEM images of the bridges.....	112
Figure 6.55. I-V curve of active device.....	112
Figure 6.56. Active directional coupler that cracked after applying voltage.	113
Figure 6.57 Junction in a directional coupler directly on the mask	114
Figure 6.58 Transferred pattern into the AlGaN/GaN/AlGaN material.....	115
Figure 6.59 Junction of a directional coupler with the new mask template and the process outlined in APPENDIX C.3	116
Figure 6.60 Different junction done with the third mask template.....	117
Figure 6.61 Measured data and corrected data taken from the directional couplers of a sample. The values are in the P_2/P_1 ratio form.....	118
Figure 6.62 The targeted new configuration for the active device.....	118
Figure 6.63 Least square fit of the data with Equations (4-10) and (4-11). Coupling length is 63.954 μm	119

Figure 6.64 Comparison of the data from sample A287-1-1 and the beam propagation method with air covering the sample.....	120
Figure 6.65 EDAX of a bare spot on the A28711 sample	121
Figure 6.66 Cross-sectional view at a contact pad for sample A287-1-1	121
Figure 6.67. Comparison of the data and simulations with the beam propagation method.	122
Figure 6.68 I-V curve of a structure in sample A287-1-1. The on resistance is between 10-12 k Ω s.....	123
Figure 6.69 I-V curve of sample A421-3-1 in which attempts were made to obtain insulating GaN	124
Figure 6.70 Image obtained from the output of a directional coupler of sample A421-3-1.	125
Figure 6.71 Light intensity variation with the application of 25 V on a device in sample A421-3-1.....	126
Figure 6.72 Modulation of the directional coupler. Image enhancements were done to accentuate the intensity variation.....	127
Figure 7.1 Photoresist before metal mask deposit. a) Junction region of a directional coupler, b) corner of a letter.....	128
Figure 7.2. Metal contact on top of the coupling region of a directional coupler.....	129
Figure 7.3 Side view of the single mode waveguide structure for AlGaN	130
Figure 7.4 Intensity profile in the single mode waveguide	130
Figure 7.5 Comparison of the 1.71 μ m waveguides.	131
Figure 7.6. Output from the 1.71 μ m branch width directional coupler, sample A12941	132
Figure 7.7 Mode chart of the interaction region for a 1.71 μ m branch width directional coupler.....	133
Figure 7.8. Structure of the modulating directional coupler	134

LIST OF TABLES

Table 1. Material Parameters for 300 K.....	52
Table 2. Coefficient for the Sellmeier dispersion formula, from reference 69	61
Table 3. Refraction index parameters for Equation (6-1)	64
Table 4 Small DOE.....	97
Table 5 Sample of data taken from a single directional coupler. The ratio is set as $P_{\text{non-incident branch}} / P_{\text{incident branch}}$	104
Table 6. Widths of the directional coupler. Height is 2.09 μm . Sample number is A12941	106
Table 7. Widths of the directional coupler. Height is 1.986 μm . Sample number is A28542.....	108

ABSTRACT

AlGaN DIRECTIONAL COUPLER SWITCH

Crespo Antonio
University of Dayton, 2002

Advisor: Dr. Mohammad A. Karim

This dissertation describes an attempt to develop, including material processing, a zero-gap directional coupler using the AlGaN material system in an *n-i-n* configuration that was grown by MBE. This work compiles the optical and electro-optical properties and models the behavior of AlGaN integrated optic waveguides. The switches are based on the zero-gap electro-optic directional coupler. The models are compared with the experimental results that were obtained. The models used were the Marcatili and the beam propagation method. Models for predicting the index of refraction of AlGaN versus Al concentration are treated. An advantage of the AlGaN integrated optic waveguides and switches is the potential to work at wavelengths from IR to the blue region. AlGaN has the potential to work at high temperatures and in harsh environments. The wavelength chosen for this work is 632.8 nm from a HeNe laser.

The results show that an electro-optic switch is viable in the AlGaN system. Material maturity is necessary to improve performance. The models chosen were shown to be

inaccurate by themselves. Together they are a viable source for the development of a directional coupler surrounded by air.

ACKNOWLEDGEMENTS

I would like to express my sincere thanks to many individuals who have helped me through out this effort. These include my family, professors, colleagues, and friends. I am indebted to them and would like to particularly thank the following individuals:

Professor Mohammad Karim, for his guidance and encouragement during my studies at the University of Dayton and for his support and expertise in bringing this dissertation to completion. I would also like to thank professors Joseph W. Haus, Frank Scarpino, and Muhammad Islam for their participation on my dissertation committee.

Special thanks would go to my colleagues Joseph Van Nostrand and Rebecca Cortez for direct support in the dissertation. Joseph grew the AlGaN/GaN epi for device processing and Rebecca spent many hours polishing the ends of the waveguides, as well as analyzing them on the SEM and the EDAX. Paul Cassity etched the AlGaN material. Dave Via, helped in the mask design. To the entire RF components team (Dave Via, Jim Sewell, and Bob Fitch) for their support and guidance in the process development. To my supervisors (Allan Tewksbury, Tim Kemerley, and Don Hanson), for their support and encouragement. To Dale Stevens, my friend and colleague, for the discussions, support, and encouragement through out this endeavor. To Joe Brandelik, for his help in correcting the final document. For all those who directly or indirectly contributed to the research effort and are too numerous to mention.

Last but not least to my wonderful wife, Luz N. Ramos, and children, Neldys C. Crespo, Javier A. Crespo, and Daniel E. Crespo, for their patience, support, sacrifices, and encouragement through out the years on this endeavor.

CHAPTER I

INTRODUCTION

As technology advances, electronic circuits increase in complexity and performance. This increase also requires an increase in the number of interconnections per chip and an increase in the interconnection's speed, otherwise the bottlenecks created will limit the overall system performance. The interconnections include: chip-to-chip on a common multichip module, multichip module to multichip module, and board-to-board communication through a back plane. The current trend in technology is heading towards multi-gigahertz communication between processing circuits and greater than 2000 pins per chip in the near future.¹ The increasing cost in terms of power, size, component count weight and reliability of implementing the required interconnects electrically has motivated serious consideration of replacing electrical interconnects with optical interconnects.² The data rates at which cost-effective communication through an electrical interconnect can be transmitted is limited to low (in the 10's of) gigahertz rates.^{2,3} This results from the fact that electrical wires and striplines incur frequency dependent dissipative losses due to conductive and dielectric properties. Electric lines have frequency dependent parasitic coupling losses due to radiative and surface wave propagation properties. However, optical interconnects can transmit data at higher frequencies with orders of magnitude lower losses than their electrical counterparts.³

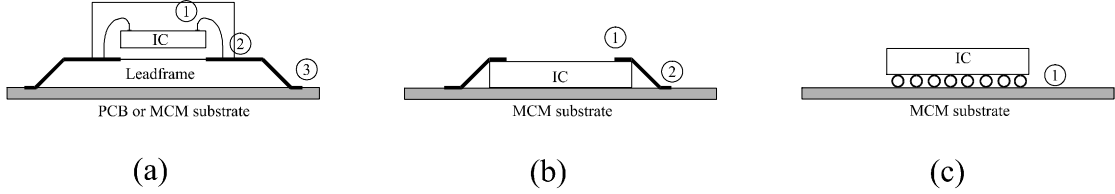


Figure 1.1 Packaging interconnection levels, (a) level 3 (wirebond), (b) level 2 (TAB), and (c) level 1 (C4); from reference [4]

In chip-to-chip connection bonding, large pads are needed to make connections between the chips and the MCM substrate. The large capacitance and inductance of the pads tends to increase the interconnect's power dissipation and reduce the interconnect's bandwidth. The number of contacts needed to connect the chip to a substrate, known as contact level, also influences the bandwidth, Figure 1.1 shows some examples. Transmission line effects will dominate the interconnection when line distances are greater than $1/10^{\text{th}}$ of the electrical signal wavelength. This results in attenuation of the electrical signals through skin effects, degradation of signal integrity due to reflections, and increased power dissipation occurring with terminating resistors.⁵ Within the MCM the electrical interconnects are well suited to handle communications below the 10's of GHz and no significant increase in MCM size.² For the MCM-MCM communications the bottleneck increases. The bandwidth and the connection densities are reduced by more than an order of magnitude. In the backplane level, electrical interconnects would have difficulty in meeting a bandwidth times length times density product exceeding 20 GHz cm/mm.²

Optical communication has an inherently high bandwidth. The optical carrier has a frequency of the order of $\sim 10^{14}$ Hz, orders of magnitude higher than any modulation source available today. Thus, it is able to meet the communication bandwidth for the

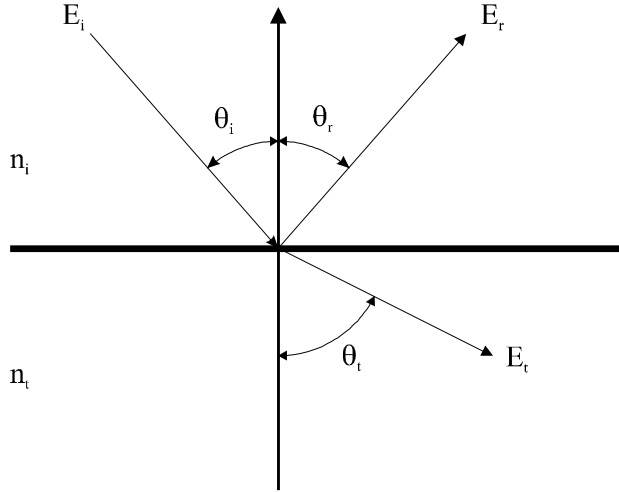


Figure 1.2 Incidence at an interface

foreseeable future. Photons will propagate across transparent material with little attenuation and power dissipation. The attenuation and power dissipation will not vary with the modulation frequency. By varying the index of refraction of the transparent material, light can be guided along a predetermined path (optical interconnection) to its final destination. This is due to the total internal reflection (TIR) phenomena. When light is incident at an interface, see Figure 1.2, it is transmitted and reflected according to:

$$n_i \sin \mathbf{q}_i = n_t \sin \mathbf{q}_t \quad \text{Snell's law} \quad (1-1)$$

$$\mathbf{q}_i = \mathbf{q}_r \quad \text{Reflection law} \quad (1-2)$$

When $n_t < n_i$ equation (1-1) tells us that there is a critical angle $\mathbf{q}_i = \mathbf{q}_c$ for which $\mathbf{q}_t = 90^\circ$. At this angle TIR occurs and light is totally reflected back into the medium. Therefore if a higher index media is sandwiched between two lower index media, light can be confined to the lower index media.

Current optical fibers have attenuation in the order of 0.2 dB/km and integrated optical interconnects are in the order of 0.2 db/cm, for plastic waveguides. The advantages of

optical interconnects include the difficulty of photons interacting with each other, their immunity to electro-magnetic interference (EMI), increased I/O density, increase communication speed, reduced crosstalk, and their ease of impedance control.^{5,6} Optical interconnects are starting to be utilized in chassis-to-chassis and board-to-board communications using glass optical fibers, although with some limitations.^{3,7,8} These optical fibers are lightweight and need little shielding from cross talk. For a rapid introduction of optical interconnects into the computer arena its manufacturing procedures must be compatible with the electrical components, for which a huge industrial base is already in place. The point at which optics will become competitive with electronics is a function of cost, interconnection distance, signal density, bit rate, and fanout.⁴ If, in addition, switching operations could be incorporated into the optical interconnection, without optical-electrical-optical conversion, reconfigurable interconnects would be achieved without a reduction in the available bandwidth. Aluminum Gallium Nitride (AlGaN), and other III-V materials, possesses an electro-optical effect that can be utilized to fabricate optical switches and modulators.

$\text{Al}_x\text{Ga}_{1-x}\text{N}$ has recently enjoyed an increased interest because of its wide and direct band gap, which ranges from 3.4 - 6.2 eV for x ranges of 0 - 1 for the wurtzite structure. This makes it ideally suited for blue to UV lasers. An additional advantage of this material is that electronic devices made from it are more tolerant, than Si or GaAs devices, to elevated temperatures and caustic environments.⁹ Also, GaN possesses a higher velocity of saturation ($\sim 2.5 \times 10^7$)⁹ than GaAs, enabling it to operate at high speed, and a lower

dielectric constant ($\epsilon_r \approx 9$)¹⁰ than Si, which reduces its capacitive contribution. Because $\text{Al}_x\text{Ga}_{1-x}\text{N}$ has not been grown in bulk crystals big enough to form substrates,¹¹ alternate materials with lattice constant close to it have been used as substrates. Only recently has it been possible to overcome some of the lattice mismatch problems, by using an optimized buffer layer on sapphire.¹⁰ Lattice mismatch between the substrates and the $\text{Al}_x\text{Ga}_{1-x}\text{N}$ layer is a major contributor to a high defect density ($\sim 5 \times 10^9$ defects/cm², for Al_2O_3)¹² with a corresponding optical loss of ~ 10 dB/cm, but researchers perceive today that 10^8 defects/cm² should be realized in the near future, if the current effort in the technology is maintained. With more effort placed on reducing the defect density and some additional time, a reliable defect density of 10^7 defects/cm² should be obtainable.¹³ A major reduction in defect density should be achieved when $\text{Al}_x\text{Ga}_{1-x}\text{N}$ substrates are realizable. Additionally, present growth techniques have high *n*-type background carrier concentrations. It is difficult to dope GaN *p*-type, but that is beginning to be overcome.

Electro-optic modulation consists of an electro-optically active dielectric medium and a means for applying an electric field to it. Application of an electric field causes a change in the refractive index of the dielectric medium.¹⁴ The relationship between the electric field and index change for an electro-optic crystal is given by the series tensor equation:¹⁵

$$\Delta \left(\frac{1}{n^2} \right)_{ij} = r_{ijk} E_k + s_{ijkl} E_k E_l + \dots \quad (1-3)$$

where \mathbf{E} is the applied electric field vector, r is the linear electro-optic tensor and s is the quadratic electro-optic tensor. Terms higher than quadratic, in the expression above, are neglected due to their small contribution to the index change. In crystals where the linear

electro-optic effect is present the quadratic effect is also neglected. Using only the linear portion and taking advantage of crystal symmetry, equation (1-3) reduces to:

$$\Delta \left(\frac{1}{n^2} \right)_i = r_{ij} E_j \quad (1-4)$$

in which contraction notation is used, see reference 15.

$\text{Al}_x\text{Ga}_{1-x}\text{N}$ possesses an index of refraction range from $\sim 2.35 - 2.0$ (for $x = 0 - 1$) which can be tuned with alloy composition. This index range makes it a close match with that of communication grade optical fibers. The advantage is reduced reflection of the optical signal due to any index mismatch. Additionally GaN possesses an electro-optical effect that can be utilized to fabricate optical switches. The measured electro-optic coefficient are $r_{33} = 1.91 \pm 0.35$, $r_{31} = 0.57 \pm 0.11$, and $r_{51} = 3.1 \pm 0.2 \text{ pm/V}$ at 633 nm,^{16, 17} which are larger than AlGaAs³. Using these parameters and the index ellipsoid for wurtzite GaN ([6mm] point group symmetry) under an applied electric field $\mathbf{E} = [E_x, E_y, E_z]$ given by:¹⁷

$$\left(\frac{1}{n_o^2} + r_{13} E_z \right) x^2 + \left(\frac{1}{n_o^2} + r_{13} E_z \right) y^2 + \left(\frac{1}{n_e^2} + r_{33} E_z \right) z^2 + 2yzr_{51} E_y + 2xzr_{51} E_x = 1 \quad (1-5)$$

we can determine the index of refraction that an optical beam is subjected to. This information is necessary for optical switching.

The index change causes a change in the optical characteristics of the material, which can be exploited to manipulate the propagation of light through the material. With this, we can create different types of integrated optical switches (modulators) that can be fabricated in a single waveguide structure^{3,18}. Among them are:

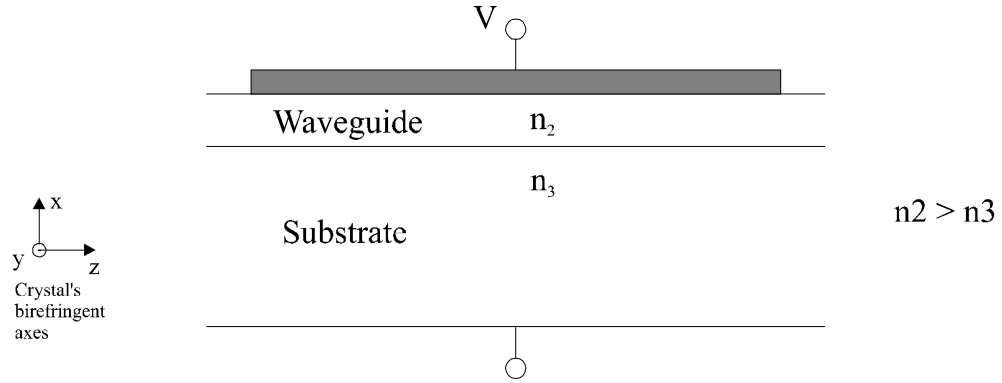


Figure 1.3 Basic electro-optic switching structure

1) Polarization switch^{3,18}: This switch works by changing the polarization of the incoming optical signal, and using a polarization sensitive detector (analyzer) to determine the state of the signal. The simple single channel switching structure on Figure 1.3 can be used to accomplish this. Launching an optical beam linearly polarized at 45° to the x and y -axes and applying a voltage will make the polarization rotate. This is accomplished by the fact that the phase changes only for the waves polarized in the y direction and not in the x direction. Difficulty in fabricating an effective analyzer monolithically has limited the use of polarization switches.

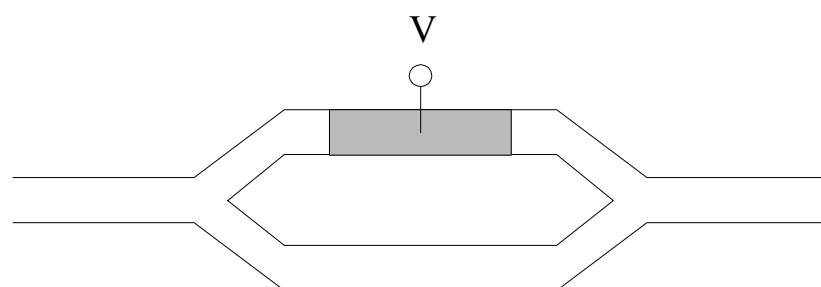


Figure 1.4. Mach-Zehnder interferometer

2) Phase switch: By applying a voltage to the device in Figure 1.3 an index change will be induced in the device for an incoming light polarized along the y direction, thus changing the phase of the polarized light. In order to detect this phase change a coherent detection system must be used. An integrated Mach-Zehnder¹⁸ interferometer, Figure 1.4, is such a system. Using the Mach-Zehnder with a π phase shift, the incoming light can be switched on and off to create a digital signal.

3) Directional coupler switch:^{18,19} When two waveguide channels are closely spaced they will function as a directional coupler, in which the energy is synchronously transferred from one guide to the other. In order to obtain a 100% power transfer the waveguides need to be identical. The directional coupler can be made into a switch by adding electrodes, as shown in Figure 1.5. The application of a voltage will change the index of refraction of the electro-optic material. This will change the propagation constant of one of the waveguides. With an appropriate voltage, the waveguide will switch guides from which the optical energy is coming out.

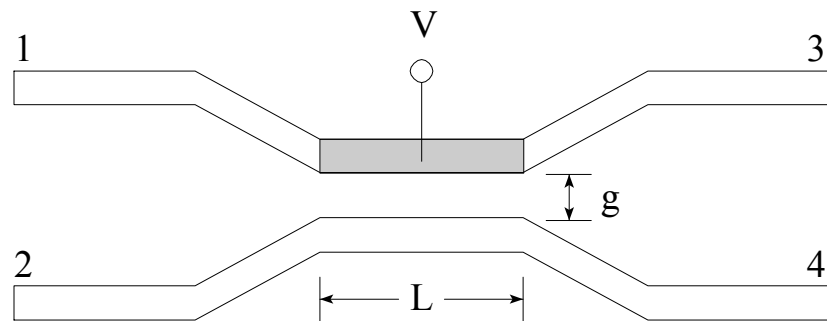


Figure 1.5 Active Directional coupler

The directional coupler switch will be the focus of this dissertation, specifically the case were the gap (g in Figure 1.5) between the waveguides is zero, zero-gap directional coupler. The relationship between length and voltage necessary to switch 100% of the light from one waveguide to the other (both identical) is given by:³

$$L = \frac{\mathbf{I} d}{n^3 r_{ik} V_p} \quad (1-6)$$

where \mathbf{I} is the free space wavelength, n is the index of refraction of the interaction region, r_{ik} is the electro-optic coefficient, and V_p is the voltage required for complete switching. Using this equation with the following parameters: $V_p = 5$ v; $\mathbf{I} = 830$ nm; $d = 1$ μm ; $r_{ik} = r_{33} = 1.91$; $n = 2.316$ [Ref. 16]; we get a GaN zero-gap directional coupler switch with $L = 7$ mm.

The advantage of investigating a directional coupler is that it can perform a number of useful functions in thin film devices. These functions include power division, modulation, switching, frequency selection, and polarization selection.²⁰ Additionally the zero-gap directional coupler uses less voltage to switch than conventional directional couplers.³ Furthermore, using AlGaN instead of AlGaAs to make these devices will have the following advantages:

- Closer index of refraction match to the optical fibers and polymer waveguides
- Potential for working with wavelengths from the IR to the blue region
- Tolerate harsh conditions

Directional couplers have been around for some years, especially in LiNbO_3 , and are well understood. The concept of directional coupler as a modulator (switch) was proposed as early as 1969 by Marcatili, but quite a few years passed before a working device was realized, largely because of the difficulty of fabricating the dual-channel structure to the required tolerances.¹⁸ Somekh fabricated dual-channel directional couplers in GaAs with 100% coupling, and theoretically analyzed the case of non-identical waveguides for a directional coupler in 1973-1974.¹⁸ Taylor theoretically analyzed the performance of a directional coupler with three electrodes, see Figure 1.6. Campbell et al. were the first ones to produce an operational directional coupler with three electrodes in GaAs, in 1975.¹⁸ Papuchon et al. reported the first two-electrode operational directional coupler modulator in Ti:LiNbO_3 , around 1975.¹⁸ In 1977 Papuchon et al. introduced the concept of, and demonstrated, a directional coupler with no gap between the waveguides, a zero-gap directional coupler, in Ti:LiNbO_3 .²¹ More recently, Grote explored zero-gap

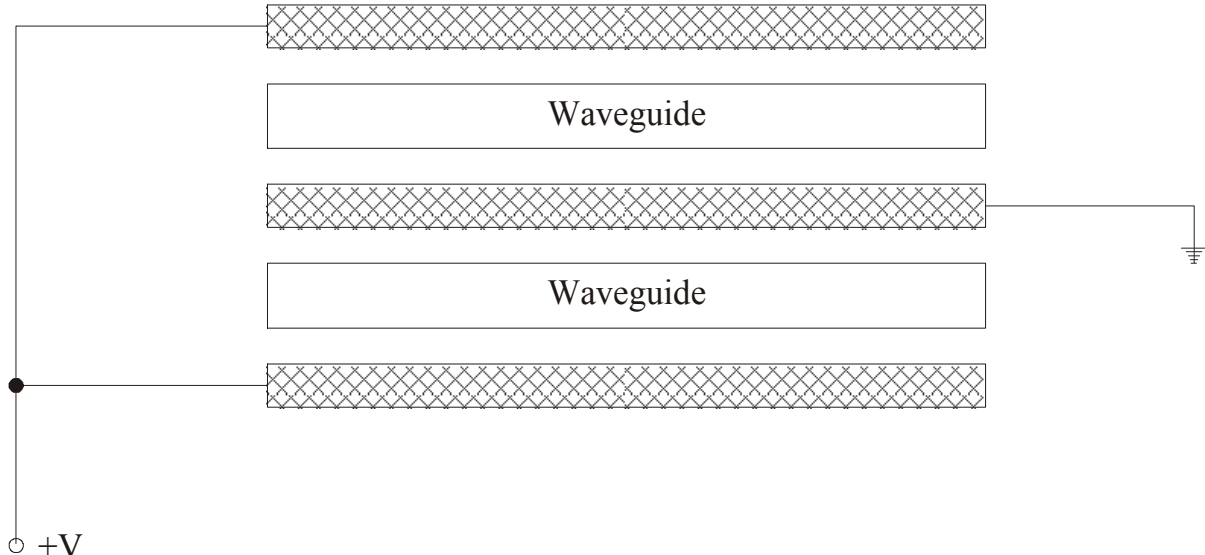


Figure 1.6 Three electrode directional coupler

directional coupler E-O switches in AlGaAs.³ For this dissertation a zero-gap directional coupler (sometimes called BOA) in AlGaN will be attempted.

The objective of this research was to investigate the behavior of an optical directional coupler switch fabricated from AlGaN in an *n-i-n* configuration. The research explored the possibility of the AlGaN material system as the basis for integrated optical devices, other than laser diodes. AlGaN is capable of withstanding elevated temperatures and harsh environments and has the potential of harboring high speed high power integrated circuits.^{9,10} This research establishes what areas of improvements are required of the material system for integrated optical devices. In addition, these optical devices could be designed to operate in the region from UV to IR. This investigation also developed the necessary processes and techniques required to create electro-optical structures in this new material system. AlGaN characteristics and requirements are very different from the current material systems used in the industry (i.e. AlGaAs, Si, LiNbO₃, etc.). These structures have features that are both very long and thin, which contrasts with electronics where both dimensions are comparable in size. The research also determines the refraction indices from published data of the AlGaN material in a layered, electro-optically active, device. The *n-i-n* configuration was used to concentrated the electric field across the core region

The directional coupler can be used as a switch for reconfigurable optical interconnects and digital circuits, such as network routing switches, without the optical-electrical-optical conversion. This is applicable to parallel systems with high speed interconnects

which could be reconfigured by software depending on the application. The use of the zero-gap directional coupler will enable the use of a simple configuration for obtaining complete power transfer, theoretically, with a single bias voltage per device. Thus reducing the complexity of the circuit. The experimental directional coupler will be compared with the results from the Marcatili method and the beam propagation method to determine their suitability to predict the behavior of the structure.

Dissertation Organization

An overview of the project and reasoning has been presented in this chapter. The following chapters will elaborate further into the topics and recount in chronological sequence the experimentation. Chapter II will review the theory of the optical waveguides as well as the Marcatili and the beam propagation methods. The electro-optic effect and the non-linearity's of crystals will be reviewed in Chapter III. The directional coupler theory will be reviewed in Chapter IV. The current status of the AlGaN material system is described in Chapter V. A chronological exposition and description of the experiments and results is found in Chapter VI. And, in Chapter VII a discussion of the results and conclusions will be made.

CHAPTER II

WAVEGUIDES

As mentioned in the previous chapter light can be confined using TIR. This is accomplished by surrounding a material that has a high index of refraction with a lower one. Taking the simple case of a slab waveguide, see Figure 2.1, light is launched at the interface between air and the wave guiding core. For light to be confined in the core region the angle that the light ray makes with the normal to the core-cladding interface must be, from Equation (1-1).

$$q_i \geq \sin^{-1} \left(\frac{n_t}{n_i} \right) \quad (2-1)$$

That would ensure that, at the core-cladding interface, there would be TIR. Otherwise, light would be escaping through the cladding region. Related to this angle, there is an external angle, q_a , which defines the radius of the cone of possible incident angles at the air-core interface for TIR. This angle is used to determine the numerical aperture (NA) of the fiber with the following equation:

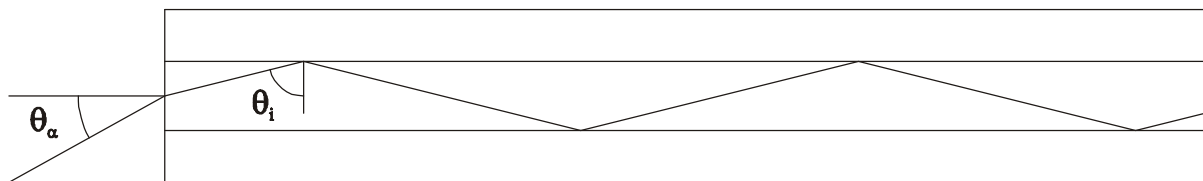


Figure 2.1 Slab Waveguide

$$NA = n_a \sin q_a \quad (2-2)$$

That is widely used to describe optical fibers. Not all of the rays incident at angles below q_a will propagate through a slab, only those whose phase fronts coincide. This could be more easily seen in Figure 2.2. The dashed lines represent the ray's phase fronts. The phase fronts will coincide when the total phase change incurred by the segment CD is a multiple of 2π . This occurs when the following relation is maintained:²²

$$n_1 (s_2 - s_1) k_0 + \mathbf{f}_2 + \mathbf{f}_3 = 2N\pi \quad (2-3)$$

where s_2 is the length of segment AB, s_1 the length of segment CD, \mathbf{f}_2 and \mathbf{f}_3 are the phase changes incurred upon reflection from the regions 2 and 3 respectively, k_0 is the free space propagation constant, and N is an integer number. Under TIR a wave polarized with its electric field parallel to the interface (TE waves) incurs a phase shift given by:

$$\mathbf{f} = -2 \arctan \left[\left(\beta^2 - n_t^2 k_0^2 \right)^{1/2} / \left(n_i^2 k_0^2 - \beta^2 \right)^{1/2} \right] \quad (2-4)$$

For a wave with it's magnetic field polarized parallel to the interface the phase shift is given by:

$$\mathbf{f} = -2 \arctan \left[\left(n_i^2 / n_t^2 \right) \left(\beta^2 - n_t^2 k_0^2 \right)^{1/2} / \left(n_i^2 k_0^2 - \beta^2 \right)^{1/2} \right] \quad (2-5)$$

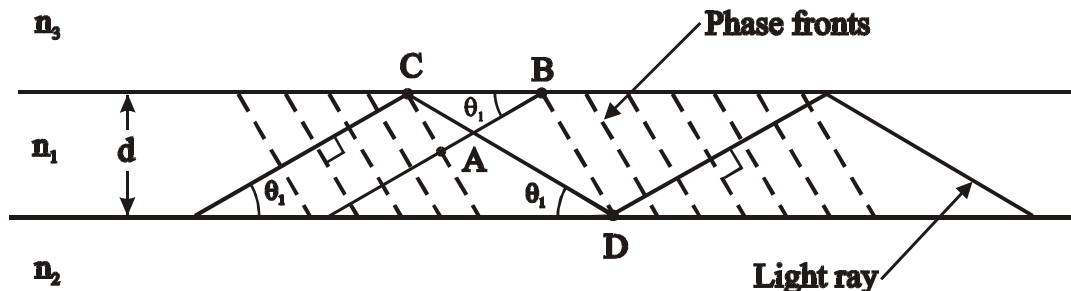


Figure 2.2 Illustration of the phase condition that leads to the eigenvalue equation, from reference 22

where \mathbf{b} is the propagation constant given by:

$$\beta = n_1 k_0 \cos \mathbf{q}_1 \quad (2-6)$$

Using equations (2-3) and (2-4) we get the eigenvalue equation for TE waves:

$$\tan \mathbf{k}d = \mathbf{k}(\mathbf{g} + \mathbf{d}) / (\mathbf{k}^2 - \mathbf{g}\mathbf{d}) \quad (2-7)$$

where:

$$\mathbf{k} = (n_1^2 k_0^2 - \beta^2)^{1/2} = n_1 k_0 \sin \mathbf{q}_1 \quad (2-8)$$

$$\mathbf{g} = (\beta^2 - n_2^2 k_0^2)^{1/2} = [(n_1^2 - n_2^2) k_0^2 - \mathbf{k}^2]^{1/2} \quad (2-9)$$

$$\mathbf{d} = (\beta^2 - n_3^2 k_0^2)^{1/2} = [(n_1^2 - n_3^2) k_0^2 - \mathbf{k}^2]^{1/2} \quad (2-10)$$

and using equations (2-3) and (2-5) the eigenvalue equation for TM waves is:

$$\tan \mathbf{k}d = n_1^2 \mathbf{k} (n_3^2 \mathbf{g} + n_2^2 \mathbf{d}) / (n_2^2 n_3^2 \mathbf{k}^2 - n_1^4 \mathbf{g}\mathbf{d}) \quad (2-11)$$

Equations (2-7) and (2-11) establish the conditions under which optical rays will propagate through a slab. These equations can be normalized in order to represent a combination of given parameters. The normalized equations for TE values is:

$$\tan(V \sqrt{1-b}) = \frac{\sqrt{b(1-b)} + \sqrt{(1-b)(b+Dif^2/V^2)}}{1-b - \sqrt{b(b+Dif^2/V^2)}} \quad (2-12)$$

and for TM is:

$$\tan(V \sqrt{1-b}) = \frac{n_1^2 (n_3^2 \sqrt{b(1-b)} + n_2^2 \sqrt{(1-b)(b+Dif^2/V^2)})}{n_2^2 n_3^2 (1-b) - n_1^4 \sqrt{b(b+Dif^2/V^2)}} \quad (2-13)$$

where V is the normalized frequency given by:

$$V = k_0 d \sqrt{n_1^2 - n_2^2}, \quad (2-14)$$

b is the normalized propagation constant given by:

$$b = \frac{(\beta/k_0)^2 - n_2^2}{n_1^2 - n_2^2}, \quad (2-15)$$

and Dif is the difference term given by:

$$Dif = k_0 d \sqrt{n_2^2 - n_3^2}. \quad (2-16)$$

Equations (2-12) and (2-13) will generate a family of curves which represent the possible modes. If we plot these curves in a b vs. V plot, with Dif constant, we obtain what is called a mode chart, which is shown on Figure 2.3. Using the mode chart, a waveguide can be designed to guide a specific number of modes. We determine the V number required (assuming that Dif is constant or determine both Dif and V) for the

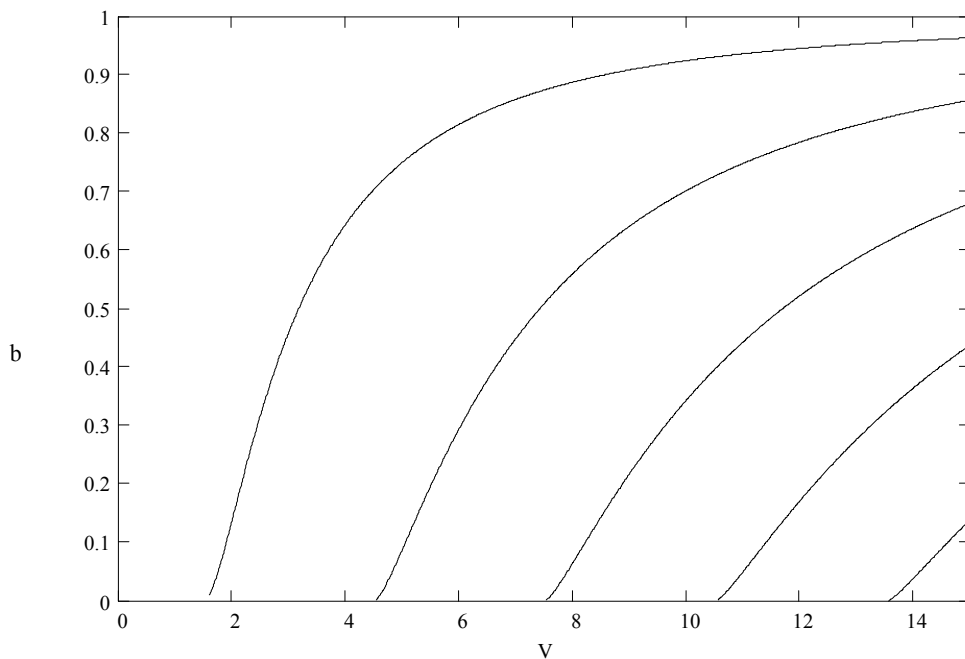


Figure 2.3. Mode chart for a symmetric slab waveguide

waveguide to have a predetermined number of modes. With this V (and Dif) number, we use equation (2-14) to solve for the desired parameters.

Rectangular Waveguides

In integrated optics more complex 3D structures are used. A common structure is a rectangular dielectric stripe surrounded by low index dielectric regions. Figure 2.4 shows such a structure. In here we see the dielectric material n_1 surrounded by 4 dielectric regions along its sides. A direct analytical analysis of the structure, as it was for the case of the dielectric slab, is impossible. Numerical simulators have been created with variable degrees of precision.²² Marcatili developed an approximate analytical solution, for a wave guiding structure far from cut-off. Far from cut-off the field is confined mostly in the core region and the shaded areas can be neglected. Using Maxwell's equations:

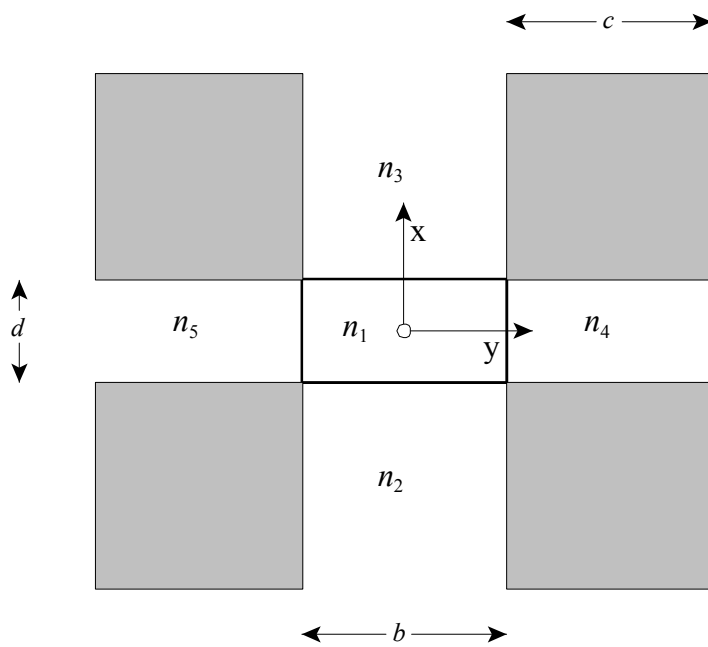


Figure 2.4. Rectangular Waveguide

$$\nabla \times \vec{H} = \epsilon_o n^2 \frac{\partial \vec{E}}{\partial t} \quad (2-17)$$

$$\nabla \times \vec{E} = \mu_o \frac{\partial \vec{H}}{\partial t} \quad (2-18)$$

and considering time harmonics and z dependence in both fields, \vec{E} and \vec{H} , of the form:

$$e^{i(\omega t - \beta z)} \quad (2-19)$$

we can define the transverse electric field components in terms of the longitudinal component, z :

$$E_x = -\left(i/K_j^2\right) \left[(\beta \partial E_z / \partial x) + (\mathbf{w} \mu_o \partial H_z / \partial y) \right] \quad (2-20)$$

$$E_y = -\left(i/K_j^2\right) \left[(\beta \partial E_z / \partial y) - (\mathbf{w} \mu_o \partial H_z / \partial x) \right] \quad (2-21)$$

$$H_x = -\left(i/K_j^2\right) \left[(\beta \partial H_z / \partial x) - (\mathbf{w} n_j^2 \epsilon_o \partial E_z / \partial y) \right] \quad (2-22)$$

$$H_y = -\left(i/K_j^2\right) \left[(\beta \partial H_z / \partial y) + (\mathbf{w} n_j^2 \epsilon_o \partial E_z / \partial x) \right] \quad (2-23)$$

where:

$$K_j = \left(n_j^2 k_o^2 - \beta^2 \right)^{1/2} \quad (2-24)$$

$$j = 1, 2, 3, 4, 5$$

and the subscripts denote the respective region. The longitudinal components must satisfy the wave equation given by:

$$\left\{ \frac{\partial^2}{\partial x^2} + \frac{\partial^2}{\partial y^2} + K_j^2 \right\} \mathbf{y}_z(x, y) = 0 \quad (2-25)$$

where \mathbf{y}_z is the longitudinal electric or magnetic field. By assuming that ψ_z is separable and using equation (2-19) we can write:

$$\mathbf{y}_z(x,y,z,t) = X(x)Y(y)e^{i(\omega t - kz)} \quad (2-26)$$

Then the wave equation can be written as:

$$\frac{1}{X} \frac{\partial^2 X}{\partial x^2} + \frac{1}{Y} \frac{\partial^2 Y}{\partial y^2} + K_j^2 = 0 \quad (2-27)$$

by substituting:

$$K_j^2 = K_{jx}^2 + K_{jy}^2 \quad (2-28)$$

Equation (2-27) can be arranged as:

$$\left\{ \frac{1}{X} \frac{\partial^2 X}{\partial x^2} + K_{jx}^2 \right\} + \left\{ \frac{1}{Y} \frac{\partial^2 Y}{\partial y^2} + K_{jy}^2 \right\} = 0 \quad (2-29)$$

A solution to this equation is

$$\begin{aligned} X(x) &= A_1 \cos K_{jx}(x + \mathbf{f}_x) + A_2 \sin K_{jx}(x + \mathbf{f}_x) \\ Y(y) &= B_1 \cos K_{jy}(y + \mathbf{f}_y) + B_2 \sin K_{jy}(y + \mathbf{f}_y) \end{aligned} \quad (2-30)$$

The waveguide is found to support a discrete number of modes that can be grouped as

E_{pq}^x and E_{pq}^y modes. E_{pq}^x is predominately polarized in the x direction while E_{pq}^y is in the y direction, p and q are the peaks in the field in the x and y direction respectively. The fields associated with E_{pq}^x are $\{E_x, H_y, E_z, H_z, E_y \equiv 0, H_x = 0\}$ and with E_{pq}^y are $\{E_y, H_x, E_z, H_z, E_x \equiv 0, H_y = 0\}$. These modes have components of both TE and TM modes, for this reason they are referred to as hybrid modes. By establishing the E_z field in the core for both modes, E_{pq}^x and E_{pq}^y , in the form of:

$$E_z(x,y,z) = A \cos \mathbf{k}_x(x + \mathbf{f}_x) \cos \mathbf{k}_y(y + \mathbf{f}_y) \quad (2-31)$$

where:

$$\mathbf{k}_x = K_{1x} \quad (2-32)$$

$$\mathbf{k}_y = K_{1y} \quad (2-33)$$

and solving for the transverse field component that vanishes, H_x , we can obtain H_z .²²

Solving equations (2-20)-(2-23) with boundary conditions for each region we obtain

the eigenvalue equations for E_{pq}^x as:²²

$$\tan \mathbf{k}_x d = \frac{n_1^2 \mathbf{k}_x (n_3^2 \mathbf{g}_2 + n_2^2 \mathbf{g}_3)}{n_3^2 n_2^2 \mathbf{k}_x^2 - n_1^4 \mathbf{g}_2 \mathbf{g}_3} \quad (2-34)$$

$$\tan \mathbf{k}_y b = \frac{\mathbf{k}_y (\mathbf{g}_4 + \mathbf{g}_5)}{\mathbf{k}_y^2 - \mathbf{g}_4 \mathbf{g}_5} \quad (2-35)$$

and for E_{pq}^y :

$$\tan \mathbf{k}_y b = \frac{n_1^2 \mathbf{k}_y (n_5^2 \mathbf{g}_4 + n_4^2 \mathbf{g}_5)}{n_4^2 n_5^2 \mathbf{k}_y^2 - n_1^4 \mathbf{g}_4 \mathbf{g}_5} \quad (2-36)$$

$$\tan \mathbf{k}_x d = \frac{\mathbf{k}_x (\mathbf{g}_2 + \mathbf{g}_3)}{\mathbf{k}_x^2 - \mathbf{g}_2 \mathbf{g}_3} \quad (2-37)$$

where:²²

$$\mathbf{k}_x^2 + \mathbf{k}_y^2 = K_1^2 = n_1^2 k_o^2 - \beta \quad (2-38)$$

$$\mathbf{g}_2 = [(n_1^2 - n_2^2) k_o^2 - \mathbf{k}_x^2]^{1/2} \quad (2-39)$$

$$\mathbf{g}_3 = [(n_1^2 - n_3^2) k_o^2 - \mathbf{k}_x^2]^{1/2} \quad (2-40)$$

$$\mathbf{g}_4 = [(n_1^2 - n_4^2) k_o^2 - \mathbf{k}_y^2]^{1/2} \quad (2-41)$$

$$\mathbf{g}_5 = [(n_1^2 - n_5^2) k_o^2 - \mathbf{k}_y^2]^{1/2}. \quad (2-42)$$

The solutions to equations (2-34) to (2-37) dictate which and how many modes will be present in a rectangular waveguide. It is possible to normalize these equations to better present the information contained in them. For the E_{pq}^y case the normalized equations are:

$$U_y = pp - \tan^{-1} \left[\left(\frac{n_4}{n_1} \right)^2 \frac{U_y}{\sqrt{V_y^2 + Dif_y^2 - U_y^2}} \right] - \tan^{-1} \left[\left(\frac{n_5}{n_1} \right)^2 \frac{U_y}{\sqrt{V_y^2 - U_y^2}} \right] \quad (2-43)$$

$$\begin{aligned} \sqrt{V^2(1-B) - r^2 U_y^2} = qp - \tan^{-1} & \left[\sqrt{\frac{V^2(1-B) - r^2 U_y^2}{V^2 B + r^2 U_y^2}} \right] \\ & - \tan^{-1} \left[\sqrt{\frac{V^2(1-B) - r^2 U_y^2}{V^2 B + r^2 U_y^2 + Dif_x^2}} \right] \end{aligned} \quad (2-44)$$

and for the E_{pq}^x :

$$U_y = pp - \tan^{-1} \left[\frac{U_y}{\sqrt{V_y^2 + Dif_y^2 - U_y^2}} \right] - \tan^{-1} \left[\frac{U_y}{\sqrt{V_y^2 - U_y^2}} \right] \quad (2-45)$$

$$\begin{aligned} \sqrt{V^2(1-B) - r^2 U_y^2} = qp - \tan^{-1} & \left[\left(\frac{n_2}{n_1} \right)^2 \sqrt{\frac{V^2(1-B) - r^2 U_y^2}{V^2 B + r^2 U_y^2}} \right] \\ & - \tan^{-1} \left[\left(\frac{n_3}{n_1} \right)^2 \sqrt{\frac{V^2(1-B) - r^2 U_y^2}{V^2 B + r^2 U_y^2 + Dif_x^2}} \right] \end{aligned} \quad (2-46)$$

where:

$$V = k d \sqrt{n_1^2 - n_2^2} \quad (2-47)$$

$$V_y = k b \sqrt{n_1^2 - n_5^2} \quad (2-48)$$

$$Dif_x = k d \sqrt{n_2^2 - n_3^2} \quad (2-49)$$

$$Dif_y = k b \sqrt{n_5^2 - n_4^2} \quad (2-50)$$

$$U_y = \mathbf{k}_y b \quad (2-51)$$

$$\mathbf{k}_x d = \sqrt{V^2 (1 - B) - r^2 U_y^2} \quad (2-52)$$

$$r = \frac{d}{b}, \text{ see Figure 2.4} \quad (2-53)$$

B is the normalized propagation constant, V is the normalized frequency, V_y is partial normalized frequency in the y direction. Dif_x and Dif_y are the differential normalized frequencies in the x and y directions. With these normalized equations it is possible to create a mode plot that will help us design integrated waveguides. Figure 2.5 illustrates such a plot. Although it looks similar to the plot in Figure 2.3, it is only a 2 dimensional slice of a multidimensional set of curves governed by $f(B, V, V_y, Dif_x, Dif_y, r)$.

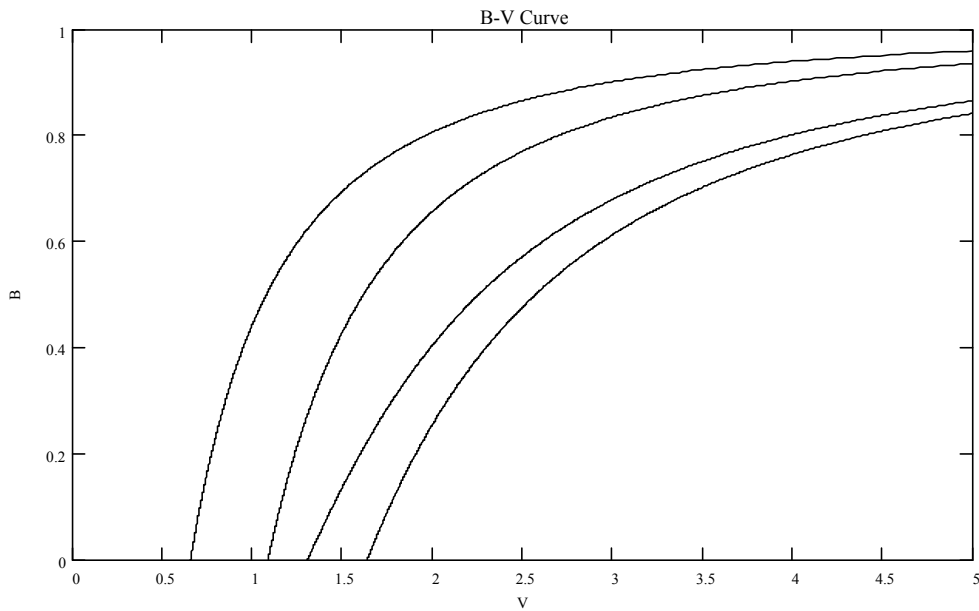


Figure 2.5. Mode chart for a rectangular waveguide

Beam Propagation Method

In the beam propagation method (BPM) we start with the scalar wave equation given by²²:

$$\nabla^2 \mathbf{y} + n^2(x, y, z)k^2 \mathbf{y} = 0 \quad (2-54)$$

where \mathbf{y} is the electric or magnetic field with propagation constant k and traveling in the medium with index of refraction $n(x, y, z)$. The complexity of arriving at the solution is reduced by the following assumptions. First, the variations in the refractive indices are small, and second the reflected waves are neglected. The BPM was conceived on the realization that as optical beam travels through an inhomogeneous medium it suffers from diffraction and from phase changes.²² These, although acting continuous, can be modeled as discrete effects, with a propagating region followed by a generalized lens. The lens would add the phase and diffraction effects that the optical beam would encounter by crossing the particular region. By assuming that the wave travels in the z direction, the trajectory can be divided into segments of length Δz , each with a constant index of refraction \bar{n} . By decomposing the waves in the medium between the segments into a spectrum of plane waves we get:²²

$$\mathbf{y}(x, y, \Delta z) = \frac{1}{(2\mathbf{p})^2} \int_{-\infty}^{\infty} \int \mathbf{f}(\mathbf{k}, \mathbf{s}) \exp[-i(\mathbf{k}x + \mathbf{s}y + \beta \Delta z)] d\mathbf{k} d\mathbf{s} \quad (2-55)$$

For this equation the parameters \mathbf{k} , \mathbf{s} , and \mathbf{b} are the propagation constants in the x , y , and z directions. Since \mathbf{b} is not arbitrary the integration does not cover it.²² By substituting equation (2-55) into equation (2-54) we get²²

$$\beta = \sqrt{\bar{n}^2 k^2 - \mathbf{k}^2 - \mathbf{s}^2} \quad (2-56)$$

where $n(x, y, z)$ is replaced by \bar{n} . In most guided wave problems, the fastest variation in the field \mathbf{y} is due to the phase variation along the direction of propagation.²³ It is beneficial to factor this rapid variation out of the problem. This is accomplished by factoring equation (2-56) as follows:

$$\beta = \bar{n} k - \frac{\mathbf{k}^2 + \mathbf{s}^2}{\bar{n} k + \sqrt{\bar{n}^2 k^2 - \mathbf{k}^2 - \mathbf{s}^2}} \quad (2-57)$$

with this equation we can now separate the rapid variation, given by $\bar{n}k$, from the more slow variation given by \mathbf{k}^2 and \mathbf{s}^2 . We can now write \mathbf{y} as:²²

$$\mathbf{y}(x, y, \Delta z) = F e^{-i\bar{n}k\Delta z} \quad (2-58)$$

where.²²

$$F = \frac{1}{(2p)^2} \iint_{\beta>0} f(\mathbf{k}, \mathbf{s}) \exp \left[i \frac{\mathbf{k}^2 + \mathbf{s}^2}{\bar{n} k + \sqrt{\bar{n}^2 k^2 - \mathbf{k}^2 - \mathbf{s}^2}} \Delta z \right] e^{-i(\kappa x + \sigma y)} \quad (2-59)$$

Not only has the rapid variation term been factored out but the range of integration has also been changed. For large values of \mathbf{k} and \mathbf{s} , \mathbf{b} becomes imaginary. This would mean that the ray would not only include plane waves that propagate in the z -direction but also waves traveling at large angles from the z -axis and evanescent waves that decay exponentially in the z -direction.²² The appearance of these evanescent waves in the calculations is undesirable. The BPM requires that the propagation process can be split into a free space propagation step, in a homogeneous media, followed by a lens step, to correct the phase in the step. The lens step requires that the rays associated with the wave

travel essentially parallel to the z -axis.²² This assumption is violated when the ray angles become large and turn imaginary so that evanescent waves appear. With these changes we have lost some flexibility and gained in computational efficiency. Factoring of the rapid phase variation enables us to represent numerically the optical ray in a grid much coarser than its wavelength.²³ The computational simplification achieved by the BPM has its price. As mentioned above, the fields are constrained to propagate primarily along the z -axis, so that the waves at large angles and especially their evanescent waves do not make significant contribution to the calculations. The rate of change of the refraction index must be small, thus be a weakly guiding structure. The backward traveling waves should not be necessary in the behavior of the device. Fields that have a complicated superposition of phase variation may not be accurately modeled if the phase variation is critical to device behavior.²³ Some of these limitations have been relaxed or eliminated through various techniques, see reference [23].

Equation (2-59) is the propagation step of the BPM. For the lens step we use the equation:²²

$$G' = \exp\{-i n(x, y, z)k \Delta z\} \quad (2-60)$$

which describes a wave traveling parallel to the z -axis. Since equation (2-59) already includes the phase shift $\exp(i \bar{n} k)$, this should be excluded from equation (2-60) giving us:

$$G = \exp\{-i [n(x, y, z) - \bar{n}]k \Delta z\} \quad (2-61)$$

Multiplying equations (2-59) and (2-61) we have:

$$\bar{\mathbf{y}} = F G \quad (2-62)$$

That is the mathematical description for the BPM. Each step is comprised of using the result from the previous step multiplied by FG . Equation (2-59) can be shown to be a two nested Fourier transform. These continuous Fourier transform can be converted to discrete Fourier transform to take advantage of FFT algorithms, see reference [22]

CHAPTER III

ELECTRO-OPTIC EFFECT

When light transverses an isotropic media it will encounter the same properties in all directions. This means that the induced polarization will be parallel to the electric field and will be related to it by a scalar factor.²⁶ For an anisotropic media, the induced polarization on the media depends on the direction and magnitude of an applied electric field.^{14,26} This implies that the speed of propagation of light in an anisotropic media is a strong function of the propagation direction and the polarization of light.¹⁴ Crystals are anisotropic in general. Those that are isotropic belong to a class known as cubic crystals. Figure 3.1 shows a mechanical depiction of an atom in a crystal lattice. In this figure the

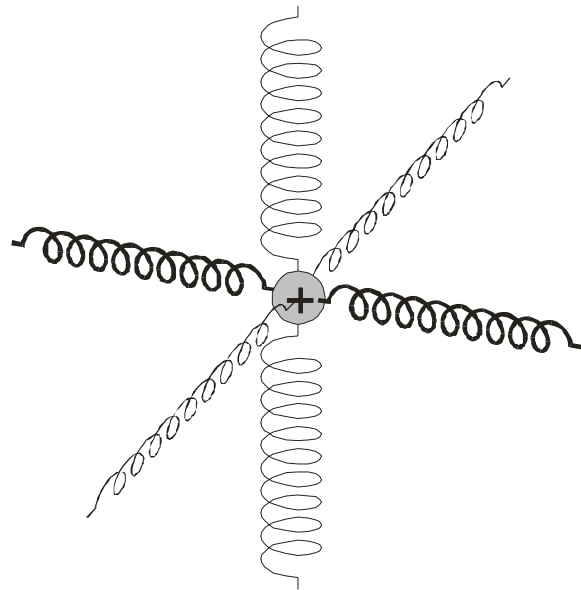


Figure 3.1 Spring model of Crystal bonding, from reference [24, 25]

springs and their constant depict the bonds and their strength. Using this mechanical model it is easily seen that the direction and polarization of the incident light on the crystal will affect its propagation speed, i.e. index of refraction.

To have a quantitative look at light traveling in a crystal we will start with Maxwell's equation for a general media:

$$\nabla \times \vec{E} = \frac{\partial \vec{B}}{\partial t} \quad (3-1)$$

$$\nabla \times \vec{H} = \frac{\partial \vec{D}}{\partial t} + \vec{J} \quad (3-2)$$

$$\nabla \cdot \vec{D} = \vec{r} \quad (3-3)$$

$$\nabla \cdot \vec{B} = 0 \quad (3-4)$$

where \vec{J} is the electric charge density, \vec{B} is the magnetic flux density, \vec{D} is the electric flux density, and \vec{r} is the charge density. In optics most of the materials used, and the ones of interest in this research, are non-magnetic. For a non-magnetic material the following relationship holds:

$$\vec{B} = \mu_0 \vec{H} \quad (3-5)$$

Using the above equations we can arrive at the general wave equation for non-magnetic materials:

$$\nabla \times (\nabla \times \vec{E}) = -\mu_0 \left[\nabla \times \frac{\partial \vec{H}}{\partial t} \right] \quad (3-6)$$

For vectorial fields, equation (2-19) changes to:

$$e^{i(\omega t - \vec{k} \cdot \vec{r})} \quad (3-7)$$

With the vectors \vec{E} , \vec{D} , and \vec{H} having the sinusoidal dependence of equation (3-7) and using equation (3-2) we get:

$$\nabla \times (\nabla \times \vec{E}) = \mu_0 \mathbf{w}^2 \vec{D} \quad (3-8)$$

The vector \vec{k} can also be expressed as $\vec{k} = k \vec{k}'$ where \vec{k}' is the unit vector and $k = |\vec{k}|$.¹⁴

From here we can express equation (3-8) as:¹⁴

$$\nabla \times (\nabla \times \vec{E}) = -k^2 [\vec{k}' \times (\vec{k}' \times \vec{E})] = -k^2 [\vec{k}' (\vec{k}' \cdot \vec{E}) - \vec{E}] \quad (3-9)$$

From equations (3-8) and (3-9) we get:

$$\frac{k^2}{\mu_0 \mathbf{w}^2} [\vec{E} - \vec{k}' (\vec{k}' \cdot \vec{E})] = \vec{D} \quad (3-10)$$

For a non absorbing media equation (3-10) has the form:¹⁴

$$\vec{D} = \vec{e} \vec{E} \quad (3-11)$$

where \vec{e} is the dielectric tensor which has the form:^{14,26}

$$\vec{e} = \begin{bmatrix} \mathbf{e}_x & 0 & 0 \\ 0 & \mathbf{e}_y & 0 \\ 0 & 0 & \mathbf{e}_z \end{bmatrix} \quad (3-12)$$

\mathbf{e}_x , \mathbf{e}_y , and \mathbf{e}_z are the non-negative principal dielectric constants of \vec{e} . For isotropic (cubic) crystals these dielectric constants are identical. When only two of the constants are identical the crystal is called uniaxial, or birefringent. When all three are different then the crystal is called a biaxial crystal. The majority of the crystals used in electro-optics are of the uniaxial kind.¹⁴

The energy density stored in an anisotropic crystal is given by:¹⁵

$$U_e = \frac{1}{2} \vec{D} \cdot \vec{E} \quad (3-13)$$

Inserting equation (3-11) and (3-12) we get:

$$2U_e = \frac{D_x^2}{\epsilon_x} + \frac{D_y^2}{\epsilon_y} + \frac{D_z^2}{\epsilon_z} \quad (3-14)$$

if we let

$$\vec{r} = \frac{\vec{D}}{\sqrt{2U_e \epsilon_0}} \quad (3-15)$$

and by using the definition of the principle indices of refraction, for a non-absorbing media:

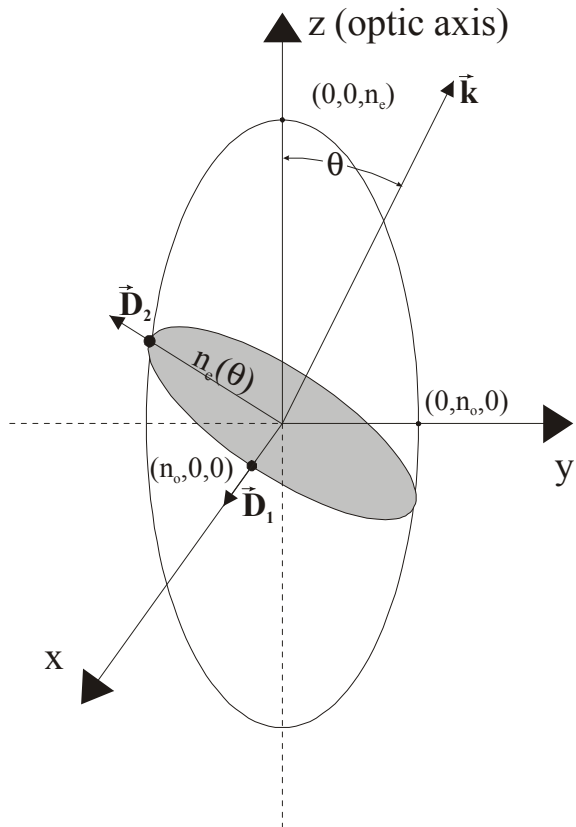


Figure 3.2 Index ellipsoid of a uniaxial crystal, from reference [25,26]

$$n_i^2 = \frac{\mathbf{e}_i}{\mathbf{e}_0} , \quad i = x, y, z \quad (3-16)$$

we have:

$$\frac{x^2}{n_x^2} + \frac{y^2}{n_y^2} + \frac{z^2}{n_z^2} = 1 \quad (3-17)$$

which describes a general ellipse with the general axes parallel to the x , y , and z directions whose respective length is $2n_x$, $2n_y$, and $2n_z$. In a uniaxial crystal we can define the principle indices of refraction as:

$$n_o = n_x, n_y ; n_e = n_z \quad (3-18)$$

so that now Equation (3-17) becomes:

$$\frac{x^2}{n_o^2} + \frac{y^2}{n_o^2} + \frac{z^2}{n_e^2} = 1 \quad (3-19)$$

Often in such a setup, the z -axis is called the optical axis.¹⁴ To find the polarization directions and the phase velocity of a given direction of propagation follow the following procedure^{25,26}, see Figure 3.2:

- Find the intersection ellipse between a plane through the origin, that is normal to the direction of propagation \vec{k} , and the index ellipsoid, Equation (3-19).
- The two axes of the intersection ellipse are equal in length to $2n_1$ and $2n_2$
- These axes are parallel, respectively to the directions of the \vec{D}_1 , and \vec{D}_2 vectors of the two allowed solutions

n_1 and n_2 corresponds to the two indices of refraction for the propagation vector \vec{k} .

\vec{D}_1 and \vec{D}_2 are the allowed solutions and the ellipse axes are parallel to \vec{D}_1 and \vec{D}_2 .²⁵ The

propagation vector \vec{k} makes an angle q with the z (optic) axis. Due to circular symmetry there will be no loss of generality if we let $x = 0$, and thus, let the projection of \vec{k} coincide with the y -axis on the x - y plane.²⁶ The allowed polarization directions will be the axes of the intersection ellipse of the plate normal to \vec{k} with the index ellipsoid, see Figure 3.2. The refraction indices of each polarization will be given by n_o (on the x -axis) and $n_e(q)$ on the y - z plane. Using Figure 3.2 we then obtain the following relations:

$$\begin{aligned} y &= -n_e(q)\cos(q) \\ z &= n_e(q)\sin(q) \end{aligned} \quad (3-20)$$

Inserting them into Equation (3-19) we get:

$$\frac{\cos^2(q)}{n_o^2} + \frac{\sin^2(q)}{n_e^2} = \frac{1}{n_e^2(q)} \quad (3-21)$$

a wave polarized along the n_o (\vec{D}_1) axis is called the ordinary wave and that along the $n_e(q)$ (\vec{D}_2) is called the extraordinary wave. Now, with Equation (3-21) and given it's orientation with respect to the crystal axes, we can determine the refraction index of a wave traveling through a uniaxial crystal. A uniaxial crystal where $n_e > n_o$ is called a positive crystal and when $n_o > n_e$ it is called a negative crystal. The index ellipsoid coordinate frame in general is expressed as:

$$\frac{x^2}{n_{xx}^2} + \frac{y^2}{n_{yy}^2} + \frac{z^2}{n_{zz}^2} + \frac{xy}{n_{xy}^2} + \frac{yz}{n_{yz}^2} + \frac{zx}{n_{zx}^2} = 1 \quad (3-22)$$

if we use the following substitution, called the optical impermeability tensor:

$$\mathbf{h}_{ij} = \frac{1}{n_{ij}^2} \quad (3-23)$$

where $i, j = 1, 2, 3$ corresponds to the principal axes x, y, z . Using the summation over repeated indices convention to rewrite Equation (3-22) we get:^{15,25}

$$\mathbf{h}_{ij} x_i x_j = 1 \quad (3-24)$$

where $x_1 = x, x_2 = y$, etc.

The electro-optic effect refers to the change in optical dielectric properties of the crystal induced by an electric field. According to quantum theory of solids, the optical impermeability tensor, η_{ij} , depends on the distribution of solids in the crystal.¹⁵ This distribution can be changed by the application of an electric field, which can also deform the ion lattice.¹⁵ The electro-optic effect can be defined as a power series expansion of η_{ij}

$$\mathbf{h}_{ij}(\vec{E}) - \mathbf{h}_{ij}(0) = \nabla \mathbf{h}_{ij} = r_{ijk} E_k + s_{ijkl} E_k E_l + \dots \quad (3-25)$$

where r_{ijk} are the linear electro-optic (Pockels) coefficients and s_{ijkl} are the quadratic electro-optic (Kerr) coefficients. For this dissertation work we will only be concerned with the linear electro-optic effect. The r_{ijk} tensor is given by:

$$r_{ijk} = \begin{bmatrix} r_{111} & r_{112} & r_{113} \\ r_{221} & r_{222} & r_{223} \\ r_{331} & r_{332} & r_{333} \\ r_{231} & r_{232} & r_{233} \\ r_{321} & r_{322} & r_{323} \\ r_{131} & r_{132} & r_{133} \\ r_{311} & r_{312} & r_{313} \\ r_{121} & r_{122} & r_{123} \\ r_{211} & r_{212} & r_{213} \end{bmatrix} \quad (3-26)$$

If the medium is lossless and the frequencies of the electric fields are much less than the optical fields then the indices i and j can be permuted.^{15,25} This enables the use of the following contracted notation:

$$\begin{aligned} 1 &= (11) \\ 2 &= (22) \\ 3 &= (33) \\ 4 &= (23) = (32) \\ 5 &= (13) = (31) \\ 6 &= (12) = (21) \end{aligned} \quad (3-27)$$

using the contracted notation we can write the linear electro-optic coefficients as:

$$r_{ik} = \begin{bmatrix} r_{11} & r_{12} & r_{13} \\ r_{21} & r_{22} & r_{23} \\ r_{31} & r_{32} & r_{33} \\ r_{41} & r_{42} & r_{43} \\ r_{51} & r_{52} & r_{53} \\ r_{61} & r_{62} & r_{63} \end{bmatrix} \quad (3-28)$$

and the optical indicatrix (index ellipsoid) as:

$$\mathbf{h}_1 x^2 + \mathbf{h}_2 y^2 + \mathbf{h}_3 z^2 + \mathbf{h}_4 yz + \mathbf{h}_5 xz + \mathbf{h}_6 xy = 1 \quad (3-29)$$

One should note that the resultant elements of the matrix r_{ik} do not have the same transformation or multiplication properties as a tensor would. Additionally we have reduced the number of elements in r_{ijk} from 27 to 18. The electro-optic effect is now given by:

$$\nabla \mathbf{h}_i = r_{ik} E_k \quad (3-30)$$

and the index ellipsoid in the presence of an electric field is given by:

$$\left(\frac{1}{n_x^2} + r_{1k} E_k \right) x^2 + \left(\frac{1}{n_y^2} + r_{2k} E_k \right) y^2 + \left(\frac{1}{n_z^2} + r_{3k} E_k \right) z^2 + 2yz r_{4k} E_k + 2zx r_{5k} E_k + 2xy r_{6k} E_k \quad (3-31)$$

which reverts to Equation (3-17) by removing the electric field. The principle axes of the new ellipsoid do not coincide with the unperturbed axes (x, y, z).¹⁵ This problem can be solved by finding a new coordinate system in which the principle axes of the ellipsoid coincide with the axes of the new system. This can be done by finding the eigenvalues of the \mathbf{h} -matrix. In contracted notation it is written as:

$$\begin{bmatrix} \mathbf{h}_1 & \mathbf{h}_6 & \mathbf{h}_5 \\ \mathbf{h}_6 & \mathbf{h}_2 & \mathbf{h}_4 \\ \mathbf{h}_5 & \mathbf{h}_4 & \mathbf{h}_3 \end{bmatrix}. \quad (3-32)$$

The electro-optic effect can be used to modulate an optical wave moving through the crystal. To do so, the crystal's optical indicatrix along with its electro-optical properties, given by the Pockel's coefficients, are used. With this, one can establish the needed optical wave's polarization and trajectory through the crystal axis for a desired effect, when an electric field is applied. Several devices implementing the electro-optic effect were briefly discussed in Chapter I.

CHAPTER IV

DIRECTIONAL COUPLER

The directional couplers are versatile devices. They can be used as modulators, filters, routing switches, and power splitters. In its most simple form, the directional coupler consists of two parallel waveguides placed close to each other. Light is launched into one of the waveguides and its optical energy is transferred synchronously back and forth between the guides by optical tunneling. To create a power splitter it is only necessary to limit the interaction region (the region where the two waveguides are close to each other) to a length that would establish the appropriate power ratio. In order for this energy transfer to actually occur the phase velocity (i.e. propagation constant) of the guided modes between the guides must be equal. The simplest way to accomplish this is to have two identical waveguides. But two dissimilar waveguides could have guided modes that are “accidentally” phased matched. This occurs only for a limited number of frequencies. Thus, its ability to act as a band pass filter.

The mechanism for power transfer is described by the couple mode theory. Using this theory, an accurate description is obtained if both single mode waveguides are seen as a single two-mode structure.²² A better understanding is obtained if the separation between the guides is reduced to zero. Now the structure can support an even and an odd mode with slightly different propagation constants, see Figure 4.1. These two modes are

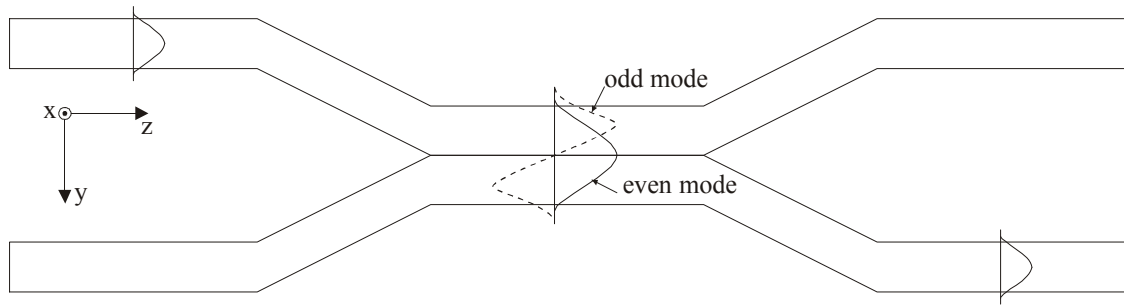


Figure 4.1 Even and odd mode of a Directional coupler

orthogonal to each other along the structure and, thus, they do not exchange energy. This condition prevails as we separate the waveguides. The propagation constant for each mode gets closer to each other, as we separate the guides, and each mode approaches the shape of an isolated waveguide, see Figure 4.2 a).²²

The directional coupler can now be explained as follows. When light is launched into the directional coupler's interaction region it will do so with a field distribution that resembles the mode of that waveguide, see Figure 4.2. This mode can be expressed as the

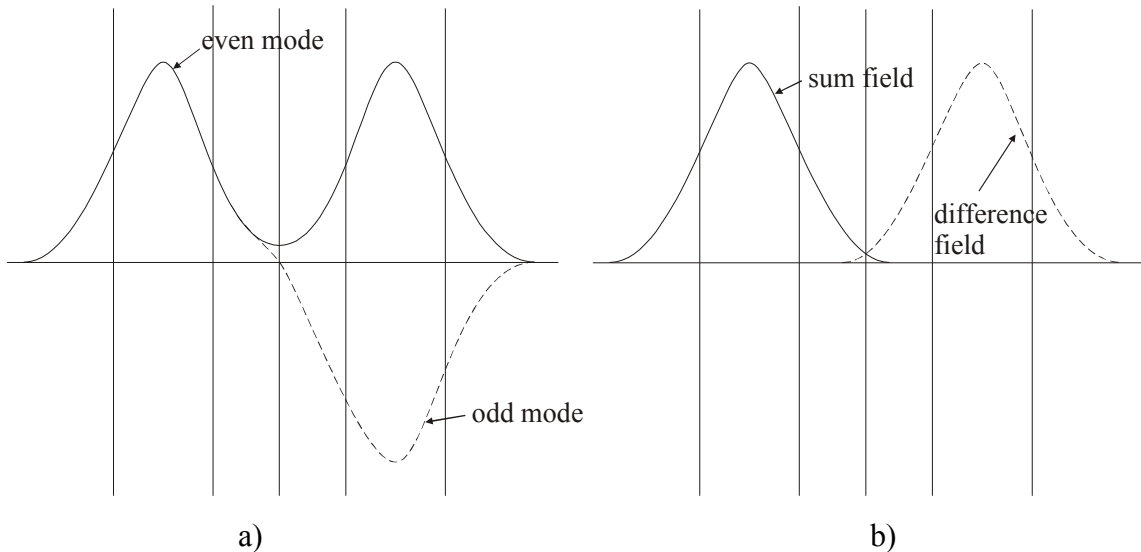


Figure 4.2 a) mode's field pattern for the two separated waveguides, b) sum of the odd and even fields

sum of the even and odd mode of the compound structure. Since the propagation constants for the even and odd modes, β_e and β_o respectively, are slightly different; these superposition fields will change their relative phase as they travel along the directional coupler.²² The length required to transfer completely the optical energy from one waveguide to the other is given by:

$$L = \frac{m\pi}{\beta_e - \beta_o} \quad (4-1)$$

The relative phase shift change can be expressed as a pair of differential equations. Instead of expressing these equations in terms of the parameters of the even and odd modes, it would be more appropriate to express them in terms of the parameters of the modes of the individual waveguides, since they can be express as a superposition of the even and odd modes. These equations are:^{18,22}

$$\frac{d A_0(z)}{d z} = -i\beta_0 A_0(z) - i\mathbf{k}_{01} A_1(z) \quad (4-2)$$

$$\frac{d A_1(z)}{d z} = -i\beta_1 A_1(z) - i\mathbf{k}_{10} A_0(z) \quad (4-3)$$

where A_0 and A_1 are the complex field amplitudes, and β_0 and β_1 are the propagation constants of the waveguide modes. The parameters \mathbf{k}_{01} and \mathbf{k}_{10} are the coupling coefficients between the waveguide modes. By convention the modes have been normalized to carry one unit of power.¹⁸ Thus the power in mode m is given by:

$$P_m(z) = A_m(z) A_m^*(z) = |A_m(z)|^2 \quad (4-4)$$

In a real guide, scattering and absorption are always present. For this reason the propagation constant takes on a complex nature. If we consider two identical waveguides with loss coefficient α so that:¹⁸

$$\beta = \beta_r - i \frac{a}{2} \quad (4-5)$$

$$\mathbf{k}_{01} = \mathbf{k}_{10} = \mathbf{k}_c \quad (4-6)$$

If we assume that light is coupled into waveguide 0 at point $z = 0$, then we have the boundary conditions:¹⁸

$$A_0(0) = 1 \quad \text{and} \quad A_1(0) = 0 \quad (4-7)$$

The solution to the waveguide coupling then becomes:

$$A_0(z) = \cos(\mathbf{k}_c z) e^{i\beta z} \quad (4-8)$$

$$A_1(z) = -i \sin(\mathbf{k}_c z) e^{i\beta z} \quad (4-9)$$

Using equation (4-4) we get the power flow in each equation as:

$$P_0 = A_0(z) A_0^*(z) = \cos^2(\mathbf{k}_c z) e^{-\alpha z} \quad (4-10)$$

$$P_1 = A_1(z) A_1^*(z) = \sin^2(\mathbf{k}_c z) e^{-\alpha z} \quad (4-11)$$

Equations (4-10) and (4-11) show that the power is actually being transferred back and forth between the waveguides. These equations also show that there is a 90° phase lag in guide 1 with respect to guide 0. This is produced by the mechanism that creates the coherent transfer of energy between the waveguides.¹⁸ The field in the driving guide causes a polarization in the dielectric material which is in phase with it, and which extends in the region between the guides because of the mode tail. This polarization then acts to generate energy in the mode of the driven guide.¹⁸

Given equations (4-10) and (4-11), the length needed for complete power transfer is also given by:

$$L = \frac{p}{2k_c} + \frac{mp}{k_c} \quad (4-12)$$

where $m = 0, 1, 2, \dots$ The coupling coefficient, k_c , is a strong function of the mode tail's shape in the guides.¹⁸ For well-confined modes in which the evanescent waves contribution can be neglected, the coupling coefficient is given by Marcatili's theory as:^{18,27}

$$k_c = \frac{2k_y^2 g_4 e^{-\gamma_4 c}}{\beta b (g_4^2 + k_y^2)} \quad (4-13)$$

where b is the channel width, c is the separation, k_y and b are the propagation constants in the y and z directions, respectively, and g_4 is the extinction coefficient in the y direction (see Equation (2-41)). In real situations it may be difficult to fabricate two identical waveguides. If the difference in their propagation constant ($\Delta b = |b_1 - b_2|$) is kept small then the power distribution in the waveguides is given by¹⁸

$$P_0 = \cos^2(gz) e^{-\alpha z} + \left(\frac{\Delta \beta}{2} \right)^2 \frac{\sin^2(gz)}{g^2} e^{-\alpha z} \quad (4-14)$$

$$P_1 = \frac{k_c^2}{g^2} \sin^2(gz) e^{-\alpha z} \quad (4-15)$$

where¹⁸

$$g^2 \equiv k_c^2 + \left(\frac{\Delta \beta}{2} \right)^2 \quad (4-16)$$

As equations (4-14) - (4-16) shows power will still be transferred between the guides.

This transfer will be incomplete since equation (4-14) has no zero.

Active Directional Coupler

From Chapter III, if the directional coupler is made from an electro-optic crystal then its behavior can be controlled by an applied electric field. Starting with a directional coupler with two identical branches, its behavior is dictated by Equations (4-10) and (4-11). The condition for total transfer of power is given by Equation (4-12). If a modulating signal voltage is applied, as shown in Figure 1.5, a variation in the index of refraction of the waveguide will be introduced. This index variation creates a mismatch between the waveguides in the form of a propagation constant difference, Δb . Under the applied electric field, Equations (4-14) - (4-16) govern the behavior of the directional coupler, and the condition for total transfer of power in this case is given by:¹⁸

$$g L = \pi + m\pi \quad (4-17)$$

where $m = 1, 2, 3, \dots$. By substituting equation (4-12) into (4-17) it can be shown that the Δb required for 100% modulation is:¹⁸

$$(\Delta\beta)L = \sqrt{3}\pi \quad (4-18)$$

The effective index of refraction in a guide is given by:¹⁸

$$n_g \equiv \frac{\beta}{k} \quad (4-19)$$

where k is the propagation constant. Thus the change in the effective index needed for 100% modulation is given by:¹⁸

$$\Delta n_g = \frac{\sqrt{3} \pi}{k L} \quad (4-20)$$

and Δn_g is a function of the electric field applied. From Equation (4-20) we can see that the longer the device the smaller Δn_g needs to be. But there is a practical limit in the length of the device. For integrated devices, the smaller the size the greater the yield. The increase in yield is due to not only to the number of devices that can be placed in a given area, but also to the reduced probability of defects in the device. An approach to reduce the size of the directional coupler without reducing Δn_g is to have a push pull configuration as illustrated in Figure 4.3.^{18,19} In this type of configuration the index of refraction is pushed up in one waveguide and pulled down in the other. Other types of configurations exist whose use depends on the application requirements.^{18,19}

Taking a second glance at Equations (4-14) to (4-16) it is noticed that they resembled a sinc^2 ($= (\sin(x)/x)^2$) function. Rearranging then Equations (4-14) and (4-15) in terms

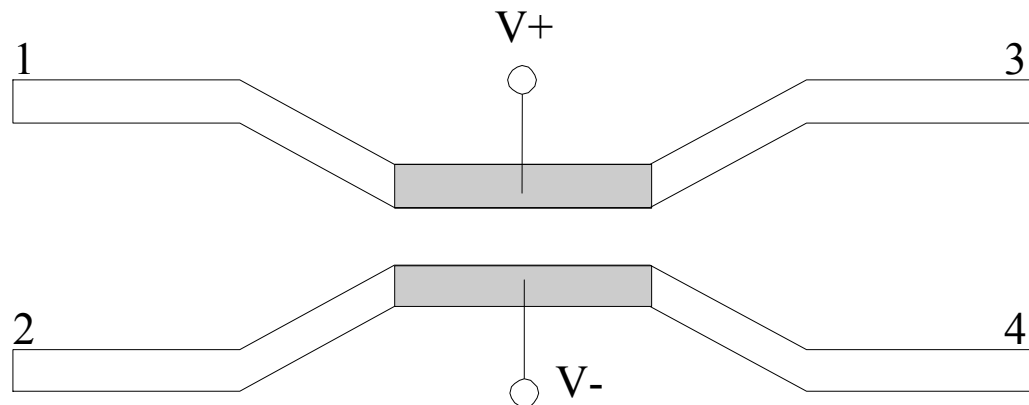


Figure 4.3 Push pull directional coupler

of $\Delta b L$ we get:¹⁹

$$P_0 = \cos^2 \left(\sqrt{(\mathbf{k}_c L)^2 + \left(\frac{\Delta \beta L}{2} \right)^2} \right) + \left(\frac{\Delta \beta L}{2} \right)^2 \frac{\sin^2 \left(\sqrt{(\mathbf{k}_c L)^2 + \left(\frac{\Delta \beta L}{2} \right)^2} \right)}{(\mathbf{k}_c L)^2 + \left(\frac{\Delta \beta L}{2} \right)^2} \quad (4-21)$$

$$P_1 = (\mathbf{k}_c L)^2 \frac{\sin^2 \left(\sqrt{(\mathbf{k}_c L)^2 + \left(\frac{\Delta \beta L}{2} \right)^2} \right)}{(\mathbf{k}_c L)^2 + \left(\frac{\Delta \beta L}{2} \right)^2} \quad (4-22)$$

Setting $\mathbf{k}_c L = \pi/2$, see Equation (4-10), and plotting the equation we get the typical switching characteristics of an active directional coupler.¹⁹ As it can be seen in Figure 4.4, when $\Delta b L = 0$ all the power comes out of guide 1. As $\Delta b L$ increases (and thus the electric field) the directional coupler switches to the off state ($\Delta b L = \pi\sqrt{3}$). If $\Delta \beta L$ is

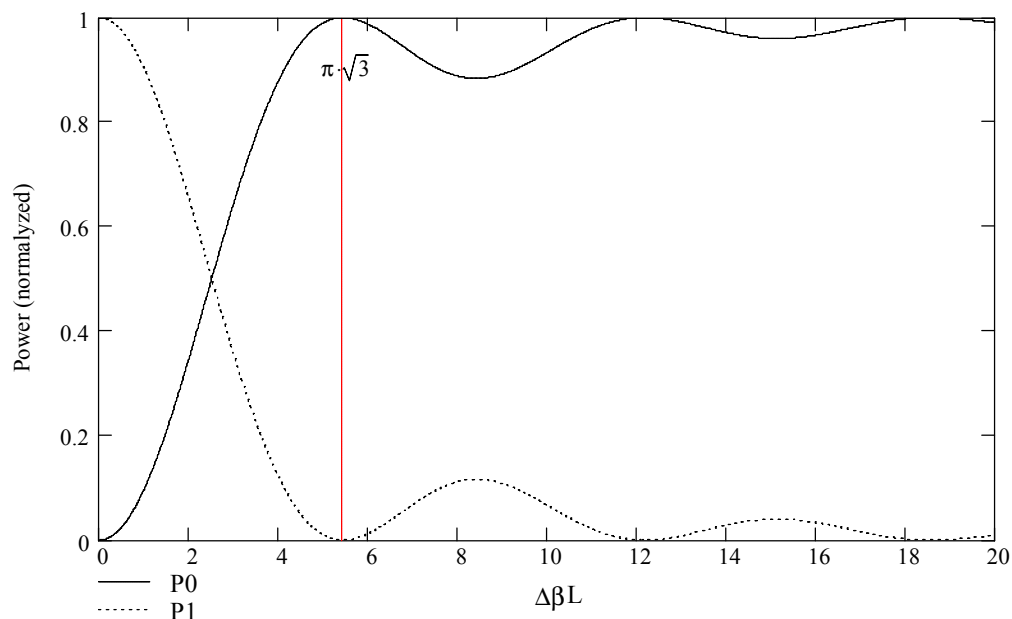


Figure 4.4 Switching a directional coupler

increased further the coupling between the guides will be destroyed. From Figure 4.4 we can deduce that the off state is electrically adjustable. If in the initial state $\mathbf{k}_c L$ is not made $\pi/2$, by a fabrication error, then the two switching states could not be obtained from the configuration on Figure 1.5 or Figure 4.3.¹⁹ To solve this problem there exist a different configuration, known as $\Delta\mathbf{b}$ reversal, in which an extra set of electrodes are added to the structure, but with inverse polarity, see references 18 and 19. Each set of electrodes is independently adjusted and with $L/2$ length.

Symmetrical Directional Coupler

At the beginning of the chapter a zero-gap directional coupler was envisioned to explain the behavior of these devices in general. Far from being a theoretical curiosity these are viable devices. In the literature at least three names, symmetric directional couplers²⁸, BOA switches²¹, and zero-gap directional coupler²⁹ have referred to these devices. The power flow equations that govern the symmetric directional couplers are the same as those for the identical guides directional coupler, Equations (4-10) and (4-11). The value of \mathbf{k}_c , as it was for the former case, is given by:

$$\mathbf{k}_c = \frac{1}{2}(\beta_e - \beta_o) \quad (4-23)$$

also it is assumed that the loss coefficient for each waveguide is identical. If a change δn is introduced, by way of the electro-optic effect, in the waveguide index the mode shapes are altered in a symmetric way, they will remain orthogonal.²⁸ With this change the perturbed propagation constants will differ from the unperturbed ones, generally by

different amounts.²⁸ Therefore equations (4-10) and (4-11) would still hold for the perturbed directional coupler but with a different coupling coefficient which is given by:

$$\mathbf{k}'_c = \mathbf{k}_c + \mathbf{k}_c^{eo} \quad (4-24)$$

where \mathbf{k}_c^{eo} is the change in the coupling coefficient due to a perturbation, the electro-optic effect in this case. Starting with a directional coupler with complete power transfer, the necessary change to switch symmetrically a directional coupler is given by:

$$d\mathbf{k}_c L = \mathbf{k}_c^{eo} L = \frac{p}{2} \quad (4-25)$$

using Equation (4-23) we get:²¹

$$\delta(\beta_e - \beta_o)L = \pi \quad (4-26)$$

or:²¹

$$\delta n \frac{\partial(\beta_e - \beta_o)}{\partial n} L = \pi \quad (4-27)$$

which gives:²¹

$$\delta n = \frac{\pi}{L} \left(\frac{\partial(\beta_e - \beta_o)}{\partial n} \right)^{-1} \quad (4-28)$$

The term $\partial(\beta_e - \beta_o)/\partial n$ depends strongly on the separation of the waveguides and increases as the separation decreases.²¹ This term has been shown to increase by an order of magnitude from an ordinary directional coupler.²¹ This makes it possible to switch a zero gap coupler with a symmetric change of δn with reasonable voltages. In the case of a directional coupler with a waveguide separation, a symmetrical change of δn would require excessively high voltages.²¹

Since the only thing that changes in the power flow equations is the coupling coefficient, it is now possible for the directional coupler to achieve both states, on or off, electrically, and with only one controlling voltage. This makes the devices able to compensate for fabrication errors by applying a bias voltage.²¹ This would be a much simpler arrangement than using the $\Delta\mathbf{b}$ reversal configuration of a traditional coupler.

Crosstalk

Crosstalk in a directional coupler is defined as the ratio of light power in the unwanted output port to the power in the desired output port.³⁰ Another measure of crosstalk is the extinction ratio. The extinction ratio is defined as the ratio of the optical power in the “on” state to the optical power in the “off” state, in the same guide branch. In a directional coupler it is desired that all the power be coupled to the other waveguide in the “off” state and none in the on state. But in reality this is not the case, there is always a small amount of unwanted residual power in the off waveguide. The source of the crosstalk is due to different mechanisms. Among them are unequal mode excitations²⁸, non-optimal coupling length¹⁹, absorption loss³⁰, waveguides asymmetry²⁸, parasitic coupling³¹, etc.

Physical asymmetries in the structure, which arise during fabrication, will lead to crosstalk due to coupling between the modes.²⁸ These asymmetries manifest themselves as differences in the width, index of refraction, and curve shape. In a perfectly symmetric directional coupler, the even mode field distribution \mathbf{y}_e at any cross section ($z = z_1$, see

Figure 4.1) is orthogonal to the odd mode field distribution \mathbf{y}_o at any other cross section ($z = z_2 = z_1 + \delta z$).^{28,29} In other words:^{28,29}

$$\int \mathbf{y}_e(y, z_1) \mathbf{y}_o(y, z_2) = 0 \quad \text{for any } z_1, z_2 \quad (4-29)$$

In the presence of asymmetries there is no longer an even and an odd mode for the total structure.²⁹ When the gap between the waveguides is zero or small, a slight structure asymmetry will produce only a small modification of the electric field profiles.^{28,29} These deviations increase as the separation between the waveguides is increased. The mode in each waveguide will start to resemble the mode of an isolated waveguide, faster than with

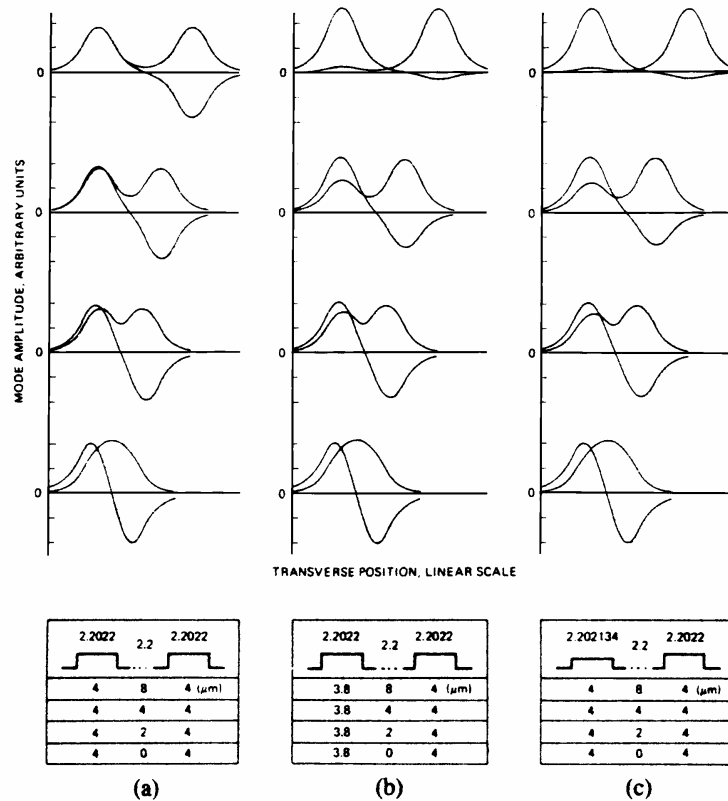


Figure 4.5 Effects of asymmetries in a directional coupler. Eigenmode profiles for various fabrication differences. From reference 28

no asymmetries present.^{28,29} Thus the smaller the guide separation the smaller the influence of any given asymmetry.^{28,29} When there is a separation between the waveguides, it has been shown that even small variations in the asymmetries cause significant deviations in the combined structure's modes.^{28,29} Figure 4.5 (from reference 28) shows different electric field profiles arising from fabrication asymmetries, index of refraction and width differences. Additionally, the figure shows the effect of the gap separation in the electric field profiles.

Any waveguide discontinuity or irregularity that differentially affects the mode propagation losses will have adverse effects on the directional coupler performance.²⁸ This would create an imbalance in the mode's amplitude that will manifest as crosstalk in the directional coupler. Crosstalk for a lossy material has been studied theoretically (see reference 30) but on a two, finite separation, waveguide directional coupler. In that study adjusting the coupling lengths could not compensate the effects of differential modal absorption. The data presented tends to indicate that a reduction in the waveguide separation, the crosstalk due to differential absorption would reduce its contribution to the overall crosstalk. A point to consider is that the reduction in the guide separation also reduced the coupling length necessary for complete power transfer.

Bending Sections

The theory presented thus far, and in most publications and textbooks, deals with the parallel coupling section and neglects the bending sections, Figure 4.6. The bending sections of a directional coupler should be a slowly converging or diverging curve to

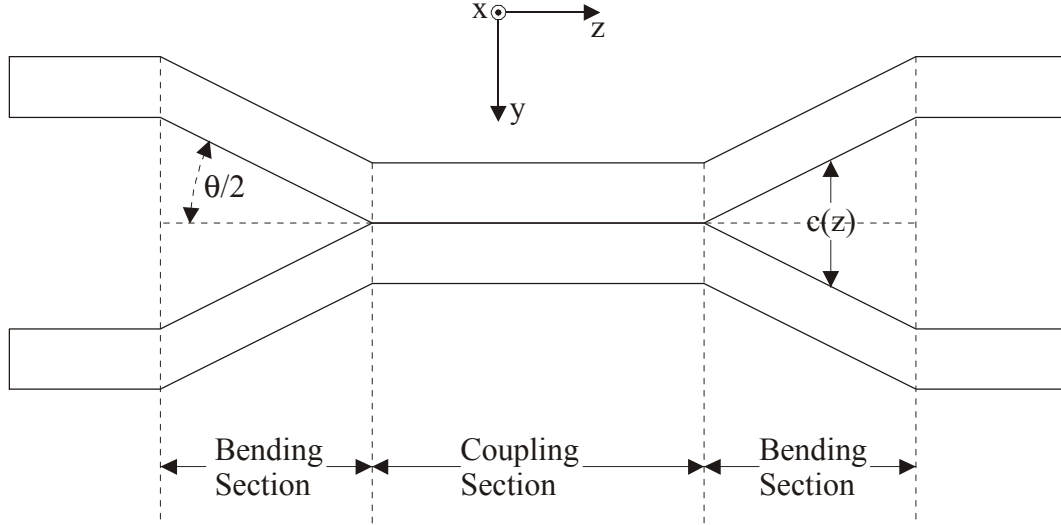


Figure 4.6 Bending sections of a directional coupler

minimize radiation losses.^{28,31} The slow convergence of the bending sections result in a longer effective coupling length for the device. From Equation (4-13), as the two guides approach each other the coupling coefficient, κ_c , increases. When κ_c is large enough the guides will start accumulating an appreciable amount of propagation phase.^{28,31} A slow curved convergence will accumulate much more propagation phase than straight convergence, as demonstrated in reference 28. Therefore the input bending sections needs to be taken into consideration when designing a directional coupler. The generalized propagation phase angle is given by:³¹

$$\mathbf{f}(z) = \int_0^z \mathbf{k}_c(z) dz \quad (4-30)$$

where in the Marcatili approach \mathbf{k}_c is given by, see Equation (4-13):

$$\mathbf{k}_c(z) = \frac{2\mathbf{k}_y^2 \mathbf{g}_4 e^{-\gamma_4 c(z)}}{\beta b (\mathbf{g}_4^2 + \mathbf{k}_y^2)} \quad (4-31)$$

Another factor that needs to be taken into consideration is the bending section angle $q/2$, see Figure 4.6. This angle establishes an optical wave front tilt that is often neglected in the analysis of the directional coupler.²⁸ The tilted wave fronts result in reduced waveguide coupling.²⁸ The tilt introduces phase differences in the regions where the coupling takes place, which decreases the waveguide interaction. An estimate of the permissible tilt can be obtain by, see Figure 4.6:²⁸

$$\sin\left(\frac{q}{2}\right) < \frac{1}{4Wn} \quad (4-32)$$

where W is the waveguide width, n is the index of refraction of the core channel. This equation is based on the assumption of well-confined modes.²⁸

By having curved bending sections the angle of the instantaneous slopes of the curves is less than if the same section was replaced with straight ones, over the section where significant mode interaction takes place (~ 2 waveguide width for a well confined modes). This permits the use of steeper equivalent tilt angles before the tilt effects diminish the waveguide coupling.²⁸ Additionally, the gradual approach of the guides minimizes the differential mode propagation loss.

CHAPTER V

AlGaN

The $\text{Al}_x\text{Ga}_{1-x}\text{N}$ alloy system can have a wurtzite (hexagonal) or a zincblende (cubic) lattice structure. Wurtzite is the preferred structure due to the better crystalline quality that can be obtained with it, at the present time.^{32, 33} The hexagonal unit cell, illustrated in Figure 5.1, is defined by two coplanar vectors, \mathbf{a}_1 and \mathbf{a}_2 , at 120° to one another and a third axis \mathbf{c} at a right angle, see Figure 5.1.³⁴ The complete lattice is built by shifting the unit cell in the plane defined by the \mathbf{a}_1 and \mathbf{a}_2 vectors. The unit cell, as seen on Figure 5.1, has a six-fold rotational symmetry along \mathbf{c} , which generates the hexagonal symmetry of

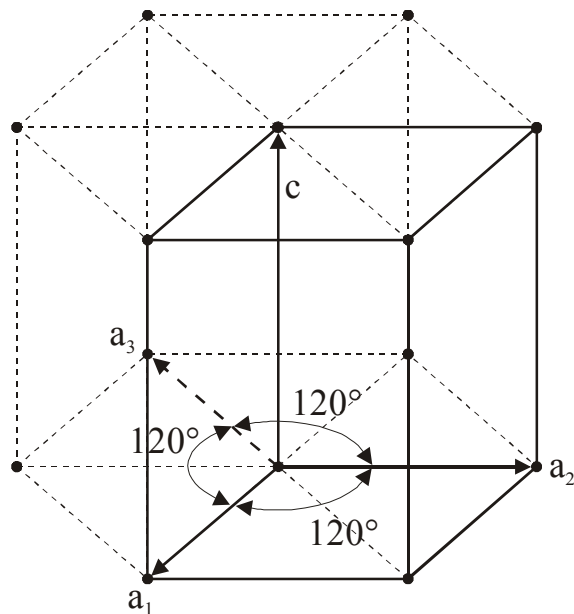


Figure 5.1 Hexagonal Unit Cell (heavy lines)

the lattice.³⁴ The third axis, of the hexagonal symmetry, which lies in the base plane of the hexagonal prism, is related to \mathbf{a}_1 and \mathbf{a}_2 in such a way that it is often used with the other two axes. Thus the Miller-Bravais indices of a plane in a hexagonal system refer to four axes written as $(hkil)$. Where h , k , i , and l are the reciprocal of the fractional intercept on the \mathbf{a}_1 , \mathbf{a}_2 , \mathbf{a}_3 , and \mathbf{c} axes respectively.³⁴

The wurtzite $\text{Al}_x\text{Ga}_{1-x}\text{N}$ alloy system covers a direct and wide band gap range. This range expands from the visible, 3.4 eV, to the UV, 6.2 eV, for $x = 0$ to 1 respectively. For this reason, the short wavelength opto-electronic applications have fueled the interest in this material system. Another reason is its advantages for high power electronics, including the large bandgap for high voltage and temperature operations. The material parameters of GaN and AlN are listed in Table 1 along with other semiconductors for comparison.

Up to this date, a native substrate for the $\text{Al}_x\text{Ga}_{1-x}\text{N}$ material system has been hard to achieve, mainly due to the large equilibrium vapor pressure of nitrogen over the liquid nitride phases.³⁸ Bulk single crystal growth has been limited to only $\sim 100 \text{ mm}^2$ with good

Table 1. Material Parameters for 300 K

Property	GaN	AlN	SiC 3C/6H	GaAs
Energy gap (eV)(direct)	3.4 ^[35]	6.2 ^[35]	2.2/2.9 ^[10]	1.423 ^[10]
Density (g/cm ³)	6.1 ^[35]	3.26 ^[35]		5.317 ^[36]
Dielectric constant (ϵ)	8.9 ^[35]	8.5 ^[35]	9.7 ^[10]	12.85 ^[36]
Electron mobility (cm ² /V-s)	1000 bulk ^[35]	135 ^[37]	1000/600 ^[10]	8500 ^[36]
Hole Mobility (cm ² /V-s)	30 ^[35]	14 ^[35]	40 ^[10]	400 ^[36]
Saturation Velocity (m/s)	2.5×10^7 ^[37]	1.4×10^7 ^[37]	2×10^7 ^[10]	2×10^7 ^[10]
Breakdown field (V/cm)	$> 5 \times 10^6$ ^[37]		4×10^6 ^[10]	0.4×10^6 ^[10]

quality, but in a limited quantity.^{39,40,41,42} For this reason, alternate substrates have been used.

Among the alternative substrates are sapphire, SiC, GaAs, and Si. Sapphire has been the most widely used substrate to date, mainly due to its wide availability.⁴³ Although from the lattice mismatch (~14%),⁴⁴ sapphire should have been a poor candidate. SiC is a much better candidate for a substrate because its lattice mismatch is only 3.4%. SiC has failed to produce better performance than films grown on sapphire, although it is improving.⁴⁵ This has made sapphire the predominant substrate for the AlGaN material system. A characteristic that sets this material system apart from other semiconductors is the fact that in spite of the high dislocation density (10^8 - 10^{10} cm^2)^{44,46}, which is orders of magnitude higher than what it is observed in other opto-electronic materials, it has

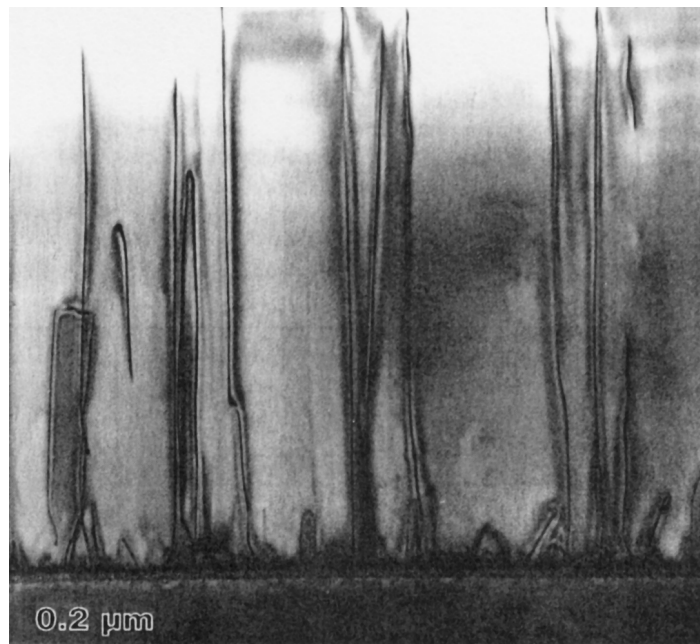


Figure 5.2 Threading dislocations in GaN Grown by MOCVD from reference 47

obtained high optoelectronic performance.⁴⁴ Figure 5.2 shows a Transmission Electron Microscopy (TEM) view of a GaN sample from reference 47.

Crystal Growth

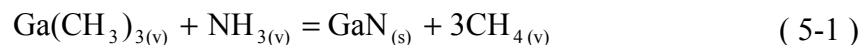
There have been several approaches in growing AlGaN epitaxy on a number of substrates. Among them, Hydride Vapor Phase Epitaxy (HVPE), Metalorganic Chemical Vapor Deposition (MOCVD), and Molecular Beam Epitaxy (MBE). Yet it wasn't until Yoshida recognized the importance of a low-temperature buffer layer for the improvement of surface morphology and crystalline quality of GaN, that devices in this material system began to take off.^{38,48} Subsequent studies improved on this approach.^{49,50,51} The approach has a few hundred angstroms of AlN deposited at a low-temperature (~600°C). The thickness and temperature is optimized for a particular reactor and substrate type.^{49,52} Subsequent layers are grown on top of this buffer layer. The buffer layer relieves the strain between the substrate and subsequent AlGaN layers.^{38,51} The low growth temperature of the buffer layer causes it to be amorphous.¹⁰ This permits the buffer to cover the substrate uniformly.¹⁰ When the heat is increased to normal growth temperature the buffer layer crystallizes and provides a good template for further epitaxy. For sapphire substrates the improvements obtained with the AlN buffer layer were:¹⁰

1. Two orders of magnitude decrease in background carrier concentration.
2. A factor of 10 in increased mobility.
3. Band-Gap photoluminescence (PL) were two orders of magnitude more intense.
4. Suppression of midgap emission

5. The x-ray diffraction peak was four times narrower.

Low temperature GaN buffer layers have also been used with no clear advantage of one over the other, although laser diodes have been obtained with GaN buffer layers with MOCVD.^{10,43}

Of the different growth techniques the ones that have grown the highest quality materials have been MBE and MOCVD. For commercial applications, MOCVD is the leading candidate with blue LEDs and violet LD already being marketed.^{38,46,53} In MOCVD, trimethylgallium (TMGa, $\text{Ga}(\text{CH}_3)_3$) and/or trimethylaluminum (TMAI, $\text{Al}(\text{CH}_3)_3$) react with NH_3 at a substrate which has been heated to $\sim 1000^\circ\text{C}$ to obtain the basic reaction given by^{10,38}



The details of this reaction are not yet well understood and the intermediate steps are

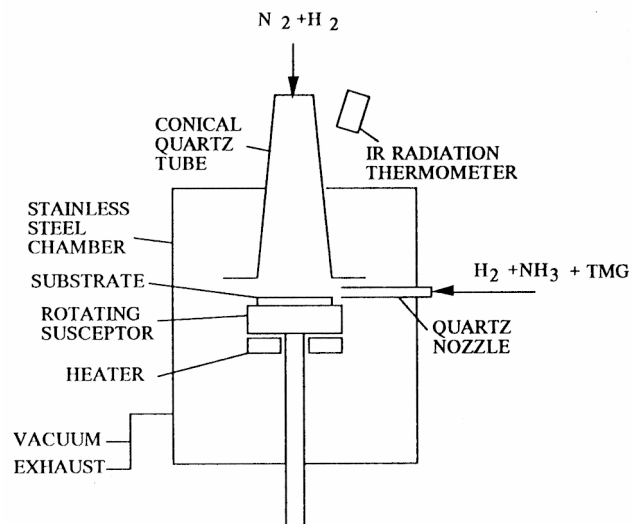


Figure 5.3 Dual Flow MOCVD, from reference 66

thought to be complex.³⁸ In a quest for superior material growth Nakamura designed a special atmospheric pressure MOCVD reactor optimized for GaN growth, see Figure 5.3.⁶⁶ In this approach the reactants are diluted in H₂. The sources are supplied from the horizontal inlet and a vertical subflow then drives the reactants to the growing film surface.^{38,66} In MOCVD, the high growth temperature required to break the N-H bond of ammonia precursors creates a problem. Due to the thermal mismatch with all the available substrates, post growth cooling introduces significant amounts of strain and defects into the nitride film.¹⁰ Additional problems of the MOCVD reactors are the film nonuniformity and the tendency of ammonia to prereact with the group III metalorganic compounds to form nonvolatile compounds.³⁸ These problems need to be overcome in the design and scale up of AlGaN deposition system by MOCVD reactors.³⁸

Another technique for growing AlGaN is MBE. MBE is in essence a specialized form

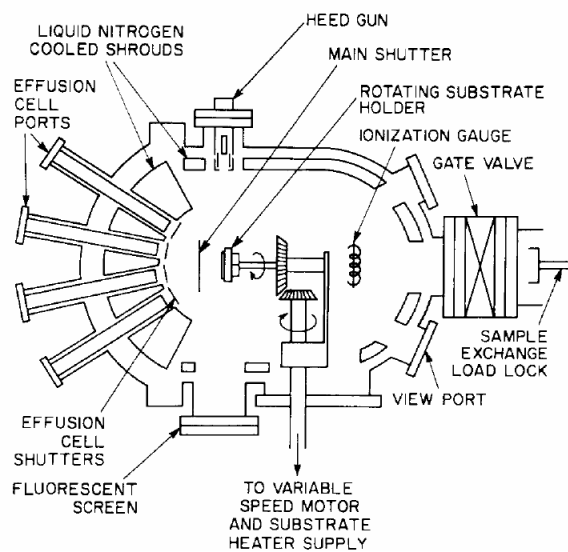


Figure 5.4 Basic MBE design from reference 54 and 55

of vacuum deposition with several important differences.⁵⁵ The growth of the semiconductor film takes place with the reaction of molecular beams of the constituent elements with a crystalline substrate surface held at a suitable substrate temperature under UHV conditions.⁵⁵ The molecular beams are generated from sources contained in effusion cells, which are aimed at the heated substrate.⁵⁵ A basic MBE system is shown on Figure 5.4.^{54,55} For the AlGaN growth, gallium and aluminum are supplied by evaporation from solid source effusion cells, and the atomic nitrogen species are obtained by either an N₂ plasma source or by thermally activated decomposition of NH₃ on the growing surface.⁴³ An advantage for MBE grown material is the low growth temperature needed.^{43,38,56} This should result in lower thermal stresses upon cooling, less diffusion, and reduced alloy segregation.³⁸ Another advantage is that as grown *p*-type GaN films don't require any passivation steps, due to the absence of atomic hydrogen species during growth. Although most of the high quality material has been grown by MOCVD, MBE has made a lot of progress toward AlGaN growth, as is evident by the realization of LEDs and electronics.^{57, 58, 59, 60}

Recently, the Lateral Epitaxy Overgrowth (LEO) technique has attracted attention as a way to reduce threading dislocations in selected areas of AlGaN layers.^{61,62} In this technique a mask is deposited on top of the standard dislocated layers and patterned.^{63,64} A regrowth is done on the pattern. The material, which grows vertically through the opening of the mask, retains the same dislocation density. But, the material that grows laterally, on top of the mask, has a much lower dislocation density.^{61,62,63} Figure 5.5

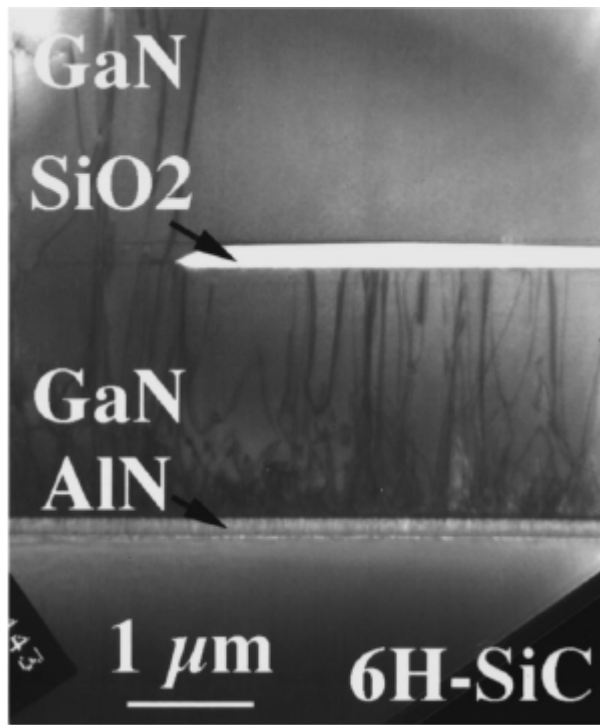


Figure 5.5 TEM showing dislocation density reduction via LEO, from reference 61

shows the dislocation density reduction on top of a SiO_2 mask. Devices have been grown on top of the LEO material with significantly improved performance compared to devices grown on normal, dislocated materials.^{63, 46}

Another big catalyst in the emergence of nitride devices was the achievement of low-resistivity *p*-type doping in the AlGaN material structure. This achievement was accomplished by Amano *et al.* in 1989 using Low-Electron Beam Irradiation (LEEBI) treatment with Mg doping on MOVPE grown material.⁶⁵ Though at that time, the acceptor activation ratio was low requiring a high Mg incorporation for high *p*-doping levels.⁹ Later Nakamura *et al.* were able to improve the *p*-type doping levels ($\sim 10^{18}/\text{cm}^3$) on MOCVD grown material.⁶⁶ A deficiency of the LEEBI treatment is that it only

activated a thin surface layer.^{65,66} This was later overcome by Nakamura et al. by discovering that *p*-type levels could also be activated by a thermal anneal at 700°C in an N₂ atmosphere, this time the entire Mg doped layer became *p*-type with low resistivity.⁶⁷ This activation is reversible when the material is annealed in NH₃ atmosphere.⁹ This reversibility pointed to hydrogen as a main factor in preventing *p*-type doping. As it turns out, during growth hydrogen is interstitially incorporated creating an H-Mg acceptor complex.³⁸ This complex causes the acceptor to be passivated. This bond has to be broken in order to achieve *p*-type material. This is achieved with high temperature annealing. With this knowledge, *p*-type material was also achieved in MBE grown material by minimizing the effect of hydrogen.^{9,68}

Optical Properties

As mentioned before, Al_xGa_{1-x}N has a large bandgap starting at 3.4 eV. For

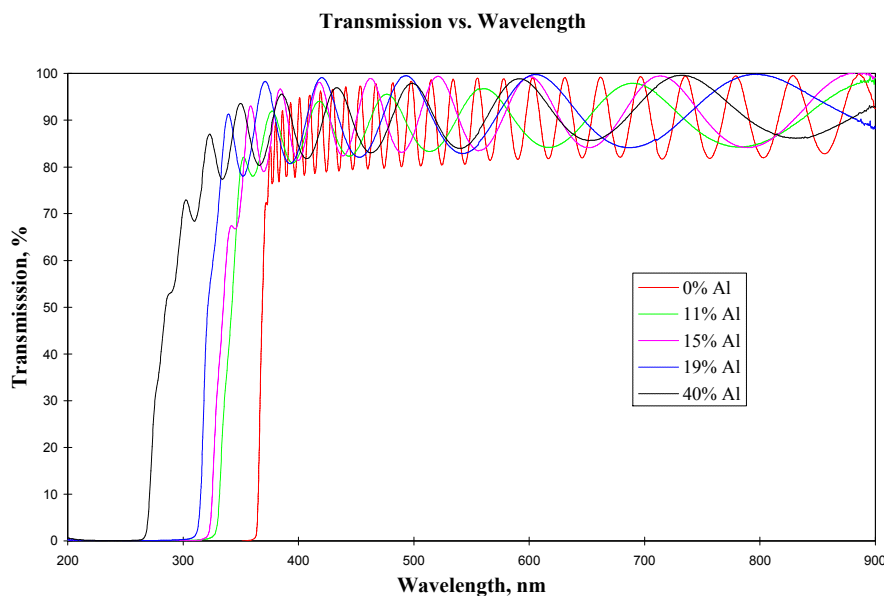


Figure 5.6 AlGaN transmissivity

semiconductors this makes the material transparent to wavelengths whose energy is below that of the bandgap. The transmisivity of $\text{Al}_x\text{Ga}_{1-x}\text{N}$ for several values of x is given in Figure 5.6. Along with this, the bandgap can be changed by varying x . The variation in x will also change the refraction index of the material. Control of the index of refraction enables one to confine the optical wave, as mentioned in chapter II. Precise knowledge of the index variation with respect to x and the wavelength is needed. There have been several studies for the index of refraction of AlGaN.^{69,70,71,72} These have inconsistencies among them regarding the values of the refraction index.⁷² This is due to the fact that these semiconductors are still in their infancy.⁷² The AlGaN wurtzite crystal is uniaxial, therefore it has two indices of refraction related to it, see chapter III. Bergmann *et al.* have done a recent study on both ordinary and extraordinary refractive indices on AlGaN.⁶⁹ The measurements were taken for the wavelengths $457 < \lambda < 980$ nm and the compositions $x = 0.00, 0.04, 0.08, 0.11$, and 0.20 with an accuracy of $\pm 10\%$.⁶⁹ The refraction indices were obtained using the prism-coupled waveguide technique, and had an accuracy of $\sim \pm 0.01$.⁶⁹ The data obtained was fit to the 1st order Sellmeier dispersion formula given by:

$$n(\lambda) = 1 + \frac{A_o \lambda^2}{\lambda^2 - I_o^2} \quad (5-2)$$

where:

$$A_o(x) = B_o + B_1 x + B_2 x^2 \quad (5-3)$$

$$I_o(x) = C_o + C_1 x \quad (5-4)$$

Table 2. Coefficient for the Sellmeier dispersion formula, from reference 69

Coefficient	n_o	n_e
B_0	4.1416 ± 0.008	4.3076 ± 0.008
B_1	-1.0 ± 0.2	-1.2 ± 0.2
B_2	-4.4 ± 0.9	-3.7 ± 0.8
C_0	$187.4 \pm 0.4 \text{ nm}$	$190.3 \pm 0.4 \text{ nm}$
C_1	$-121 \pm 3 \text{ nm}$	$-121 \pm 4 \text{ nm}$

Table 2 lists the coefficients for the Sellmeier formula. The major source of problems in establishing the accuracy of the refractive index equations is not only the index data itself but also the accuracy of the Al mole fraction in the $\text{Al}_x\text{Ga}_{1-x}\text{N}$ material.⁷² According to Laws et al., the determination of the Al composition on $\text{Al}_x\text{Ga}_{1-x}\text{N}$ is very difficult and the results depend on the homogeneity of the samples as well as the measurement technique employed.⁷²

GaN ‘s hexagonal crystal symmetry corresponds to the 6mm group. This enables it to have linear electro-optic (Pockels) effect. Its contracted electro-optic tensor (see Chapter III) is given by:

$$\vec{r} = \begin{pmatrix} 0 & 0 & r_{13} \\ 0 & 0 & r_{13} \\ 0 & 0 & r_{33} \\ 0 & r_{51} & 0 \\ r_{51} & 0 & 0 \\ 0 & 0 & 0 \end{pmatrix} \quad (5-5)$$

substituting this equation into equation (3-31) we get equation (1-5), which is shown here for convenience:

$$\left(\frac{1}{n_o^2} + r_{13}E_z \right)x^2 + \left(\frac{1}{n_o^2} + r_{13}E_z \right)y^2 + \left(\frac{1}{n_e^2} + r_{33}E_z \right)z^2 + 2yz r_{51}E_y + 2xz r_{51}E_x = 1 \quad (5-6)$$

This equation gives one the change in the index of refraction as a function of the applied electric field. Long *et al.* has measured and reported on some of the nonlinear coefficients.¹⁶ These are $r_{13} = \sim 0.57 \pm 0.11$ pm/V and $r_{33} = \sim 1.91 \pm 0.35$ pm/V. The third electro-optic coefficient was measured by Khan *et al.* and is given by $r_{51} = 3.1 \pm 0.2$ pm/V.¹⁷ All these were measured for the wavelength 632.8 nm. Not only does it have linear electro-optic but also second order non-linearities, which are beyond the scope of this work.^{73,74}

CHAPTER VI

EXPERIMENTATION AND RESULTS

The proposed directional coupler design for this work is based on a rectangular dielectric waveguide with zero gap between the branches, see Chapter IV, and is based on the $\text{Al}_x\text{Ga}_{1-x}\text{N}$ material system. The waveguides will have a clad-core-clad configuration, as shown in Figure 6.1 a). The advantages of this structure are that the top and bottom cladding can be doped *p* and *n* while the core is insulating. This will create a PIN structure that in reverse bias will concentrate the electric field *E* in the core region. This would result in greater index variation for a given voltage. In-house material was grown using an MBE machine on top of sapphire substrates. For the in-house MBE, *p*-type doping was not feasible. Therefore, instead of a *p-i-n* structure an *n-i-n* structure is

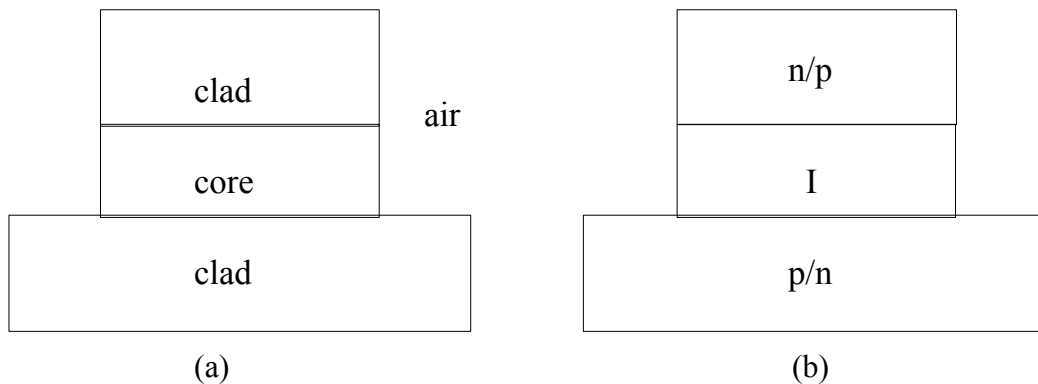


Figure 6.1 Proposed structure a) single waveguide b) interaction region

chosen.

Design

For the design of the optical waveguides, as stated in the chapters above, an index of refraction variation is needed for the confinement of light. At the beginning of this work the studies made by Brunner *et al.* were used as a basis for the index of refraction calculations.⁷¹ The wavelength selected for the operation of the directional coupler was 632.8 nm. This was based to the fact that the available information on GaN's linear electro-optic coefficient was done at this wavelength and the accessibility of HeNe lasers.¹⁶ The equations needed to obtain the index of refraction, according to Brunner *et al.*, are:⁷¹

$$n_o^2(hn, x) = C(x) + A(x)y^{-2} \left(2 - (1+y)^{1/2} - (1-y)^{1/2} \right) \quad (6-1)$$

$$n_e \approx n_o + 0.02$$

where:

$$y = \frac{hn}{E_g(x)}$$

$$C(x) = \text{const}(x) \quad (6-2)$$

Table 3. Refraction index parameters for Equation (6-1)

x (Al composition)	$A(x)$	$C(x)$	Bandgap (eV)
0.00	9.76472	2.74493	3.42
0.11	10.04172	2.59099	3.64
0.20	11.65128	2.04179	3.89
0.38	11.87005	1.96916	4.16
0.50	12.72810	1.25847	4.63
0.65	12.56483	1.21344	4.73
0.79	12.64459	0.78265	5.21
0.86	12.64948	0.64295	5.50
1.00	13.50000	0.75000	6.13

$E_g(x)$ is the effective bandgap. $A(x)$ is a function of the oscillator strength of the optical transition, and $E_g(x)$. $A(x)$ and $C(x)$ experimental values are given in Table 3. These numbers were supplied by Dr. O. Ambacher and are part of reference 71. With Equation (6-1) we can calculate the index variation as a function of Al composition for each of the Al concentrations in Table 3. In Figure 6.2 the diamonds are the calculated refraction indices and the solid line is the trend line. The trend line equation is given by:

$$n_o = 3.9968 x^5 - 7.0603 x^4 + 3.8812 x^3 - 0.9418 x^2 - 0.1613 x + 2.3024 \quad (6-3)$$

With this index variation in terms of Al concentration we can now design waveguides in a clad-core-clad configuration.

As it can be seen from Figure 6.2 the refractive index decreases as the Al concentration

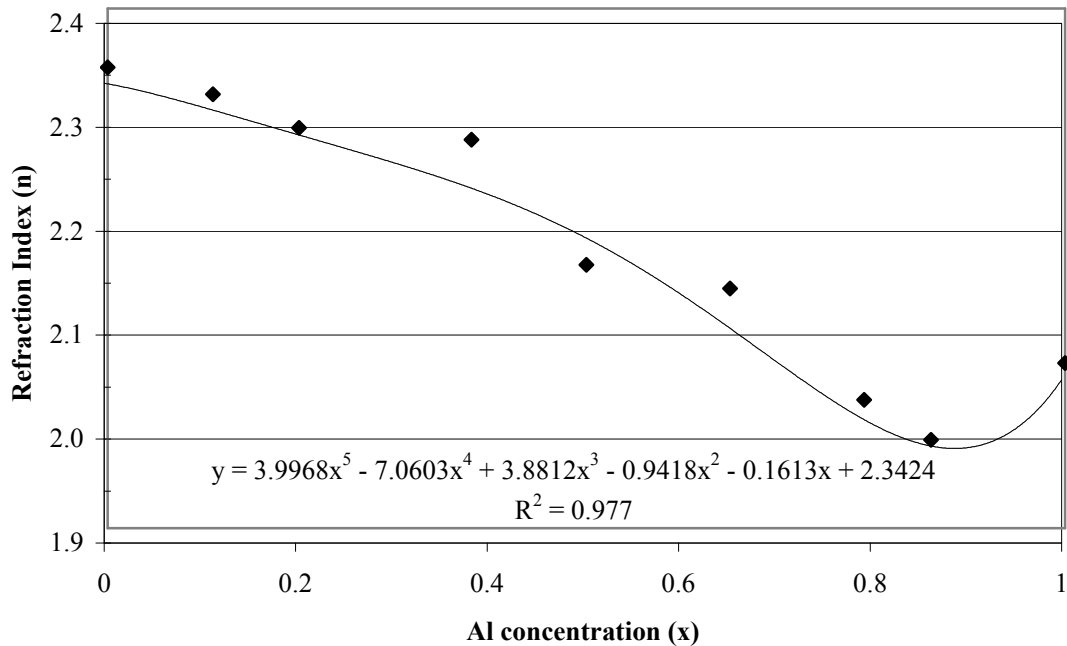


Figure 6.2 Refraction index variation for $\lambda = 632.8$ nm from ref 71

increases. For this reason GaN is chosen for the core material. Due to growth constraints 10% Al concentration was chosen in the beginning. The refraction indices given by Equation (6-3) for the core and cladding are then

	n_o	n_e
Core, GaN	2.342	2.362
Cladding, $Al_{0.1}Ga_{0.9}N$	2.320	2.340
Cladding, $Al_{0.05}Ga_{0.95}N$	2.332	2.352

In a non-native substrate like sapphire, the $Al_x Ga_{1-x} N$ material system grows in the c-axis direction, see Figure 5.1. This means that the electric field will be along the z direction in the crystal axes and simplifies Equation (5-6) to:

$$\left(\frac{1}{n_o^2} + r_{13}E_Z \right)x^2 + \left(\frac{1}{n_o^2} + r_{13}E_Z \right)y^2 + \left(\frac{1}{n_e^2} + r_{33}E_Z \right)z^2 = 1 \quad (6-4)$$

Since of these two r_{33} is the highest coefficient, the polarization direction was chosen to be along the z-axis. That will give us

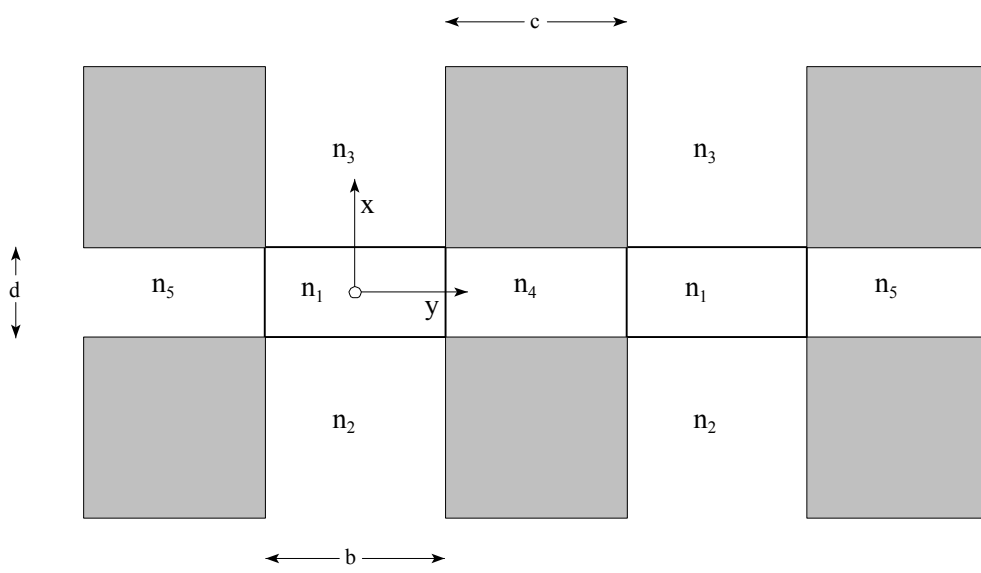


Figure 6.3 Cross sectional view of a directional coupler in the interacting region

$$\frac{1}{n_e^2} + r_{33}E_Z = 1 \quad (6-5)$$

Which corresponds to the e-ray polarization.

In order for the directional coupler to work, each of the waveguides needs to be single mode and the region where the two waveguides are joined needs to be dual mode, see Chapter IV. We can first start with the Marcatili model, since, it can give us a rough estimate of the waveguides dimensions, using Figure 6.3 and Equations (2-45) - (2-53), with little computational time. We first need to plot the mode chart along with the normalized waveguide frequency. This will indicate the modes present in the structure. Several iterations were done to obtain a viable structure. The results are shown in Figure 6.4. This corresponds to a waveguide with the following parameters:

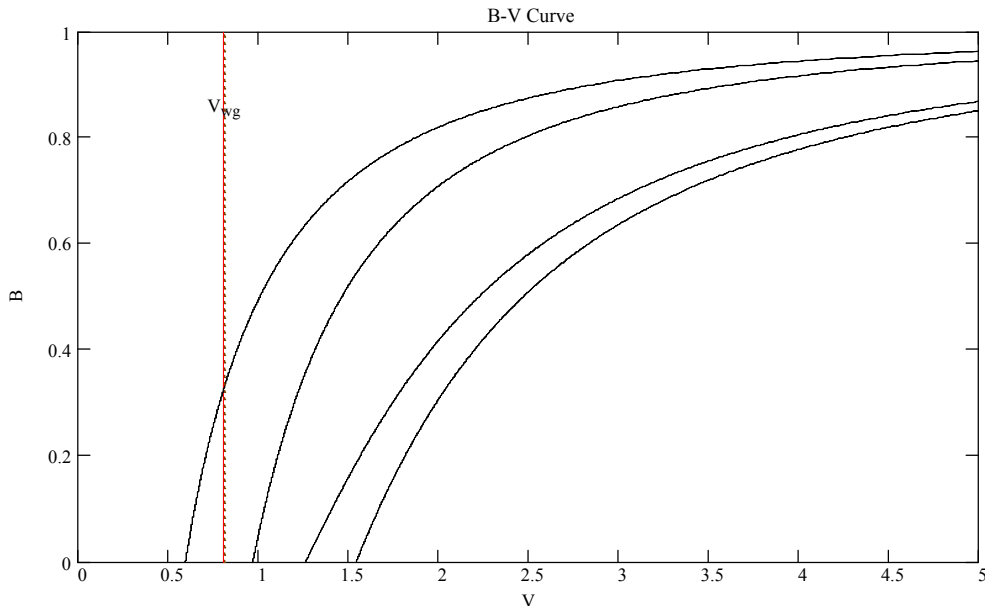


Figure 6.4 Mode chart for the single mode rectangular waveguide using the Marcatili's model, waveguide width 2.0 μm

$$\begin{aligned} b &= 2 \text{ } \mu\text{m} & d &= 0.8 \text{ } \mu\text{m} & n_1 &= 2.362 & n_2 = n_3 &= 2.34 & (6-6) \\ n_4 &= n_5 = 1 \end{aligned}$$

where Figure 6.3 was used. Since, in Marcatili's method, the waveguides are assumed far from cutoff, the waveguide structure was chosen to between the two lower modes, V_{wg} . A waveguide with a width of $1.5 \mu\text{m}$, which is closer to the cut off, was also modeled using the Marcatili's method. The results for the smaller width must be used carefully, since Marcatili's method is not reliable close to cut off. The results of this simulation are shown in Figure 6.5. For the height of the cladding region (n_2 and n_3), it was desired that the evanescent wave would be sufficiently attenuated to reduce the losses due to surface roughness at the clad-air and the clad-sapphire interfaces. The evanescent waves attenuates as:

$$e^{\gamma_{2,3} x} \quad (6-7)$$

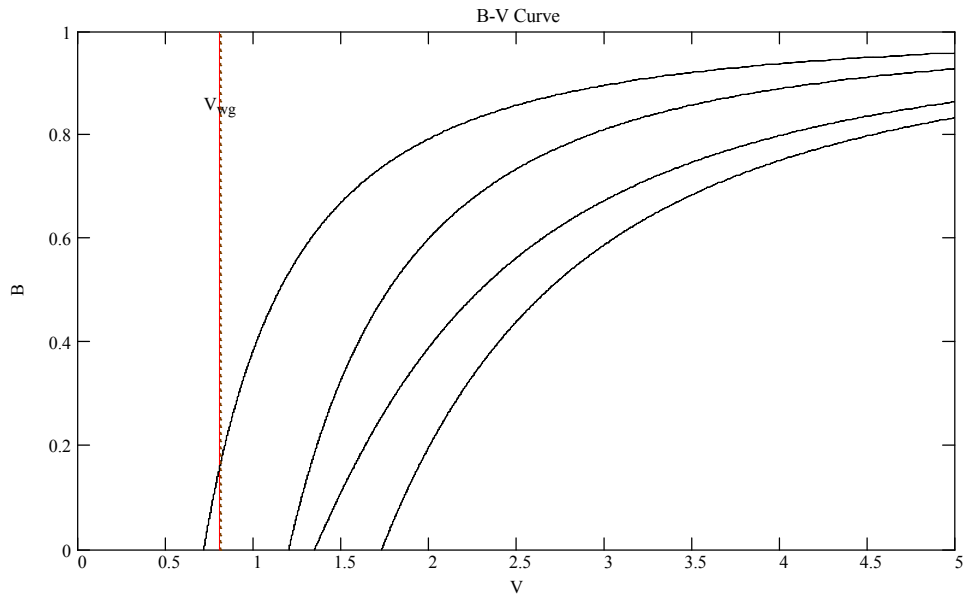


Figure 6.5 Mode chart for the single mode rectangular waveguide using the Marcatili's model, waveguide width 1.5 μm

starting at the core-clad interface and into regions 2 and 3. In the equation above, x would be the distance from the interface and $g_{2,3}$ are given by Equations (2-39) and (2-40). An additional constrain is the total height of the epitaxial layer that can be grown on the sapphire with the in-house MBE machine, which is 3 μm . A 1.2 μm layer was chosen for the cladding in contact with the sapphire and 1 μm for the cladding in contact with air.

The cladding in contact with sapphire was chosen to be larger because the dislocation density gets reduced as you move away from the sapphire/AlGaN interface. At these thicknesses the attenuation of the electric field is (using Equations (2-39), (2-40), and (6-7)) 0.041 for 1 μm and 0.022 for 1.2 μm . From this, the design of the waveguide structure is given in Figure 6.6. The minimum coupling length needed for complete power transfer for the 2.0 μm width is, using Figure 6.3 and Equations (2-41), (4-12) and (4-13), $\sim 483 \mu\text{m}$, and for the 1.5 μm width the coupling length is $\sim 209 \mu\text{m}$.

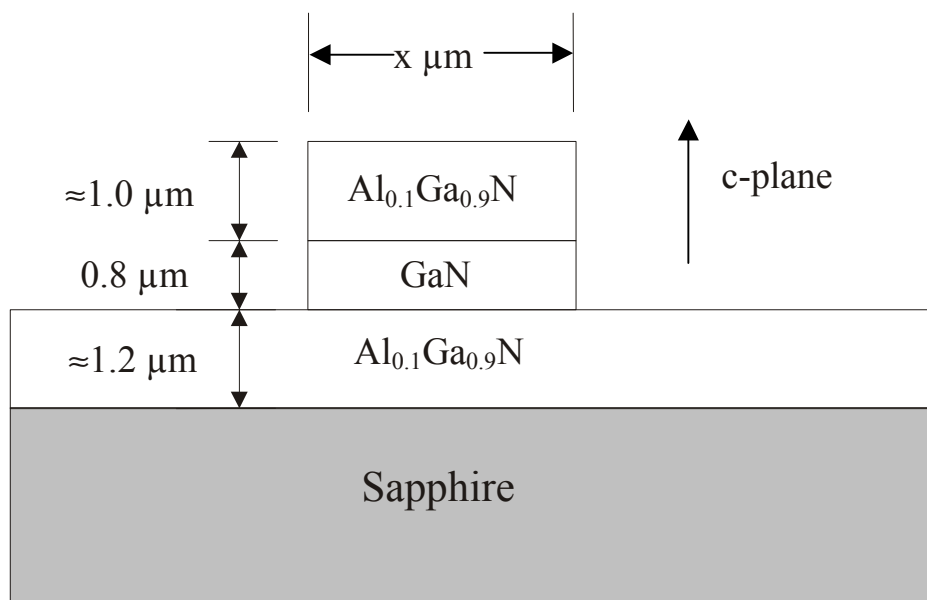


Figure 6.6 Side view of the single mode waveguide structure for AlGaN, x is chosen to be 1.5 and 2.0 μm

After using Marcatili's model the design for a directional coupler with $2.0 \mu\text{m}$ waveguides was further refined. BeamProp from Rsoft Inc was used as the beam propagation method program. Instead of creating a program from scratch the commercial program was used. For the directional coupler design, a straight input was used to simplify the design and reduce the computational time, see Figure 6.7. This enables one to concentrate on the interaction region. In Figure 6.7 one sees a cross-sectional top view of the intensity profile of the optical signal in the directional coupler. The cross-section was taken at half the height of the core region. In it one can see the light coupling back and forth between the guides. Figure 6.8 is the power in the core for each waveguide path

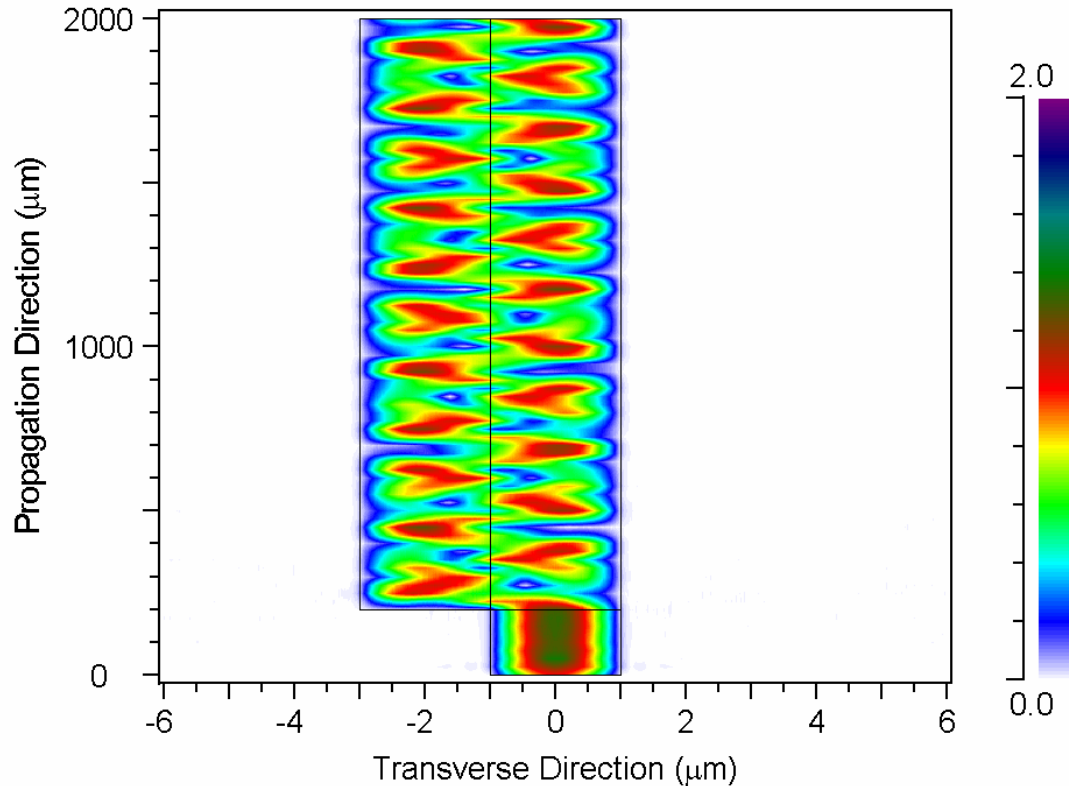


Figure 6.7 Intensity profile of a straight directional coupler, Waveguide width $2.0 \mu\text{m}$ Based on Brunner *et al.*⁷¹

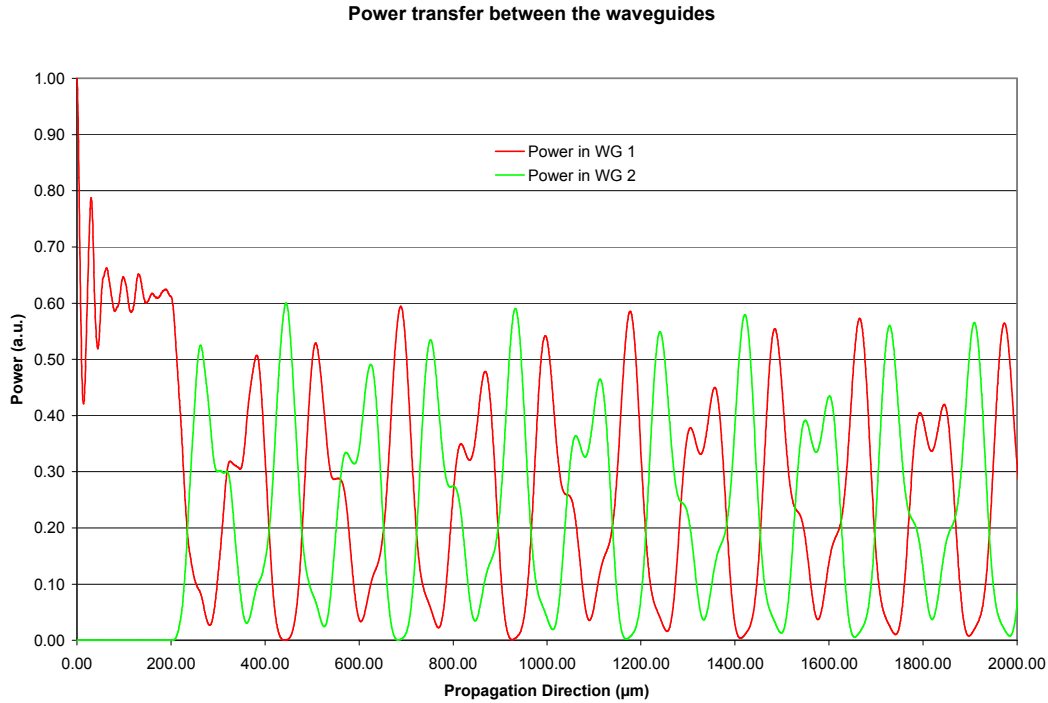


Figure 6.8 Mode power for each waveguide, waveguide width $2.0\mu\text{m}$. Based on Brunner *et al.*⁷¹

as a function of the propagation direction. This figure is a much better illustration of how the optical signal couples between the waveguides. Figure 6.8 tends to suggest the presence of an additional mode in the structure. Figure 6.9's cross sectional front view of the directional coupler shows a weak third mode, according to the beam propagation method, between the guides. This third mode is not present in the Marcatili's method analysis, as illustrated in Figure 6.10. Furthermore, Figure 6.8, gives the minimum length for complete power transfer between the guides as $\sim 89\ \mu\text{m}$ which is much smaller than what Marcatili's theory predicts, $\sim 483\ \mu\text{m}$.

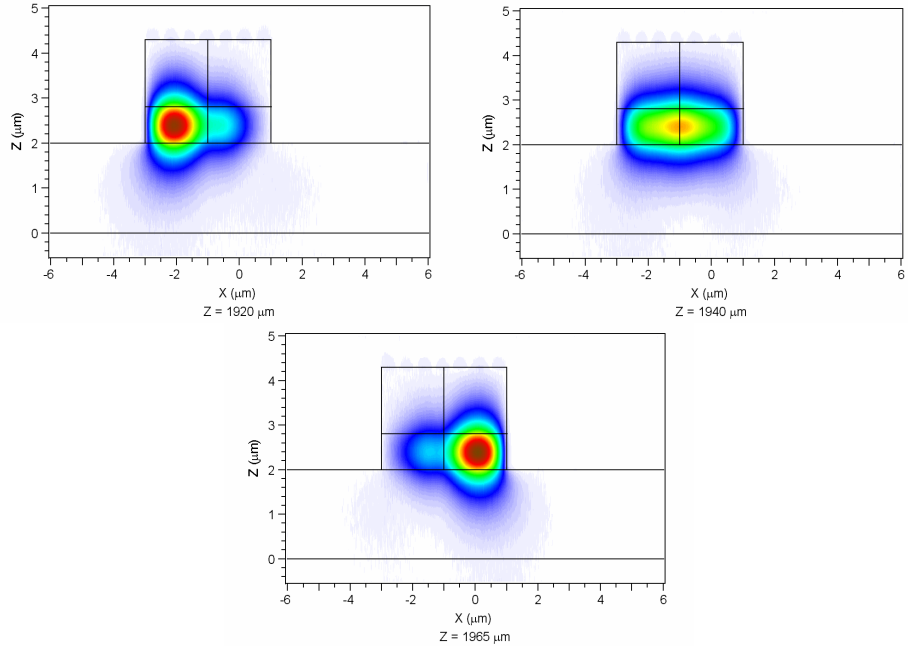


Figure 6.9 Cross sectional view of the directional coupler in the direction of propagation, according to the beam propagation method by BeamProp. Waveguide width is $2.0\mu\text{m}$. Based on Brunner *et al.*⁷¹

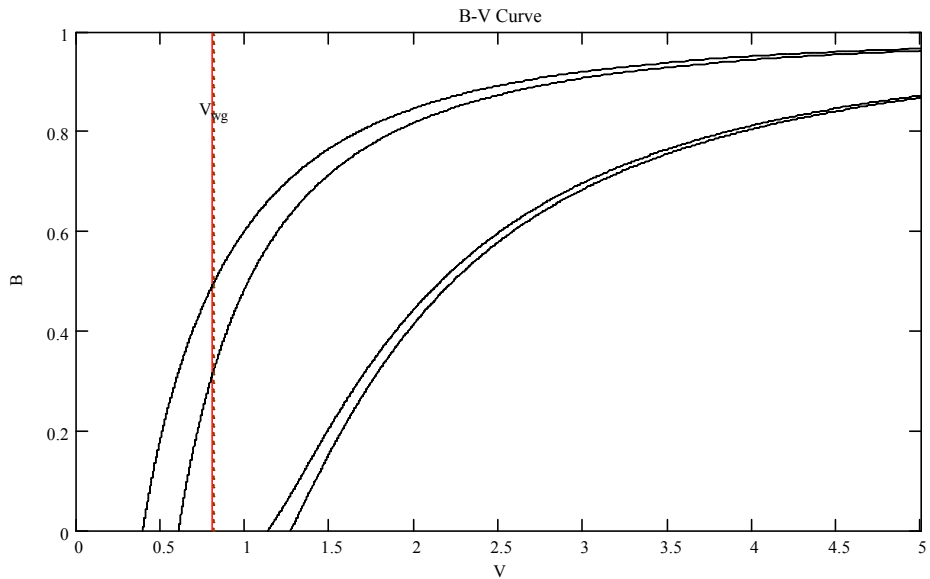


Figure 6.10 Mode chart for the interaction region of the directional coupler, using the Marcatili's model, corresponding to the $2\mu\text{m}$. Total width is $4\mu\text{m}$. Based on Brunner *et al.*⁷¹

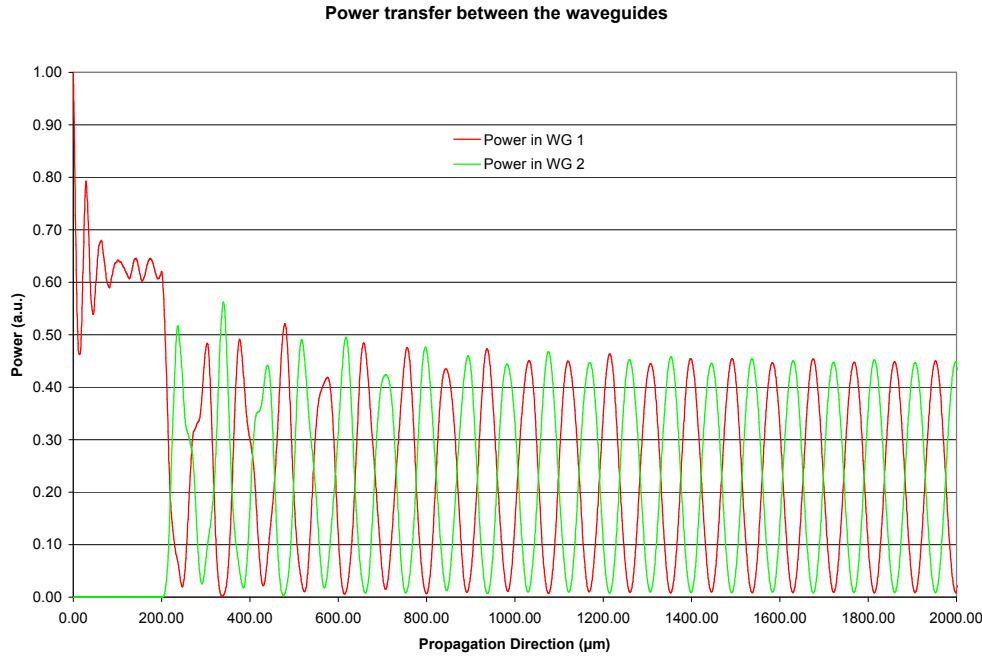
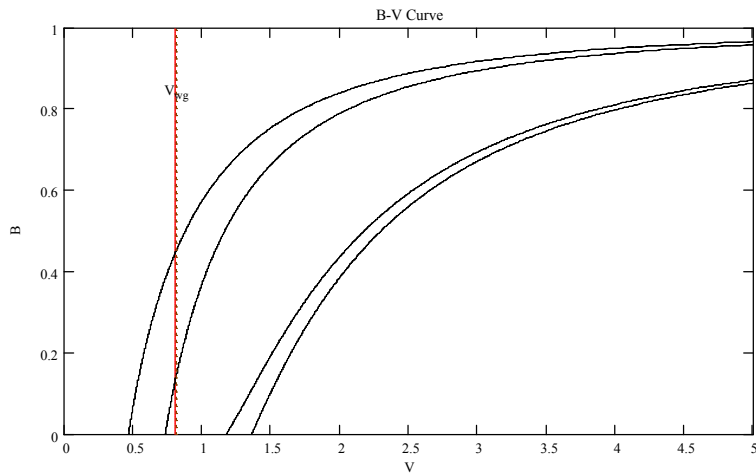


Figure 6.11 Mode power for each waveguide, Waveguide width $1.5\mu\text{m}$. Based on Brunner *et al.*⁷¹

The directional coupler with the $1.5\mu\text{m}$ branches was simulated with the beam propagation method, the results are shown in Figure 6.11. With this width the third mode



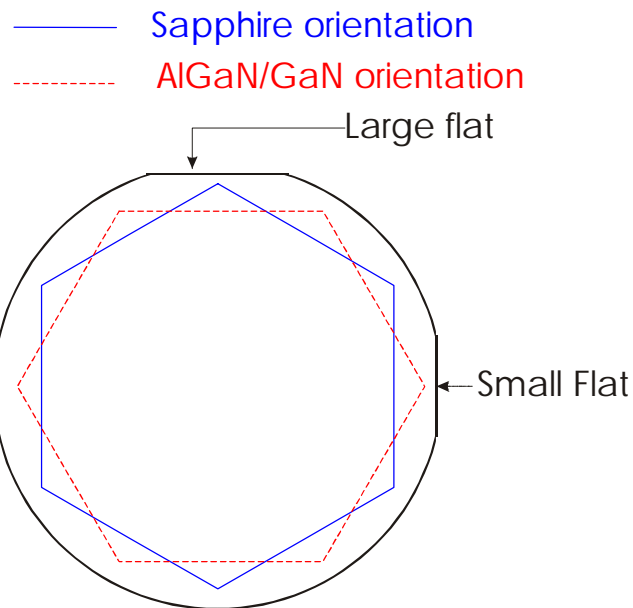


Figure 6.13 Crystal orientation between sapphire and AlGaN

appears to disappear. There are still discrepancies between the simulation methods. In the Marcatili's method there is no third mode and, according to Figure 6.12, the second mode is close to cut off. Additionally, it gives a coupling length for complete power transfer of $\sim 209 \mu\text{m}$ while the beam propagation method gives us $\sim 53 \mu\text{m}$. From Figure 6.11 we can see that the third mode was not entirely gone in the first 1000 μms , it dissipated slowly.

First Mask Set Processing, and Results

With these analyses two initial mask templates were designed. In it there were waveguides of different widths and lengths along with different configurations of directional couplers, see APPENDIX A. These mask templates were done to produce solely passive devices, initiate the development of device processing in AlGaN, and determine which structures are suitable for a directional coupler design. The difference

between the two mask templates was that on one of them the structures were defined by the metal in the template (light field mask) and the other by the absence of it (dark field mask). The AlGaN material was grown in-house on an MBE machine using sapphire substrates. One disadvantage of using the sapphire substrates is that the crystal orientation of sapphire is 30° offset to that of the AlGaN material system, see Figure 6.13. This makes it very difficult, if not impossible, to cleave the sample. A good method to cut the sample is to saw it all the way.

Being a material that withstands high temperature and caustic environments makes it difficult to etch. Up to date the most successful methods to etch AlGaN are dry etching, although some progress has been done with wet etching techniques.^{37,75,76,77,78,79,80} For this work, the load locked Plasma-Therm SLR 770 ICP reactor was used to etch AlGaN. Initially, there was not a suitable mask or recipe to etch a waveguide that was deep enough or steep enough. For this particular application the waveguides had to be $\sim 2 \mu\text{m}$ high with steep sidewalls, see Figure 6.6. Many combinations of masks and recipes were investigated until a suitable one was found, see APPENDIX B.1. A suitable masking material turns out to be Ni. This was the only material able to withstand the etching of the AlGaN materials and have slow degradation. The other materials had to be at least half the thickness of the desired etching height. Standard processes were used as the initial starting points to transfer the pattern into the AlGaN material. The lift off process was used to create a metal pattern while the etch masking process was use for a photoresist pattern with the dark and light field masks respectively.³⁶ Figure 6.14 shows the

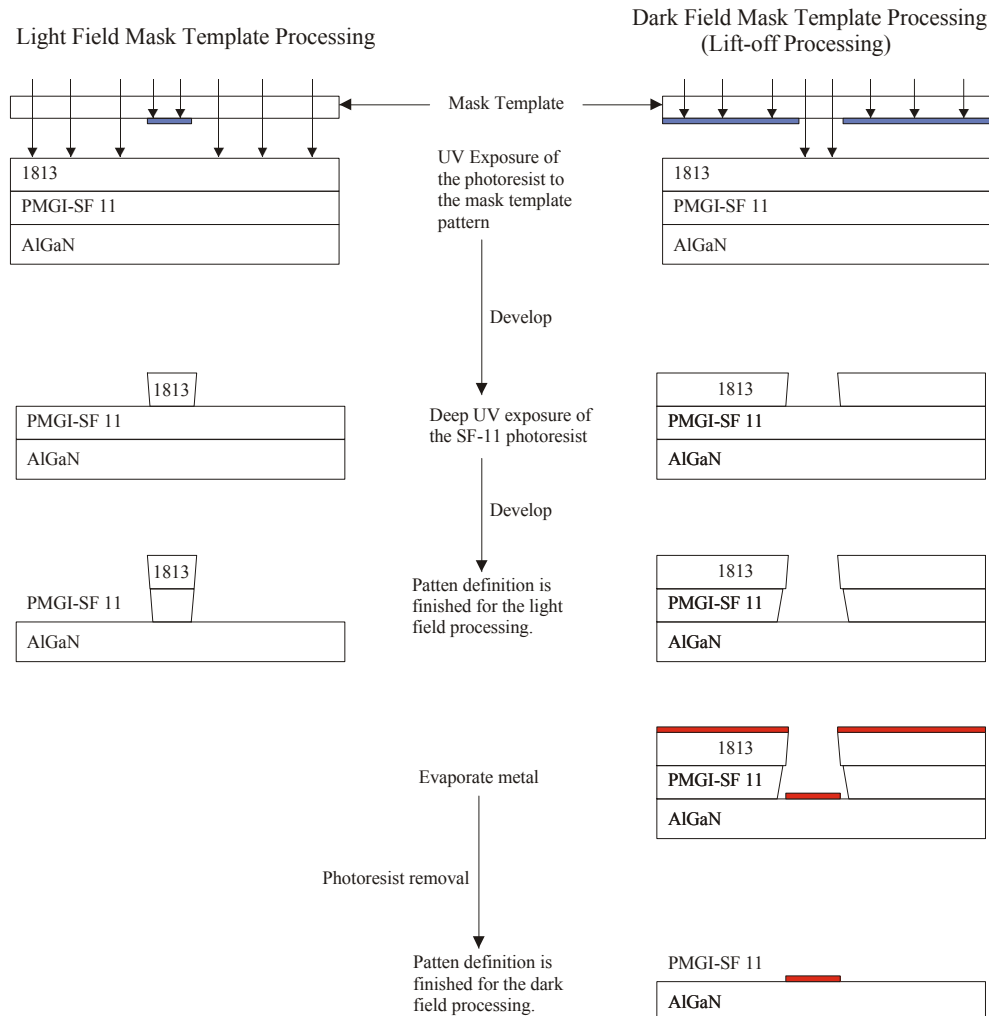


Figure 6.14 Process flow for the transfer of the Mask template pattern into the sample

schematic flow of the process followed for both the dark field and the light field templates. APPENDIX C.1 shows the details of the dark field process. The process in APPENDIX C.1 adds an optional SiN layer to detach Ni at the end of the process. In both processes, a dual layer of positive photoresist is used (1813 and SF-11).

Although sawing the sample is effective in dividing it into smaller pieces it doesn't leave the end points of the waveguides in a good enough condition to launch light into or

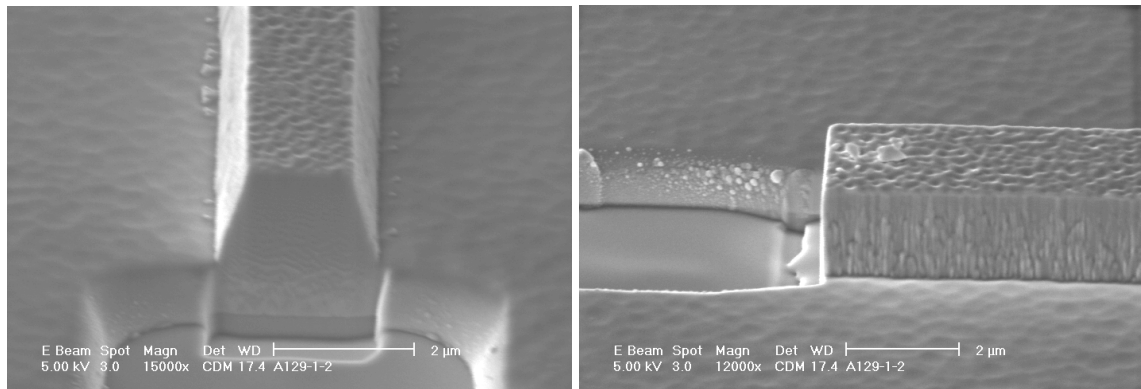


Figure 6.15 End polishing of a waveguide using the FIB

out of them. To polish the ends of the waveguides a FEI Dual Beam 620 FIB/SEM workstation was used. This type of polishing has been shown to improve the facets of GaN laser diodes.⁸¹ Figure 6.15 shows the results of polishing with the Focused Ion Beam (FIB). As it can be seen, the polishing of the end of the waveguide is much better than the etching from the ICP.

Another problem that showed up was that once the light was launched into the waveguide the output was obscured by the background stray light emanating from the laser. In order to solve this, a $\sim 45^\circ$ angle was cut into the waveguide with the FIB, this

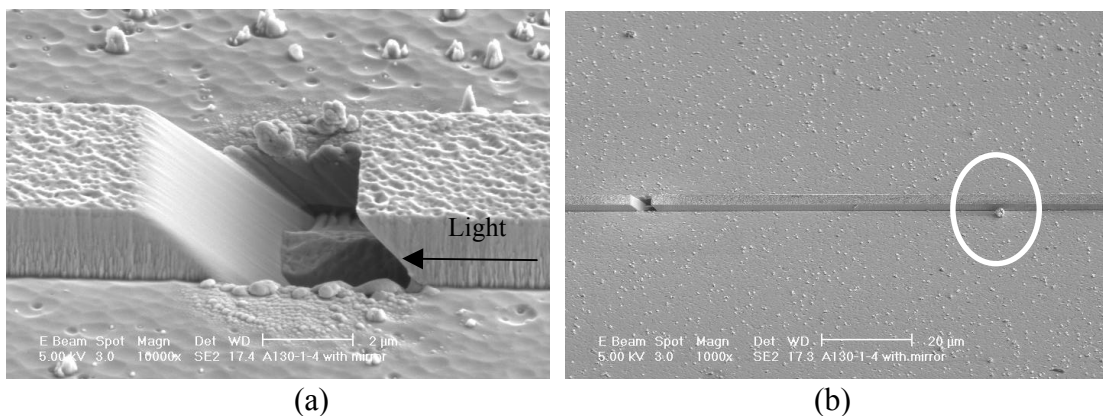


Figure 6.16 Etched mirror (a) close up of the mirror, (b) mirror with respect to spec present near the waveguide

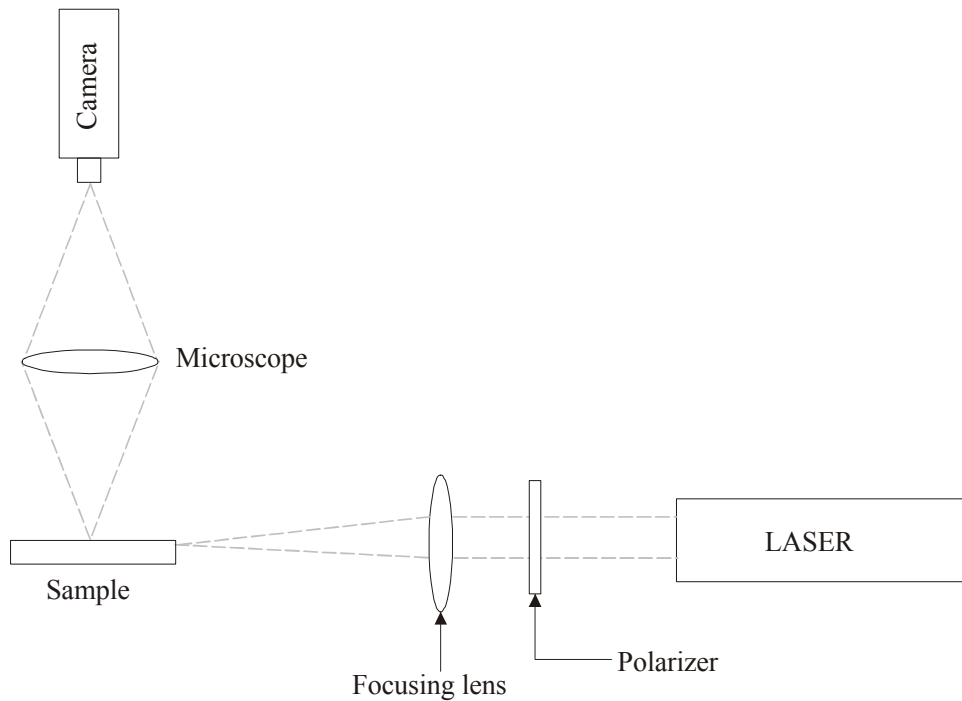


Figure 6.17 Schematic of testing setup

made the light shoot straight up thus avoiding any stray light from the laser (see Figure 6.16). The mirror shown on Figure 6.16 was etched at $\sim 1\text{mm}$ from the input end of the waveguide.

The schematic of the experimental setup used to launch light into the waveguides and examine them from the top is shown on Figure 6.17. In the experimental setup a 5 mW, 632.8 nm, laser light is expanded and then collimated, not shown. The laser light is then passed through a polarizer in which only light polarized normal to the surface of the sample is selected, see Equation (6-5). The light is then focused into the waveguide. Alignment is made through a 5 degrees of freedom stepper motor system. The stepper motor system can be controlled by a computer or manually. Light is then collected from the top of the sample with a microscope system and imaged into a camera. The camera

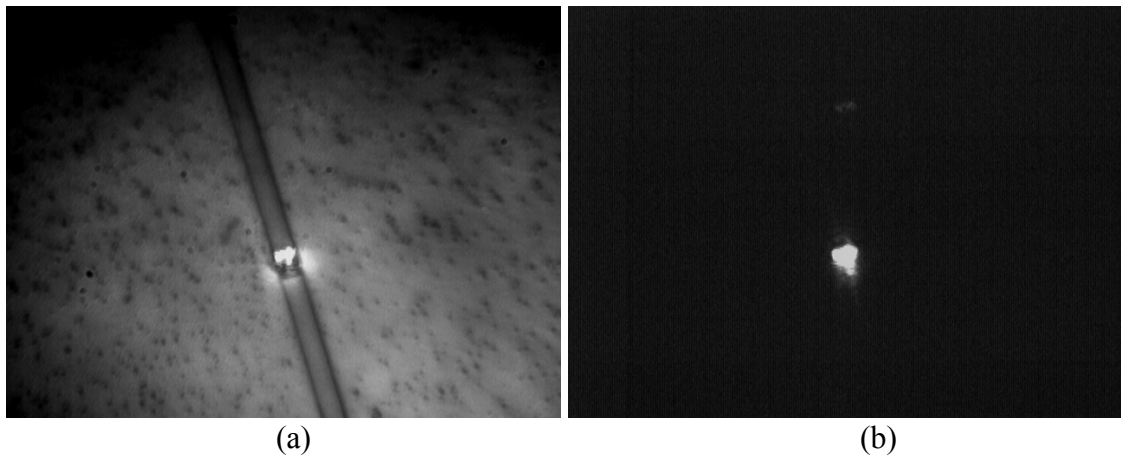


Figure 6.18 Light guidance. Both images are of the same region (a) output with lights on and (b) output with lights off

was a COHU 6310 series monochrome camera capable of 640 x 480 resolution and the output is fed into an image capture card.

Figure 6.18 shows the output from the waveguide shown in Figure 6.16. This particular waveguide was $\sim 6 \mu\text{m}$ wide, and thus multimode on both the simulation models, but it illustrated the success of the wave guiding capability of the structure and the success of the $\sim 45^\circ$ mirror. Light escaping from the top of the waveguide (not the mirror output) cannot be observed, although a very strong signal is emerging from the waveguide. Figure

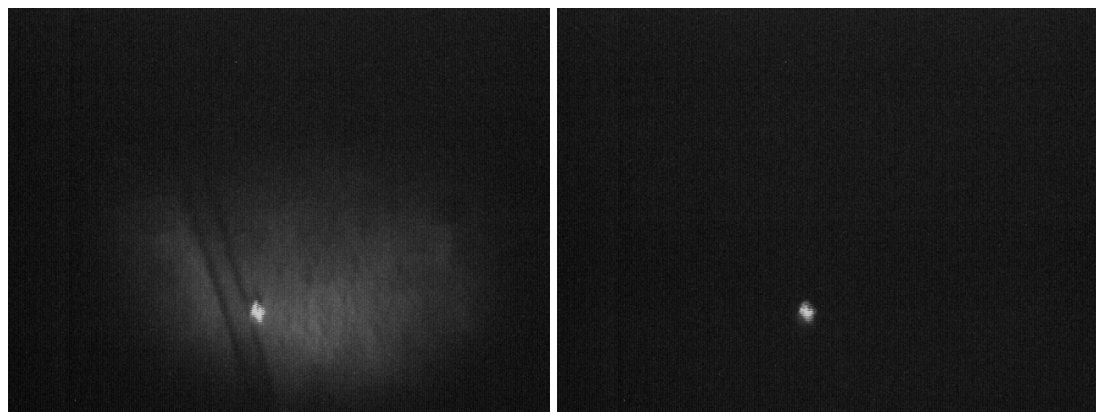


Figure 6.19 Light coupling into the spec shown in Figure 6.16 b)

6.19 shows the spec next to the waveguide lighted up, see Figure 6.16 b). It is suspected that most of the loss mechanism in the waveguide is through the rough sidewalls where the core is exposed to air, see Figure 6.15 and Figure 6.16. It is known that interface deformations will result in losses.²²

In order to see if the light was escaping the waveguides from the sides rather than from the top, a modification was made to the setup to see a greater portion of the sides. The sides were viewed at an angle of $\sim 11^\circ$ from normal and the amount of light observed was

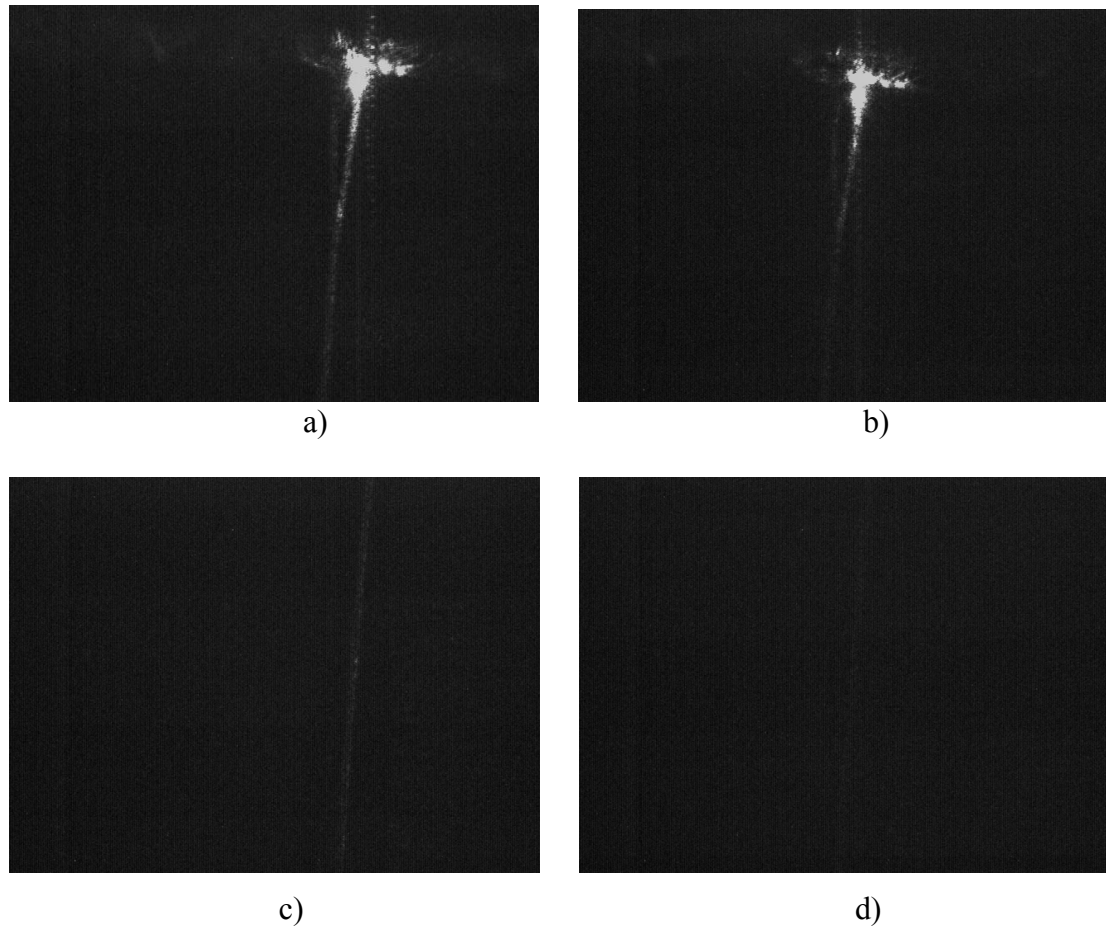


Figure 6.20 Light being launch in a directional coupler and viewed a), c) at 11° from normal, b), d) viewed normal to the sample. c) and d) were taken 1.2 mm down from a) and b)

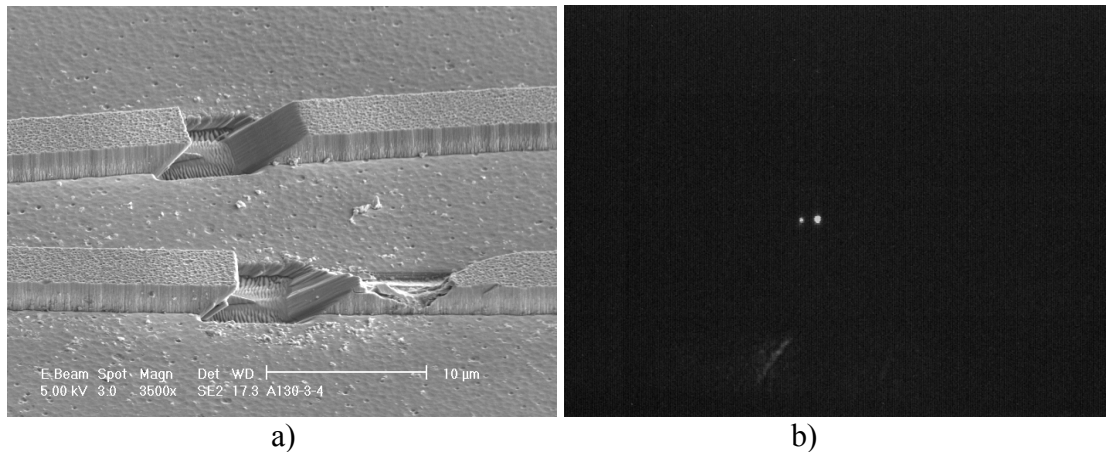


Figure 6.21 Output of the directional coupler. a) electron micrograph b) optical output greater than looking at normal incidence. The device being viewed from the sides and top was a passive zero-gap directional coupler, see Figure 6.20, with the interaction and branches regions having a width of $\sim 5\mu\text{m}$ and $\sim 3\mu\text{m}$ respectively. The amount of light observed was still dim and was difficult to analyze. At the output both branches had an optical signal present at a distance of ~ 2 mm from the front end, Figure 6.21. The signal had equal intensity. Due to the widths of the waveguides, they were multimode.

A problem that occurs is that the widths of the devices using the lift-off process, see Figure 6.14, tends to be bigger than the structures in the mask template. In order to compensate for this, a structure with 5% Al concentration was grown, see Figure 6.6. New devices were grown with this structure. Figure 6.22 shows the result of the device constructed, a bright signal light is shown coming from the end of the waveguide. The problem is that, according to calculations (see Figure 6.23) the waveguide should not have been guiding at all.

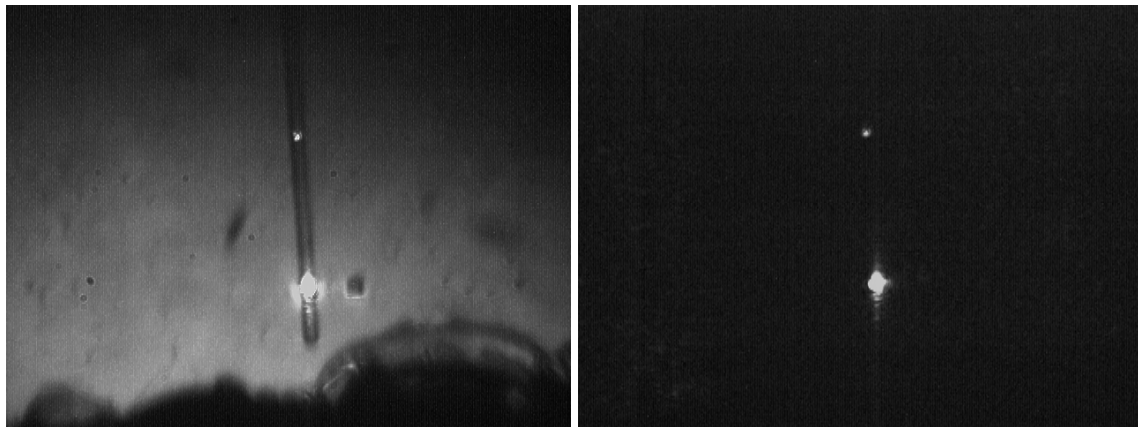


Figure 6.22 $1.4 \mu\text{m}$ waveguides using AlGaN at 5% Al concentration for cladding layer

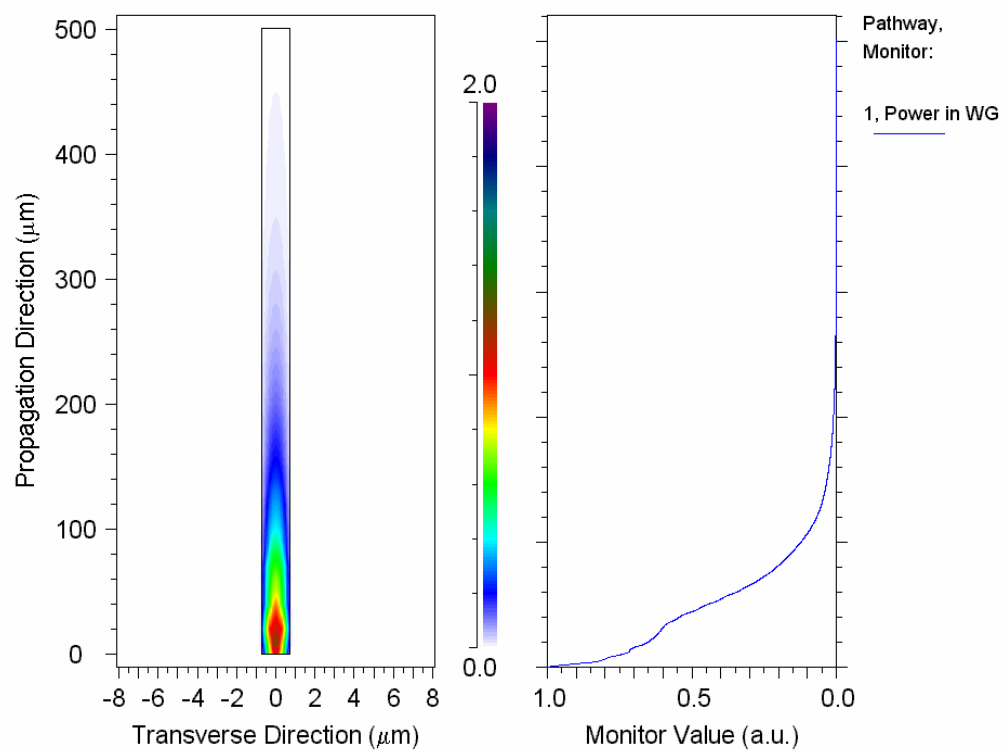


Figure 6.23 Simulation of a $1.4 \mu\text{m}$ waveguide by the beam propagation method. Based on Brunner *et al.*⁷¹

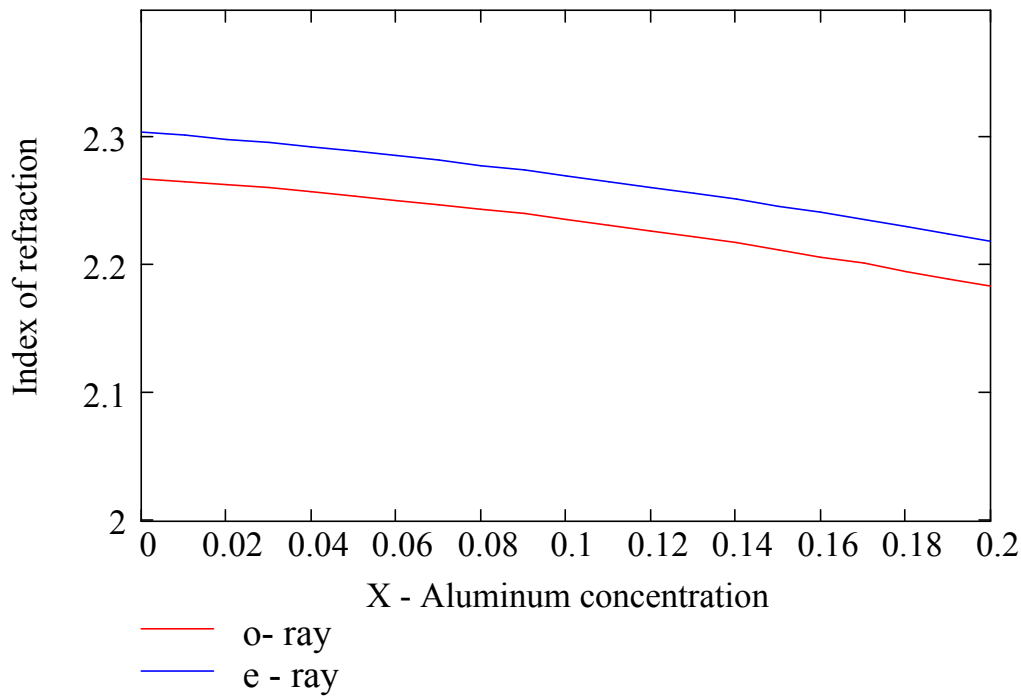


Figure 6.24 Indices of refraction based on Bergman et al. at room temperature and 632.8 nm, reference 69

In trying to obtain better agreement with the results, another index of refraction model for AlGaN was used.⁶⁹ This model was obtained by M. J. Bergmann *et al.*, see Chapter 5. From equations (5-2) - (5-4) and Table 2 we obtain the refraction index graph illustrated on Figure 6.24. For the Al concentration of interest we get, at room temperature:

	n_o	n_e
Core, GaN	2.268	2.304
Cladding, $\text{Al}_{0.1}\text{Ga}_{0.9}\text{N}$	2.236	2.270
Cladding, $\text{Al}_{0.05}\text{Ga}_{0.95}\text{N}$	2.254	2.289

The new refraction indices increase the index difference between the core and the cladding. This index difference is given by:

$$\frac{n_{\text{core}} - n_{\text{cladding}}}{n_{\text{core}}} \quad (6-8)$$

This equation gives us an index difference of 0.0042 for the Brunner *et al.* parameters⁷¹ and 0.0065 for the Bergmann *et al.*⁶⁹ parameters. The increase index difference means that the modes will be more strongly guiding. These were enough to have the beam propagation simulations of the 1.4 μm waveguide show light confinement and guidance, as Figure 6.25 shows. The Marcatili simulations show the waveguide in cut off, non-guiding (see Figure 6.26).

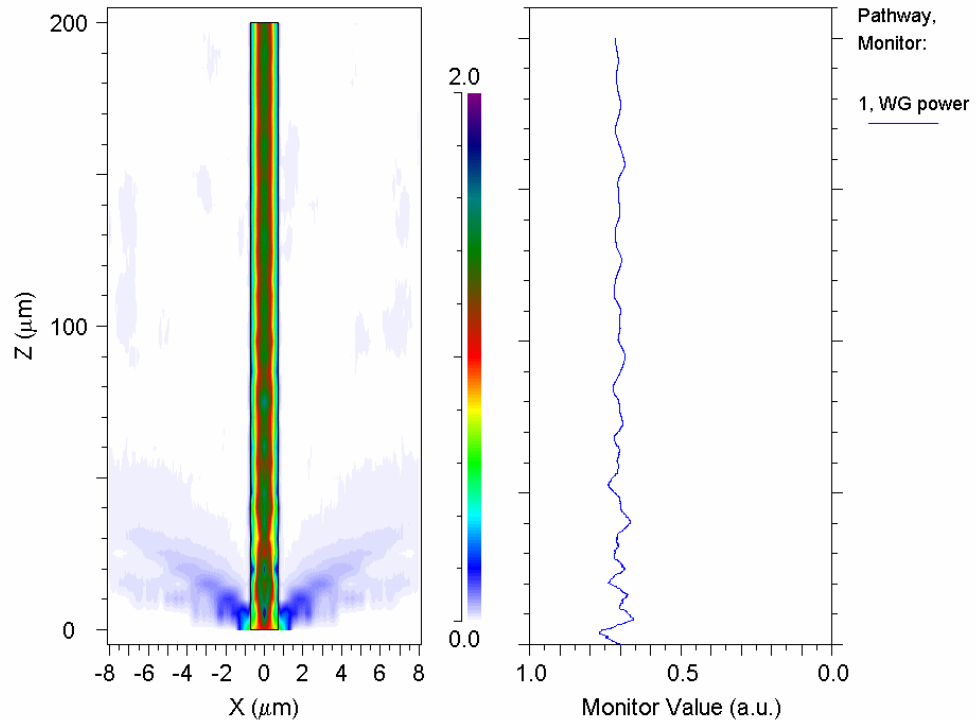


Figure 6.25 New simulations of the waveguide that shows strong guidance. The parameters for this one is as follows: width 1.4 μm , core 0.8 μm , Al concentration 5%. Based on Bergmann *et al.*⁶⁹

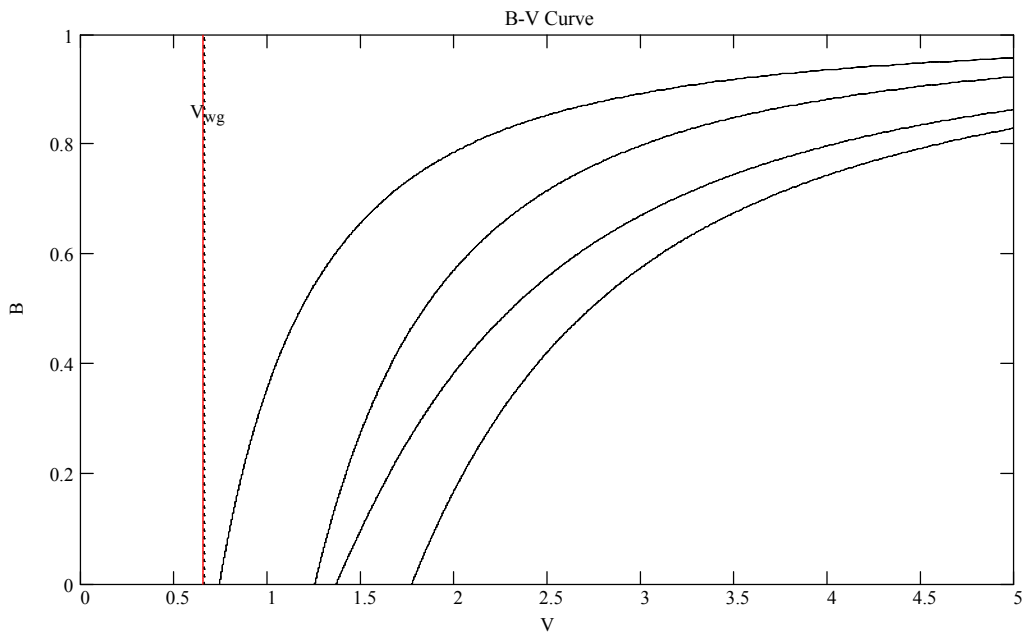


Figure 6.26 Marcatili's simulation using the new refraction indices and the $1.4 \mu\text{m}$ waveguide, Al concentration 5%. Based on Bergmann *et al.*.⁶⁹

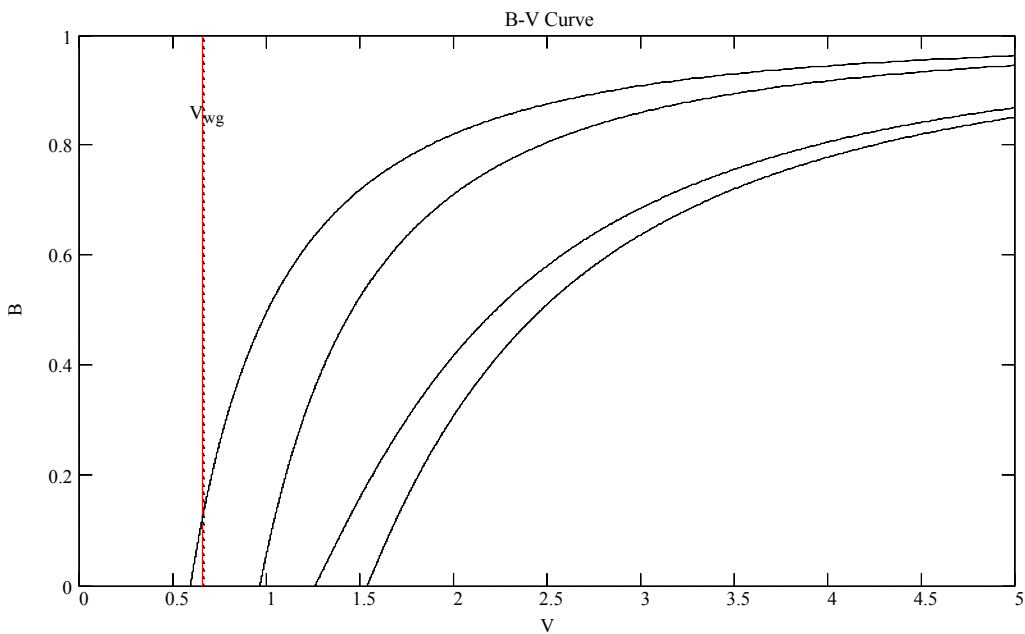


Figure 6.27 Marcatili's simulation using the new refraction indices and the $2.0 \mu\text{m}$ waveguide, Al concentration 5%. Based on Bergmann *et al.*.⁶⁹

More precise measurements of the waveguide's dimension were made using an Atomic Force Microscope (AFM). The measured width of the waveguide was $\sim 2\mu\text{m}$. Also the Al concentration is not exact, according to the MBE grower it might be off by 1- 2%. With these more precise measurements more simulations were made. The simulations showed wave guiding. Figure 6.27 shows one possible scenario for wave guiding using the Marcatili method. All of this shows that the index of refraction formulas established by M. J. Bergmann *et al.* are more suited for the design of the waveguides, at least for the current in-house growth conditions.

Further simulations were done that concentrated on the coupling region Figure 6.28 shows the Marcatili simulation for the coupling region of a directional coupler whose waveguides are $2.0\mu\text{m}$ each, $4.0\mu\text{m}$ total width in the coupling region. According to the

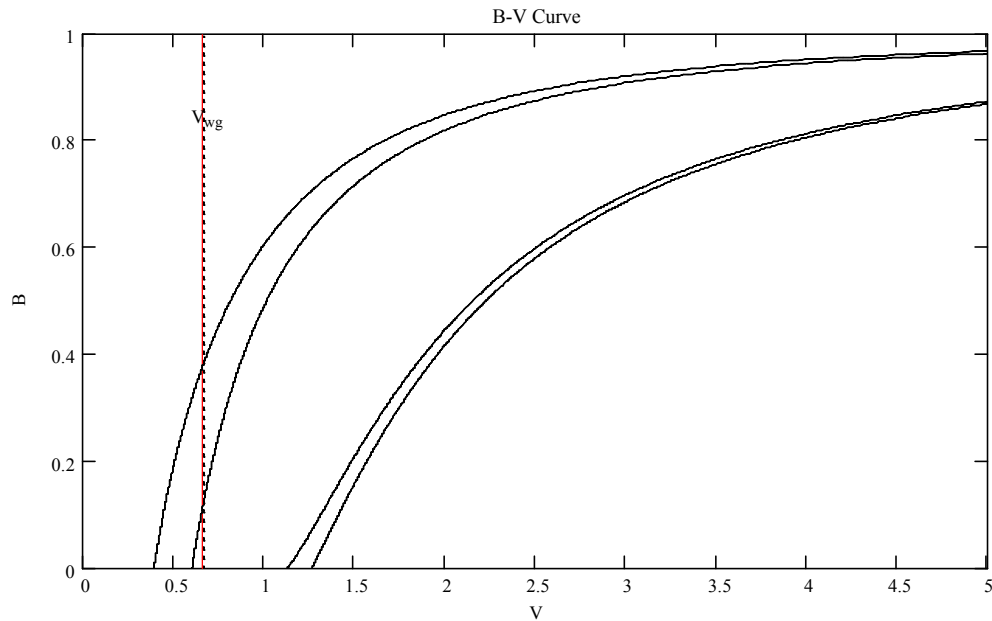


Figure 6.28 Mode chart for the interaction region of the directional coupler, using the Marcatili's model, corresponding to the $2\mu\text{m}$. Total width is $4\mu\text{m}$. Based on Bergmann *et al.*⁶⁹

simulation there are two modes present with one close to cut off. According to Marcatili, the coupling region in the 1.4 μm directional coupler has only one mode present. Also, the Marcatili simulations gives us the minimum coupling length for complete power transfer for a 1.4 μm waveguide as $\sim 163 \mu\text{m}$ and for the 2.0 μm waveguide the coupling length is $\sim 458.4 \mu\text{m}$. With the new index of refraction the attenuation given by Marcatili is ~ 0.074 at a 1 μm distance.

For the beam propagation method an entire directional coupler was simulated. Its results are shown in Figure 6.29. An advantage that the beam propagation method has over the Marcatili method is that of being able to simulate the entire directional coupler structure. The beam propagation method shows a coupling length for complete power

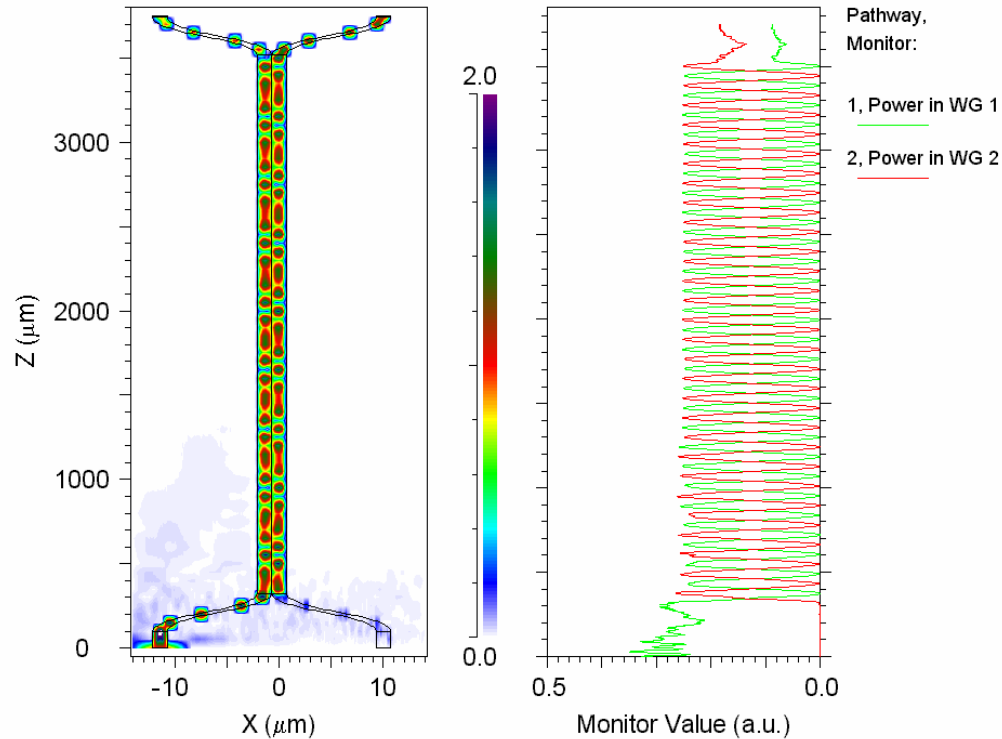


Figure 6.29 An entire directional coupler simulated by the beam propagation method. The waveguide branches are 1.4 μm wide. The coupling region is 3750 μm long.

transfer of only 63 μm for the 1.4 waveguide width. This is in contrast with the $\sim 163 \mu\text{m}$ with the Marcatili simulation. From Figure 6.29, note that once in the coupling region, there is a transition period before the modes settle into a nice two-mode transition.

Through out the course of this research, small variations were made to the process in an attempt to improve the sidewall roughness. A variation to the ICP etching recipe was also attempted with better results. APPENDIX B.2 shows the experimental attempts to improve the sidewalls. The logic of the attempt is as follows: In the ICP etching there is a chemical component and sputtering component.³⁷ The physical sputtering is dominated by the accelerations of energetic ions in the plasma towards the sample material.³⁷ In reducing the rf power, the contribution of the chemical etching is increased while that of sputtering is reduced. With the experimental procedure it was found that a reduction of the rf power to 75 W improved the sidewall roughness, with little damage to the sample and little effect to the sidewall slope.

During the experiments, it was found that good waveguide widths on the mask template were 1.4 μm and 2.0 μm . This is due to processing which will transfer to a pattern with larger line sizes. Additionally, the separation chosen at the input and output of the waveguide branches was too small. Figure 6.20 a) and b) shows that when light was attempted to be launched into one of the input branches of the directional coupler, the spot size was large enough to couple light into the other input branch. This would make it difficult to evaluate the directional coupler, since there could be two simultaneous inputs to the coupling region, see Figure 4.6.

Second Mask Set Design, Processing, and Results

Based on this information, a new directional coupler was designed, see Figure 6.30. This new design for the directional coupler will be for widths of 1.4 and 2.0 μm . In this new design the waveguides in the input sections are separated by 100 μm while in the exit section they are separated by 40 μm . This is done so that the output sections are not in the direct path of the input optical beam. The bending sections were designed to have an angle of $\theta \approx 6^\circ$ (see Figure 4.6) although Equation (4-32) will give us 5.6° and 3.9° for the 1.4 and 2.0 μm widths respectively. The difference in the entrance angle stems from the fact that it is the instantaneous angle that needs to meet Equation (4-32) criteria and not the total angle, see Chapter IV.²⁸ For the second mask set, the coupling region was

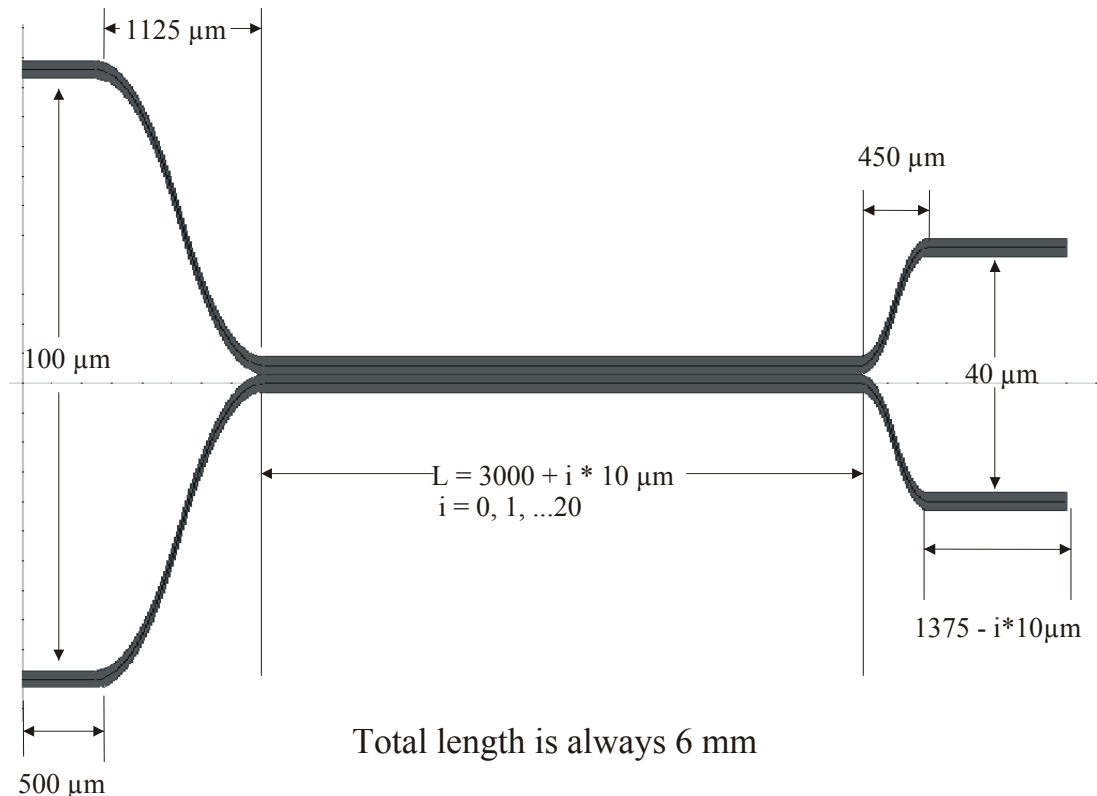


Figure 6.30 New directional coupler design.

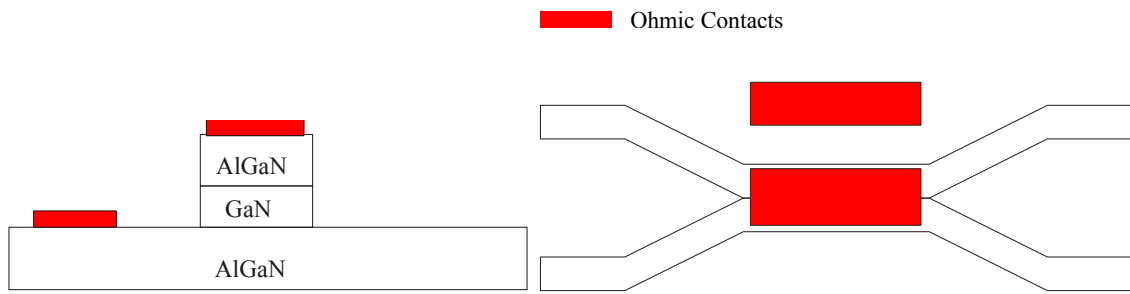


Figure 6.31 Metal contacts on the directional coupler.

varied from 3000 to 3200 μm in increments of 10 μm , while maintaining the same total length of the device. This would enable us to determine the experimental coupling length and compare it with the models.

For the second mask template, that encompassed the structure on Figure 6.30, additional attempts were made to create an active device. As shown in Figure 6.1, the structure to be envisioned would be an n-(semi-i)-n and if possible an p-(semi-i)-n. Contacts were placed as shown in Figure 6.31. The bottom layer served as a common ground for the devices. This will enable the electric field to flow from one contact to the other. By having the AlGaN conductive and the GaN as insulating as possible it was hoped that the electric field would be concentrated in the GaN core region. In creating a process to accomplish this, several factors have to be taken into account. One of them is the placement of the metal on top of the coupling region. The scope of this problem entails the precise placement of a metal line on top of a mesa ~ 3000 μm long and ~ 2.8 μm wide with little room to spare. This needed to be done consistently through out the wafer. Prior to the complete mask development, tests were made to rule out alternatives. One attempt was placing the top metal contact before the AlGaN etching. This was done

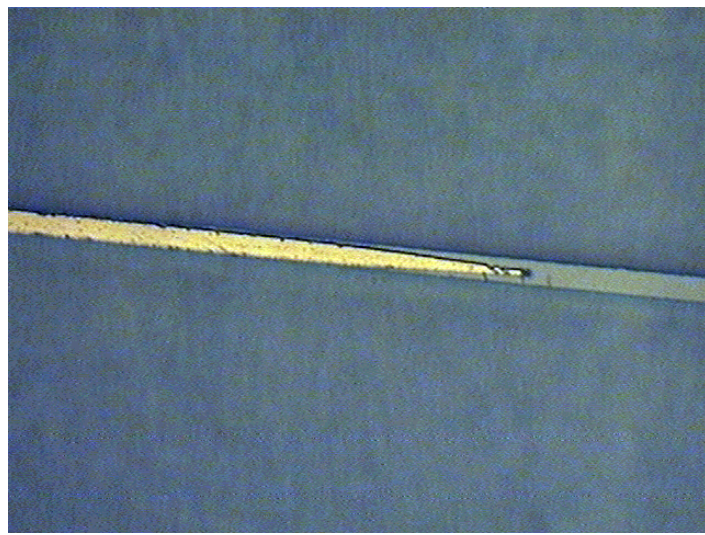


Figure 6.32 Test for placing a metal contact on top of the coupling region in a directional coupler.

with the hope that, during the etching, any metal contact not aligned with the coupling region would be etched out. The problem was that Ni mask and a possible SiN under layer were removed with chemicals that would attack the ohmic contacts. The ohmic contacts used for the n-type region were Ti/Al/Ti/Au, with the Ti in contact with the surface. After depositing the metals, the sample goes through a rapid thermal annealing (RTA) cycle to create an alloy. The Ni mask could not be left on the structure because it would apply an electric field through out the structure and it could be an avenue for other problems to emerge. The one that was successful was the placement of the metal contact after the directional coupler mesa was etched, as shown in Figure 6.32.

Another problem was the placement and connection of a pad that would make contact to the metal on top of the mesa. Due to the dimensions of the coupling region it was impossible to place an electrical probe on it. A separate metal pad had to be created that would make contact with it. Implantation of an insulating region, or any type of

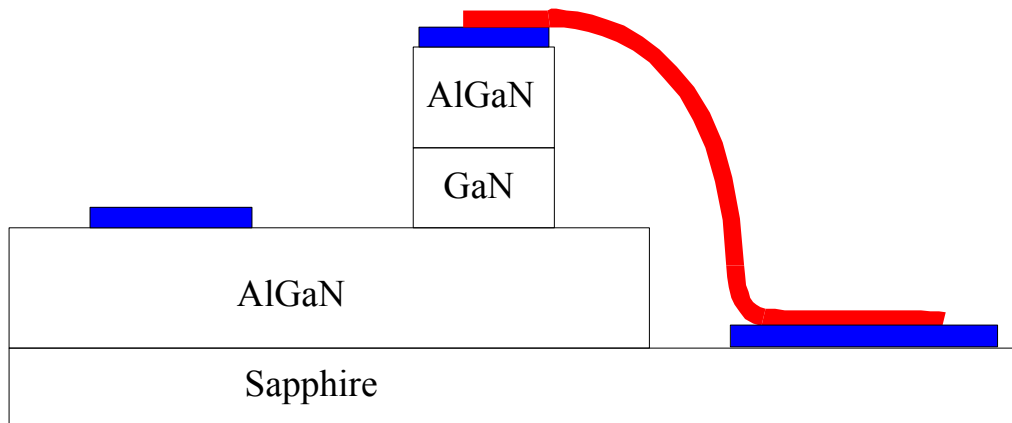


Figure 6.33 Ohmic contact configuration with metal pad and an air bridge

implantation in AlGaN for that matter, was not an option. The approach taken was to etch a trench all the way to the sapphire, which is insulating in nature. An air bridge was used to make contact between the metal pad and the mesa contact. Figure 6.33 illustrates this approach. The metal used for the bridge and the pad at the bottom of the trench didn't have a special contact or electrical requirement to be met.

With this information a second mask template set was designed. This one was targeted to further investigate the passive directional coupler as well as to develop the processing steps necessary to create an active directional coupler. The steps that were to be implemented are shown in Figure 6.34. Figure 6.34 shows the cross-sectional view as seen from the coupling region. The ohmic contacts to be deposited on top of the directional coupler and on the common ground plane are identical for the n-i-n structure. But, on a p-i-n structure they would be different, therefore different mask templates had to be used for each one. For the p-type contact, the most often used alloy is Ni/Au, which was run through an RTA cycle to obtain the desired ohmic contact.

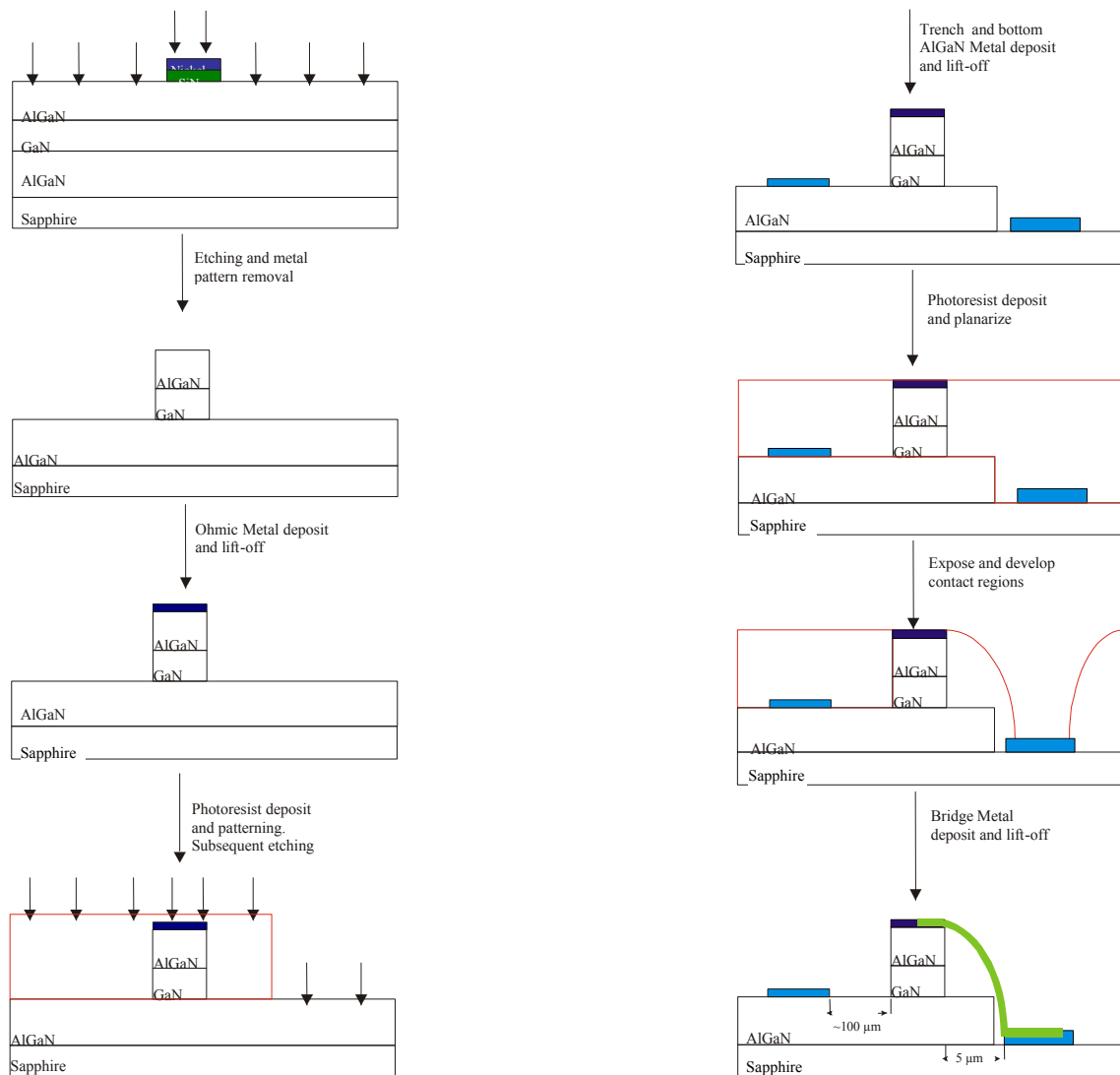


Figure 6.34 Overview of the processing steps that were implemented on the second mask set.

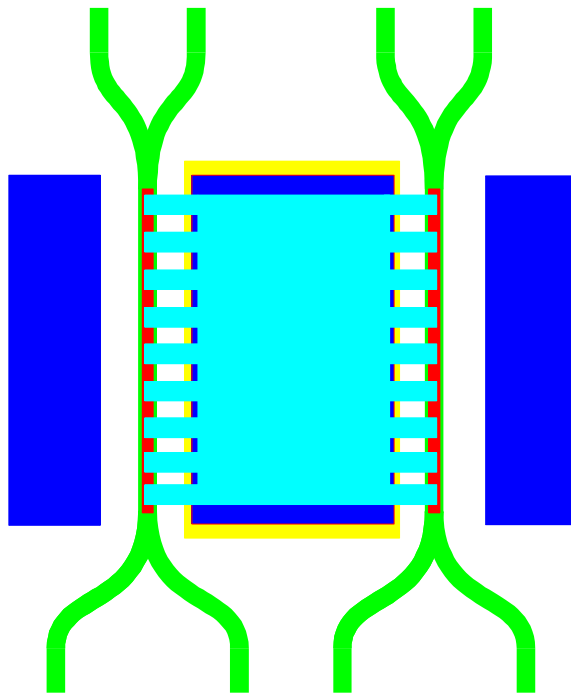


Figure 6.35 Top view diagram of the active directional coupler. Not to scale

Figure 6.35 shows the top view of the active directional coupler building cell. The interleaving fingers are the bridges shown in Figure 6.33. Instead of using a single bridge multiple smaller bridges were used. This made it easier to take out the photoresist from underneath the bridges. Following the processing steps of Figure 6.34, each of the different shades indicates a separate feature that was transferred from a mask template. There were a total of six mask templates for the second set. Of the six five are shown in Figure 6.35. Additionally, redundancy was built in the mask set by having sets of four directional couplers with equal coupling length, before increasing to the next length.

With the new mask set some problems were more prevalent in constructing the directional coupler. One of the problems was at the waveguide junction in the directional coupler, Figure 6.36 a). As the waveguides come closer together the width of the material

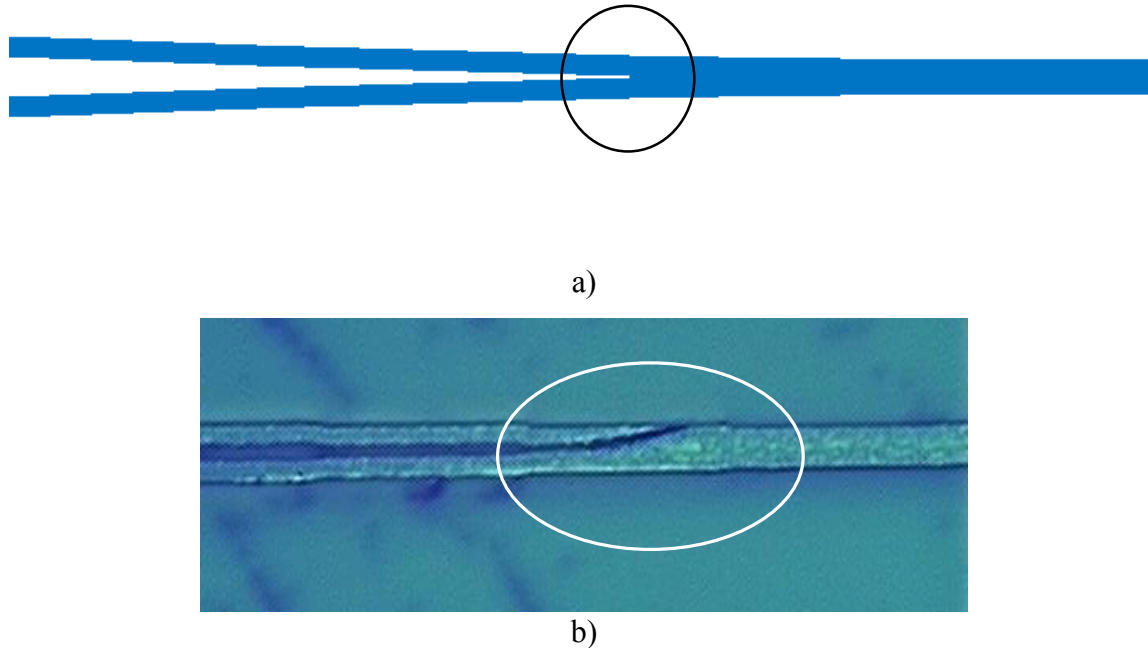


Figure 6.36 Waveguide Junction in a directional coupler a) sketch of the template mask for the $1.4\mu\text{m}$, b) failed transfer of the pattern to the photoresist.

separating them becomes smaller and smaller. In theory it becomes very small until it vanishes. In actual manufacturing the minimum separation is dependent on the mask template writing tools and lithography resolution. For the second mask set, the resolution was $\sim 0.25\ \mu\text{m}$. For the transferred pattern the process itself will also weigh in on the final feature size.

For the pattern transfer using the lift-off processing, see Figure 6.14, dual layer photo resist was used. When attempting to establish the pattern into the photo resist the material between the waveguides peeled off as shown in Figure 6.36 b). This presents a problem when constructing the waveguide, since it will create an opening in the path of the optical signal and disrupt it. The source of this problem can be seen in Figure 6.37. As seen in

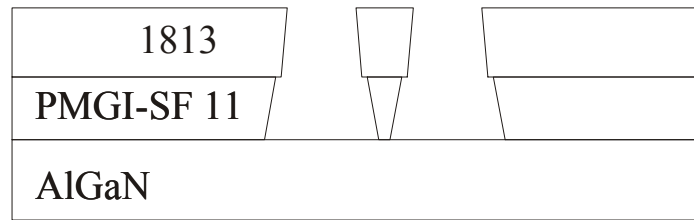


Figure 6.37 Crossectional view of the photoresist pattern transfer of the junction region of the directional coupler.

Figure 6.14 and Figure 6.37 for the metal lift-off, the bottom photoresist layer etches slightly more than the top layer. This is convenient since otherwise the metal would have been deposited along the sidewall, in addition to the bottom of the pattern. This would create winglets in the metal pattern, which would interfere with the pattern transfer to the AlGaN/GaN material. This works against the shrinking separation at the junction. Looking at Figure 6.37 we can see that at a certain point the bottom photoresist layer would detach itself from the AlGaN material while leaving the top photoresist layer, thus the peeling as seen in Figure 6.36 would occur.

When a mask template is produced the curves are not created in a continuous fashion. Rather, the curves are created in a stepwise fashion, as is seen in Figure 6.36. This can be used to our advantage in creating a process. In order to minimize the peeling, the process has to be tweaked so that the photoresist between the waveguides is not etched enough to peel or etch away the entire finer step and leave the next step increase intact. To do this the exposure times, the developing times, and the O₂ plasma ashing times had to be tweaked to obtain the desired characteristics. The process follower in APPENDIX C.2 for the “WG definition” process shows the result of these iterations.

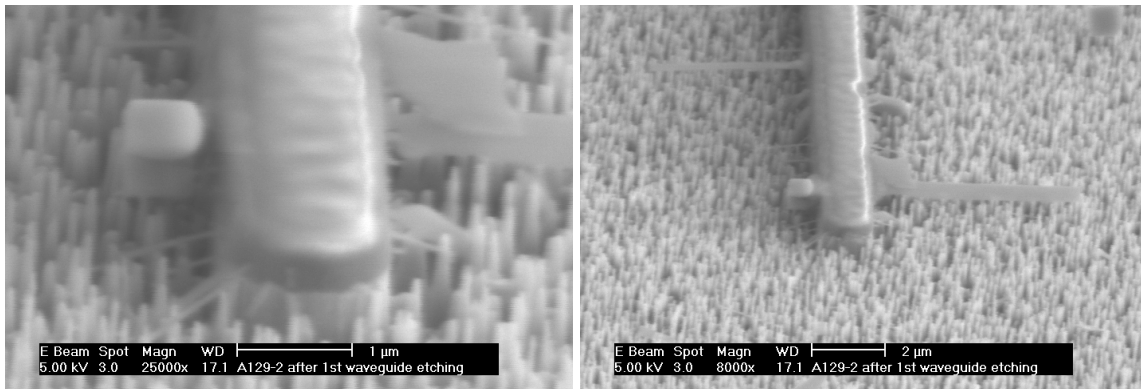


Figure 6.38 SEM of etched samples with uneven etching

With the new template mask set, a few samples were etched. When the samples were etched they had a dull black appearance to the naked eye. When a Scanning Electron Microscope (SEM) was used it was evident that the samples were etched unevenly, unetched pillars were permeating the entire exposed region, see Figure 6.38. Some of the previous samples turned out this bad and some to a lesser degree. This behavior was investigated to determine its causes. A small design of experiments (DoE) was conducted towards this end, see Table 4. These studies showed that there is an interaction between the freon etch (F-23 or F14) that seeds the formation of the column structures in the ICP etch. If the AlGaN/GaN sample with no Si_3N_4 was put through the freon process, the ICP etch comes out clean (no columns). This is also true if a sample with Si_3N_4 is

Table 4 Small DOE

Trials	Sample	Freon (RIE)	SiN thickness in angstroms	Asher	Pattern	mask	Output
1	252-2-1	Over etched	no	no	no	none	Good
2	252-2-2	Over etched	yes	5751	no	none	Bad
3	252-2-3	no	no	yes	no	none	Good
4	252-2-4	Over etched	yes	5751	yes	none	Bad
5	252-2-5	Over etched	yes	5751	yes	SiN	Bad

etched without the freon step. The freon step is used to pattern the Si_3N_4 for later etching the AlGaN/GaN sample. Over etching of the Si_3N_4 was done with little or no success, the freon etch doesn't etch the GaN/AlGaN and the surface is still smooth at the end. When the sample was over etched an EDAX (Energy Depressive X-ray Spectrum) analysis was done (see Figure 6.39). This revealed that there was fluorine residue in the sample. The analysis only shows elements presents and not chemical formulas.

It seems that the fluorine residue by itself or in a chemical composition with another element present prevents the etching of the AlGaN/GaN material. Several attempts in cleaning the sample after a freon etch, but before the ICP etch, were done. This showed that by over etching the Si_3N_4 and then dipping the sample for 5 min in phosphoric acid a clean ICP etch was obtained. This step does not work if there is Si_3N_4 remaining, before the rinse, on the area intended for etching. BOE could also be used, but since it dissolves Si_3N_4 it needs to be diluted and have a controlled timing to etch the affected area. Additionally, it etches Si_3N_4 isotropically and it would under cut the patterns. This

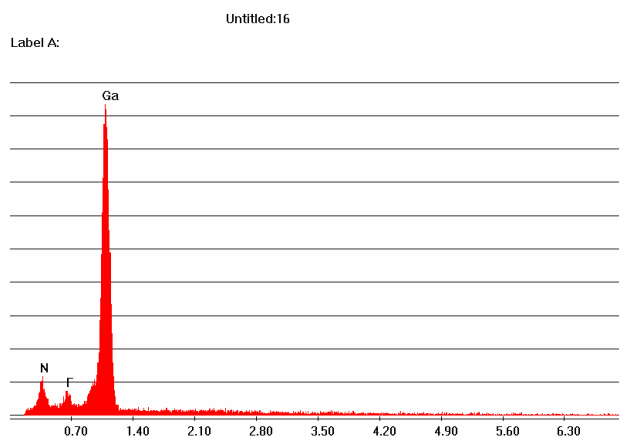


Figure 6.39 EDAX of sample after freon over etch

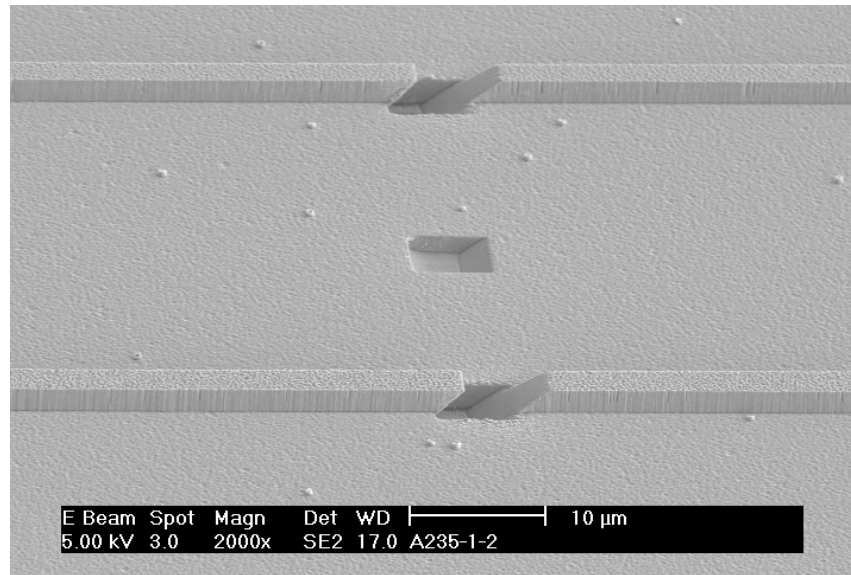


Figure 6.40 Directional coupler output region

prompted a slight change in the process. RIE cleaning of Si_3N_4 was eliminated. Now either no Si_3N_4 was used or it was left to be patterned with the AlGaN in the ICP, the optional parts in the “WG definition” process follower in APPENDIX C.2.

Once the process was de-bugged, new devices were constructed using the 5% Al concentration. Figure 6.40 shows the output region of the directional coupler. This figure clearly shows the angle cut on the waveguides plus an angle cut between the waveguides. This angle cut between the waveguide was done in order to test for any wave guiding that

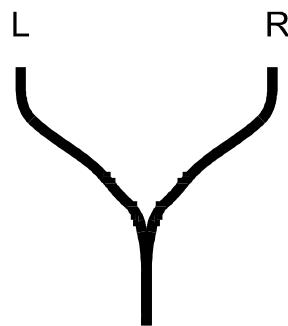
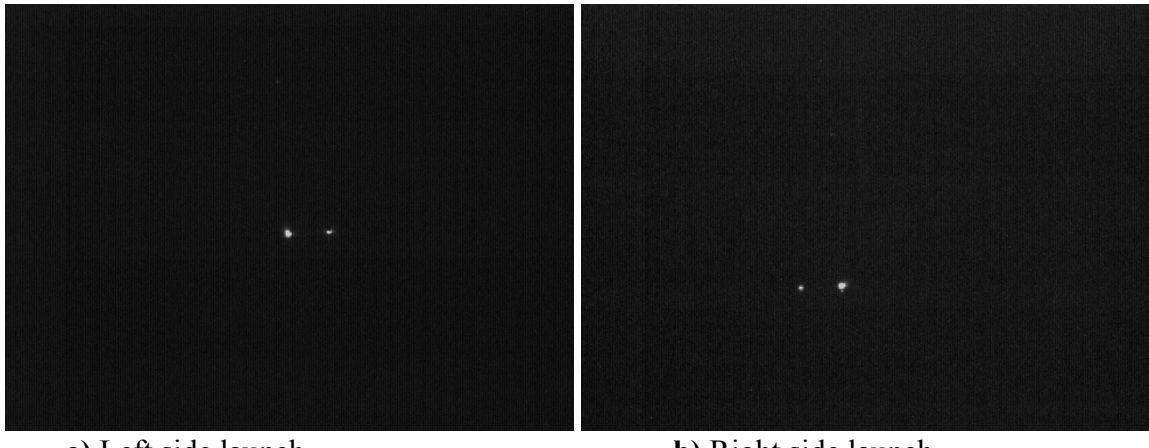


Figure 6.41 Launching convention for the experiments



a) Left side launch

b) Right side launch

Figure 6.42 Light exiting the directional coupler with a theoretical interaction length of 3190 μm . Magnification is 200x

might have occurred in the AlGaN layer directly on top of the sapphire, see Figure 6.6.

Additionally, the center cut helps in locating the output section using the testing set up of Figure 6.17.

Light was launched into the left side and then into the right side of the device. Figure 6.41 shows the launching conventions for the experiments. The output was monitored using the camera set up in Figure 6.17. Figure 6.42 shows the output of one such device in which light was launched into the a) left side b) and the right side of the device. In both images we see that one of the branches is brighter than the other one, and that they change when changing the input branch. Theoretically this is expected due to the symmetry of the device. It is an indication that the device might be working properly, at least in the passive mode. This simple test reduces the probability that at least one of the branches might be obstructed or damaged. This might present a problem in analyzing the structures



Figure 6.43 Higher magnification (800x)of the directional coupler of Figure 6.42 with a) the lights off and b) the lights on.

because it will skew the results. Several devices of different lengths were tested but gave indications of partial obstructions in the waveguides.

Additional testing of the waveguides was preformed. Figure 6.43 shows the same directional coupler as Figure 6.42 at a higher magnification. Figure 6.43 b) shows all three angle-cuts shown in Figure 6.40. At this magnification the signals were so strong that they appeared to be undistinguishable in magnitude, they saturated the detector (see

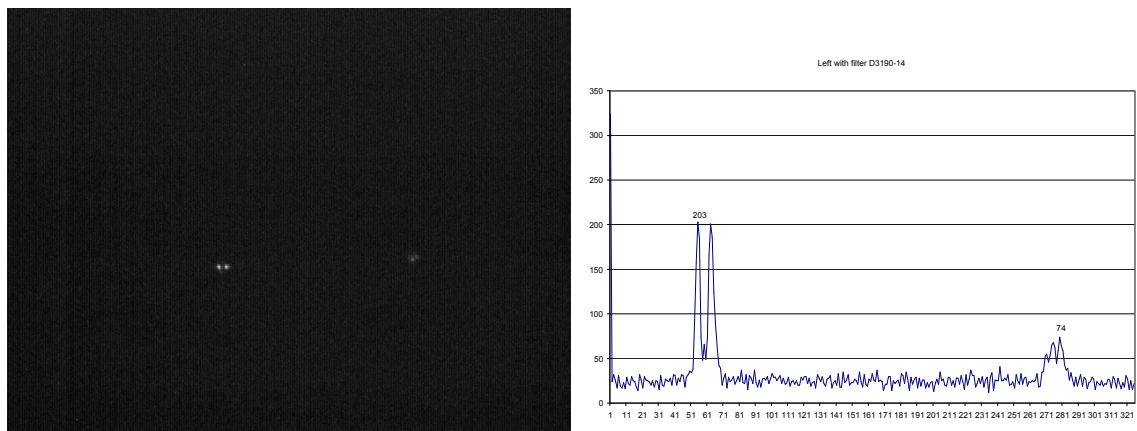


Figure 6.44 Attenuation of the laser using the directional coupler of Figure 6.43. Light was launched on the left side. Light launched at the left side.

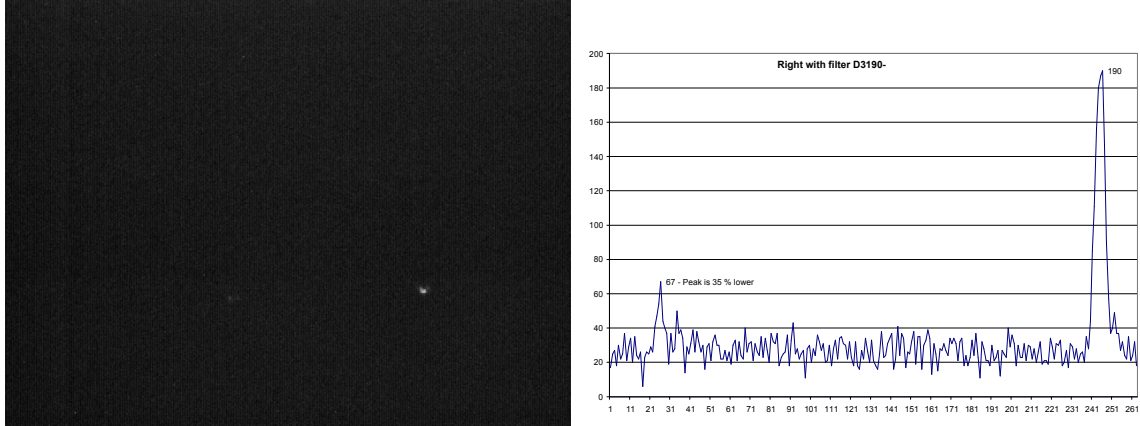


Figure 6.45 Right side launching in same structure as in Figure 6.44 and with attenuation

Figure 6.43 a)). Because of this, an attenuator had to be used with the laser. It was only then that the intensity difference was measurable, see Figure 6.44. Figure 6.44 and Figure 6.45 are for left and right launched light respectively. The measurements were obtained from the image by reading the intensity of the pixel, which was scaled from 0 – 255, for an 8 bit gray scale.

In Figure 6.44, the dual peak could be caused by an imperfection in the facet milling, since only one waveguide showed it, and the branch is not in a dual mode region. For the Marcatili approximation, the results are skewed because we have a tapered entrance and exit from the device, see the section on the “bending section” in Chapter 4. Figure 6.44 and Figure 6.45 illustrates the problem with uneven attenuation in the output branches. This uneven attenuation could have been caused by the process, resulting in small imperfections in the waveguides. This would render many of the waveguides unusable for a direct comparison. In order to circumvent this problem some mathematical manipulation can be accomplished in order to extract the data from the experiment.

If we assume that in the coupling region any imperfection or attenuation affects both modes equally, or an insignificantly small uneven amount, then the output branches would be the source of uneven attenuation. Therefore, if the output ratio of the intensity with light incident on one of the branches, say the right one, is given by:

$$C = \frac{b P_2}{a P_1} \quad (6-9)$$

where a and b are the attenuation in each of the branches, P_1 is the ideal output power in the incident branch and P_2 is the ideal output power in the non-incident branch (without any attenuation). Then output power ratio with the incident light in the other branch, say the left one, is given by:

$$D = \frac{a P'_2}{b P'_1} \quad (6-10)$$

where the prime indicates light incident on the branch opposite to Equation (6-9). The attenuations a and b change since they are fixed to the individual branches. By the symmetry of the device we have $P_1 = P'_1$ and $P_2 = P'_2$. By dividing Equation (6-9) by Equation (6-10) we obtain

$$\frac{C}{D} = \frac{b^2}{a^2} = AR^2 \quad (6-11)$$

where AR would be the attenuation ratio. With this value we can now obtain the power ratio without the uneven attenuation.

A full set of passive waveguides were grown and tested with the experimental set up of Figure 6.17. In testing the waveguides there was some vibration present in the set up,

although the entire set up was mounted in vibration isolation tables. For testing the waveguides light was launched in either the left side or the right side of the input branches. In the output, several images were taken. Since the vibration smudged many of the images only those that were not smudge were selected. Once one of the branches was finished, we proceeded to the next one. For each of the branches several images were taken. They were analyzed in the same fashion as in Figure 6.44 and Figure 6.45 and the ratio of both output branches was obtained.

All the data concerning a branch was statistically analyzed by averaging and obtaining a standard deviation. Table 5 shows a sample of the data taken for a single directional coupler. The R and L notation signifies the output power from the right or left branch respectively. Using Equation (6-11) the uneven attenuation was then canceled out of the data. Figure 6.46 shows the data obtained from various directional couplers of the same sample and the corrected values of the data. There was no specific pattern in the uneven attenuation implying that its origin was not in the material, but the structure itself. In two of the structures only a single branch was available to launch the light into and therefore impossible to correct.

Table 5 Sample of data taken from a single directional coupler. The ratio is set as $P_{\text{non-incident branch}} / P_{\text{incident branch}}$

D3050-14			
Left (R/L)		Right (L/R)	
eb	0.3842	e2	0.6118
ec	0.4451	e3	0.6278
		e4	0.6185
Average	0.41465		0.6194
STDEV	0.043063		0.0080

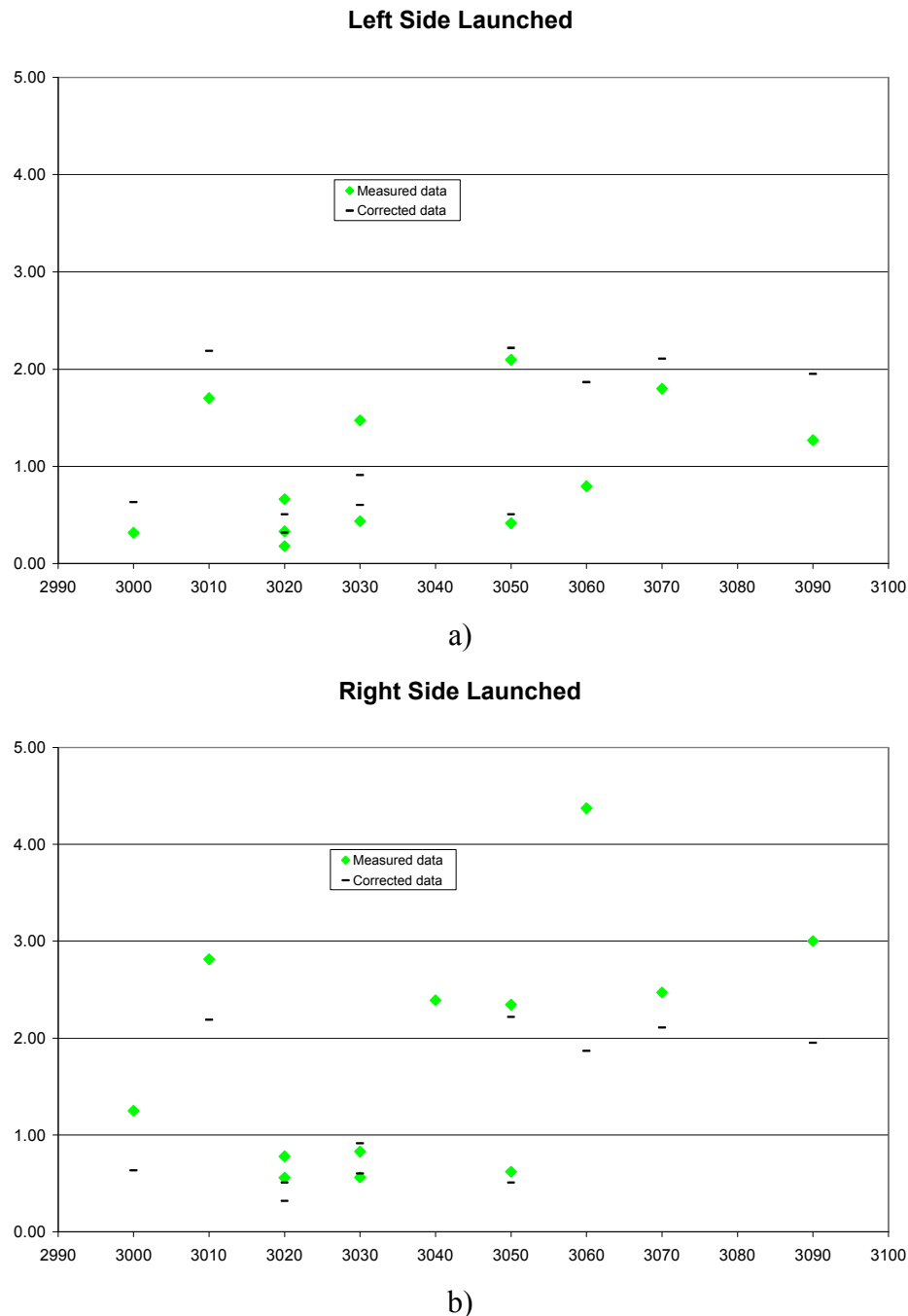


Figure 6.46 Measured data and corrected data taken from the directional couplers of a single sample. The values are in the P_2/P_1 ratio form.

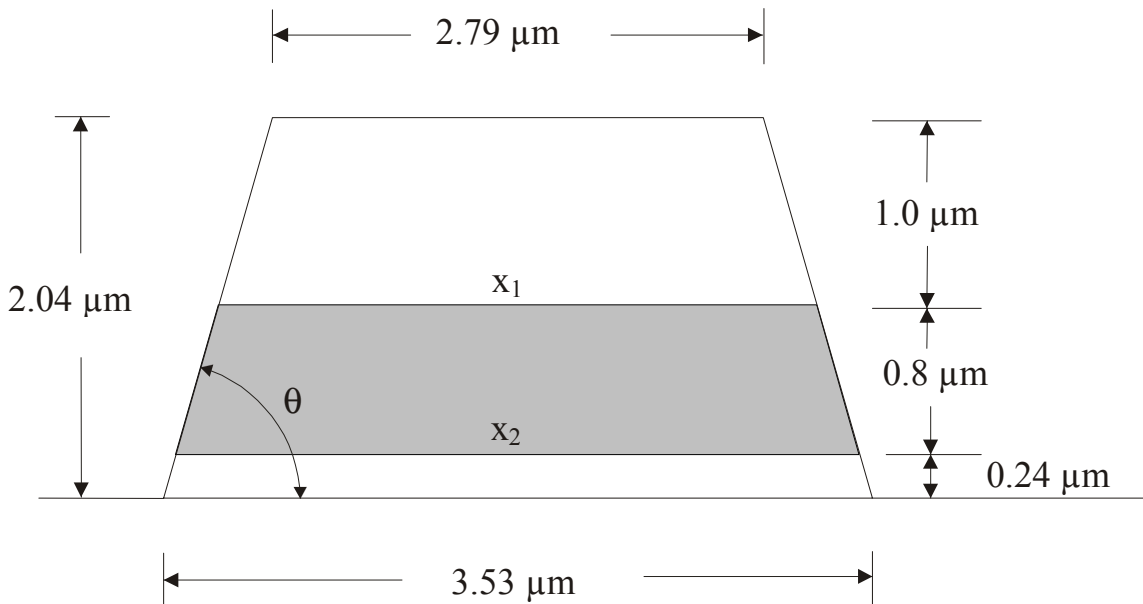


Figure 6.47 Detailed dimensions of a directional coupler sample

In order to compare the data with the theoretical results, precise measurements of the waveguides are needed. As it can be seen in Figure 6.15 the waveguides constructed are not perfectly square. Also, the waveguide width is not identical to the template mask. Measurements were taken to determine the exact shape of the etched waveguide. These measurements indicated that instead of the waveguide being a square it is actually trapezoidal in shape. Figure 6.47 shows the results of the measurements, the grayed area is the GaN core region and the white area is the AlGaN cladding region. With these

Table 6. Widths of the directional coupler. Height is 2.09 μm. Sample number is A12941

Coupler #	Width (μm)	
	coupling region	Single waveguide
#4	2.79/3.53	1.48/2.14
#5	2.89/3.6	
#17	3.03/3.74	
#28	3.08/3.8	

Experimental Data with theoretical prediction for A12941

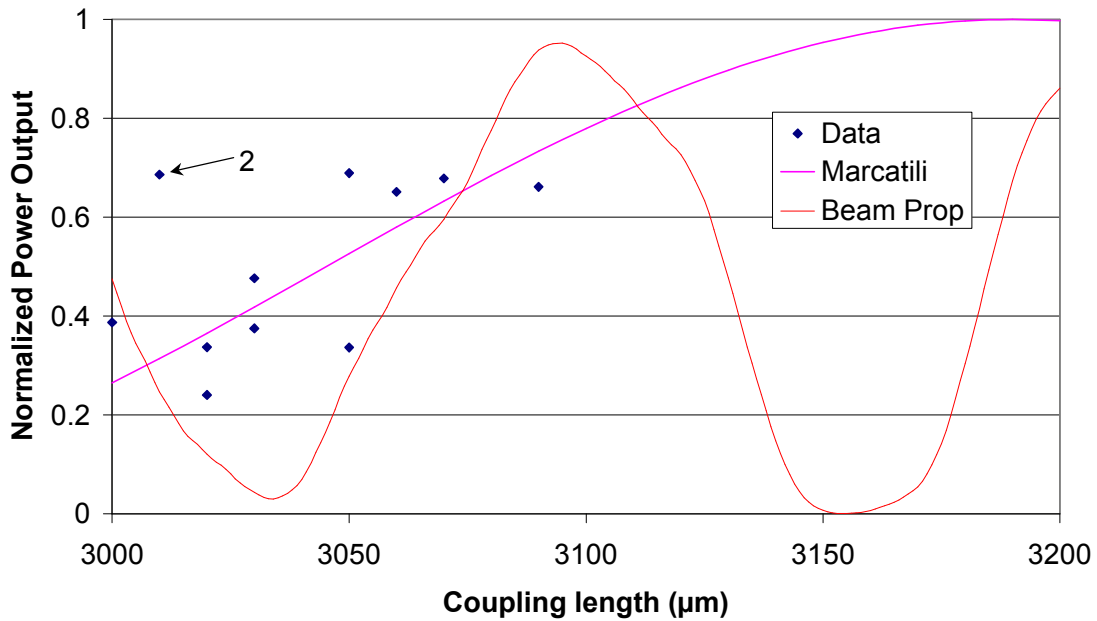


Figure 6.48 Comparison of the data from sample A12941 with theoretical predictions for 1.71 μm width branches.

results one can calculate the slope angle θ to be 79.72° ($\sim 80^\circ$), the upper width of the core, x_1 , is 3.15 μm , and the lower width of the core, x_2 , is 3.44 μm . Table 6 shows the measurements of other directional couplers in the same sample

With these measurements, the averages were then plotted and compared with the theoretical results from Marcatili's method and the beam propagation method. Since the waveguide is trapezoidal an effective width can be found that would match the behavior of the directional coupler. Figure 6.48 shows the corrected experimental data and the plotted theoretical behavior. For Marcatili's method, the sum of square error was done for various coupling lengths. The result was a width of $\sim 3.42 \mu\text{m}$ for the coupling region,

corresponding to a coupling length of ~ 290 μm , or $\sim 1.71\mu\text{m}$ for the single waveguide width. This width is within the boundaries of the core width calculated from Figure 6.47. With the data point labeled 2 the SSE (sum of square errors) between the Marcatili's results and the data is 0.222 (with a coupling length of 289.4 μm). Without this data point the SSE was reduced by half to 0.111 (and the coupling length was 290.021 μm). The structures with a normalized intensity above 0.5 showed a crossover in intensity, when the maximum intensity switches from one branch to the other. The data didn't support the beam propagation method simulation, which predicted a much smaller coupling length for the same 1.71 μm widths of the branches, as illustrated in Figure 6.48. The width in the beam propagation simulation would have to be much larger than the actual physical device to obtain the same coupling length. The SSE for the beam propagation method was 0.7 without data point 2.

A second sample was analyzed in the same fashion as sample A12941. This time a different set of coupling lengths were used. Table 7 shows the dimensions on some of the structures in the sample. Figure 6.49 shows the corrected data with the Marcatili and the

Table 7. Widths of the directional coupler. Height is 1.986 μm . Sample number is A28542

Coupler #	Width (μm)	
	Interaction region	Single waveguide
#10	3.12/3.83	
#13	3.08/3.81	1.83/2.52
#21	3.12/3.87	
#23	3.17/3.87	

Experimental data and theoretical results for a28542

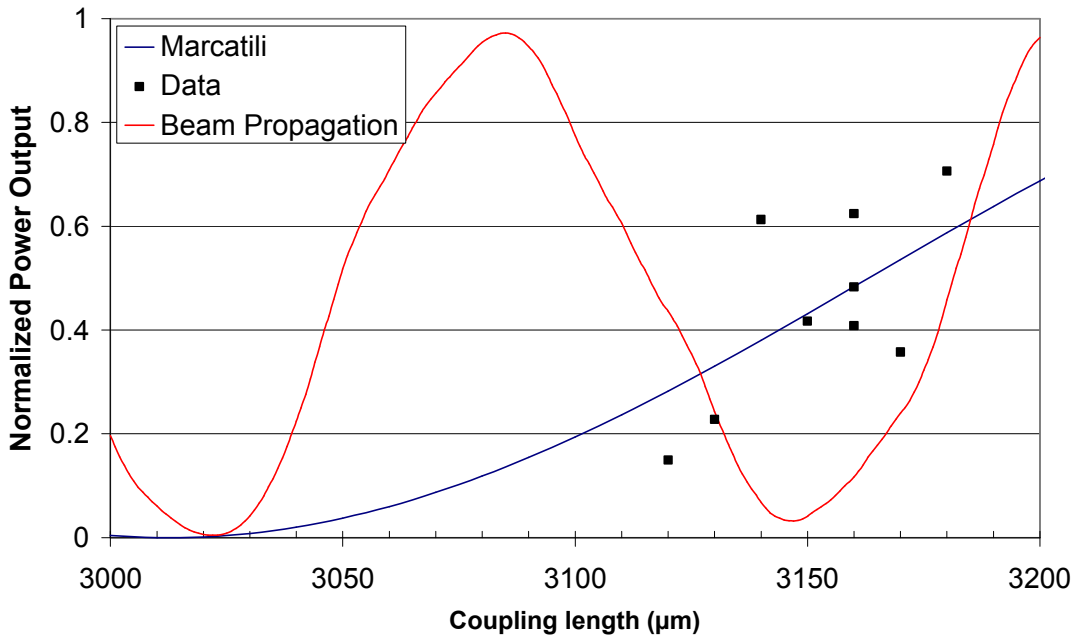


Figure 6.49 Comparison of the data from sample A28542 with theoretical predictions for 1.73 μm width branches

beam propagation methods. This particular sample had more experimental errors but it still tracked the Marcatili simulation better than the beam propagation simulation. The SSE for the Marcatili simulation was 0.154 and for the beam propagation simulation is 4.135.

With this mask set, the processing for the active directional coupler was also developed. Depositing the contact on top of the waveguide was difficult but achievable. The “Top Contact” process in APPENDIX C.2 shows the process followed to deposit the ohmic contact on the directional coupler. The composition of the contact is Ti/Al/Ti/Au and the heights used for each are detailed in the process follower. Figure 6.50 shows an SEM image of the contact on the directional coupler. Notice that although the contact strip is

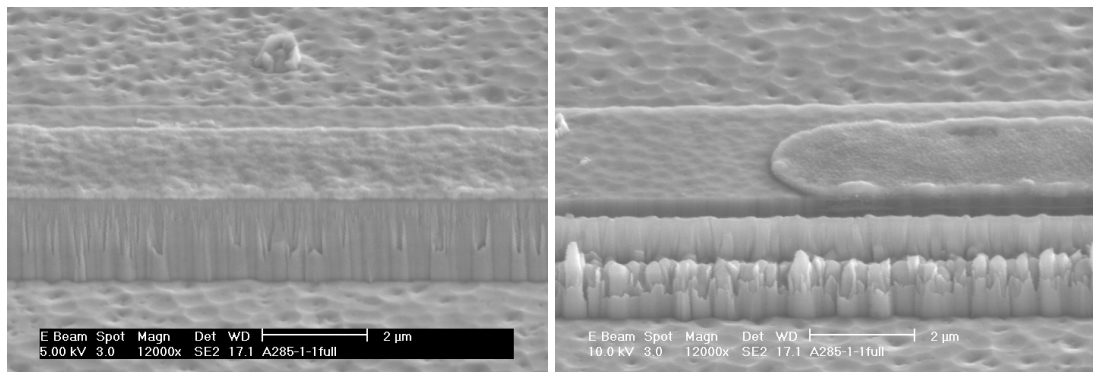


Figure 6.50 SEM image of contact on top of the directional coupler.

up to the edge it didn't flow to the sidewall. The trench and the metal contacts processes, see Figure 6.34, were created with little difficulty, see APPENDIX C.2. In order to activate the ohmic contact, annealing is required.

A first annealing attempt is shown in Figure 6.51. The annealing was done in a rapid thermal annealer (RTA)with a nitrogen flow. Figure 6.51 a) and b) were obtained from the same directional coupler at different locations. Note that Figure 6.51 a) seems to have a different morphology than b). Figure 6.52 seems to indicate that the difference in morphology is due to bottom AlGaN contact acting as a radiator and subjecting the areas

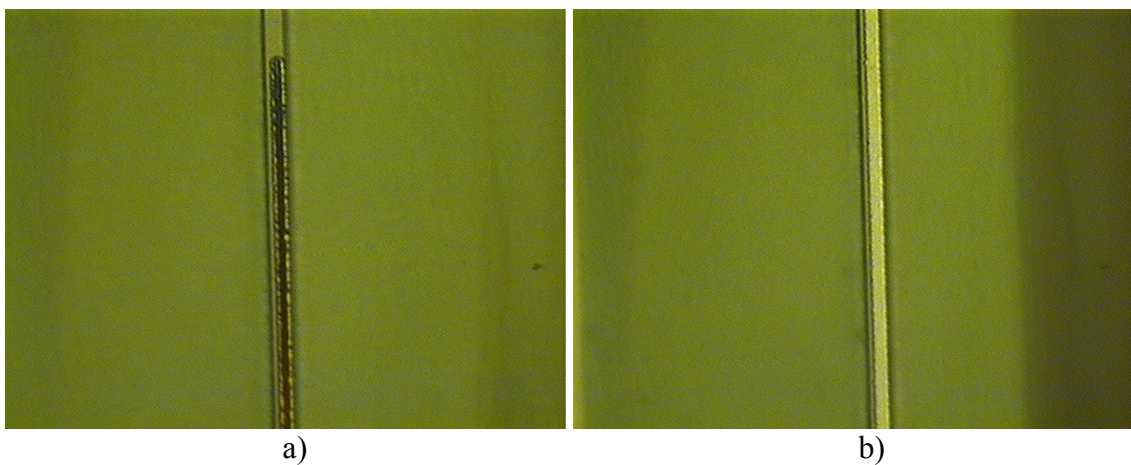


Figure 6.51. First annealing attempt with an RTA at 850° C for 30s



Figure 6.52 Lower magnification than figure Figure 6.51

surrounding it to less thermal stress. Additional examination under the SEM showed little surface difference. The SEM images of Figure 6.50 were taken from these two regions. Figure 6.53 is inconclusive as to the cause of the difference in appearance. The difference could have been from oxygen, nitrogen, or a secondary Ti peak.

The first attempt at creating a bridge was not very successful. The composition used was Ti/Au with the thickness of 200/500 Å. Altering the bridge composition to

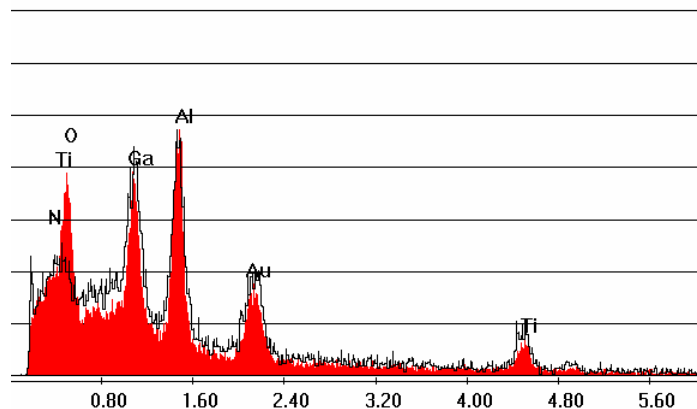


Figure 6.53 EDAX analysis of the contacts after annealing. The Black outline is from the center section and the solid graph is from the morphologically different tip.

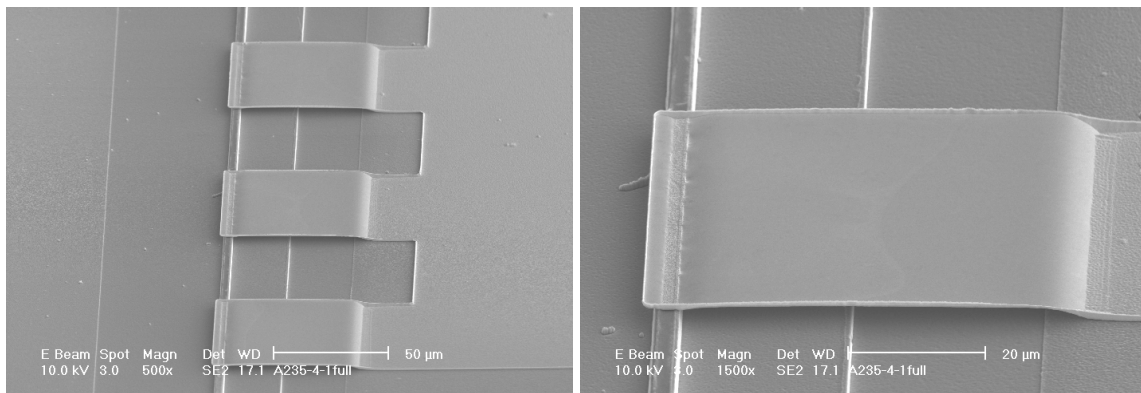


Figure 6.54 SEM images of the bridges

300/4000Å permitted us to obtain nearly 100 percent survivability. In APPENDIX C.2 starting with the process “Contact Opening and Reflow” and ending with the process “Bridge” give a description of how the bridges were created and their compositions. Figure 6.54 shows the SEM images of the bridges.

The I-V curve of the device is shown on Figure 6.55. The device resistance was $\sim 12.3 \Omega$ s. A low resistance was expected, since in-house efforts were not producing

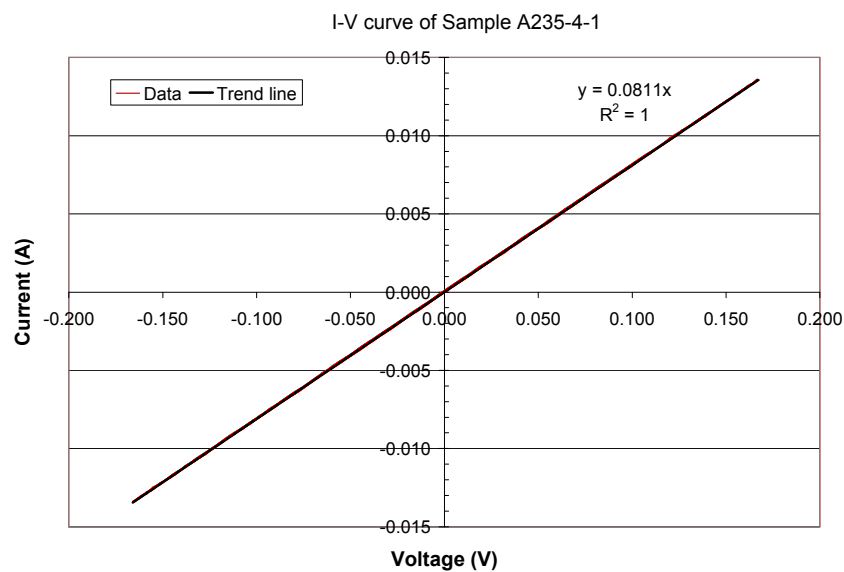


Figure 6.55. I-V curve of active device

semi-insulating GaN layer at the time. When ~ 5 V was applied to an active device it showed an unusual behavior. The optical signal was coming out of both branches. When a voltage was applied both, turned off. One of the samples cracked right through the waveguide, see Figure 6.56. The circled region in Figure 6.56 is where the electrical probe was making contact. The sample broke right through the location where the other probe was located.

Another sample was tested and the probes were observed to be moving, thermal expansion was suspected. When the sample was taken out of the holder the explanation surfaced. The sample was getting so hot that it melted a plastic holder. A new holder was made out of aluminum and installed. The sample holder was insulated from the rest of the set up. When voltage (≤ 6 V) was applied, small “sparks” were seen to be coming out of

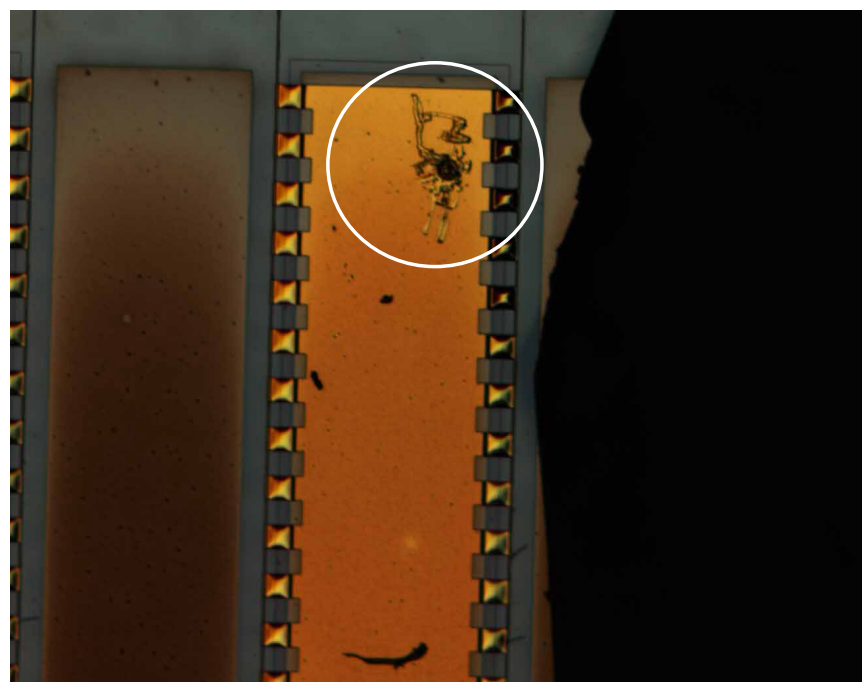


Figure 6.56. Active directional coupler that cracked after applying voltage.

the negative probe and damaged the contact pad underneath. The probes didn't "move" this time. This showed that the plastic holder being melted was the cause of the probe movement. An approach that was later attempted was to insulate the contact pads with SiN. This ensured the functionality of the device as a field only device.

During the course of the manufacturing of the device structures, slight variations were noted on the devices from one side to the other. Figure 6.57 shows a view in the mask template near the junction of the directional coupler. There is a slight variation in the width of the two branches. This error in the mask could have been a major contributor of

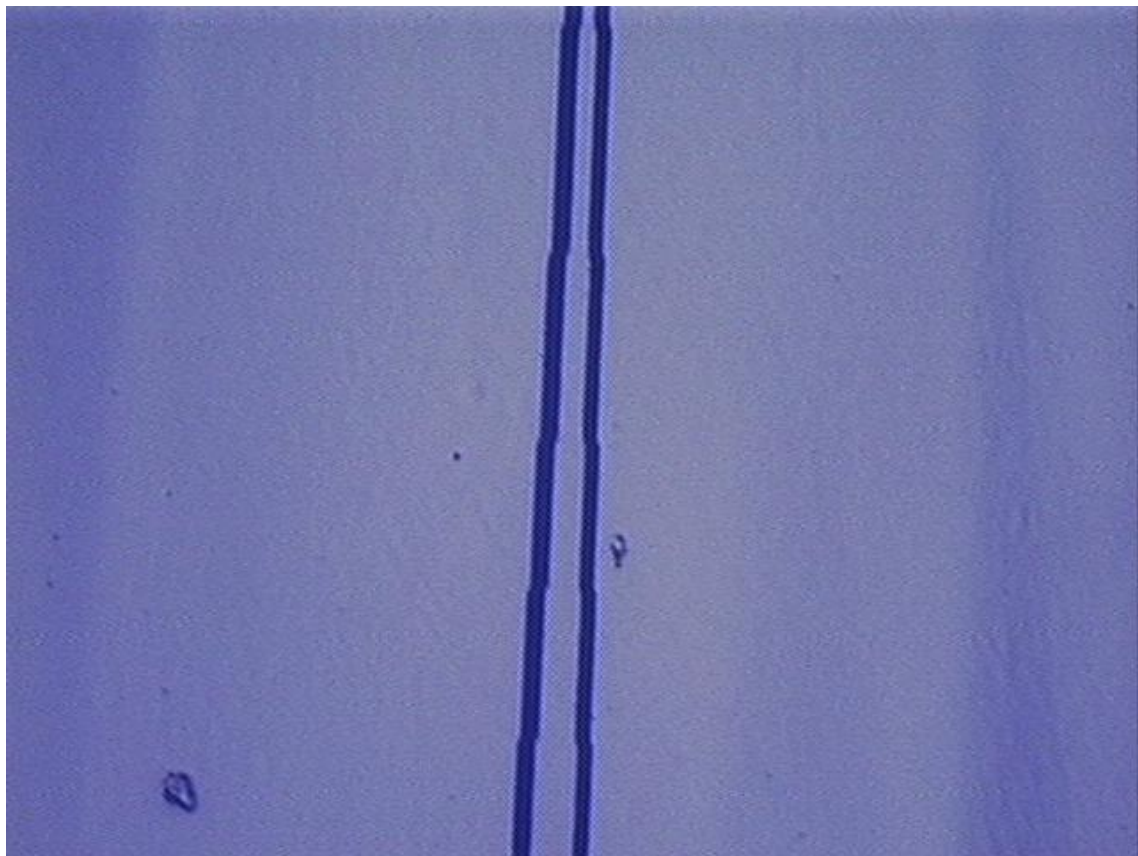


Figure 6.57 Junction in a directional coupler directly on the mask

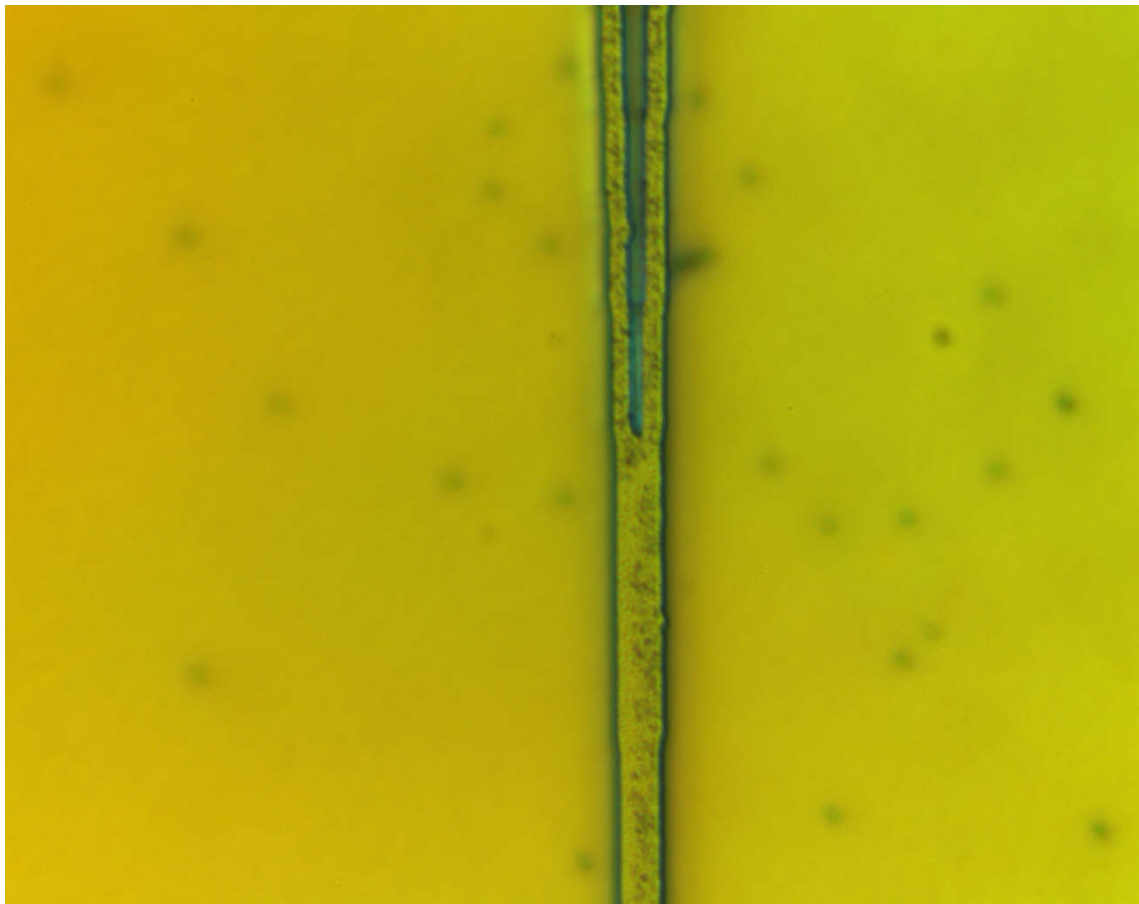


Figure 6.58 Transferred pattern into the AlGaN/GaN/AlGaN material

the uneven symmetry of the data seen in Figure 6.46. Figure 6.58 shows the pattern transferred to the material, after ICP etching. The difference between the branches is nearly unnoticeable at this stage. Although, they could have been enough for the discrepancy in the data.

Third Mask Set Processing, and Results

Another mask set was needed in which the errors in this mask set was corrected. With the experience gained, modifications were made to the mask to make the alignment easier. The mask arrangement is given in APPENDIX C.2. When the new mask set was

sent to the company, and after informing them of the errors that was encountered they were able to fix the error in their machine. This time, along with fixing software errors, the new mask set was done with finer resolution. The new resolution was 0.2 μm . This brought back the problems in the junction, see Figure 6.36 and Figure 6.37. This was because the thin feature, circled in these figures, were smaller than in the previous mask set template.

In order to resolved it this time, a thinner photoresist was used. The new process is listed in APPENDIX C.3. These process followers were arrived at after several iterations. With the new mask set and process followers, a much finer detail was achieved. Figure 6.59 shows the junction on the directional coupler. This time, with the new mask set, both

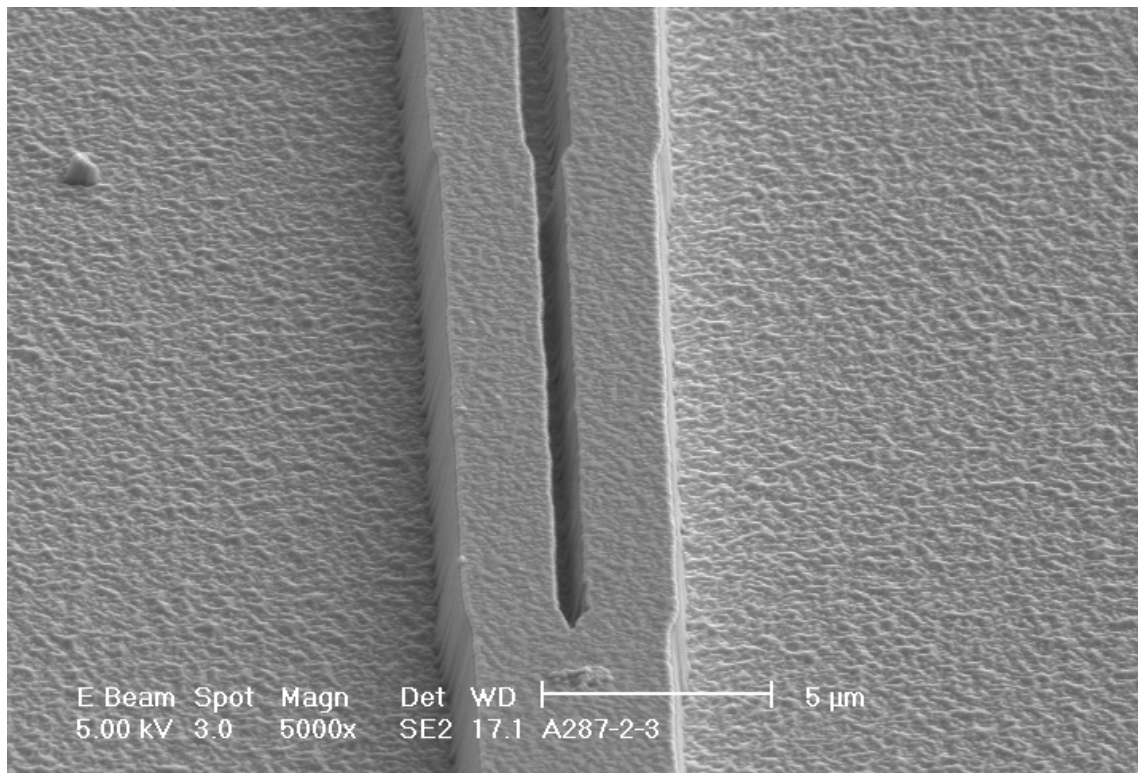


Figure 6.59 Junction of a directional coupler with the new mask template and the process outlined in APPENDIX C.3

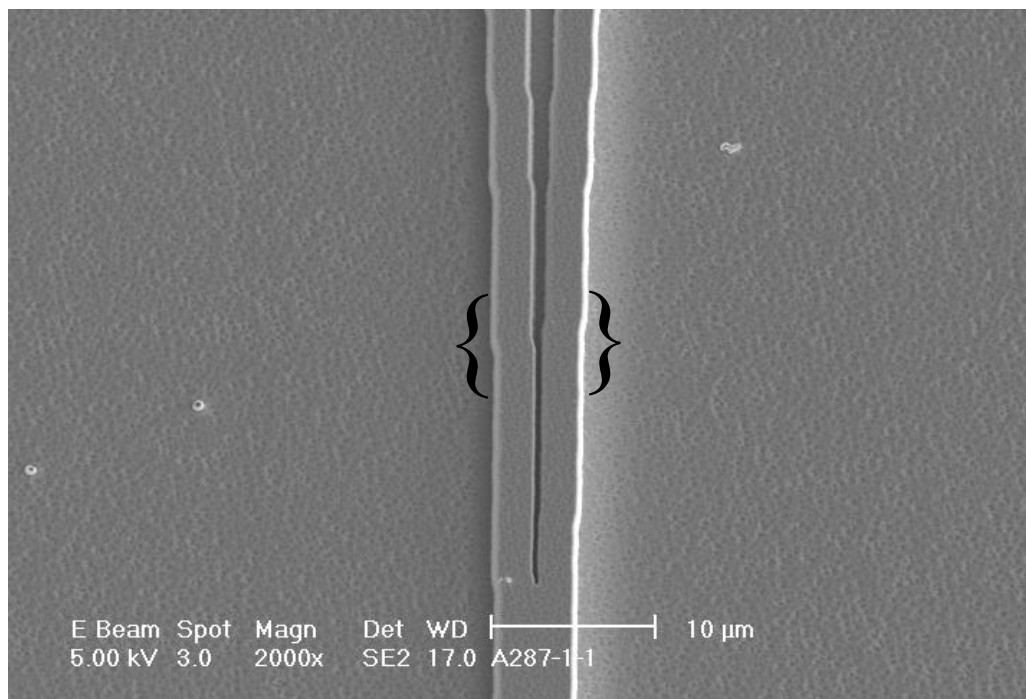


Figure 6.60 Different junction done with the third mask template

branches are identical in width. In Figure 6.60 the same mask set was used to create the pattern. A discrepancy is seen between the branches, Figure 6.60 inside the brackets. This is also present in the mask template and is due to quantization error when transferring the pattern from the software into the mask template.

Since the AlGaN couldn't be made insulating enough for the device to work properly, see previous section, a work around was devised. This time the contacts were insulated from the AlGaN/GaN material by a SiN layer, as illustrated in Figure 6.62. In that configuration, the electric field that the core would be subjected to would be a lot smaller. This is because the voltage is not concentrated in the core but distributed between the contacts. Therefore, a larger voltage is required to operate the directional coupler.

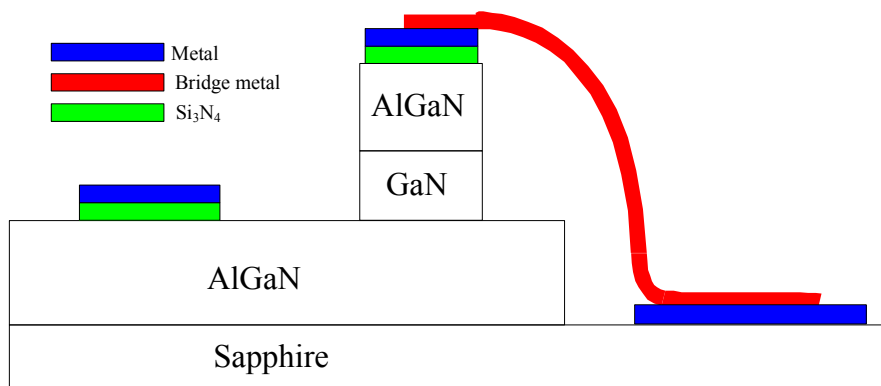


Figure 6.62 The targeted new configuration for the active device

A new sample was prepared with this configuration using the new mask template and the process detailed in APPENDIX C.3. A uniform layer of 1000 Å of Si_3N_4 was deposited on the sample, with a new PECVD system. After the metal contacts were deposited, the sample was placed on an RIE chamber to etch the Si_3N_4 where it was exposed. This should have left only the Si_3N_4 under the contacts. The bridge was then

Comparison of data collected with corrected data for A18711

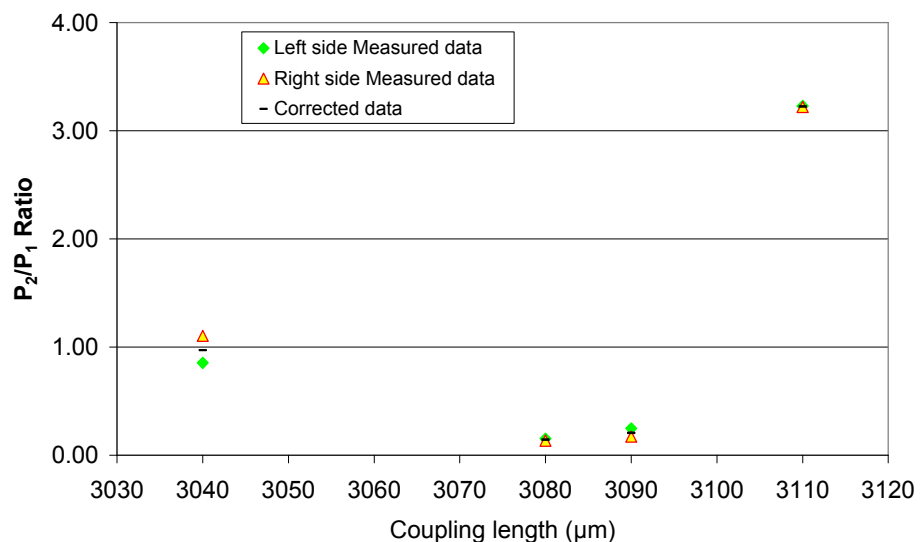


Figure 6.61 Measured data and corrected data taken from the directional couplers of a sample. The values are in the P_2/P_1 ratio form.

made and the ends polished. Data was taken on the devices before applying a voltage. Figure 6.61 shows the data gathered from the devices. As it can be seen the measured and the corrected data vary very little from each other, in contrast with that of Figure 6.46. This can be attributed to the improved mask template, which has finer resolution and has corrected the previous errors.

In examining the data, discrepancies started to show. The width of the coupling section was measured with in the SEM and turned out to be 3.55/4.21 μms with a height of 2.42 μm , see Figure 6.47. This would give us a single waveguide width between 1.91-2.02 μm . The data pointed to a smaller coupling length than Marcatili's approach would indicate for these dimensions, see Figure 6.48 and Figure 6.49. Using Equations (4-10)

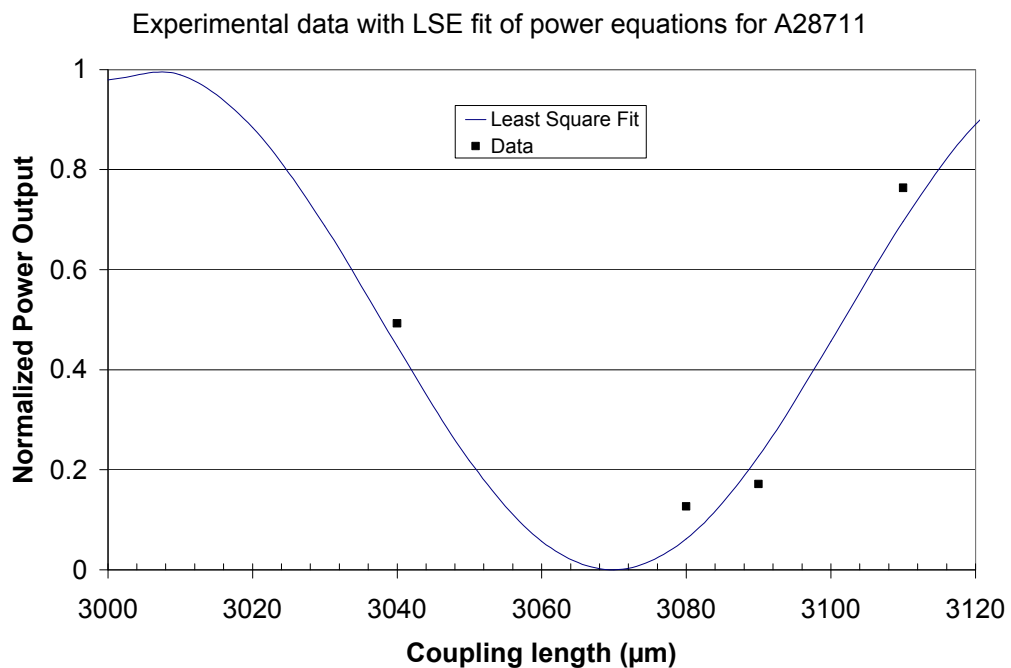


Figure 6.63 Least square fit of the data with Equations (4-10) and (4-11). Coupling length is 63.954 μm

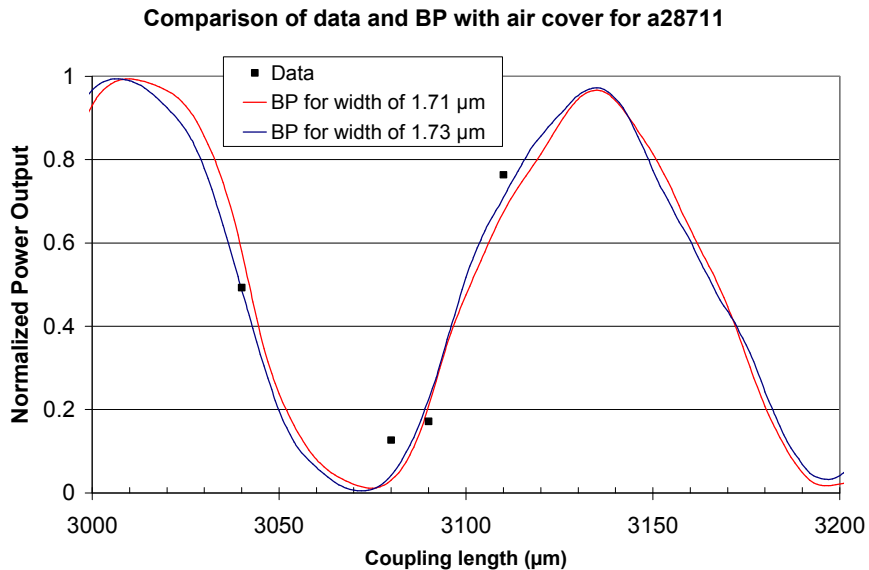


Figure 6.64 Comparison of the data from sample A287-1-1 and the beam propagation method with air covering the sample.

and (4-11) with $\alpha = 0$ and doing a least square fit, one arrives at a coupling length of $\sim 64 \mu\text{m}$, the sum of square errors is 0.014 for this value, see Figure 6.63. This would be the approximate coupling length that we would have arrived for a 1.71-1.73 μm branches, with a 3.42 - 3.46 μm total width of the coupling region, using the beam propagation method, see Figure 6.64. Investigation of the surface of the sample pointed to the reason of the discrepancy in the data.

Examining the surface of the sample using the EDAX tool pointed to the cause of the discrepancy. Figure 6.65 illustrates that Si_3N_4 is still on the surface. The index of refraction of the grown Si_3N_4 is ~ 2.26 , which is very close to that of the core ~ 2.304 . This proximity to the index of refraction of the core will affect the coupling length of the directional coupler. Attempts were made to determine the height of the Si_3N_4 left on the sample. Figure 6.66 shows the cross sectional view of a pad after milling. From the cross

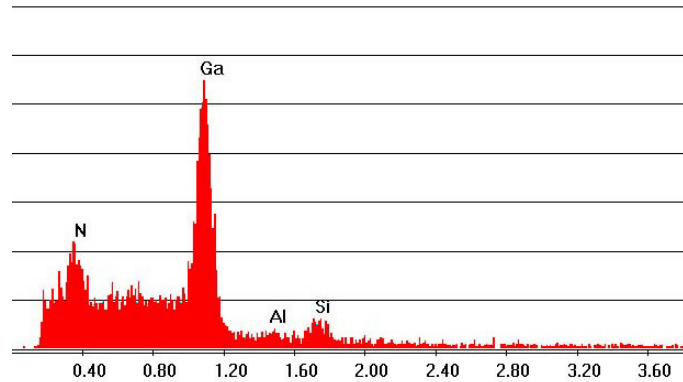


Figure 6.65 EDAX of a bare spot on the A28711 sample

sectional view, the Si_3N_4 could not be discerned, making the height impossible to be determined. An EDAX done on top of the metal contact showed that Si_3N_4 was present along with the metal.

A series of simulations were done on the beam propagation method and the Marcatili method in which the entire covering material was changed from air to Si_3N_4 . The Marcatili method gave a coupling length of $\sim 87 \mu\text{m}$ for branches width of $1.7 \mu\text{m}$, which

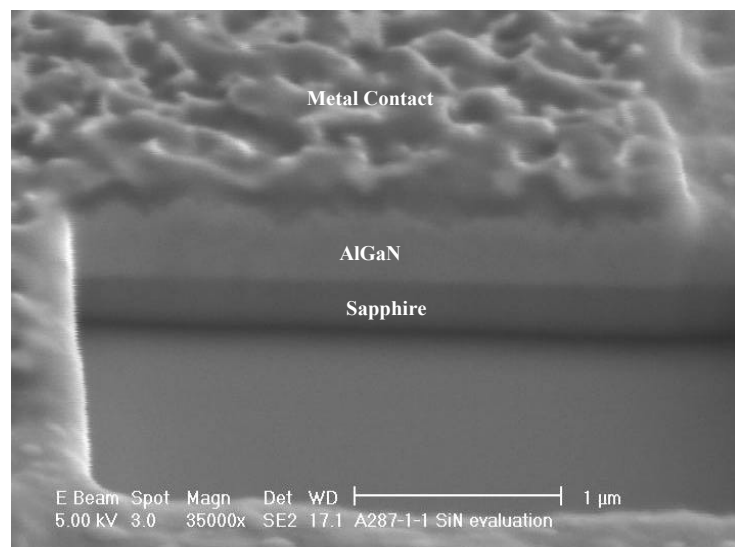


Figure 6.66 Cross-sectional view at a contact pad for sample A287-1-1

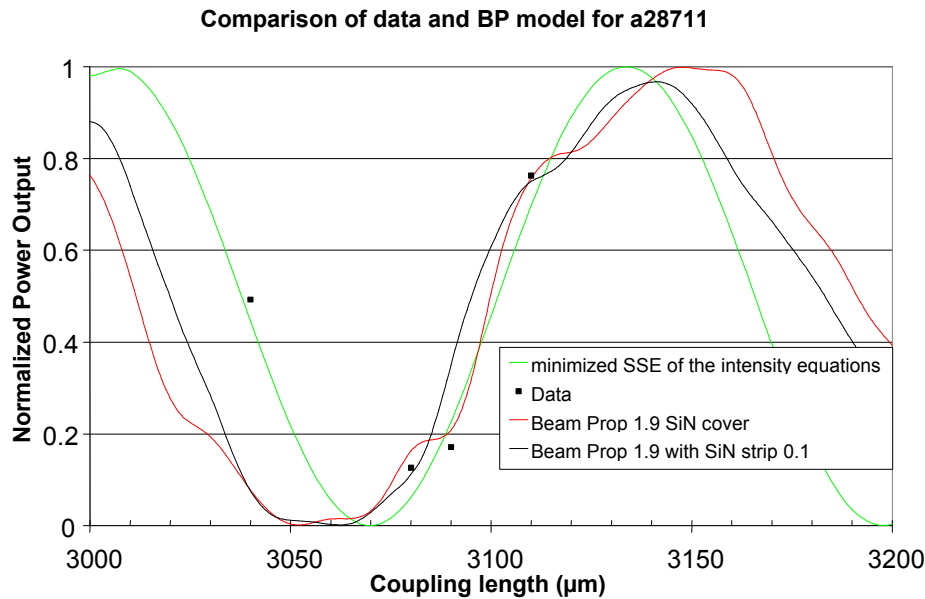


Figure 6.67. Comparison of the data and simulations with the beam propagation method.

is bigger than the suggested by the data, see Figure 6.63. With the beam propagation simulation two approaches were attempted one in which Si_3N_4 covered the entire structure and one in which only a $0.1 \mu\text{m}$ film covered the structure. This thickness was used because it was the maximum thickness that the sample could have, assuming that the RIE with freon had little or no effect on the Si_3N_4 . The simulations, using the beam propagation method, seems to have additional modes present as seen in Figure 6.67.

Voltage was applied to the structure to attempt to see if the optical signals would switch or modulate. After the voltage was applied there was no apparent change in the intensity of the output signal. An I-V curve of one of the structure was obtained and a possible reason emerged. Figure 6.68 shows the I-V curve of the structure. The Si_3N_4 was not acting as an insulator. When the sweeping voltage was set to $\pm 10 \text{ V}$ the structure was acting as a diode with a forward a turn on voltage of $\sim 0.7 \text{ V}$. When the sweep was

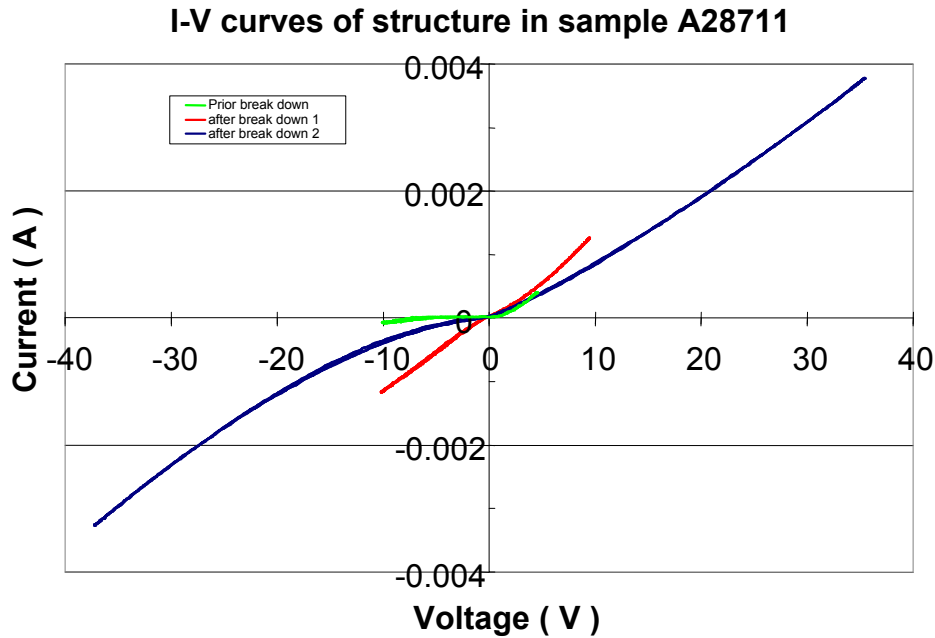


Figure 6.68 I-V curve of a structure in sample A287-1-1. The on resistance is between 10-12 k Ω s

increased beyond 15 V the device appeared to have gone beyond breakdown and from then on it went into a resistive behavior, no matter how small the voltage sweep was set at. While taking the I-V curves, and after device breakdown, the curves were jittery, the slope and shape of the curve was oscillating. It was suggested that there might be some type of traps in the structure accounting for the jittery behavior. Apparently the structure's resistive behavior prevented the electric field in the core region to be sufficient to noticeably change the refraction index.

In-house efforts to obtain semi-insulating (compensated) and p-type doping have been improving. A sample was prepared in an attempt to make the GaN layer insulating, see Figure 6.6. In this structure the cladding, Al_{0.05}Ga_{0.95}N, layers were both doped n-type, $\sim 10^{18}$ cm⁻². For this purpose Mg was incorporated in the growth to compensate the

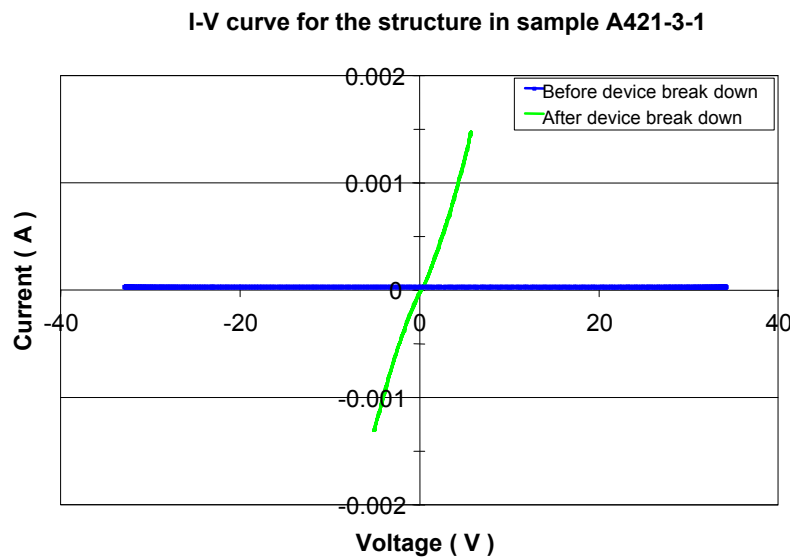


Figure 6.69 I-V curve of sample A421-3-1 in which attempts were made to obtain insulating GaN

unintentionally doped n concentration. Si_3N_4 was deposited prior to the contacts on the entire surface, $\sim 1000 \text{ \AA}$. This time no attempts to remove it were made. For the contacts, Ti/Au was used, since this has been shown to be resistive for n-type AlGaN without alloying.³⁷

Testing was started on the sample. Prior to testing the structure in the optical set up an I-V curve was made of the structure. It was a different device than the one to be tested. Figure 6.69 shows the I-V curves taken from a sample. From this figure it is seen that, after breakdown, the device goes into a resistive mode with a resistance of $\sim 5 \text{ k}\Omega$. The current of the device was monitored during testing, in the optical set up, to prevent any degradation of the structure, see Figure 6.17. The structure presented some diode behavior during testing, with one polarity of the voltage presenting slightly less resistance than the other. The structure should have presented a highly resistive behavior.

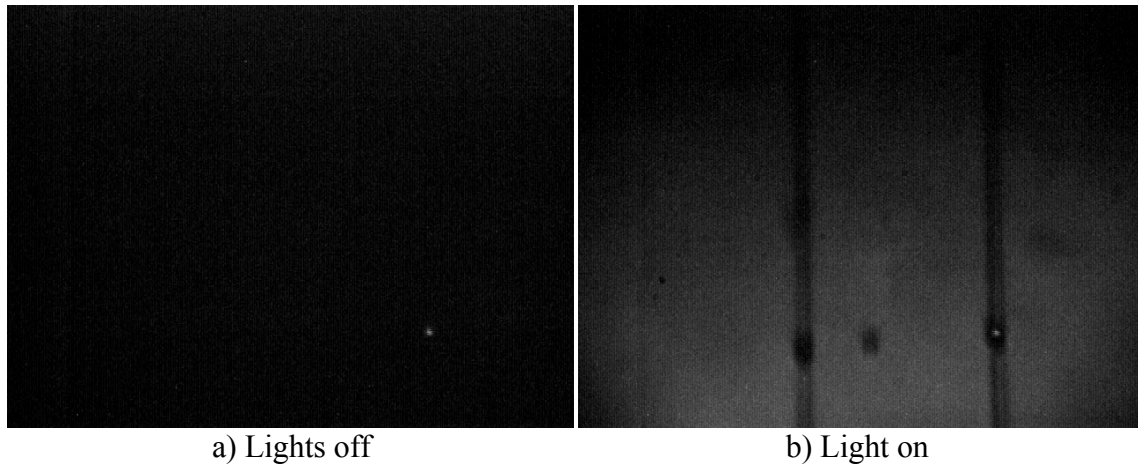


Figure 6.70 Image obtained from the output of a directional coupler of sample A421-3-1.

Data was collected on one of the structures in the sample. Figure 6.70 shows the output of the directional coupler. Behavior as a directional coupler was immediately noticed. Light was launched in the left branch, the opposite branch from that shown in Figure 6.70, and light came out in the left branch. Once all the data was collected from the device, voltage was applied and increased slowly. During that time, the current was monitored for a possible breakdown of the device. The voltage increase was stopped when the current started to increase rapidly. The values of the current and voltage were $0.76 \mu\text{A}$ and 25 V respectively. The intensity of the output appeared to change. The voltage was turned off and on to verify a change in intensity. Figure 6.71 shows instances in which the voltage was turned on and off. The difference in intensity is more noticeable in the intensity profile, section c) of the figure. There was no apparent change in the branch that had no optical signal in the output. A possible reason is that the branch is below the noise level and any variation would be difficult or impossible to detect.

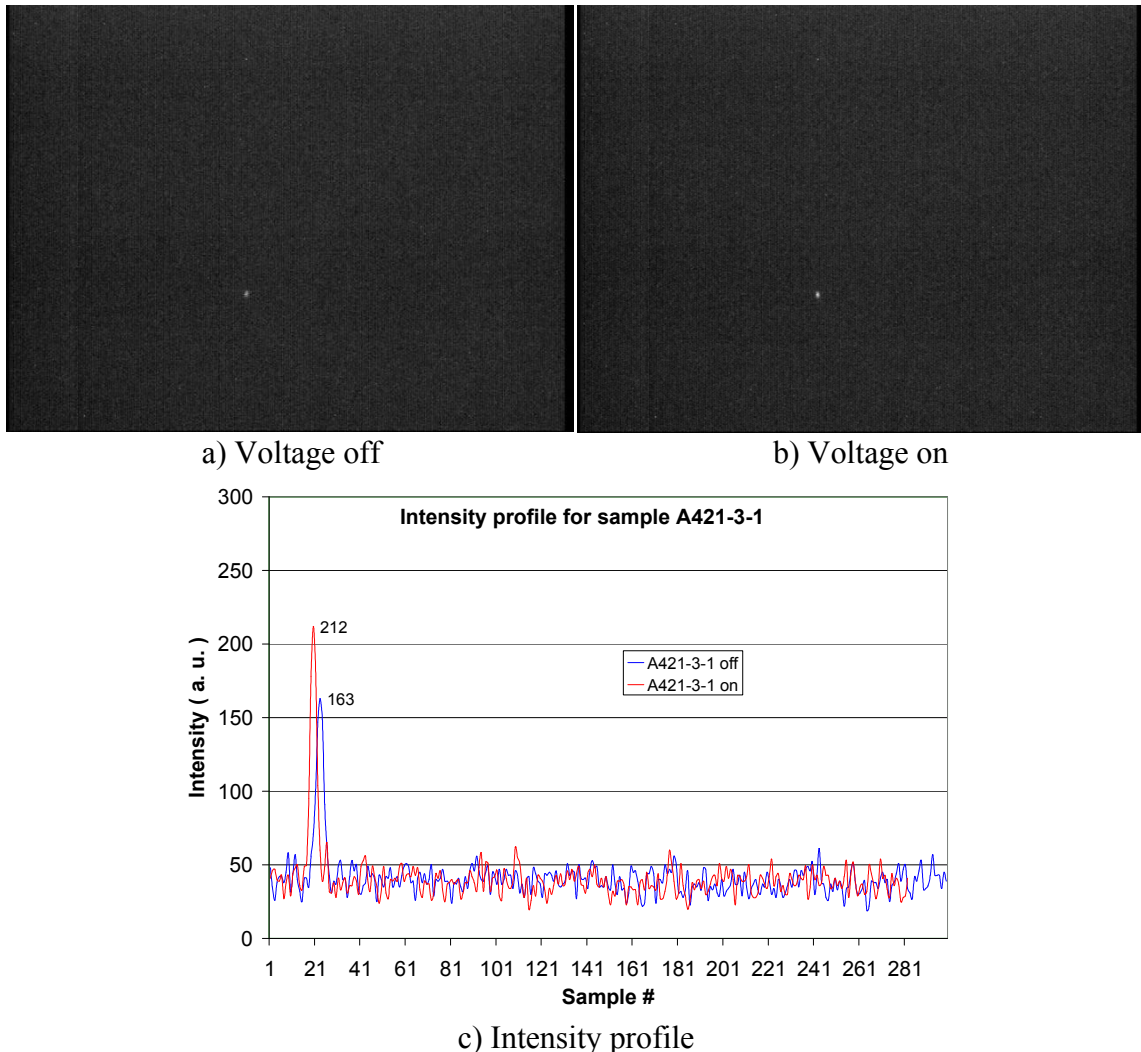


Figure 6.71 Light intensity variation with the application of 25 V on a device in sample A421-3-1.

The output of the camera was manipulated to optimize the contrast and intensity. That was done electronically rather than with image manipulation. This accentuated the variation of the signal, by removing a portion of the dc component of the image and focusing on the intensity variation. Figure 6.72 shows the results of the modulation of the directional coupler. The noise in the signal is due to building vibrations.

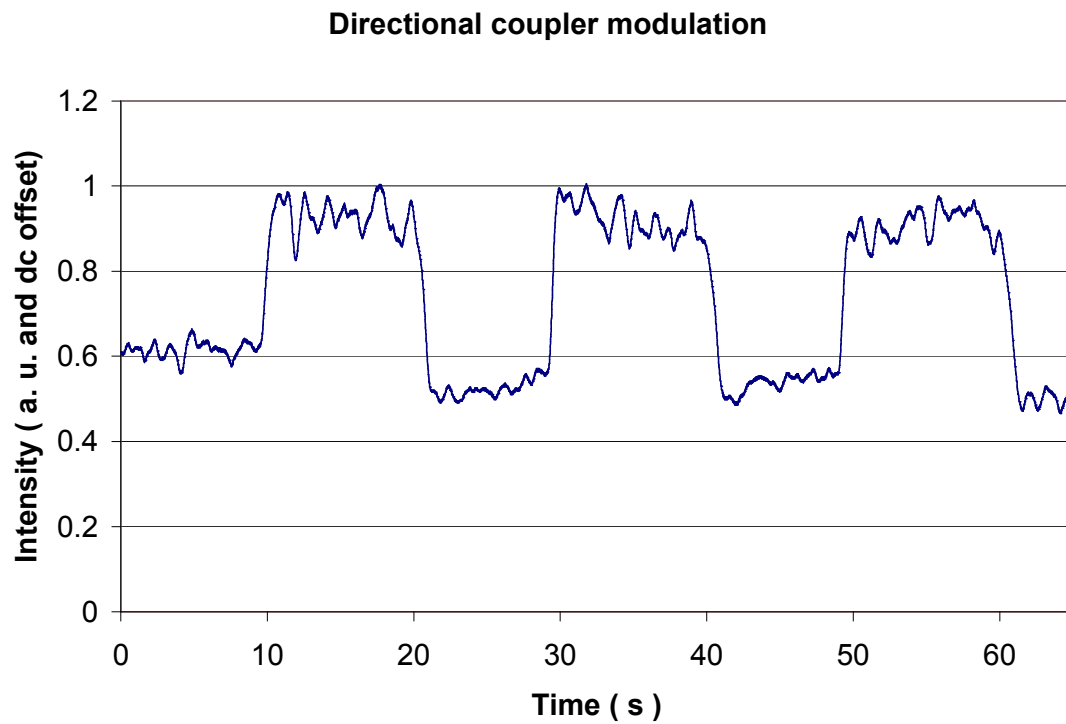


Figure 6.72 Modulation of the directional coupler. Image enhancements were done to accentuate the intensity variation.

CHAPTER VII

DISCUSSION OF RESULTS AND CONCLUSION

Developing the process for etching the AlGaN/GaN material system proved to be more difficult than initially anticipated. This was due mostly to the newness of the material and the limited experience in processing it. This is illustrated by the initial search for an appropriate masking material and the process development as seen in appendices B and C. Since GaN/AlGaN is highly tolerant of harsh environments, the normal masking materials that would fare well on other materials would only be marginal at best. The photoresist, normally used as a masking material, etches a little faster than the AlGaN material system. This would be adequate for shallow structures, but not very good for deep structures, such as a directional coupler. Figure 7.1 shows photoresist after being

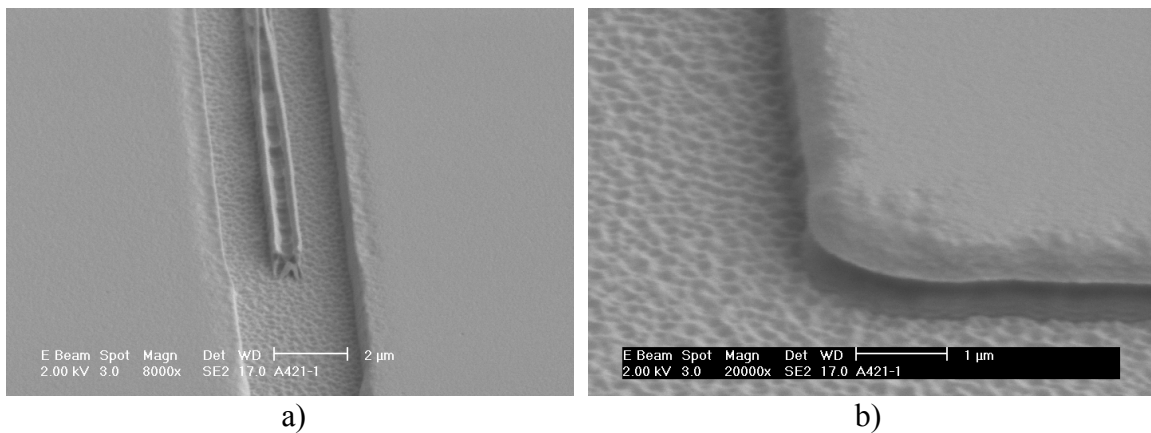


Figure 7.1 Photoresist before metal mask deposit. a) Junction region of a directional coupler, b) corner of a letter

processed into a mask. The sidewalls of the photoresist shown in Figure 7.1b are not very promising for a mask material. A problem that would immediately surface would be the sidewall slope and roughness. For the targeted structure of this work the sidewalls needed to be steep and as smooth as possible. Finding Ni as a mask was very advantageous. Only 1000 Å of material was needed to etch $\sim 2\mu\text{m}$ of material, it also permitted steep sidewalls. Placing the electrode on top of the directional coupler presented an alignment challenge. The electrodes were less than 3 μm wide and ~ 3 mm long and they required a laborious alignment procedure. Figure 7.2 shows the successful placement of the contact on top of the coupling section of a directional coupler.

The structure that this research focused on is shown in Figure 7.3. This is a complicated structure to simulate. As seen in Figure 7.4, in the vertical direction the evanescent waves

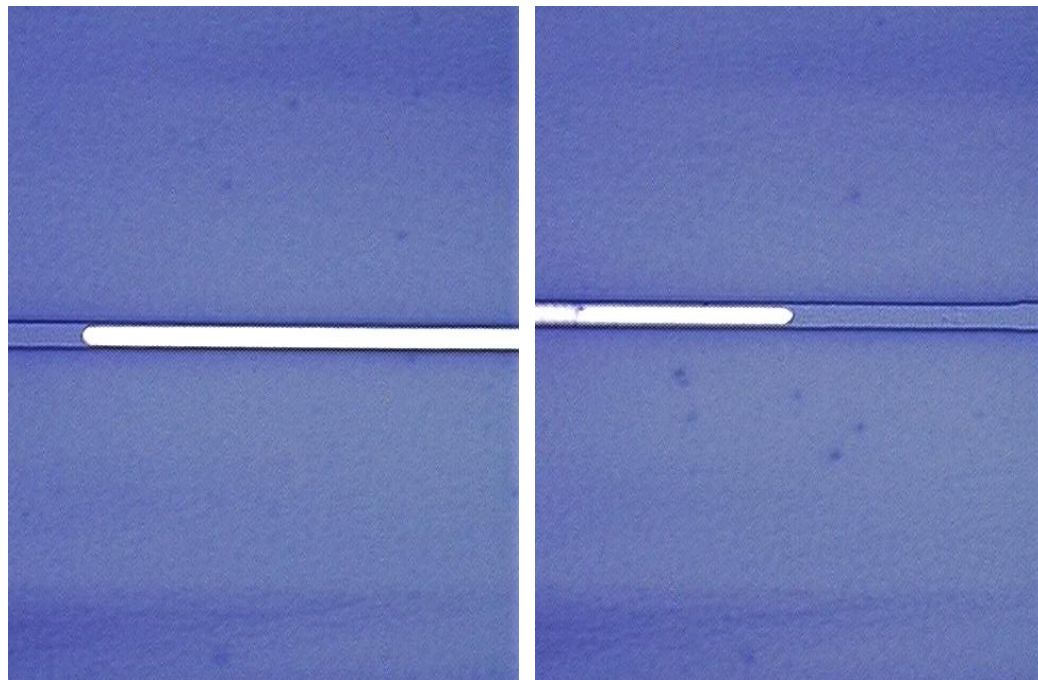


Figure 7.2. Metal contact on top of the coupling region of a directional coupler.

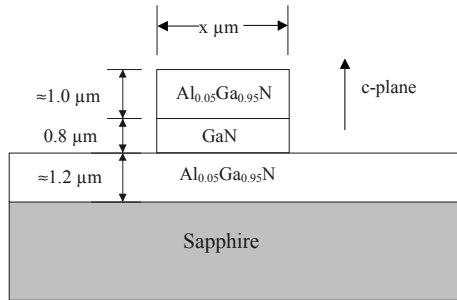


Figure 7.3 Side view of the single mode waveguide structure for AlGaN

extend into the AlGaN cladding region. In a two-dimension structure this would be close to the cut off region. In the horizontal direction the evanescent waves don't penetrate the cladding region, which is air in that direction. That would be far from cut-off in a two dimensional structure. Having both of these conditions present is what makes this structure complicated to simulate.

The Marcatili method is well suited for simulation in the horizontal direction, where air ($n \approx 1$) acts as the cladding region. In that direction, the index of refraction has abrupt

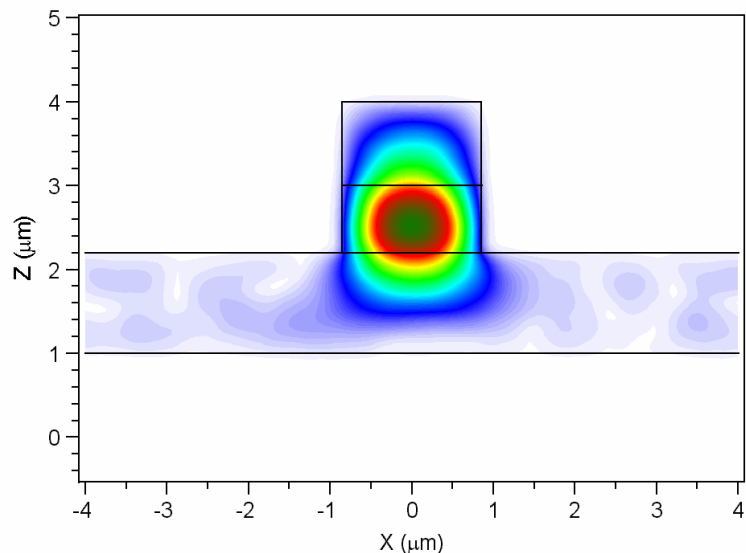


Figure 7.4 Intensity profile in the single mode waveguide

changes and the Marcatili method is tailored for abrupt changes, see CHAPTER 2. But for the parts that correspond to the shaded area in Figure 2.4, where AlGaN is present, its suitability could be sketchy. The beam propagation method is more suited for the vertical direction because the change in the index of refraction is smaller and the BPM is better with small refraction index increments, see CHAPTER 2.

In the 1.4 μm waveguide width simulations, Figure 6.25 and Figure 6.26, there was a discrepancy between the methods. The Marcatili method showed a waveguide that shouldn't be guiding, Figure 6.26, while the beam propagation method showed a guiding waveguide. Although the mask template had this dimension, the actual waveguide was wider than this. The thinnest waveguide tested was $\sim 1.71 \mu\text{m}$. In Figure 7.5 both the BPM and the Marcatili method are compared side by side. While the Marcatili model is very close to cut off, the BPM is guiding very well. Figure 7.6 shows the output of the 1.71 μm branch width directional coupler. It points toward the beam propagation method as a better representation of the wave being guided in the waveguide. This can be explained by knowing that one of the assumptions of the Marcatili method is that the

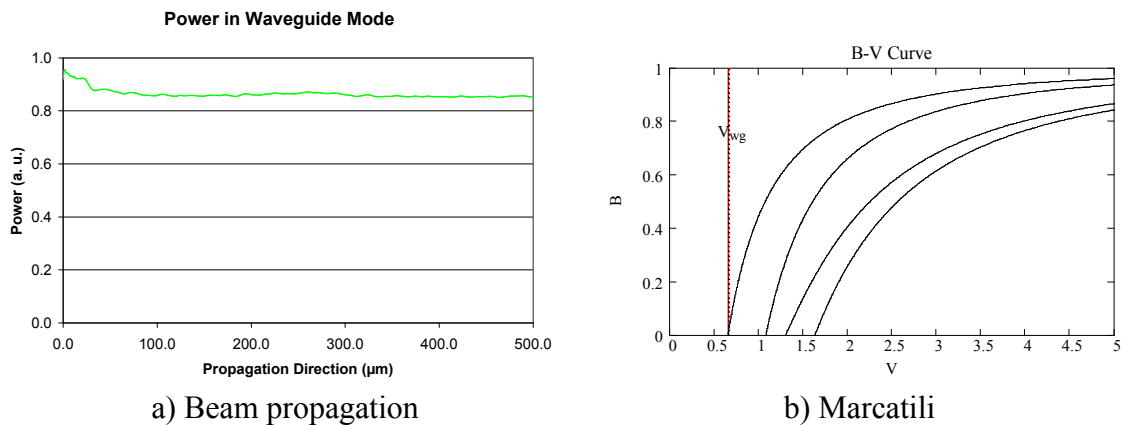


Figure 7.5 Comparison of the 1.71 μm waveguides.



Figure 7.6. Output from the $1.71 \mu\text{m}$ branch width directional coupler, sample A12941

optical signal needs to be far from cut off, see CHAPTER 2. When the optical signal is close to cut off in the waveguide, the Marcatili method will not accurately account for the behavior of the optical signal in the waveguide, see reference 22. Figure 7.5b shows a waveguide too close to cut off to be effectively propagating light. The beam propagation method shows an optical signal that is propagating effectively through the waveguide, giving a better representation of what it is observed. Also, the errors incurred in the paraxial approximation were not a major factor in the behavior with a single waveguide simulation.

For the directional coupler the results were different. Figure 6.48 and Figure 6.49 favors the Marcatili approximation for establishing the coupling length in the directional coupler. The paraxial approximation of the beam propagation method neglects large angles from the z-direction and thus introduces an error in the calculation of the coupling length. A directional coupler is very sensitive to these errors and thus gives an erroneous representation of directional coupler behavior. In a different way, the beam propagation

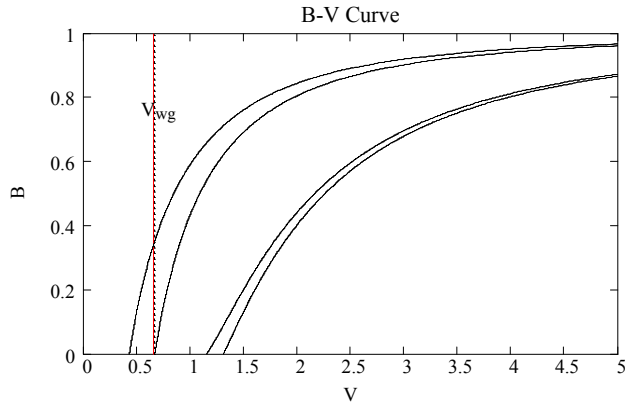


Figure 7.7 Mode chart of the interaction region for a $1.71\mu\text{m}$ branch width directional coupler

method assumes small variations in the index of refraction not only in the propagation direction, but also in the transverse direction. The abrupt changes in the air-core interface introduce errors in the propagation constants of the two modes, odd and even, in the coupling region. This in turn gives us an erroneous coupling length. The B-V curves from the Marcatili method, shown in Figure 7.7, shows one of the modes near cut off. In spite of the method of being unreliable near mode cut-off its results were close to what was expected, see Figure 6.47 and surrounding text. The reasoning for this is that the coupling length is determined by the difference between the modes, and the errors in the Marcatili approach had little effect on the difference for this case.

When the medium surrounding the directional coupler has a smaller step increase in the index of refraction, the Marcatili method will no longer be able to predict the behavior of the waveguide. That is because the shaded areas, see Figure 2.4 and Figure 6.3, can no longer be neglected. When SiN was introduced surrounding the structure, it was enough to be in a shaded region where neither the beam propagation nor the Marcatili method could

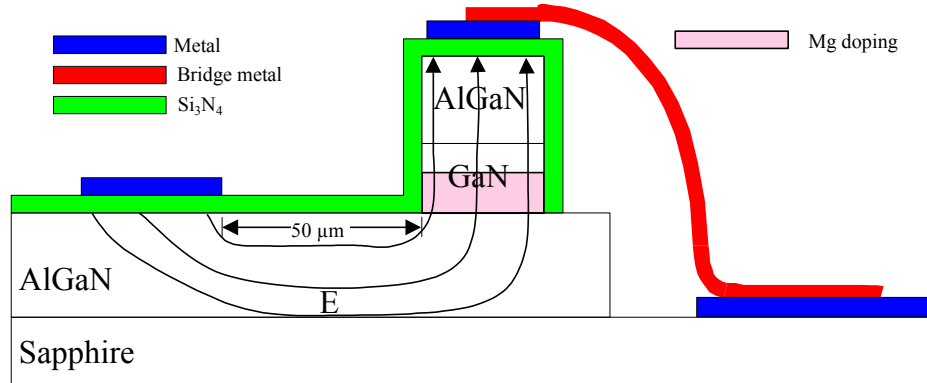


Figure 7.8. Structure of the modulating directional coupler

establish theoretically the coupling length. Although this time, the beam propagation method was much closer than before. Possible variations in the Al%, the core size, and the index of refraction could have also accounted for this discrepancy. Though it is still believed that better modeling methods are needed in this region.

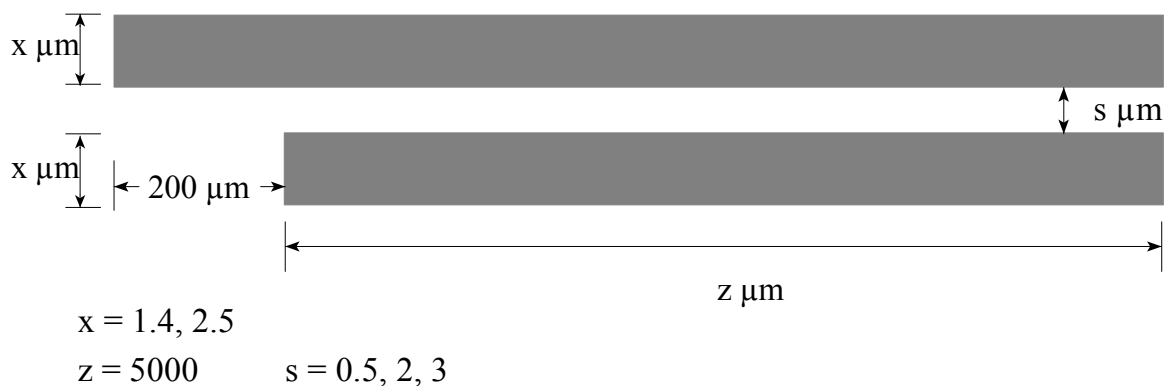
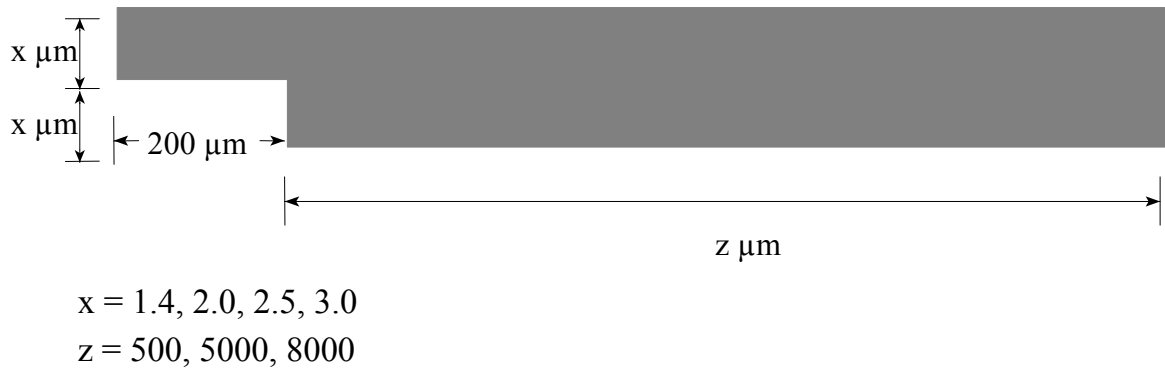
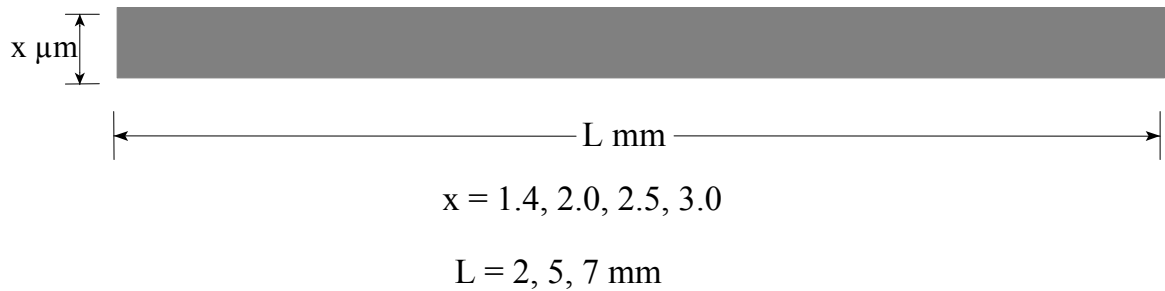
Modulation was obtained in the structure of Figure 7.8. That indicated that, indeed the electro-optic effect is present in the material, although, confirmation of its value was not possible. The modulation depth was much lower than was originally sought after. In this structure, after device breakdown, SiN didn't act as an insulator, as expected. Another unexpected result was the entire structure having a low resistive value $\sim 5 \text{ k}\Omega$ after SiN breakdown, see Figure 6.69. In other research, this dielectric has been shown to fail on III-V materials.³⁷ Because Mg diffuses, it was added to the growth for only 0.5 μm of the GaN region, see Figure 7.8, the rest of the GaN was undoped. This was done in the expectation that Mg would diffuse over the entire GaN region and create a compensated insulator. The weak modulation could be attributed to the fact that the voltage is applied

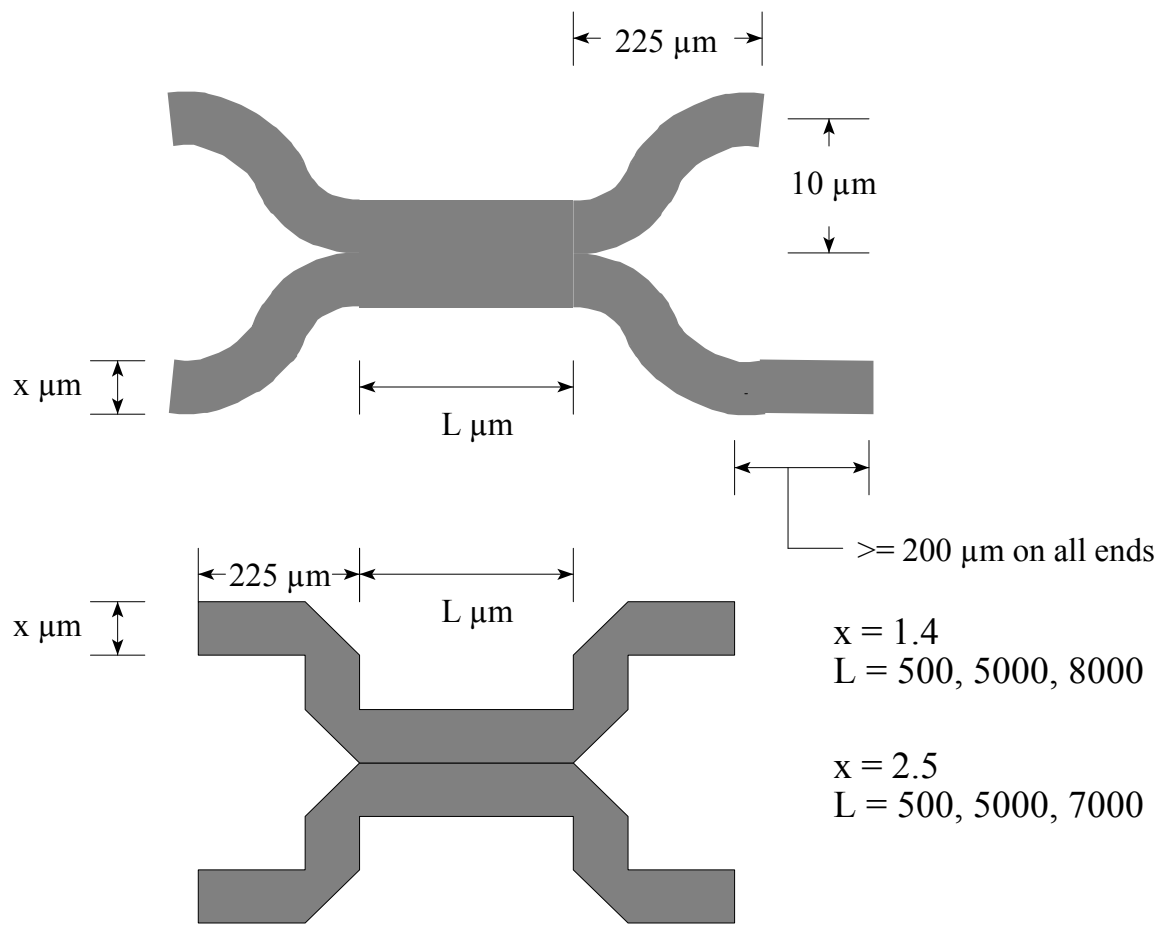
to a distance of more than 50 times as great as intended, $> 50 \mu\text{m}$ instead of $0.8 \mu\text{m}$. That reduced the electric field intensity in the core, thus we have only a small index variation

Future Work

Through out this project one thing was constantly surfacing, the material is still in the development stage. The material growth needs to improve the development of insulating, or semi-insulating, layers with out requiring compensation. Better control and improved p-type layers are needed. Additionally, a reduction in defect density should be pursued since this could reduce the background n concentration. In the modeling for the structure under investigation, more robust models should be pursued. Alternatives include the use of the finite element approach to obtain better B-V curves than can be obtained by the Marcatili method. The beam propagation method is a good tool to use to model the behavior of the entire structure. This includes the study of small imperfections that can be added to the structure, which could be produced by the manufacturing process, and observe the guides behavior. Unfortunately, its domain of operation does not include the abrupt changes in the index of refraction in the transverse direction. If possible, modifications should be sought to make it less susceptible to abrupt index changes without sacrificing much of its computational advantages. Another possibility is to use the finite difference-time domain (FD-TD) approach for the full structural analysis.⁸² The problem is that this approach is very computational intensive and memory hungry.

APPENDIX A
CONFIGURATION OF MASK 1





APPENDIX B
ETCHING MASK AND ICP RECIPE DEVELOPMENT

Recipe Number	ICP Recipe detail	
1	(Paul's Recipe)	
	Cl ₂	4 sccm
	BCl ₃	15 sccm
	Pressure	5 mTorr
	RF Power	75 W
	ICP Power	300 W
2	(Dr Shull's Recipe)	
	Cl ₂	32 sccm
	BCl ₃	8 sccm
	Ar	5 sccm
	Pressure	2 mTorr
	RF Power	150 W
	ICP Power	500 W
3	Cl ₂	20 sccm
	Ar	5 sccm
	Pressure	5 mTorr
	RF Power	150 W
	ICP Power	500 W
4	Cl ₂	20 sccm
	BCl ₃	20 sccm
	Ar	5 sccm
	Pressure	2 mTorr
	RF Power	150 W
	ICP Power	500 W

B.1 Initial Mask and ICP Recipe Development

Sample	Process #	Temp °C	DC bias (meas.)	Etched Time(m:s)	Mask layer (Top-Bottom)	Etched height	Comments
A121-3-1	1	0.4	246	10:01	1813:PMGI	14.1 kÅ	Sidewalls weren't steep enough. The bare surface was GaN and AlGaN on top of the waveguide. Dark region is photoresist. Photoresist sidewall is being etched at a slope. Veils are present after photo resist removal.
A121-3-2	2	0.4	622	0:30	1813:PMGI		The run was set to DC-bias instead of rf power. This made the power jump to the maximum output (500 W). The photoresist was Scorched.
A121-3-3	3	0.4	300	1:01	1813:PMGI	8.165 kÅ?	Sidewalls weren't steep enough. Photoresist sidewall is being etched at a slope.
A121-3-4	2	0.4	288	1:01	1813:PMGI	8.29 kÅ?	Sidewalls weren't steep enough. Photoresist sidewall is being etched at a slope.

Sample	Process #	Temp °C	DC bias (meas.)	Etched Time (m:s)	Mask layer (Top-Bottom)	Etched height	Comments
A121-2-1	2	29.5	319	2:15	1277 Å Ti	2.4 kÅ	Ti Was Etched Away. Metal mask is in direct contact with the surface. Mask/surface etch ratio. ~1.8/1. Height in picture is skewed due to software problems.
A121-2-2	2	0.5	320	0:30	1635 Å Ti	2.9 kÅ	Problems with the profilometer. The Ti is almost gone. No speckle
A121-2-3	2	0.5		3:02	~1000 Ni	21.6 kÅ	No Boron Present. Nickel mask still present. Etched all the way to the bottom AlGaN Layer. Sidewall aren't totally smooth, stepped sidewall
A121-2-4	2	25	322	2:40	~1000 N	19.1 kÅ	Nice sidewalls, but has some Speckle etching less than in the A121-2-3. In the bare spots there is Boron background. The SiN was etched out of the non-masking areas. ~100 Å/s for AlGaN 10% and 151.7 Å/s for GaN (6000 Å/m and 9000 Å/m on GaN)

Sample	Process #	Temp °C	DC bias (meas.)	Etched Time (m:s)	Mask layer (Top-Bottom)	Etched height	Comments
A121-2-5	2	0.5	316	2:45	~1000 Ni: 1000 SiN	17.1 kÅ	No speckle is present. The SiN film was deposited before the Ni and left in the sample before it was etched in the ICP. Rough sidewalls, little indication of step.

B.2 ICP Recipe Development for Sidewall Improvement

Sample	Process #	Temp °C	DC bias (meas.)	Etched Time (m.s)	Mask layer (Top-Bottom)	Etched height	Comments
A130-1-3	4	25.0?		2.45 2.15	~1000 SiN: 1000 Ni	17.64 kÅ	Looked bad. Like a pine forest
A130-2-5	modified # 2 with RF = 40W	25.0		150 3.30	1000 SiN: 1000 Ni	~23.63 kÅ	First trial at reducing the etch rates and improving sidewall definition.
A188-1-1	modified # 2 with RF = 100W	25.0		241 4.30	~1000 SiN: 1000 Ni	26.96 kÅ	Trial at reducing the etch rates and improving sidewall definition.
188-1-2	modified # 2 with RF = 40W	25.0		148 6.00	~1000 SiN: 1000 Ni	20.38 kÅ	Trial at reducing the etch rates and improving sidewall definition

On the sample there were cluttered (dirty) areas and clean areas.

Sample	Process #	Temp °C	DC bias (meas.)	Etched Time (m:s)	Mask layer (Top-Bottom)	Etched height	Comments
A188-1-3	modified # 2 with RF = 75W	25.0	207	5:00	~1000 SiN: 1000 Ni	24.69 kÅ	Trial at reducing the etch rates and improving sidewall definition
A188-1-4	modified # 2 with RF = 75W	27.0	214	3:00	~1000 SiN: 1000 Ni	13.89 kÅ	Trial at reducing the etch rates and improving sidewall definition
188-1-5	modified # 2 with RF = 75W	25.0	207	4:30	~1000 SiN: 1000 Ni	23.83 kÅ	Trial at reducing the etch rates and improving sidewall definition

APPENDIX C
PROCESS FOLLOWERS

C.1 First process follower for passive Waveguides

Step	Process Step
1	Pre SiN SAMPLE PREPARATION (OPTIONAL): <input type="checkbox"/> 30 sec spray with Acetone Bottle at 500 RPM <input type="checkbox"/> 30 sec Isopropyl Alcohol at 500 RPM <input type="checkbox"/> Dry with N ₂ at 500 RPM <input type="checkbox"/> Dry with N ₂ on clean Texwipes <input type="checkbox"/> Prepare surface with a dip of Ammonia Hydroxide:DI (1:20) for 1 min <input type="checkbox"/> Deposit 1000 Å of SiN
2	SAMPLE PREPARATION: <input type="checkbox"/> 30 sec spray with Acetone Bottle at 500 RPM <input type="checkbox"/> 30 sec Isopropyl Alcohol at 500 RPM
3	DEHYDRATION BAKE: <input type="checkbox"/> 1 min 110°C Hot Plate Bake
4	PMGI COAT: <input type="checkbox"/> Flood wafer with PMGI (SF-11) <input type="checkbox"/> 30 sec Spin at 4000 RPM, Ramp=200 <input type="checkbox"/> 1 min Air Bake <input type="checkbox"/> 5 min 270 °C Hot Plate Bake <input type="checkbox"/> Cool Wafer
5	1813 COAT: <input type="checkbox"/> Flood wafer with 1813 <input type="checkbox"/> 30 sec Spin at 4,000 RPM, Ramp=200 <input type="checkbox"/> 75 sec 110°C Hot Plate Bake <input type="checkbox"/> Check cleanliness of wafer backside
6	EXPOSE 1813 with BASE MASK: (Note which exposure was done first) <input type="checkbox"/> Align <input type="checkbox"/> 4.0 sec Exposure (405 nm) on Mask Aligner @ 20mW/cm ² optical intensity
7	1813 DEVELOP: <input type="checkbox"/> 40 sec Develop with (1:5) 351:DI H ₂ O at 500 RPM <input type="checkbox"/> 30 sec DI H ₂ O Rinse at 500 RPM <input type="checkbox"/> Rinse wafer backside with DI H ₂ O Bucket Rinse <input type="checkbox"/> Dry with N ₂ on clean Texwipes
8	INSPECT LITHOGRAPHY: <input type="checkbox"/> Place wafer flat towards top of microscope <input type="checkbox"/> Inspect wafer alignment with yellow filter on microscope <input type="checkbox"/> Check Lithography: <input type="checkbox"/> Open <input type="checkbox"/> Clean <input type="checkbox"/> Sharp Definition
9	DEEP UV (254 nm): <input type="checkbox"/> 100 sec Deep UV Exposure @ 16mW/cm ² optical intensity

Step	Process Step
10	PMGI DEVELOP: <input type="checkbox"/> 50 sec 101 Develop Immersion <input type="checkbox"/> 4X Bucket Rinse with DI H ₂ O <input type="checkbox"/> Dry with N ₂ on clean Texwipes
11	DEEP UV (254 nm): <input type="checkbox"/> 100 sec Deep UV Exposure @ 16mW/cm ² optical intensity
12	PMGI DEVELOP: <input type="checkbox"/> 50 sec 101 Develop Immersion <input type="checkbox"/> 4X Bucket Rinse with DI H ₂ O <input type="checkbox"/> Dry with N ₂ on clean Texwipes
13	INSPECT WAFER: <input type="checkbox"/> Inspect PMGI. Under cut should be obvious (0.5 μm)
14	O₂ PLASMA ASHER: <input type="checkbox"/> 4 min LFE Barrel Asher
15	EVAPORATE BASE METAL: <input type="checkbox"/> Evaporate 1000 Å Ni
16	REMOVAL OF BASE METAL: <input type="checkbox"/> Heat 1165 to 90°C <input type="checkbox"/> Remove base metal using Acetone on a petri dish <input type="checkbox"/> 20 sec spray with Acetone Bottle at 500 RPM <input type="checkbox"/> 30 sec Isopropyl Alcohol at 500 RPM <input type="checkbox"/> Dry with N ₂ at 500 RPM <input type="checkbox"/> Dry with N ₂ on clean Texwipes <input type="checkbox"/> Check backside and clean if necessary
17	REMOVE PMGI: <input type="checkbox"/> 2 min 1165 at 90°C <input type="checkbox"/> 6x DI H ₂ O Rinse <input type="checkbox"/> Dry with N ₂ on clean Texwipes
18	O₂ PLASMA ASHER: <input type="checkbox"/> 4 min LFE Barrel Asher
19	SiN DEFINITION (OPTIONAL): <input type="checkbox"/> Etch using the dual chamber RIE reactor
20	ETCH AlGaN: <input type="checkbox"/> Etch using the ICP reactor
21	PREPARATIONS: <input type="checkbox"/> Mix (1:1) BOE:DI H ₂ O using at least 25 ml BOE with 25 ml DI H ₂ O in proper container
22	REMOVE SiN (OPTIONAL): <input type="checkbox"/> 3 min BOE:DI(1:1) <input type="checkbox"/> 6x DI H ₂ O Rinse <input type="checkbox"/> Dry with N ₂ on clean Texwipes

C.2 Process follower for second Mask set

Purpose	Mask	Process
Active waveguide	Nitride etch (dark field)	WG definition

Step.	Process Step
1	<p>Pre SiN SAMPLE PREPARATION (OPTIONAL):</p> <ul style="list-style-type: none"> <input type="checkbox"/> 30 sec spray with Acetone Bottle at 500 RPM <input type="checkbox"/> 30 sec Isopropyl Alcohol at 500 RPM <input type="checkbox"/> Dry with N₂ at 500 RPM <input type="checkbox"/> Dry with N₂ on clean Texwipes <input type="checkbox"/> 1 min ammonium hydroxide <input type="checkbox"/> Prepare surface with Ammonia Hydroxide:DI (1:20) for 20 sec <input type="checkbox"/> Deposit 1000 Å of SiN
2	<p>SAMPLE PREPARATION:</p> <ul style="list-style-type: none"> <input type="checkbox"/> 30 sec spray with Acetone Bottle at 500 RPM <input type="checkbox"/> 30 sec Isopropyl Alcohol at 500 RPM <input type="checkbox"/> Dry with N₂ at 500 RPM <input type="checkbox"/> Dry with N₂ on clean Texwipes
3	<p>DEHYDRATION BAKE:</p> <ul style="list-style-type: none"> <input type="checkbox"/> 1 min 110°C Hot Plate Bake
4	<p>PMGI COAT:</p> <ul style="list-style-type: none"> <input type="checkbox"/> Flood wafer with PMGI (SF-11) <input type="checkbox"/> 30 sec Spin at 4000 RPM, Ramp=200 <input type="checkbox"/> 1 min Air Bake <input type="checkbox"/> 5 min 270 °C Hot Plate Bake <input type="checkbox"/> Cool Wafer
5	<p>1813 COAT:</p> <ul style="list-style-type: none"> <input type="checkbox"/> Flood wafer with 1813 <input type="checkbox"/> 30 sec Spin at 4,000 RPM, Ramp=200 <input type="checkbox"/> 75 sec 110°C Hot Plate Bake <input type="checkbox"/> Check cleanliness of wafer backside
6	<p>EXPOSE 1813 with Contact MASK:</p> <ul style="list-style-type: none"> <input type="checkbox"/> Align <input type="checkbox"/> 50 sec Exposure (405 nm) on Mask Aligner (8.60 settings) @ 20mW/cm² optical intensity
7	<p>1813 DEVELOP:</p> <ul style="list-style-type: none"> <input type="checkbox"/> 60 sec Develop with (1:5) 351:DI H₂O at 500 RPM <input type="checkbox"/> 30 sec DI H₂O Rinse at 500 RPM <input type="checkbox"/> Rinse wafer backside with DI H₂O Bucket Rinse <input type="checkbox"/> Dry with N₂ on clean Texwipes

Step.	Process Step
8	INSPECT LITHOGRAPHY: <input type="checkbox"/> Place wafer flat towards top of microscope <input type="checkbox"/> Inspect wafer alignment with <u>yellow filter</u> on microscope <input type="checkbox"/> Check Lithography: <input type="checkbox"/> Open <input type="checkbox"/> Clean <input type="checkbox"/> Sharp Definition
9	DEEP UV (254 nm): <input type="checkbox"/> 100 sec Deep UV Exposure @ 16mW/cm ² optical intensity
10	PMGI DEVELOP: <input type="checkbox"/> 60 sec SAL 101 Develop Immersion <input type="checkbox"/> 4x bucket Rinse <input type="checkbox"/> Dry with N ₂ on clean Texwipes
11	INSPECT WAFER: <input type="checkbox"/> Inspect PMGI. Under cut should be obvious (0.5 µm)
12	DEEP UV (254 nm): <input type="checkbox"/> 100 sec Deep UV Exposure @ 16mW/cm ² optical intensity
13	PMGI DEVELOP: <input type="checkbox"/> 60 sec SAL 101 Develop Immersion <input type="checkbox"/> 4x bucket Rinse <input type="checkbox"/> Dry with N ₂ on clean Texwipes
14	INSPECT WAFER: <input type="checkbox"/> Inspect PMGI. Under cut should be obvious (0.5 µm)
15	O₂ PLASMA ASHER: <input type="checkbox"/> 4 min LFE Barrel Asher (place in front)
16	EVAPORATE Contact METAL: <input type="checkbox"/> Evaporate 1000 Å Ni
17	REMOVAL OF BASE METAL: <input type="checkbox"/> Heat 1165 to 90°C <input type="checkbox"/> Tape lift off <input type="checkbox"/> Remove remaining metal using Acetone on a petri dish <input type="checkbox"/> 20 sec spray with Acetone Bottle at 500 RPM <input type="checkbox"/> 30 sec Isopropyl Alcohol at 500 RPM <input type="checkbox"/> Dry with N ₂ at 500 RPM <input type="checkbox"/> Dry with N ₂ on clean Texwipes <input type="checkbox"/> Check backside and clean if necessary
18	REMOVE PMGI: <input type="checkbox"/> 2 min 1165 at 90°C <input type="checkbox"/> 6x DI H ₂ O Rinse <input type="checkbox"/> Dry with N ₂ on clean Texwipes

Step.	Process Step												
19	O₂ PLASMA ASHER: <input type="checkbox"/> 4 min LFE Barrel Asher												
20	SiN DEFINITION (OPTIONAL): <input type="checkbox"/> Etch using the dual chamber RIE reactor												
21	PATTERN AlGaN/GaN: <input type="checkbox"/> Place sample in sapphire carrier attached with heat pump oil <input type="checkbox"/> Place sample in ICP/RIE chamber for 5:00 (m:s) <table> <tr><td>Cl₂</td><td>32 sccm</td></tr> <tr><td>BCl₃</td><td>8 sccm</td></tr> <tr><td>Ar</td><td>5 sccm</td></tr> <tr><td>RIE</td><td>75 W</td></tr> <tr><td>ICP</td><td>500 W</td></tr> <tr><td>Pressure</td><td>2mT</td></tr> </table> <input type="checkbox"/> Remove sample and clean with Acetone and Isopropyl	Cl ₂	32 sccm	BCl ₃	8 sccm	Ar	5 sccm	RIE	75 W	ICP	500 W	Pressure	2mT
Cl ₂	32 sccm												
BCl ₃	8 sccm												
Ar	5 sccm												
RIE	75 W												
ICP	500 W												
Pressure	2mT												
22	REMOVE Ni (OPTIONAL): <input type="checkbox"/> Mix the following <table> <tr><td>HNO₃ (Nitric acid)</td><td>80 mL</td></tr> <tr><td>CH₃COOH (Acetic Acid)</td><td>80 mL</td></tr> <tr><td>2 H₂SO₄ (Sulfuric Acid)</td><td>32 mL</td></tr> <tr><td>H₂O (AS DESIRED)</td><td>0 mL</td></tr> </table> <input type="checkbox"/> 1 min rinse in above solution or until Ni dissolves <input type="checkbox"/> 3x DI H ₂ O Rinse <input type="checkbox"/> Dry with N ₂ on clean Texwipes	HNO ₃ (Nitric acid)	80 mL	CH ₃ COOH (Acetic Acid)	80 mL	2 H ₂ SO ₄ (Sulfuric Acid)	32 mL	H ₂ O (AS DESIRED)	0 mL				
HNO ₃ (Nitric acid)	80 mL												
CH ₃ COOH (Acetic Acid)	80 mL												
2 H ₂ SO ₄ (Sulfuric Acid)	32 mL												
H ₂ O (AS DESIRED)	0 mL												
23	REMOVE SiN (OPTIONAL): <input type="checkbox"/> 3 min BOE:DI(1:1) <input type="checkbox"/> 6x DI H ₂ O Rinse <input type="checkbox"/> Dry with N ₂ on clean Texwipes												

Purpose	Mask	Process
Nitride process	Top Contact	Top Contact

Step #	Process Step
1	SAMPLE PREPARATION: <ul style="list-style-type: none"> <input type="checkbox"/> 3 min BOE:DI(1:1) <input type="checkbox"/> 6x DI H₂O Rinse <input type="checkbox"/> Dry with N₂ on clean Texwipes <input type="checkbox"/> 30 sec spray with Acetone Bottle at 500 RPM <input type="checkbox"/> 30 sec Isopropyl Alcohol at 500 RPM <input type="checkbox"/> Dry with N₂ at 500 RPM <input type="checkbox"/> Dry with N₂ on clean Texwipes
2	DEHYDRATION BAKE: <ul style="list-style-type: none"> <input type="checkbox"/> 1 min 110°C Hot Plate Bake
3	PMGI COAT: <ul style="list-style-type: none"> <input type="checkbox"/> Flood wafer with PMGI (SF-11) <input type="checkbox"/> 30 sec Spin at 4000 RPM, Ramp=200 <input type="checkbox"/> 1 min Air Bake <input type="checkbox"/> 5 min 270 °C Hot Plate Bake <input type="checkbox"/> Cool Wafer
4	1813 COAT: <ul style="list-style-type: none"> <input type="checkbox"/> Flood wafer with 1813 <input type="checkbox"/> 30 sec Spin at 4,000 RPM, Ramp=200 <input type="checkbox"/> 75 sec 110°C Hot Plate Bake <input type="checkbox"/> Check cleanliness of wafer backside
5	EXPOSE 1813 with Contact MASK: <ul style="list-style-type: none"> <input type="checkbox"/> Align (very critical) <input type="checkbox"/> 40 sec Exposure (405 nm) on Mask Aligner (90 settings) @ 20mW/cm² optical intensity
6	1813 DEVELOP: <ul style="list-style-type: none"> <input type="checkbox"/> 50 sec Develop with (1:5) 351:DI H₂O at 500 RPM <input type="checkbox"/> 30 sec DI H₂O Rinse at 500 RPM <input type="checkbox"/> Rinse wafer backside with DI H₂O Bucket Rinse <input type="checkbox"/> Dry with N₂ on clean Texwipes
7	INSPECT LITHOGRAPHY: <ul style="list-style-type: none"> <input type="checkbox"/> Place wafer flat towards top of microscope <input type="checkbox"/> Inspect wafer alignment with <u>yellow filter</u> on microscope <input type="checkbox"/> Check Lithography: <input type="checkbox"/> Open <input type="checkbox"/> Clean <input type="checkbox"/> Sharp Definition
8	DEEP UV (254 nm): <ul style="list-style-type: none"> <input type="checkbox"/> 200 sec Deep UV Exposure @ 16mW/cm² optical intensity

Step #	Process Step
9	PMGI DEVELOP: <ul style="list-style-type: none"> <input type="checkbox"/> 50 sec 101 Develop @ 500 rpm <input type="checkbox"/> 40 sec DI @ 500 rpm <input type="checkbox"/> Rinse wafer backside with DI H₂O Bucket Rinse <input type="checkbox"/> Dry with N₂ on clean Texwipes
10	INSPECT WAFER: <ul style="list-style-type: none"> <input type="checkbox"/> Inspect PMGI. Under cut should be obvious (0.5 μm)
11	O₂ PLASMA ASHER: <ul style="list-style-type: none"> <input type="checkbox"/> 4 min LFE Barrel Asher (place in front)
12	EVAPORATE Contact METAL: <ul style="list-style-type: none"> <input type="checkbox"/> Pre-metal dip on Amonium Hydroxide:DI (1:4) for 1 min <input type="checkbox"/> Evaporate 100 Å/ 1000 Å/ 500 Å/200 Å Ti/Al/Ti/Au (Ti on AlGaN surface)
13	REMOVAL OF BASE METAL: <ul style="list-style-type: none"> <input type="checkbox"/> Heat 1165 to 90°C <input type="checkbox"/> Tape lift off <input type="checkbox"/> Remove remaining metal using Acetone on a petri dish <input type="checkbox"/> 20 sec spray with Acetone Bottle at 500 RPM <input type="checkbox"/> 30 sec Isopropyl Alcohol at 500 RPM <input type="checkbox"/> Dry with N₂ at 500 RPM <input type="checkbox"/> Dry with N₂ on clean Texwipes <input type="checkbox"/> Check backside and clean if necessary
14	REMOVE PMGI: <ul style="list-style-type: none"> <input type="checkbox"/> 2 min 1165 at 90°C <input type="checkbox"/> 6x DI H₂O Rinse <input type="checkbox"/> Dry with N₂ on clean Texwipes
15	O₂ PLASMA ASHER: <ul style="list-style-type: none"> <input type="checkbox"/> 4 min LFE Barrel Asher

Purpose	Mask	Process
Nitride process	Mesa Isolation	Trench for Contact Pad

Step #	Process Step
	CLEAN SAMPLE: <input type="checkbox"/> 15 sec spray with Acetone Bottle at 500 RPM <input type="checkbox"/> 15 sec Isopropyl Alcohol at 500 RPM
	DEHYDRATION BAKE: <input type="checkbox"/> 1 min 110°C Hot Plate Bake
	PMGI COAT #1: <input type="checkbox"/> Flood wafer with PMGI (SF-11) <input type="checkbox"/> 30 sec Spin at 4000 RPM, Ramp=200 <input type="checkbox"/> 1 min Air Bake <input type="checkbox"/> 5 min 270 °C Hot Plate Bake <input type="checkbox"/> Cool Wafer
	PMGI COAT #2: <input type="checkbox"/> Flood wafer with PMGI (SF-11) <input type="checkbox"/> 30 sec Spin at 4000 RPM, Ramp=200 <input type="checkbox"/> 1 min Air Bake <input type="checkbox"/> 5 min 270 °C Hot Plate Bake <input type="checkbox"/> Cool Wafer
	1813 COAT: <input type="checkbox"/> Flood wafer with 1813 <input type="checkbox"/> 30 sec Spin at 4,000 RPM, Ramp=200 <input type="checkbox"/> 75 sec 110°C Hot Plate Bake <input type="checkbox"/> Check cleanliness of wafer backside
	EXPOSE 1813 with Mesa Isolation MASK: <input type="checkbox"/> Align <input type="checkbox"/> 50 sec Exposure (405 nm) on Mask Aligner (90 settings) <i>@ 20mW/cm² optical intensity</i>
	1813 DEVELOP: <input type="checkbox"/> 50 sec Develop with (1:5) 351:DI H ₂ O at 500 RPM <input type="checkbox"/> 30 sec DI H ₂ O Rinse at 500 RPM <input type="checkbox"/> Rinse wafer backside with DI H ₂ O Bucket Rinse <input type="checkbox"/> Dry with N ₂ on clean Texwipes
	INSPECT LITHOGRAPHY: <input type="checkbox"/> Place wafer flat towards top of microscope <input type="checkbox"/> Inspect wafer alignment with yellow filter on microscope <input type="checkbox"/> Check Lithography : <input type="checkbox"/> Open <input type="checkbox"/> Clean <input type="checkbox"/> Sharp Definition
	DEEP UV (254 nm): <input type="checkbox"/> 250 sec Deep UV Exposure @ 16mW/cm ² optical intensity

Step #	Process Step
	PMGI DEVELOP: <input type="checkbox"/> 50 sec Develop with SAL 101 @ 500 rpm <input type="checkbox"/> 40 sec DI @ 500 rpm <input type="checkbox"/> Bucket Rinse with DI H ₂ O <input type="checkbox"/> Dry with N ₂ on clean Texwipes
	DEEP UV (254 nm): <input type="checkbox"/> 250 sec Deep UV Exposure @ 16mW/cm ² optical intensity
	PMGI DEVELOP: <input type="checkbox"/> 50 sec Develop with SAL 101 @ 500 rpm <input type="checkbox"/> 40 sec DI @ 500 rpm <input type="checkbox"/> Bucket Rinse with DI H ₂ O <input type="checkbox"/> Dry with N ₂ on clean Texwipes
	INSPECT WAFER: <input type="checkbox"/> Inspect PMGI.
	O₂ PLASMA ASHER: <input type="checkbox"/> 4 min LFE Barrel Asher (place in front)
	PATTERN AlGaN/GaN : <input type="checkbox"/> Place sample in ICP/RIE chamber for 3:15 (m:s) Cl ₂ 32 sccm BCl ₃ 8 sccm Ar 5 sccm RIE 75 W ICP 500 W Pressure 2mT
	REMOVE 1813: <input type="checkbox"/> Heat 1165 to 90°C <input type="checkbox"/> 15 sec Acetone at 500 RPM <input type="checkbox"/> 15 sec Isopropyl alcohol at 500 RPM <input type="checkbox"/> Dry with N ₂ on clean Texwipes
	REMOVE PMGI: <input type="checkbox"/> 2 min 1165 at 90°C <input type="checkbox"/> 6x DI H ₂ O Rinse <input type="checkbox"/> Dry with N ₂ on clean Texwipes
	O₂ PLASMA ASHER: <input type="checkbox"/> 4 min LFE Barrel Asher

Purpose	Mask	Process
Nitride process	Contacts	Contact

Step #	Process Step
	DEHYDRATION BAKE: <input type="checkbox"/> 1 min 110°C Hot Plate Bake
	PMGI COAT #1: <input type="checkbox"/> Flood wafer with PMGI (SF-11) <input type="checkbox"/> 30 sec Spin at 4000 RPM, Ramp=200 <input type="checkbox"/> 1 min Air Bake <input type="checkbox"/> 5 min 270 °C Hot Plate Bake <input type="checkbox"/> Cool Wafer
	PMGI COAT #2: <input type="checkbox"/> Flood wafer with PMGI (SF-11) <input type="checkbox"/> 30 sec Spin at 4000 RPM, Ramp=200 <input type="checkbox"/> 1 min Air Bake <input type="checkbox"/> 5 min 270 °C Hot Plate Bake <input type="checkbox"/> Cool Wafer
	1818 COAT: <input type="checkbox"/> Flood wafer with 1818 <input type="checkbox"/> 30 sec Spin at 4,000 RPM, Ramp=200 <input type="checkbox"/> 75 sec 110°C Hot Plate Bake <input type="checkbox"/> Check cleanliness of wafer backside
	EXPOSE 1818 with Top and Bottom Contact MASK: <input type="checkbox"/> Align <input type="checkbox"/> 70 sec Exposure (405 nm) on Mask Aligner (90 settings) @ 20mW/cm ² optical intensity
	1818 DEVELOP: <input type="checkbox"/> 50 sec Develop with (1:5) 351:DI H ₂ O at 500 RPM <input type="checkbox"/> 30 sec DI H ₂ O Rinse at 500 RPM <input type="checkbox"/> Rinse wafer backside with DI H ₂ O Bucket Rinse <input type="checkbox"/> Dry with N ₂ on clean Texwipes
	INSPECT LITHOGRAPHY: <input type="checkbox"/> Place wafer flat towards top of microscope <input type="checkbox"/> Inspect wafer alignment with yellow filter on microscope <input type="checkbox"/> Check Lithography: <input type="checkbox"/> Open <input type="checkbox"/> Clean <input type="checkbox"/> Sharp Definition
	DEEP UV (254 nm): <input type="checkbox"/> 200 sec Deep UV Exposure @ 16mW/cm ² optical intensity
	PMGI DEVELOP: <input type="checkbox"/> 50 sec Develop with SAL 101 @ 500 rpm <input type="checkbox"/> 40 sec DI @ 500 rpm <input type="checkbox"/> Bucket Rinse with DI H ₂ O <input type="checkbox"/> Dry with N ₂ on clean Texwipes

Step #	Process Step
	DEEP UV (254 nm): <input type="checkbox"/> 200 sec Deep UV Exposure @ 16mW/cm ² optical intensity
	PMGI DEVELOP: <input type="checkbox"/> 50 sec Develop with SAL 101 @ 500 rpm <input type="checkbox"/> 40 sec DI @ 500 rpm <input type="checkbox"/> Bucket Rinse with DI H ₂ O <input type="checkbox"/> Dry with N ₂ on clean Texwipes
	INSPECT WAFER: <input type="checkbox"/> Inspect PMGI. Under cut should be obvious (0.5 μm)
	O₂ PLASMA ASHER: <input type="checkbox"/> 4 min LFE Barrel Asher (place in front)
	PRE-METAL DIP: <input type="checkbox"/> 1 min Amonium hydroxide:DI (1:4) <input type="checkbox"/> 4x DI full Bucket Rinse <input type="checkbox"/> Dry with N ₂ on clean Texwipes
	EVAPORATE Contact METAL: <input type="checkbox"/> Evaporate Ti/Al/Ti/Au (100 Å/ 1000 Å/500 Å/200 Å Ti on surface)
	REMOVAL OF BASE METAL: <input type="checkbox"/> Heat 1165 to 90°C <input type="checkbox"/> Tape lift off <input type="checkbox"/> Remove remaining metal using Acetone on a petri dish <input type="checkbox"/> 20 sec spray with Acetone Bottle at 500 RPM <input type="checkbox"/> 30 sec Isopropyl Alcohol at 500 RPM <input type="checkbox"/> Dry with N ₂ at 500 RPM <input type="checkbox"/> Dry with N ₂ on clean Texwipes <input type="checkbox"/> Check backside and clean if necessary
	REMOVE PMGI: <input type="checkbox"/> 2 min 1165 at 90°C <input type="checkbox"/> 6x DI H ₂ O Rinse <input type="checkbox"/> Dry with N ₂ on clean Texwipes
	O₂ PLASMA ASHER: <input type="checkbox"/> 4 min LFE Barrel Asher
	ALLOYING: <input type="checkbox"/> Set n2 flow to 10 mm <input type="checkbox"/> Run RTA at 900 C FOR 30 sec with no sample (dummy run) <input type="checkbox"/> Place sample on RTA and purge with N2 for 5 min <input type="checkbox"/> Run RTA at 900 C FOR 30 sec <input type="checkbox"/> Let RTA cool to ~250 C and retrieve

Purpose

Nitride process

Mask

Top Contact PMGI VIA

Process

Contact Opening and Reflow

Step #	Process Step
	DEHYDRATION BAKE: <input type="checkbox"/> 1 min 110°C Hot Plate Bake
	PMGI COAT #1: <input type="checkbox"/> Flood wafer with PMGI (SF-11) <input type="checkbox"/> 30 sec Spin at 4000 RPM, Ramp=200 <input type="checkbox"/> 1 min Air Bake <input type="checkbox"/> 5 min 270 °C Hot Plate Bake <input type="checkbox"/> Cool Wafer
	PMGI COAT #2: <input type="checkbox"/> Flood wafer with PMGI (SF-11) <input type="checkbox"/> 30 sec Spin at 4000 RPM, Ramp=200 <input type="checkbox"/> 1 min Air Bake <input type="checkbox"/> 5 min 270 °C Hot Plate Bake <input type="checkbox"/> Cool Wafer
	PMGI COAT #3: <input type="checkbox"/> Flood wafer with PMGI (SF-11) <input type="checkbox"/> 30 sec Spin at 4000 RPM, Ramp=200 <input type="checkbox"/> 1 min Air Bake <input type="checkbox"/> 5 min 270 °C Hot Plate Bake <input type="checkbox"/> Cool Wafer
	1813 COAT: <input type="checkbox"/> Flood wafer with 1813 <input type="checkbox"/> 30 sec Spin at 4,000 RPM, Ramp=200 <input type="checkbox"/> 75 sec 110°C Hot Plate Bake <input type="checkbox"/> Check cleanliness of wafer backside
	EXPOSE 1813 with Top Contact MASK: <input type="checkbox"/> Align <input type="checkbox"/> 50 sec Exposure (405 nm) on Mask Aligner (90 settings) @ 20mW/cm ² optical intensity
	EXPOSE 1813 with PMGI VIA MASK: <input type="checkbox"/> Align <input type="checkbox"/> 50 sec Exposure (405 nm) on Mask Aligner (90 settings) @ 20mW/cm ² optical intensity
	1813 DEVELOP: <input type="checkbox"/> 40 sec Develop with (1:5) 351:DI H ₂ O at 500 RPM <input type="checkbox"/> 30 sec DI H ₂ O Rinse at 500 RPM <input type="checkbox"/> Rinse wafer backside with DI H ₂ O Bucket Rinse <input type="checkbox"/> Dry with N ₂ on clean Texwipes

Step #	Process Step
	<p>INSPECT LITHOGRAPHY:</p> <p><input type="checkbox"/> Place wafer flat towards top of microscope <input type="checkbox"/> Inspect wafer alignment with yellow filter on microscope <input type="checkbox"/> Check Lithography: <input type="checkbox"/> Open <input type="checkbox"/> Clean <input type="checkbox"/> Sharp Definition</p>
	<p>DEEP UV (254 nm):</p> <p><input type="checkbox"/> 200 sec Deep UV Exposure @ 16mW/cm² optical intensity</p>
	<p>PMGI DEVELOP:</p> <p><input type="checkbox"/> 60 sec 101 Develop Immersion <input type="checkbox"/> 4X Bucket Rinse with DI H₂O <input type="checkbox"/> Dry with N₂ on clean Texwipes</p>
	<p>DEEP UV (254 nm):</p> <p><input type="checkbox"/> 200 sec Deep UV Exposure @ 16mW/cm² optical intensity</p>
	<p>PMGI DEVELOP:</p> <p><input type="checkbox"/> 60 sec 101 Develop Immersion <input type="checkbox"/> 4X Bucket Rinse with DI H₂O <input type="checkbox"/> Dry with N₂ on clean Texwipes</p>
	<p>INSPECT WAFER:</p> <p><input type="checkbox"/> Inspect PMGI. Under cut should be obvious (0.5 μm)</p>
	<p>Remove 1813:</p> <p><input type="checkbox"/> 30 sec spray with Acetone Bottle at 500 RPM <input type="checkbox"/> 30 sec Isopropyl Alcohol at 500 RPM <input type="checkbox"/> 30 sec H₂O at 500 RPM <input type="checkbox"/> Dry with N₂ at 500 RPM <input type="checkbox"/> Dry with N₂ on clean Texwipes</p>
	<p>O₂ PLASMA ASHER:</p> <p><input type="checkbox"/> 4 min LFE Barrel Asher (place in front)</p>
	<p>REFLOW:</p> <p><input type="checkbox"/> Place in 250°C oven <input type="checkbox"/> Close door and start timer <input type="checkbox"/> Heat for 65 sec <input type="checkbox"/> Remove from oven <input type="checkbox"/> Cool wafer</p>
	<p>INSPECT WAFER:</p> <p><input type="checkbox"/> Inspect PMGI.</p>

Purpose	Mask	Process
Nitride process	Bridge	Bridge

Init.	Process Step
	DEHYDRATION BAKE: <input type="checkbox"/> 1 min 110°C Hot Plate Bake
	1813 COAT: <input type="checkbox"/> Flood wafer with 1813 <input type="checkbox"/> 30 sec Spin at 4,000 RPM, Ramp=200 <input type="checkbox"/> 75 sec 110°C Hot Plate Bake <input type="checkbox"/> Check cleanliness of wafer backside
	EXPOSE 1813 with Bridge MASK: <input type="checkbox"/> Align <input type="checkbox"/> 50 sec Exposure (405 nm) on Mask Aligner (90 settings) (@ 20mW/cm ² optical intensity)
	1813 DEVELOP: <input type="checkbox"/> 40 sec Develop with (1:5) 351:DI H ₂ O at 500 RPM <input type="checkbox"/> 30 sec DI H ₂ O Rinse at 500 RPM <input type="checkbox"/> Rinse wafer backside with DI H ₂ O Bucket Rinse <input type="checkbox"/> Dry with N ₂ on clean Texwipes
	INSPECT LITHOGRAPHY: <input type="checkbox"/> Place wafer flat towards top of microscope <input type="checkbox"/> Inspect wafer alignment with yellow filter on microscope <input type="checkbox"/> Check Lithography: <input type="checkbox"/> Open <input type="checkbox"/> Clean <input type="checkbox"/> Sharp Definition
	EVAPORATE Bridge METAL: <input type="checkbox"/> Evaporate 300 Å/ 4000 Å Ti/Au (Ti on surface, Au on top of Ti)
	REMOVAL OF BASE METAL: <input type="checkbox"/> Tape lift off <input type="checkbox"/> Remove remaining metal using Acetone on a petri dish <input type="checkbox"/> 20 sec spray with Acetone Bottle at 500 RPM <input type="checkbox"/> 30 sec Isopropyl Alcohol at 500 RPM <input type="checkbox"/> 30 sec DI water at 500 RPM <input type="checkbox"/> Dry with N ₂ at 500 RPM <input type="checkbox"/> Dry with N ₂ on clean Texwipes <input type="checkbox"/> Check backside and clean if necessary
	DEHYDRATION BAKE: <input type="checkbox"/> 1 min 110°C Hot Plate Bake
	1818 COAT & SLICE: <input type="checkbox"/> Flood wafer with 1818 <input type="checkbox"/> 30 sec Spin at 4,000 RPM, Ramp=200 <input type="checkbox"/> 75 sec 110°C Hot Plate Bake <input type="checkbox"/> Check cleanliness of wafer backside <input type="checkbox"/> Saw the devices

Init.	Process Step
	REMOVE PMGI: <input type="checkbox"/> Heat 1165 to 90°C <input type="checkbox"/> 2 min 1165 at 90°C <input type="checkbox"/> 6x DI H ₂ O Rinse <input type="checkbox"/> Dry with N ₂ on clean Texwipes
	INSPECT WAFER: <input type="checkbox"/> Inspect

C.3 Process follower for Third Mask set

Purpose	Mask	Process
Active waveguide	Nitride etch (dark field)	WG definition

Step	Process Step
	SAMPLE PREPARATION: <ul style="list-style-type: none"> <input type="checkbox"/> 30 sec spray with Acetone Bottle at 500 RPM <input type="checkbox"/> 30 sec Isopropyl Alcohol at 500 RPM <input type="checkbox"/> 1 min ammonium hydroxide
	DEHYDRATION BAKE: <ul style="list-style-type: none"> <input type="checkbox"/> 1 min 110°C Hot Plate Bake
	PMGI COAT: <ul style="list-style-type: none"> <input type="checkbox"/> Flood wafer with PMGI (SF-08) <input type="checkbox"/> 30 sec Spin at 4000 RPM, Ramp=200 <input type="checkbox"/> 1 min Air Bake <input type="checkbox"/> 5 min 270 °C Hot Plate Bake <input type="checkbox"/> Cool Wafer
	1805 COAT: <ul style="list-style-type: none"> <input type="checkbox"/> Flood wafer with 1805 <input type="checkbox"/> 30 sec Spin at 4,000 RPM, Ramp=200 <input type="checkbox"/> 75 sec 110°C Hot Plate Bake <input type="checkbox"/> Check cleanliness of wafer backside
	EXPOSE 1805 with Contact MASK <ul style="list-style-type: none"> <input type="checkbox"/> Align <input type="checkbox"/> 14.0 sec Exposure (405 nm) on Mask Aligner (8.60 settings) @ 20mW/cm² optical intensity
	1805 DEVELOP: <ul style="list-style-type: none"> <input type="checkbox"/> 60 sec Develop with (1:5) 351:DI H₂O at 500 RPM <input type="checkbox"/> 30 sec DI H₂O Rinse at 500 RPM <input type="checkbox"/> Rinse wafer backside with DI H₂O Bucket Rinse <input type="checkbox"/> Dry with N₂ on clean Texwipes
	INSPECT LITHOGRAPHY: <ul style="list-style-type: none"> <input type="checkbox"/> Place wafer flat towards top of microscope <input type="checkbox"/> Inspect wafer alignment with yellow filter on microscope <input type="checkbox"/> Check Lithography: <input type="checkbox"/> Open <input type="checkbox"/> Clean <input type="checkbox"/> Sharp Definition
	DEEP UV (254 nm): <ul style="list-style-type: none"> <input type="checkbox"/> 95 sec Deep UV Exposure @ 16mW/cm² optical intensity
	PMGI DEVELOP: <ul style="list-style-type: none"> <input type="checkbox"/> 50 sec SAL 101 @ 500 rpm <input type="checkbox"/> Back side Rinse <input type="checkbox"/> Dry with N₂ on clean Texwipes

Step	Process Step
	INSPECT WAFER: <input type="checkbox"/> Inspect PMGI with yellow filter on microscope <input type="checkbox"/> Check Lithography: <input type="checkbox"/> Open <input type="checkbox"/> Clean
	O₂ PLASMA ASHER: <input type="checkbox"/> 4 min LFE Barrel Asher (place flat with a scrap wafer underneath)
	EVAPORATE Contact METAL: <input type="checkbox"/> Pre-metal dip on Ammonium Hydroxide:DI (1:4) for 1 min <input type="checkbox"/> Evaporate 250 Å Ti/900 Å Ni
	REMOVAL OF BASE METAL: <input type="checkbox"/> Heat 1165 to 90°C <input type="checkbox"/> Tape lift off <input type="checkbox"/> Remove remaining metal using Acetone on a petri dish <input type="checkbox"/> 20 sec spray with Acetone Bottle at 500 RPM <input type="checkbox"/> 30 sec Isopropyl Alcohol at 500 RPM <input type="checkbox"/> Dry with N ₂ at 500 RPM <input type="checkbox"/> Dry with N ₂ on clean Texwipes <input type="checkbox"/> Check backside and clean if necessary
	REMOVE PMGI: <input type="checkbox"/> 2 min 1165 at 90°C <input type="checkbox"/> 6x DI H ₂ O Rinse <input type="checkbox"/> Dry with N ₂ on clean Texwipes
	O₂ PLASMA ASHER: <input type="checkbox"/> 4 min LFE Barrel Asher <input type="checkbox"/> Measure metal mask height _____
	PATTERN AlGaN/GaN: <input type="checkbox"/> Place sample in sapphire carrier attached with heat pump oil <input type="checkbox"/> Place sample in ICP/RIE chamber for 5:00 (m:s) Cl ₂ 32 sccm BCl ₃ 8 sccm Ar 5 sccm RIE 75 W ICP 500 W Pressure 2mT <input type="checkbox"/> Remove sample and clean with Acetone and Isopropyl
	REMOVE SiN: <input type="checkbox"/> 3 min BOE:DI (1:1) <input type="checkbox"/> 6x DI H ₂ O Rinse <input type="checkbox"/> Dry with N ₂ on clean Texwipes

Purpose	Mask	Process
Nitride process	Mesa Isolation	Trench for Contact Pad

Step #	Process Step
	CLEAN SAMPLE: <input type="checkbox"/> 15 sec spray with Acetone Bottle at 500 RPM <input type="checkbox"/> 15 sec Isopropyl Alcohol at 500 RPM
	DEHYDRATION BAKE: <input type="checkbox"/> 1 min 110°C Hot Plate Bake
	PMGI COAT #1: <input type="checkbox"/> Flood wafer with PMGI (SF-11) <input type="checkbox"/> 30 sec Spin at 4000 RPM, Ramp=200 <input type="checkbox"/> 1 min Air Bake <input type="checkbox"/> 5 min 270 °C Hot Plate Bake <input type="checkbox"/> Cool Wafer
	PMGI COAT #2: <input type="checkbox"/> Flood wafer with PMGI (SF-11) <input type="checkbox"/> 30 sec Spin at 4000 RPM, Ramp=200 <input type="checkbox"/> 1 min Air Bake <input type="checkbox"/> 5 min 270 °C Hot Plate Bake <input type="checkbox"/> Cool Wafer
	1813 COAT: <input type="checkbox"/> Flood wafer with 1813 <input type="checkbox"/> 30 sec Spin at 4,000 RPM, Ramp=200 <input type="checkbox"/> 75 sec 110°C Hot Plate Bake <input type="checkbox"/> Check cleanliness of wafer backside
	EXPOSE 1813 with Mesa Isolation MASK: <input type="checkbox"/> Align <input type="checkbox"/> 50 sec Exposure (405 nm) on Mask Aligner (90 settings) <i>@ 20mW/cm² optical intensity</i>
	1813 DEVELOP: <input type="checkbox"/> 50 sec Develop with (1:5) 351:DI H ₂ O at 500 RPM <input type="checkbox"/> 30 sec DI H ₂ O Rinse at 500 RPM <input type="checkbox"/> Rinse wafer backside with DI H ₂ O Bucket Rinse <input type="checkbox"/> Dry with N ₂ on clean Texwipes
	INSPECT LITHOGRAPHY: <input type="checkbox"/> Place wafer flat towards top of microscope <input type="checkbox"/> Inspect wafer alignment with yellow filter on microscope <input type="checkbox"/> Check Lithography: <input type="checkbox"/> Open <input type="checkbox"/> Clean <input type="checkbox"/> Sharp Definition
	DEEP UV #1 (254 nm): <input type="checkbox"/> 250 sec Deep UV Exposure @ 16mW/cm ² optical intensity

Step #	Process Step
	PMGI DEVELOP #1: <input type="checkbox"/> 50 sec Develop with SAL 101 @ 500 rpm <input type="checkbox"/> 40 sec DI @ 500 rpm <input type="checkbox"/> Bucket Rinse with DI H ₂ O <input type="checkbox"/> Dry with N ₂ on clean Texwipes
	DEEP UV #2 (254 nm): <input type="checkbox"/> 250 sec Deep UV Exposure @ 16mW/cm ² optical intensity
	PMGI DEVELOP #2: <input type="checkbox"/> 50 sec Develop with SAL 101 @ 500 rpm <input type="checkbox"/> 40 sec DI @ 500 rpm <input type="checkbox"/> Bucket Rinse with DI H ₂ O <input type="checkbox"/> Dry with N ₂ on clean Texwipes
	INSPECT WAFER: <input type="checkbox"/> Inspect PMGI. <input type="checkbox"/> Measure step height _____
	O₂ PLASMA ASHER: <input type="checkbox"/> 4 min LFE Barrel Asher
	PATTERN AlGaN/GaN: <input type="checkbox"/> Place sample in ICP/RIE chamber for 3:15 (m:s) Cl ₂ 32 sccm BCl ₃ 8 sccm Ar 5 sccm RIE 75 W ICP 500 W Pressure 2 mT
	REMOVE 1813: <input type="checkbox"/> Heat 1165 to 90°C <input type="checkbox"/> 15 sec Acetone at 500 RPM <input type="checkbox"/> 15 sec Isopropyl alcohol at 500 RPM <input type="checkbox"/> Dry with N ₂ on clean Texwipes
	REMOVE PMGI: <input type="checkbox"/> 2 min 1165 at 90°C <input type="checkbox"/> 6x DI H ₂ O Rinse <input type="checkbox"/> Dry with N ₂ on clean Texwipes
	O₂ PLASMA ASHER: <input type="checkbox"/> 4 min LFE Barrel Asher

Purpose	Mask	Process
Nitride process	Bottom Contacts	Contacts
	Top Contacts	

Step #	Process Step
	DEHYDRATION BAKE: <input type="checkbox"/> 1 min 110°C Hot Plate Bake
	PMGI COAT #1: <input type="checkbox"/> Flood wafer with PMGI (SF-11) <input type="checkbox"/> 30 sec Spin at 4000 RPM, Ramp=200 <input type="checkbox"/> 1 min Air Bake <input type="checkbox"/> 5 min 270 °C Hot Plate Bake <input type="checkbox"/> Cool Wafer
	PMGI COAT #2: <input type="checkbox"/> Flood wafer with PMGI (SF-11) <input type="checkbox"/> 30 sec Spin at 4000 RPM, Ramp=200 <input type="checkbox"/> 1 min Air Bake <input type="checkbox"/> 5 min 270 °C Hot Plate Bake <input type="checkbox"/> Cool Wafer
	1818 COAT: <input type="checkbox"/> Flood wafer with 1818 <input type="checkbox"/> 30 sec Spin at 4,000 RPM, Ramp=200 <input type="checkbox"/> 75 sec 110°C Hot Plate Bake <input type="checkbox"/> Check cleanliness of wafer backside
	EXPOSE 1818 with top & Bottom Contact MASK: <input type="checkbox"/> Align <input type="checkbox"/> 70 sec Exposure (405 nm) on Mask Aligner (90 settings) @ 20mW/cm ² optical intensity
	1818 DEVELOP: <input type="checkbox"/> 50 sec Develop with (1:5) 351:DI H ₂ O at 500 RPM <input type="checkbox"/> 30 sec DI H ₂ O Rinse at 500 RPM <input type="checkbox"/> Rinse wafer backside with DI H ₂ O Bucket Rinse <input type="checkbox"/> Dry with N ₂ on clean Texwipes
	INSPECT LITHOGRAPHY: <input type="checkbox"/> Place wafer flat towards top of microscope <input type="checkbox"/> Inspect wafer alignment with yellow filter on microscope <input type="checkbox"/> Check Lithography: <input type="checkbox"/> Open <input type="checkbox"/> Clean <input type="checkbox"/> Sharp Definition
	DEEP UV #1 (254 nm): <input type="checkbox"/> 250 sec Deep UV Exposure @ 16mW/cm ² optical intensity

Step #	Process Step
	PMGI DEVELOP #1: <input type="checkbox"/> 50 sec Develop with SAL 101 @ 500 rpm <input type="checkbox"/> 40 sec DI @ 500 rpm <input type="checkbox"/> Bucket Rinse with DI H ₂ O <input type="checkbox"/> Dry with N ₂ on clean Texwipes
	DEEP UV #2(254 nm): <input type="checkbox"/> 250 sec Deep UV Exposure @ 16mW/cm ² optical intensity
	PMGI DEVELOP #2: <input type="checkbox"/> 50 sec Develop with SAL 101 @ 500 rpm <input type="checkbox"/> 40 sec DI @ 500 rpm <input type="checkbox"/> Bucket Rinse with DI H ₂ O <input type="checkbox"/> Dry with N ₂ on clean Texwipes
	INSPECT WAFER: <input type="checkbox"/> Inspect PMGI. Under cut should be obvious (0.5 μm)
	O₂ PLASMA ASHER: <input type="checkbox"/> 4 min LFE Barrel Asher (place in front)
	PRE-METAL DIP: <input type="checkbox"/> 1 min Ammonium hydroxide:DI (1:4) <input type="checkbox"/> 4x DI full Bucket Rinse <input type="checkbox"/> Dry with N ₂ on clean Texwipes
	EVAPORATE Contact METAL: <input type="checkbox"/> Evaporate Ti/Al/Ti/Au (100 Å/ 1000 Å/500 Å/200 Å Ti on surface)
	REMOVAL OF BASE METAL: <input type="checkbox"/> Heat 1165 to 90°C <input type="checkbox"/> Tape lift off <input type="checkbox"/> Remove remaining metal using Acetone on a petri dish <input type="checkbox"/> 20 sec spray with Acetone Bottle at 500 RPM <input type="checkbox"/> 30 sec Isopropyl Alcohol at 500 RPM <input type="checkbox"/> Dry with N ₂ at 500 RPM <input type="checkbox"/> Dry with N ₂ on clean Texwipes <input type="checkbox"/> Check backside and clean if necessary
	REMOVE PMGI: <input type="checkbox"/> 2 min 1165 at 90°C <input type="checkbox"/> 6x DI H ₂ O Rinse <input type="checkbox"/> Dry with N ₂ on clean Texwipes
	O₂ PLASMA ASHER: <input type="checkbox"/> 4 min LFE Barrel Asher
	ALLOYING: <input type="checkbox"/> Set n2 flow to 10 mm <input type="checkbox"/> Run RTA at 750 C FOR 30 sec with no sample (dummy run) <input type="checkbox"/> Place sample on RTA and purge with N2 for 5 min <input type="checkbox"/> Run RTA at 750 C FOR 30 sec <input type="checkbox"/> Let RTA cool to ~250 C and retrieve

Purpose

Nitride process

Mask

Top Contact PMGI VIA

Process

Contact Opening and Reflow

Step #	Process Step
	DEHYDRATION BAKE: <input type="checkbox"/> 1 min 110°C Hot Plate Bake
	PMGI COAT #1: <input type="checkbox"/> Flood wafer with PMGI (SF-11) <input type="checkbox"/> 30 sec Spin at 4000 RPM, Ramp=200 <input type="checkbox"/> 1 min Air Bake <input type="checkbox"/> 5 min 270 °C Hot Plate Bake <input type="checkbox"/> Cool Wafer
	PMGI COAT #2: <input type="checkbox"/> Flood wafer with PMGI (SF-11) <input type="checkbox"/> 30 sec Spin at 4000 RPM, Ramp=200 <input type="checkbox"/> 1 min Air Bake <input type="checkbox"/> 5 min 270 °C Hot Plate Bake <input type="checkbox"/> Cool Wafer
	PMGI COAT #3: <input type="checkbox"/> Flood wafer with PMGI (SF-11) <input type="checkbox"/> 30 sec Spin at 4000 RPM, Ramp=200 <input type="checkbox"/> 1 min Air Bake <input type="checkbox"/> 5 min 270 °C Hot Plate Bake <input type="checkbox"/> Cool Wafer
	1813 COAT: <input type="checkbox"/> Flood wafer with 1813 <input type="checkbox"/> 30 sec Spin at 4,000 RPM, Ramp=200 <input type="checkbox"/> 75 sec 110°C Hot Plate Bake <input type="checkbox"/> Check cleanliness of wafer backside
	EXPOSE 1813 with Top Contact MASK: <input type="checkbox"/> Align <input type="checkbox"/> 50 sec Exposure (405 nm) on Mask Aligner (90 settings) @ 20mW/cm ² optical intensity
	EXPOSE 1813 with PMGI VIA MASK: <input type="checkbox"/> Align <input type="checkbox"/> 50 sec Exposure (405 nm) on Mask Aligner (90 settings) @ 20mW/cm ² optical intensity
	1813 DEVELOP: <input type="checkbox"/> 40 sec Develop with (1:5) 351:DI H ₂ O at 500 RPM <input type="checkbox"/> 30 sec DI H ₂ O Rinse at 500 RPM <input type="checkbox"/> Rinse wafer backside with DI H ₂ O Bucket Rinse <input type="checkbox"/> Dry with N ₂ on clean Texwipes

Step #	Process Step
	INSPECT LITHOGRAPHY: <input type="checkbox"/> Place wafer flat towards top of microscope <input type="checkbox"/> Inspect wafer alignment with yellow filter on microscope <input type="checkbox"/> Check Lithography: <input type="checkbox"/> Open <input type="checkbox"/> Clean <input type="checkbox"/> Sharp Definition
	DEEP UV #1 (254 nm): <input type="checkbox"/> 250 sec Deep UV Exposure @ 16mW/cm ² optical intensity
	PMGI DEVELOP #1: <input type="checkbox"/> 50 sec Develop with SAL 101 @ 500 rpm <input type="checkbox"/> 40 sec DI @ 500 rpm <input type="checkbox"/> Bucket Rinse with DI H ₂ O <input type="checkbox"/> Dry with N ₂ on clean Texwipes
	DEEP UV #2 (254 nm): <input type="checkbox"/> 250 sec Deep UV Exposure @ 16mW/cm ² optical intensity
	PMGI DEVELOP #2: <input type="checkbox"/> 50 sec Develop with SAL 101 @ 500 rpm <input type="checkbox"/> 40 sec DI @ 500 rpm <input type="checkbox"/> Bucket Rinse with DI H ₂ O <input type="checkbox"/> Dry with N ₂ on clean Texwipes
	INSPECT WAFER: <input type="checkbox"/> Inspect PMGI. Under cut should be obvious (0.5 μm)
	Remove 1813: <input type="checkbox"/> 30 sec spray with Acetone Bottle at 500 RPM <input type="checkbox"/> 30 sec Isopropyl Alcohol at 500 RPM <input type="checkbox"/> 30 sec H ₂ O at 500 RPM <input type="checkbox"/> Dry with N ₂ at 500 RPM <input type="checkbox"/> Dry with N ₂ on clean Texwipes
	O₂ PLASMA ASHER: <input type="checkbox"/> 4 min LFE Barrel Asher (place in front)
	REFLOW: <input type="checkbox"/> Place in 250°C oven <input type="checkbox"/> Close door and start timer <input type="checkbox"/> Heat for 70 sec <input type="checkbox"/> Remove from oven <input type="checkbox"/> Cool wafer
	INSPECT WAFER: <input type="checkbox"/> Inspect PMGI.

Step #	Process Step
	DEHYDRATION BAKE: <input type="checkbox"/> 1 min 110°C Hot Plate Bake
	1813 COAT: <input type="checkbox"/> Flood wafer with 1813 <input type="checkbox"/> 30 sec Spin at 4,000 RPM, Ramp=200 <input type="checkbox"/> 75 sec 110°C Hot Plate Bake <input type="checkbox"/> Check cleanliness of wafer backside
	EXPOSE 1813 with Bridge MASK: <input type="checkbox"/> Align <input type="checkbox"/> 50 sec Exposure (405 nm) on Mask Aligner (90 settings) @ 20mW/cm ² optical intensity
	1813 DEVELOP: <input type="checkbox"/> 40 sec Develop with (1:5) 351:DI H ₂ O at 500 RPM <input type="checkbox"/> 30 sec DI H ₂ O Rinse at 500 RPM <input type="checkbox"/> Rinse wafer backside with DI H ₂ O Bucket Rinse <input type="checkbox"/> Dry with N ₂ on clean Texwipes
	INSPECT LITHOGRAPHY: <input type="checkbox"/> Place wafer flat towards top of microscope <input type="checkbox"/> Inspect wafer alignment with yellow filter on microscope <input type="checkbox"/> Check Lithography : <input type="checkbox"/> Open <input type="checkbox"/> Clean <input type="checkbox"/> Sharp Definition
	EVAPORATE Bridge METAL: <input type="checkbox"/> Evaporate 300 Å/ 4000 Å Ti/Au (Ti on surface, Au on top of Ti)
	METAL LIFT-OFF: <input type="checkbox"/> Heat 1165 to 90°C <input type="checkbox"/> Tape lift off <input type="checkbox"/> Remove remaining metal using Acetone on a petri dish <input type="checkbox"/> 20 sec spray with Acetone Bottle at 500 RPM <input type="checkbox"/> 30 sec Isopropyl Alcohol at 500 RPM <input type="checkbox"/> 30 sec DI water at 500 RPM <input type="checkbox"/> Dry with N ₂ at 500 RPM <input type="checkbox"/> Dry with N ₂ on clean Texwipes <input type="checkbox"/> Check backside and clean if necessary
	DEHYDRATION BAKE: <input type="checkbox"/> 1 min 110°C Hot Plate Bake
	1818 COAT & SLICE: <input type="checkbox"/> Flood wafer with 1818 <input type="checkbox"/> 30 sec Spin at 4,000 RPM, Ramp=200 <input type="checkbox"/> 75 sec 110°C Hot Plate Bake <input type="checkbox"/> Check cleanliness of wafer backside <input type="checkbox"/> Saw the devices
	REMOVE PMGI: <input type="checkbox"/> 2 min 1165 at 90°C <input type="checkbox"/> 6x DI H ₂ O Rinse <input type="checkbox"/> Dry with N ₂ on clean Texwipes

	INSPECT WAFER: <input type="checkbox"/> Inspect
--	---

APPENDIX D
MASK TEMPLATE ARRANGEMENT

D.1 Second mask template arrangement

D3000-14	D3030-20	D3040-20
D3010-14	D3020-20	D3050-20
D3020-14	D3010-20	D3060-20
D3030-14	D3000-20	D3070-20
D3040-14	D3200-14	D3080-20
D3050-14	D3190-14	D3090-20
D3060-14	D3180-14	D3100-20
D3070-14	D3170-14	D3110-20
D3080-14	D3160-14	D3120-20
D3090-14	D3150-14	D3130-20
D3100-14	D3140-14	D3140-20
D3110-14	D3130-14	D3150-20
D3120-14	D3120-14	D3000-14 S0.5
D3120-14	D3120-14	D3000-14 S0.5

D.2 Third mask template arrangement

D3000-14	D3300 14 S05 R	D3000 14 S10 R
D3000-14	D3300 14 S05 L	D3000 14 S10 L
D3000-14	D3300 14 S05 R	D3000 14 S10 R
D3000-14	D3300 14 S05 L	D3000 14 S10 L
D3010-14	D3300 14 S05 R	D3000 14 S10 R
D3010-14	D3300 14 S05 L	D3000 14 S10 L
D3010-14	D3300 14 S05 R	D3000 14 S10 R
D3010-14	D3300 14 S05 L	D3000 14 S10 L
D3020-14	D3000 14 S05 R	D3300 14 S10 R
D3020-14	D3000 14 S05 L	D3300 14 S10 L
D3020-14	D3000 14 S05 R	D3300 14 S10 R
D3020-14	D3000 14 S05 L	D3300 14 S10 L
D3030-14	D3000 14 S05 R	D3300 14 S10 R
D3030-14	D3000 14 S05 L	D3300 14 S10 L
D3030-14	D3000 14 S05 R	D3300 14 S10 R
D3030-14	D3000 14 S05 L	D3300 14 S10 L
D3040-14	D3200-14	D3000 14 S15 R
D3040-14	D3200-14	D3000 14 S15 L
D3040-14	D3200-14	D3000 14 S15 R
D3040-14	D3200-14	D3000 14 S15 L
D3050-14	D3190-14	D3000 14 S15 R
D3050-14	D3190-14	D3000 14 S15 L
D3050-14	D3190-14	D3000 14 S15 R
D3050-14	D3190-14	D3000 14 S15 L
D3060-14	D3180-14	D3300 14 S15 R
D3060-14	D3180-14	D3300 14 S15 L
D3060-14	D3180-14	D3300 14 S15 R
D3060-14	D3180-14	D3300 14 S15 L
D3070-14	D3170-14	D3300 14 S15 R
D3070-14	D3170-14	D3300 14 S15 L
D3070-14	D3170-14	D3300 14 S15 R
D3070-14	D3170-14	D3300 14 S15 L
D3080-14	D3160-14	D3000 14 S10 R
D3080-14	D3160-14	D3000 14 S10 L
D3080-14	D3160-14	D3000 14 S10 R
D3080-14	D3160-14	D3000 14 S10 L
D3090-14	D3150-14	D3000 14 S10 R
D3090-14	D3150-14	D3000 14 S10 L
D3090-14	D3150-14	D3000 14 S10 R
D3090-14	D3150-14	D3000 14 S10 L
D3100-14	D3140-14	D3120 14
D3110-14	D3130-14	D3300 14 S10 R
D3110-14	D3130-14	D3300 14 S10 L
D3110-14	D3130-14	D3300 14 S10 R
D3110-14	D3130-14	D3300 14 S10 L
D3120-14	D3120-14	D3300 14 S10 R
D3120-14	D3120-14	D3300 14 S10 L

REFERENCES

- 1 David Maliniak, "On The Road (map): Interconnects face the future", Electronic Design, pp. 77, Oct 13, 1995.
- 2 J. P. Bristow, A. Husain et all, "Progress and status of guided-wave optical interconnection technology", Optoelectronic Interconnects, SPIE vol. 1849, pp. 4-10, 1993.
- 3 James G. Grote, "Digital logic and reconfigurable interconnects using Aluminum Gallium Arsenide Electro-Optic Fredkin Gates", technical report # WL-TR-94-5028, 1994.
- 4 Ronald A. Nordin, A. F. J. Levi, Richard N. Nottenburg, J. O'Gorman, T. Tanbun-Ek, And Ralph A. Logan, "A Systems Perspective on Digital Interconnection Technology", Journal of Lightwave Technology, vol. 10 no. 6, pp. 811-827, June 1992
- 5 Christopher Tocci, H. John Caulfield, "Optical interconnection Foundation and Applications", Artech House, Inc, 1994, Norwood, MA
- 6 Y. S. Liu, H. S. Cole, J. Bristow, Yue Liu, "Polymer-based Optical Interconnect Technology - A Route to Low-cost Optoelectronic Packaging and Interconnect", Optoelectronic Interconnects III, SPIE vol. 2400, pp. 80-88, 1995.
- 7 Chadd Noddings, Tom Hirsch, Michael Olla, Charles Spooner, and Jason Yu, "Low-cost optical interconnect module for parallel optical data links", Optoelectronic Interconnects III, SPIE vol. 2400, pp. 44-47, 1995.
- 8 Julian Bristow, "Intra computer optical interconnects: progress and challenges", Optoelectronic interconnects and packaging, SPIE vol. CR62, pp. 318-326, 1996.
- 9 S. N. Mohammad, Arnel A. Salvador, and Hadis Morkoç, "Emerging Gallium Nitride Based Devices", Proceedings of the IEEE. vol. 83 pp. 1306-1355, 1995.
- 10 H. Morkoç, S. Strite, G. B. Gao, M. E. Lin., B. Sverdlov, and M. Burns, "Large-band-gap SiC, III-V nitride, and II-VI ZnSe-based semiconductor device technologies", Journal of Applied Physics, vol. 76, no. 3, pp. 1363-1398, 1994.

11 Samuel Strite, "Workshop summarizes gallium nitride research", *Laser Focus World*, vol. 32 no. 8 pp. 26 - 28, 1996.

12 X. J. Ning, F. R. Chien, P. Pirouz, J. W. Yang, Asif Khan, "Growth defects in GaN films on sapphire: The probable origin of threading dislocations", *Journal of materials research*. vol. 11 pp. 580-592, 1996.

13 Private conversations with Dr. Asif Khan May 96.

14 Mohammad A. Karim "Electro-Optical Devices and Systems", PWS-KENT publishing company, Boston, Massachusetts 1990

15 Amnon Yariv and Pochi Yeh "Optical Waves in Crystals", John Wiley & Sons, Inc., New York 1984.

16 X. C. Long, R. A. Myers, S. R. J. Brueck, R. Ramer, K. Zheng, "GaN linear electro-optic effect", *Applied Physics Letters* vol. 67 pp. 1349-1351, 1995.

17 M.A Khan, J. N. Kuznia, S. Gupta, and R. K. Jain, "Direct measurement of the electro-optic effect in GaN", *To appear in IEE Electronic Journal*, 1997.

18 R. G. Hunsperger "Integrated Optics: Theory and Technology", Third Edition. Springer-Verlag, New York, NY 1991.

19 Richard Syms, and John Cozens "Optical Guided Waves and Devices" McGraw-Hill Book Company, Berkshire, England 1992.

20 Amnon Yariv "Optical Electronics", Fourth Edition. Saunders College Publishing, a division of Holt, Rinehart and Winston, Inc. Chicago, IL 1991.

21 M. Papuchon, Am. Roy, D. B. Ostrowsky "Electrically active optical bifurcation:BOA", *Applied Physics Letters*, vol 31, no 4, pp. 266-267, 1977

22 Marcuse, Dietrich, "Theory of Dielectric Optical Waveguides", second edition. Academic press, Inc., 1250 Sixth Avenue San Diego, CA 92101, 1991

23 R. Scarmozzino, A. Gopinath, R. Pregla, and S. Helfert, "Numerical Techniques for Modeling Guided-Wave Photonic Devices", *IEEE Journal of selected topics in quantum electronics*, vol. 6, no. 1, pp. 150-162

24 Eugene Hecht "Optics", Second Edition. Addison-Wesley Publishing Company, Printed in the United States of America, 1989

25 J. M. O'Hare, "Optical Radiation and Matter" EOP 502 class booklet. Center for electro-optics, University of Dayton, 1991

26 Amnon Yariv "Optical Electronics in Modern Communications", Fifth Edition. Oxford University Press Inc. 198 Madison Avenue, New York, New York 10016-4314, 1997

27 E. A. J. Marcatili "Dielectric Rectangular Waveguide and Directional Coupler for integrated Optics", The Bell System Technical Journal, vol. 48, pp. 2071-2102, 1969

28 Richard A. Forber and Emanuel Marom "Symmetric Directional Coupler Switches", IEEE Journal of Quantum Electronics, vol. QE-22, no.6, pp. 911-919, 1986

29 Kamal Goel and William S. C. Chang "Extinction Ratio Degradation Due to Asymmetry in Zero-Gap Directional Coupling and Crossing Channel Switches", IEEE Journal of Quantum Electronics, vol. QE-23, no. 22, pp. 2216-2223, 1987

30 V. R. Chinni, T. C. Huang, P. -K. A. Wai, C. R. Menyuk, G. J. Simonis "Crosstalk in a Lossy Directional Coupler Switch", Journal of Lightwave Technology, vol. 13, no 7, 1995

31 Chang-Min Kim and Dong-Gak Kim "Influence of parasitic couplings in bending sections on directional coupler optical switching", Journal of Optical and Quantum Electronics, vol. 30, no. 2, pp. 133-140, 1998

32 Dapeng Xu, Hui Yang, D. G. Zhao, S. F. Li, and R. H. Wu "Room-temperature optical transitions in Mg-doped cubic GaN/GaAs (100) grown by metalorganic chemical vapor deposition", Journal of Applied Physics, vol. 87, no. 4, pp. 2064-2066, 2000

33 Oliver Branndt, Hui Yang, Jochen R. Müllhäuser, Achim Trampert, Klaus H. Ploog "Properties of cubic GaN grown by MBE", Material Science and Engineering B, vol. 43, no. 1 / 3, pp. 215-221

34 B. D Cullity "Elements of X-ray Diffraction", second edition. Addison-Wesley Publishing Company, Inc. Reading Massachusetts, 1978.

35 Michael S. Shur, M. Asif Khan “GaN/AlGaN Heterostructure devices: Photodetectors and Field-Effect Transistors. MRS Bulletin, vol. 22, no. 2, pp. 44-50, Feb 1997

36 Ralph Williams, “Modern GaAs Processing Methods”, Artech House, Inc, 1990, Norwood, MA

37 S. J. Pearton, J. C. Zolper, R. J. Shul, F. Ren, “GaN: Processing, Defects, and Devices”, Journal of Applied Physics, vol. 86, no. 1, pp. 1-78, 1999

38 S. P. Denbaars “Gallium-Nitride-Based Materials for Blue to Ultraviolet Optoelectronics Devices”, Proceedings of the IEEE, vol. 85, no. 11, 1740-1749, 1997

39 I. Grzegory, M. Bockowski, B. Lucznik, S. Krukowski, M. Wroblewski, S. Porowski, “Recent Results in the Crystal Growth of GaN at High N₂ Pressure”, MRS Internet Journal Nitride Semiconductor Research, vol. 1, article 20, 1996

40 T. Suski, J. Jun, M. Leszczynski, H. Teisseyre, I. Grzegory, S. Porowski, G. Dollinger, K. Saarinen, T. Laine, J. Nissilä, W. Burkhard, W. Kriegseis, B. K. Meyer “High pressure fabrication and processing of GaN:Mg”, Materials Science and Engineering B Solid State, vol. 59, no. 1/3, pp. 1-5, 1999

41 S. Porowski, “Near Defect Free GaN Substrates”, MRS Internet Journal Nitride Semiconductor Research, vol. 4S1, article G1.3, 1999

42 Takayuki Inoue, Yoji Seki, Osamu Oda, Satoshi Kurai, Yoichi Yamada, Tsunemasa Taguchi “Growth of Bulk GaN Single Crystals by the Pressure-Controlled Solution Growth Method”, Japanese journal of applied physics part 1, vol. 39, no. 4B, pp. 2394-2398, 2000

43 N. Grandjean, M. Leroux, M. Laügt, and J. Massies, “Gas source molecular beam epitaxy of wurtzite GaN on sapphire substrates using GaN buffer layers”, Applied Physics Letters, vol. 71, no. 2, 1997

44 F. A. Ponce “Defects and interfaces in GaN Epitaxy”, MRS Bulletin, vol. 22, no. 2, pp. 51-57, Feb 1997

45 V. Ramachandran, R. M. Feenstra, W. L. Sarney, L. Salamanca-Riba, D. W. Greve “Optimized structural properties of wurtzite GaN on SiC(0001) grown by

molecular beam epitaxy”, Journal of Vacuum Science and Technology A, vol. 18 no. 4, pp. 1915-1918, 2000

46 Shuji Nakamura, “InGaN/GaN/AlGaN Based Laser Diodes with an estimated lifetime of longer than 10,000 hours”, MRS Bulletin, vol. 23, no. 5, pp. 37-43, 1998

47 S. J. Pearlton, F. Ren, A. P. Zhang, et all. “GaN Electronics For High Power, High Temperature Applications”, The electrochemical society interface, vol. 9, no. 2, pp. 34-39 Sumr 2000

48 S. Yoshida S, S. Misawa, S. Gonda, “Epitaxial-Growth of GaN/AlN Heterostructures, Journal of Vacuum Science and Technology B-Microelectronics Processing and Phenomena, vol. 1, no. 2, pp. 250-253, 1983

49 H. Amano, N. Sawaki, I. Akasaki, Y. Toyoda, “Metalorganic vapor phase epitaxial growth of a high quality GaN film using an AlN buffer layer”, Applied Physics Letters, vol. 48, no. 5, 1986

50 S. N. Mohammad, W. Kim, A. Salvador, H. Morkoç, “Reactive Molecular Beam Epitaxy for Wurtzite GaN”, MRS Bulletin, vol. 22, no. 2, pp. 22-28, Feb 1997

51 P. Waltereit, O. Brandt, A. Trampert, M. Ramsteiner, M. Reiche, M. Qi, K. H. Ploog, “Influence of AlN nucleation layers on growth mode and strain relief of GaN grown on 6H-SiC(0001)”, Applied Physics Letters, vol. 74, no. 24, pp. 3660-3662, 1999

52 H. Angerer, O. Ambacher, R. Dimitrov, Th. Metzger, W. Rieger, M. Stutzmann, “PEMBE-Growth of Gallium Nitride on (0001) Sapphire: A comparison to MOCVD grown GaN”, MRS Internet Journal Nitride Semiconductor Research, vol. 1, article 15, 1996

53 Shuji Nakamura, Takashi Mukai, Masayuki Senoh, “Candela-class high-brightness InGaN/AlGaN double-heterostructure blue-light-emitting diodes”, Applied Physics Letters, vol. 64, no. 13, pp. 1687-1689, 1994

54 A. Y. Cho and K. Y. Cheng, “Growth of Extremely Uniform Layers by Rotating Substrate Holder with Molecular Beam Epitaxy for applications to Electro-Optic and microwave devices”, Applied Physics Letters, vol. 38, no. , pp. 360-362, 1981

55 K. Y. Cheng, “ Molecular Beam Epitaxy Technology of III.V Compound Semiconductors for Optoelectronic Applications”, Proceedings of the IEEE, vol. 85, no 11, 1997

56 N. Grandjean, J. Massies, “Molecular beam epitaxy growth of nitride materials”, Material Science and Engineering B, vol. 59, no. 1/3, pp. 39-46, 1999

57 S. Dalmasso, B. Damilano, N. Grandjean, J. Massies, M. Leroux, J.-L. Reverchon, J.-Y. Duboz, “Optoelectronic characterization of blue InGaN/GaN LEDS grown by MBE”, Materials Science and Engineering B, vol. 82, no. 1-3, pp. 256–258, 2001

58 J. S. Moon, M. Micovic, P. Janke, P. Hashimoto, W.-S. Wong, R. D. Widman, L. McCray, A. Kurdoghlian, C. Nguyen “GaN/AlGaN HEMTs operating at 20 GHz with continuous-wave power density $> 6\text{W/mm}$ ”, Electronic Letters, vol 37, no. 8, pp. 528-530

59 D.E. Grider, N.X. Nguyen, C. Nguyen, “GaN MODFET microwave power technology for future generation radar and communications systems”, Solid-State Electronics vol. 43, no. 8, pp. 1473-1478, 1999

60 A. Vescan, R. Dietrich, A. Wieszt, H. Tobler, H. Leier, J.M. Van Hove, P.P. Chow, A.M. Wowchak, “MBE grown AlGaN/GaN MODFETs with high breakdown voltage”, Journal of Crystal Growth, vol. 201/202, pp. 327-331, 1999

61 Tsvetanka S. Zheleva, Ok-Hyun Nam, Michael D. Bremser, Robert F. Davis, “Dislocation density reduction via lateral epitaxy in selectively grown GaN structures”, Applied Physics Letters, vol. 71, no. 17, pp. 2472-2474, 1997

62 Akira Usui, Haruo Sunakawa, Akira Sakai, A. Atsushi Yamaguchi, “Thick GaN Epitaxial Growth with Low Dislocation Density by Hydride Vapor Phase Epitaxy”, Japanese Journal of Applied Physics Part 2, vol. 36, no. 7B, pp. L899-L902, 1997

63 P. Kozodoy, J. P. Ibbetson, H. Marchand, P. T. Fini, S. Keller, J. S. Speck, S. P. DenBaars, U. K. Mishra, “Electrical characterization of GaN p-n junctions with and without threading dislocations”, Applied Physics Letters, vol. 73, no. 7, pp. 975-977, 1998

64 X. Zhang, P. D. Dapkus, D. H. Rich, "Lateral epitaxy overgrowth of GaN with NH₃ flow rate modulation", Applied Physics Letters, vol. 77, no. 10, pp. 1496-1498, 2000

65 Hiroshi Amano, Masahiro Kito, Kazumasa Hiramatsu, Isamu Akasaki, "P-Type Conduction In Mg-Doped Gan Treated With Low-Energy Electron Beam Irradiation (LEEBI)", Japanese Journal of Applied Physics Part 2, vol. 28, no. 12, pp. L2112-L2114, 1989

66 Shuji Nakamura, Masayuki Senoh, Takashi Mukai, " Highly P-typed Mg-Doped GaN Films Grown with GaN Buffer Layers", Japanese Journal of Applied Physics Part 2, vol. 30, no. 10A, pp. L1708-L1711, 1991

67 Shuji Nakamura, Takashi Mukai, Masayuki Senoh, Naruhito Iwasa "Thermal Annealing Effects on P-Type Mg-Doped GaN Films", Japanese Journal of Applied Physics Part 2, vol. 31, no. 2B, pp. L139-L142, 1992

68 M. E. Lin, C. Xue, G. L. Zhou, , H. Morkoç, "P-Type Zincblende GaN on GaAs substrates", Applied Physics Letters, vol. 63, no., pp. 932-933, 1993

69 M. J. Bergmann, Ü. Özgür, H. C. Casey Jr., H. O. Everitt, J. F. Muth, "Ordinary and extraordinary refractive indices for Al_xGa_{1-x}N epitaxial layers", Applied Physics Letters, vol. 75, no. 1, pp. 67-69, 1999

70 O. Ambacher, M. Arzberger, D. Brunner, H. Angerer, F. Freudenberg, N. Esser, T. Wethkamp, K. Wilmers, W. Richter, M. Stutzmann, "AlGaN-Based Bragg Reflectors", MRS Internet Journal of Nitride Semiconductor Research, vol 2, article 22, 1997

71 D. Brunner, H. Angerer, E. Bustarret, F. Freudenberg, R. Höpler, R. Dimitrov, O. Ambacher, M. Stutzmann, "Optical constants of epitaxial AlGaN films and their temperature dependence", Journal of Applied Physics, vol. 82, no. 10, pp. 5090-5096, 1997

72 G. M. Laws, E. C. Larkins, I. Harrison, C. Molloy, D. Somerford, "Improved refractive index formulas for the Al_xGa_{1-x}N and In_yGa_{1-y}N alloys", Journal of Applied Physics, vol. 89, no. 2, pp. 1108-1115, 2001

73 J. Miragliotta, D. K. Wickenden, T. J. Kistenmacher, and W. A. Bryden, "Linear- and nonlinear-optical properties of GaN thin films", Journal of the Optical Society of America B, vol. 10, no. 8, pp. 1447-1456

74 D. N. Hahn, G. T. Kiehne, J. B. Ketterson, G. K. L. Wong, P. Kung, A. Saxler, M. Razeghi, "Phase-matched optical second-harmonic generation in GaN and AlN slab waveguides", Journal of Applied Physics, vol. 85, no. 5, pp. 2497-2501

75 R. J. Shul, L. Zhang, C. G. Willison, J. Han, S. J. Pearton, J. Hong, C. R. Abernathy, L. F. Lester, "Group-III Nitride Etch Selectivity in BCl_3/Cl_2 ICP Plasmas", MRS Internet Journal of Nitride Semiconductor Research, vol 4S1, article G8.1, 1999

76 J.C. Zolper, R. J. Shul, "Implantation and Dry Etching of Group-III-Nitride Semiconductors" MRS Bulletin, vol. 22, no. 2, pp. 36-43, 1997

77 R. J. Shul, C.G. Willison, M. M. Bridges, J. Han, J. W. Lee, S. J. Pearton, C. R. Abernathy, J. D. MacKenzie, S. M. Donovan, L. Zhang, L. F. Lester, " Selective inductively coupled plasma etching of group-III nitrides in Cl_2 - and BCl_3 -based plasmas" Journal of Vacuum Science Technology A, vol. 16, no. 3, pp. 1621-1626

78 Jewon Lee, Hyun Cho, David C. Hays, Cammy R. Abernathy, Stephen J. Pearton, Randy J. Shul, G. Allen Vawter, J. Han, "Dry etching of GaN and related materials: comparison of techniques" IEEE Journal on Selected Topics in Quantum Electronics , vol. 4, no. 3, pp. 557-563, 1998

79 D. A. Stocker, E. F. Schubert, J. M. Redwing, "Crystallographic wet chemical etching of GaN", Applied Physics Letters, vol 73, no. 18, pp. 2654-2656

80 C. Youtseya, I. Adesida, G. Bulman, "Highly anisotropic photoenhanced wet etching of n-type GaN", Applied Physics Letters, vol. 71, no. 15, pp. 2151-2153

81 M. P. Mack, G. D. Via, A. C. Abare, M. Hansen, P. Kozodoy, S. Keller, J. S. Spek, U. K. Mishra, L. A. Coldren, S. P. DenBaars, " Improvement of GaN-Based Laser Diode Facets by FIB Polishing" Electronic Letters, vol. 34, no 13, pp. 1315-1316

82 Karl S. Kunz, Raymond J. Luebbers, "The finite difference time domain method for electromagnetics", Boca Raton : CRC Press, c1993.